Computational Turbulent Incompressible Flow

Applied Mathematics: Body & Soul Vol 4

Johan Hoffman and Claes Johnson

24th February 2006

Contents

Preface

Applied Mathematics: Body&Soul is a mathematics education reform project including a series of books, together with associated educational material and open source software freely available from the project web page at `www.bodysoulmath.org`.

Body&Soul reflects the revolutionary new possibilities of mathematical modeling opened by the modern computer in the form of *Computational Mathematical Modeling (CMM)*, which is now changing the paradigm of mathematical modeling in science and technology with new methods, questions and answers.

The Body&Soul series of books presents a synthesis of computational mathematics (Body) and analytical mathematics (Soul) including applications. Volumes 1-3 [28] give a modern version of calculus and linear algebra starting at a basic undergraduate level, and subsequent volumes on a graduate level cover different areas of applications with focus on computational methods:

- Volume 4: Computational Turbulent Incompressible Flow.
- Volume 5: Computational Turbulent Compressible Flow.
- Volume 6: Computational Dynamical Systems

The present book is Volume 4, with Volumes 5 and 6 to appear in 2007 and further volumes on solid mechanics and electromagnetics being planned. An gentle introduction to the Body&Soul series is given in [54].

The overall goal of the Body&Soul project may be formulated as the *Automation of CMM* involving the key steps of automation of (i) discretization, (ii) optimization and (iii) modeling. The objective of the Automation of CMM is to open for massive use of CMM in science, engineering, medicine, and other areas of application. Automation of CMM is realized in the *FEniCS project* (`www.fenics.org`), which represents the top software part of Body&Soul.

The automation of discretization (i) involves automatic translation of a given differential equation in standard mathematical notation into a discrete system of equations, which can be automatically solved using numerical linear algebra to produce an approximate solution of the differential equation. The translation is performed using adaptive stabilized finite element methods, which we refer to as General Galerkin or G2 with the adaptivity based on a posteriori error estimation by duality and the stabilization representing a weighted least squares control of the residual.

The automation of optimization (ii) is performed similarly starting from the differential equations expressing stationarity of an associated Lagrangian. Finally, one can couple modeling to optimization by seeking from an Ansatz a model with best fit to given data.

The present book on *Computational Fluid Dynamics* (CFD) may be viewed as a test of the functionality of the general technique for the Automation of CMM based on G2. In this book we apply G2 to the specific problem of solving the incompressible Navier–Stokes (NS) and Euler equations computationally. The challenge includes computational simulation of turbulent flow, since solutions of the NS and Euler equations in general are turbulent, and thus the challenge in particular includes the open problem of computational turbulence modeling.

We show in the book that G2 passes this test successfully: By direct application of G2 to the Navier–Stokes or Euler equations, we can on a PC compute quantities of interest of turbulent flow in the form of mean values such as drag and lift, up to tolerances of interest. G2 does not require any user specified turbulence model or wall model for turbulent boundary layers; by the direct application of G2 to the NS or Euler equations, we avoid introducing Reynolds stresses in averaged NS equations requiring turbulence models. Instead the weighted least squares stabilization of G2 automatically introduces sufficient turbulent dissipation on the finest computational scales and thus acts as an automatic turbulence model. Furthermore, the adaptivity of G2 ensures that the flow is automatically resolved by the mesh where needed. G2 thus opens for the *Automation of CFD*, which could be an alternative title of this book.

Applying G2 to the NS and Euler equations opens a vast area for exploration, which we demonstrate by resolving several scientific mysteries, including d'Alembert's Mystery of zero drag in inviscid flow, and uncovering several secrets of fluid dynamics including the secret of flying. In particular we are led to a new formulation of thermodynamics based on deterministic microscopical mechanics with deterministic mean value outputs coupled with indeterminate pointwise outputs. The new formulation is not based on microscopical statistics as statistical mechanics, and thus offers a rational scientific basis of thermodynamics based on computation. It appears that this approach also may give insight to physics following the idea that Nature in one way or the other is performing an analog computation when evolving in time from one moment to the next.

We are also led to a new computational approach to basic mathematical questions concerning existence and uniqueness of solutions of the NS and Euler equations, for which analytical methods have not shown to be productive.

In short, we show that G2 opens to new insights into both mathematics, physics and mechanics with an amazingly rich range of possible applications. The main message of this book thus is that of a breakthrough: Using G2 one can simulate turbulent flow on a a standard PC with a 2 GHz processor and 1-2 Gb memory computing on adaptive meshes with $10^5 - 10^6$ mesh points in space (but not less). We hope the reader will have a good time browsing through the book and trying out the G2 FEniCS software on the Navier-Stokes and Euler equations.

Stockholm and Göteborg in February 2006

Johan Hoffman and Claes Johnson

Part I

Overview

1
Main Objective

> Turbulence is one of the principal unsolved problems of physics today. ....The real challenge, it seems to us, is that no adequate model for turbulence exists today.... The equations of motion have been analyzed in great detail, but it is still next to impossible to make accurate quantitative predictions without relying heavily on empirical data. (Tennekes and Lumley in A First Course in Turbulence, 1994).

This book is devoted to *computational fluid dynamics* with focus on *turbulent incompressible flow*. In this first Part I we give a glimpse of the central themes of the book, which are developed in detail in Part II on Computational Method and Part III on Flow Fundamentals. In a companion forthcoming volume, we extend to turbulent compressible flow.

A *fluid* may appear in the form of a liquid like water or a gas like air. Water is virtually *incompressible*; the relative change in volume for each atmosphere in pressure is less than 10^{-6}. Air can be viewed to be incompressible as long as the flow speed is well below the speed of sound, that is for flow speeds less than say 200 miles per hour.

Turbulence in fluid flow represents a basic phenomenon of our world of crucial importance in a wide range of phenomena in Nature and technical applications. Turbulent flow has a complex, seemingly chaotic, variation in space and time on a wide range of scales from small to large, and typically appears for fluids with *small viscosity*, such as air and water.

The basic mathematical models for fluid flow, incompressible and compressible, are given by the the *Euler equations* and the *Navier–Stokes equations* expressing conservation of mass, momentum and energy. The Euler equations model the flow of a fluid with zero viscosity, referred to as an *ideal*

fluid, and were formulated by Euler in 1755. The Navier–Stokes equations model the flow of a fluid with positive viscosity, and were formulated during 1821-45 by Navier, Stokes, Poisson and Saint-Venant, assuming the fluid to be *Newtonian*, with the viscous forces depending linearly on velocity strains.

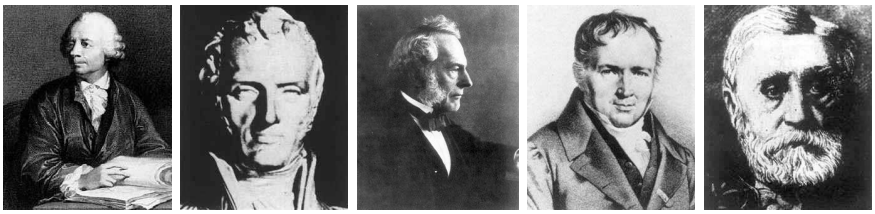

FIGURE 1.1. Leonhard Euler (1707-1783), Claude Louis Marie Henri Navier (1785–1836), George Gabriel Stokes (1819–1903), Siméon Denis Poisson (1781–1840), and Adhémar Jean Claude Barré de Saint-Venant (1797–1886).

We all have practical experience of fluid motion and the concept of *viscosity* for fluids with large viscosity such as heavy oil or tooth paste, and fluids with small viscosity such as air and water. The Navier–Stokes equations appear to be an accurate mathematical model of fluid flow with varying viscosity from small to large, including in particular turbulent flow for fluids with small viscosity. There are also non-Newtonian fluids with a nonlinear dependendence of the viscosity, typically fluids with large viscosity such as polymers.

The basic mathematical models for turbulence thus appear to be known since very long, but nevertheless turbulence is viewed as the basic open problem of classical mechanics. How can it be? The main reason is that the progress of solving the Navier–Stokes equations equations using analytical mathematical methods to obtain quantitative information about turbulent flow, has been very slow or rather non-existent, because the complexity of turbulent solutions to the Navier-Stokes equations defy analytical representations. Even basic qualitative mathematical questions concerning existence and uniqueness of solutions represent open problems seemingly inaccessible to analytical mathematical treatment using classical methods of calculus and functional analysis.

The main objective of this book is to show that it is possible to accurately simulate turbulent fluid flow by solving the Navier-Stokes or Euler equations computationally using solid mathematical principles, in simple geometries on a PC, and in complex geometries on clusters of PCs. The main objective is thus to demonstrate that *computational turbulence* now is available for massive use in a wide range of applications.

2
Mysteries and Secrets

> ...the whole procedure was an act of despair because a theoretical interpretation had to be found at any price, no matter how high that might be... (Planck on the statistical mechanics basis of his radiation law)
>
> Sommerfeld's very exhaustive discussion of Couette flow led to the conclusion that this type of flow remains stable for all viscosities. For a time, after this negative result had been obtained, it was thought that the method of small oscillations was unsuitable for the theoretical solution of the problem of transition to turbulence. It transpired later that this view was not justified, because Couette flow is a very special and restricted example. (Schlichting in Boundary Layer Theory, p 465, McGraw-Hill 1979)

2.1 Mysteries

We shall also demonstrate the usefulness of computational turbulence in basic science by resolving the following unsolved mysteries, which have haunted scientists over centuries:

- d'Alembert's Mystery: Zero drag of inviscid flow.
- Loschmidt's Mystery: Violation of the 2nd law of thermodynamics.
- Sommerfeld's Mystery: Stability of Couette flow.

All these mysteries reflect *paradoxes*, where phenomena predicted by mathematics are not at all observed in reality. Since science is supposed to be rational and based on mathematics, paradoxes are catastrophical for the credibility of science, and thus have to be resolved (or covered up), in one way or the other, at any price.

In d'Alembert's Mystery formulated in 1752 [22], mathematics predicts that a body may move through a fluid with zero (very small) viscosity, like air and water, with zero (very small) resistance or *drag*. But everbody knows that this is impossible; the drag increases roughly quadratically with the velocity and becomes very substantial for higher velocities.

In Loschmidt's Mystery formulated in 1876 [72], mathematics of systems with zero viscosity predicts that time reversal and a perpetum mobile is possible. But everybody knows that time is always moving forward and that a perpetum mobile is impossible, as expressed by the 2nd law of thermodynamics.

In Sommerfeld's Mystery from 1908 [84], mathematics predicts that the simplest of all flows, Couette flow with a stationary linear velocity profile, is stable and thus should exist. But nobody has ever observed this flow in a fluid with small viscosity.

The cover up of d'Alembert's Mystery is to blame the assumption of zero viscosity for the erronous prediction: In reality there is always some possibly very very small viscosity (of some nature), which changes everything (in some mysterious way). We will below argue that such explanations are not scientifically satisfactory and we shall instead present a new resolution based on computational turbulence in the inviscid Euler equations.

The cover up of Loschmidt's Mystery is to introduce statistical mechanics based on microscopic games of roulette. We will below argue that such an explanation is cumbersome scientifically, and we shall instead present a new resolution demonstrated through computational turbulence in the Euler equations.

The cover up of Sommerfeld's Mystery is to say that a linear velocity profile is too simple for the mathematical theory to apply, which evidently is not scientifically satisfactory either. We will below computationally study Couette flow and we will find that it is not stable, just as observed. After this experience we will be able to theoretically understand, using mathematics and avoiding the pitfall of Sommerfeld, *why* Couette flow is not stable.

2.2 Secrets

As applications of computational turbulence we shall uncover (some of the) secrets of the following activities based on turbulent incompressible flow of air:

- ball sports,
- flying,
- sailing,
- racing.

In all ball sports including soccer, baseball, tennis, golf and table-tennis, the player that can control the spin of the ball to give it a desired curved path, has an important advantage. The fluid mechanics giving the spinning ball a curved path, depending on the direction of the spin, is referred to as the *Magnus effect* which creates a *lift* force perpendicular to the direction of motion (and spin). Below we will study the Magnus effect computationally including the dependence on the spin, speed and the roughness of the surface of the ball. Of course, the flow of air around a spinning ball is turbulent.

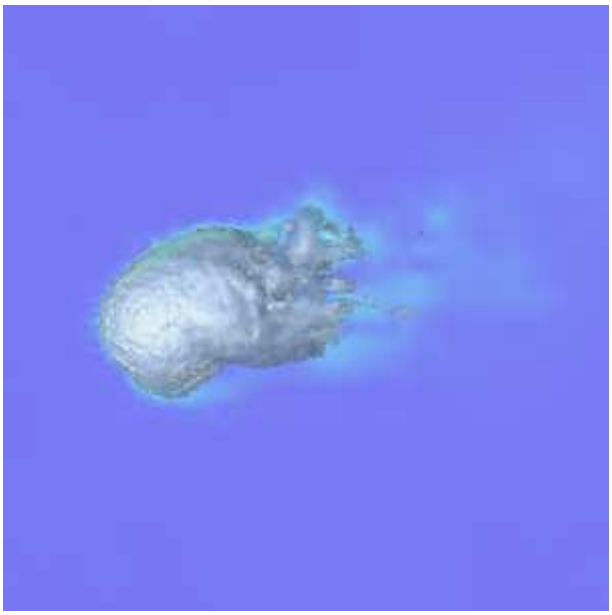

FIGURE 2.1. Turbulent flow around a spinning ball.

To understand why flying is possible, we will below simulate the turbulent flow around a wing, and this way uncover how the necessary lift and unavoidable drag is generated. We shall also see that without computational turbulence it is impossible to mathematically predict lift and drag, in particular at take-off and landing, where the *angle of attack* of the wing against the flow is large and the flow is very turbulent. We shall thus compute the turbulent flow around a wing at different angles of attack and

discover that the flow features are very different for the low angle of attack at crusing speed and the high angle of attack at take-off and landing. We shall see that classical analytical mathematical methods may give fairly reasonable predictions for (very) long wings at small angles of attack, but not so for normal wings and/or large angles of attack. To cruise at 30.000 feet is one thing, and to take off and land a completely different game.

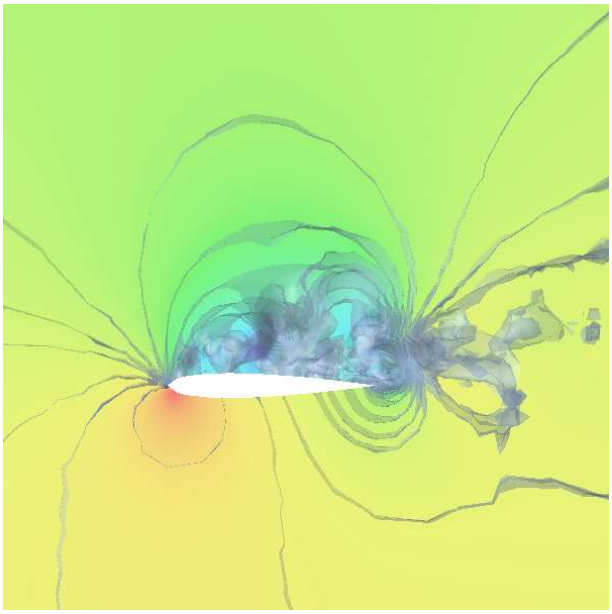

FIGURE 2.2. Turbulent flow around a wing.

Sailing is similar to flying from a fluid mechanics point of view, with the sail when going against the wind acting like a wing giving a lift force pulling the sail and boat against the wind but also tilting the boat. Needless to say, the flow of air around a sail is turbulent, and thus computational turbulence certainly opens new insights into the art of sailing and how to win Americas Cup. Also the keel of a sailing boat acts like a wing and gives a pull partly balancing the side force from the sail.

Modern cars are designed to have small drag, since fuel consumption directly couples to drag, and for racing cars also the lift is of concern since a flying racing car is hard to control. Computational turbulence offers new possibilities of car design, since traditional experimental testing of prototypes in wind tunnels is very slow and costly.

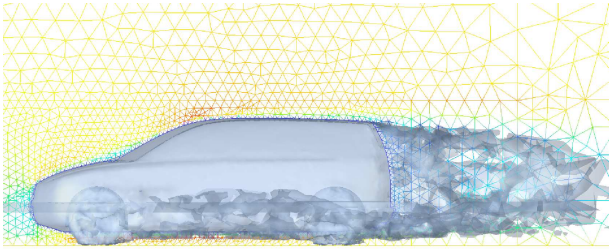

FIGURE 2.3. Turbulent flow around a car.

3

Turbulent flow and History of Aviation

> I feel perfectly confident, however, that this noble art will soon be brought home to man's general convenience, and that we shall be able to transport ourselves and families, and their goods and chattels, more securely by air than by water, and with a velocity of from 20 to 100 miles per hour. (George Cayley 1809)

3.1 Leonardo da Vinci, Newton and d'Alembert

Is it conceivable that with proper mathematics, humans would have been flying, at least gliders (without engine), several hundred years before this actually came true in the late 19th century? Well, let's face some facts.

The idea of flying, like the birds, goes back at least to Greek mythology about the inventor and master craftsman Deadalus, who built wings for himself and his son Icaros in order to escape from imprisonment in the Labyrinth of Knossos on the island of Crete.

Leonardo da Vinci made impressive and comprehensive investigations into aerodynamics collected into his *Treatise on the Flight of Birds* from 1505, and designed a large variety of devices for muscle-powered human flight. After extensive testing da Vinci realized that even if both arms and legs got involved through elaborate mechanics, human power was insufficient to get off the ground.

Newton confirmed these experiences by calculating the lift of a tilted flat plate, representing a wing, in a horisontal stream of "air particles" hitting

the plate from below, to obtain a disappointingly small (erronous) value of the lift.

Newton's result was further supported by d'Alembert's Mystery predicting that both the drag and the lift of a body traveling through air would be close to zero, clearly at variance with many early observations of birds flying long distances even without flapping wings. d'Alembert built his computations of drag (and lift) on particular solutions to the Euler equations referred to as *potential solutions*, with the velocity given as the gradient of a potential satisfying Laplace's equation. But nobody could come up with any kind of resolution of the paradox before Ludwig Prandtl (1875-1953), called the Father of Modern Fluid Dynamics, in a short note from 1904 suggested a resolution based on boundary layer effects from vanishingly small viscosity, which no fluid dynamicist dared to question. As already indicated, we shall below present computational evidence that Prandtl's resolution is not credible and instead put forward a new scientifically more satisfactory resolution.

3.2 Cayley and Lilienthal

Despite the pessimistic predictions by Newton and d'Alembert, the 29 years old engineer George Cayley (uncle of the mathematician Arthur Cayley) in 1799 sketched the by now familiar configuration of an airplane with fixed cambered wings and aft horisontal and vertical tails, and also investigated the characteristics of airfoils using a whirling arm apparatus. Cayley outlined his ideas about the principles of flying in *On Aerial Navigation* (1809). But Cayley did not produce any mathematical description of the motion of an aircraft and thus had no quantitative basis for designing airplanes. In 1849 Cayley built a large glider, along the lines of his 1799 design, and tested the device with a 10-year old boy aboard. The glider carried the boy aloft on at least one short flight.

The next major step was taken by the German engineer Otto Lilienthal, who made careful experiments on the lift and drag of wings of different shapes and designed various gliders, and himself made 2000 more or less successful flights starting from a little hill, see Fig 3.1, before he broke his neck in 1896 after the glider had stalled 15 meter above ground.

3.3 Kutta, Zhukovsky and the Wright Brothers

Stimulated by Lilienthal's successful flights and his widely spread book *Bird Flight as the Basis of Aviation* from 1899, the mathematician Martin Kutta (1867-1944) in his thesis from 1902 modified the erronous classical potential flow solution by including a new term corresponding to a rotating

FIGURE 3.1. Otto Lilienthal (1848-1896), some of the 137 known photos from 1891 to 1896. To document the development of his flight technique he was regulary joined by photographers during his flight practise (photos from Archive Otto-Lilienthal-Museum / `www.lilienthal-museum.de`).

flow around the wing with the strength of the vortex determined so that the combined flow velocity became zero at the trailing edge of the wing. This *Kutta condition* reflected the observation of Lilienthal that the flow should come off the wing smoothly, at least for small angles of attack. The strength of the vortex was equal to the *circulation* around the wing of the velocity, which was also equal to the lift. Kutta could this way predict the lift of various airfoils with a precision of practical interest. But the calculation assumed the flow to be fully two-dimensional and the wings to be very long and became inaccurate for shorter wings and large angles of attack.

The first successful powered piloted controled flight was performed by the brothers Orwille and Wilbur Wright on December 17 1903 on the windy fields of Kitty Hawk, North Carolina, with Orwille winning the bet to be the pilot of the *Flyer* and Wilbur watching on ground, see Fig 3.2. In the words of the Wright brothers from Century Magazine, September 1908: "The flight lasted only twelve seconds, a flight very modest compared with that of birds, but it was, nevertheless, the first in the history of the world in which a machine carrying a man had raised itself by its own power into the air in free flight, had sailed forward on a level course without reduction of speed, and had finally landed without being wrecked. The second and third flights were a little longer, and the fourth lasted fifty-nine seconds, covering a distance of 852 feet over the ground against a twenty-mile wind." The modern era of aviation had started.

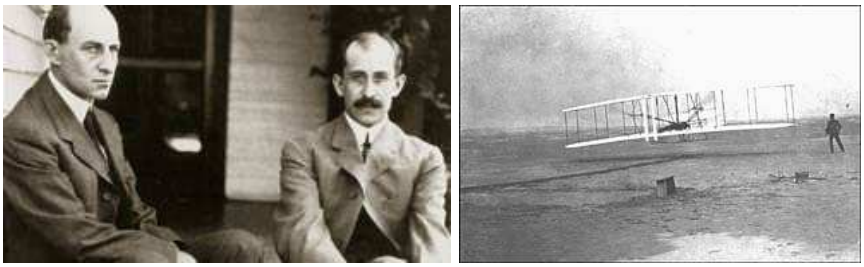

FIGURE 3.2. Orwille Wright (1871-1948) and Wilbur Wright (1867-1912) and the lift-off at Kitty Hawk, North Carolina, the 17th December 1903.

The mathematician Nikolai Zhukovsky (1847-1921), called the Father of Russian Aviation, in 1906 independently derived the same mathematics for computing lift as Kutta, after having observed several of Lilienthal's flights, which he presented before the Society of Friends of the Natural Sciences in Moscow as: "The most important invention of recent years in the area of aviation is the flying machine of the German engineer Otto Lilienthal". Zhukovsky also purchased one of the eight gliders which Lilienthal sold to members of the public.

Kutta and Zhukovsky thus could modify the mathemathical potential theory of lift of a wing to give reasonable results, but of course could not give anything but a very heuristic justification of their Kutta-Zhukovsky condition of zero velocity at the trailing edge of the wing, and could not treat realistic wings in three dimensions. Further, their modified potential solutions were not turbulent at all, so their calculations would seem merely like happy coincidences (knowing ahead the correct answer to obtain). We will return below in more detail to the basic problem of lift and drag of wings in turbulent flow.

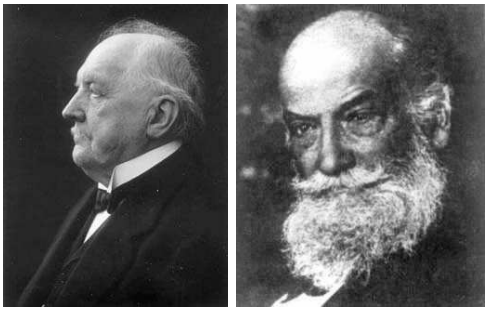

FIGURE 3.3. Martin Kutta (1867-1944) and Nikolai Egorovich Zhukovsky (1847-1921).

Today computational methods open new possibilities of solving the equations for fluid flow using the computational power of modern computers.

Thus, for the first time the mathematical fluid models of Euler and Navier-Stokes may come to a real use, which opens new revolutionary possibilities of computational simulation and prediction of fluid flow in science and technology. The range of possible applications is incredibly rich! For example, it is now becoming possible to simulate the turbulent flow around an entire aircraft and thus systematically investigate questions of stability and control, which caused severe head-ache for the Wright brothers, as well as the designers of the modern Swedish jet fighter JAS Gripen. Actually, both the 1903 Wright *Flyer* airplane with a forward canard instead of an aft tail, and the JAS are unstable and require careful control to fly. The instability of the fighter is intentional allowing quick turns, but the Wrights later replaced the canard with the conventional aft tail to improve stability. The stability of an airplane is similar to that of a boat, with the important design feature being the relative position of the center of gravity and the center of the forces from the fluid (center of buoyancy for a boat), with the center of gravity ahead (below) giving stability.

FIGURE 3.4. The 1903 Wright *Flyer* and JAS Gripen (JAS photo from `http://www.gripen.com/`.

It is remarkable that 400 years passed between Leonardo da Vinci's investigations and the largely similar ones by Lilienthal. Why did it take so long time from almost success to success? Can we blame the erronous mathematics of Newton and d'Alembert for the delay? Or was the reason that the (secret) writings of da Vinci were made public with a delay of 300 years? We leave the question open.

4

The Navier–Stokes and Euler Equations

> However sublime are the researches on fluids which we owe to Messrs Bernoulli, Clairaut and d'Alembert, they flow so naturally from my two general formulae that one cannot sufficiently admire this accord of their profound meditations with the simplicity of the principles from which I have drawn my two equations ...(Euler 1752)

4.1 The Navier–Stokes Equations

For an incompressible Newtonian fluid of constant unit density and constant *viscosity* $\nu > 0$ enclosed in a volume Ω in $\mathbb{R}^3$ with boundary Γ over a time interval $I = (0, T]$, the Navier–Stokes equations (NS) read as follows:

$$\begin{aligned} \dot{u} + (u \cdot \nabla)u - \nu\Delta u + \nabla p &= f, && \text{in } \Omega \times I, \\ \nabla \cdot u &= 0, && \text{in } \Omega \times I, \\ u &= 0, && \text{on } \Gamma \times I, \\ u(\cdot, 0) &= u^0, && \text{in } \Omega, \end{aligned} \tag{4.1}$$

where $u = u(x,t) = (u_1(x,t), u_2(x,t), u_3(x,t))$ is the *velocity* and $p = p(x,t)$ the *pressure* of the fluid at $(x,t) = (x_1, x_2, x_3, t) \in \Omega \times I$ with u_i the velocity in the coordinate direction x_i, and the dot indicates differentiation with respect to time. Further, $f = (f_1, f_2, f_3)$ is a given *volume force* (like gravity) acting on the fluid, and $u^0 = u^0(x)$ is a given initial velocity. We here assume homogeneous Dirichlet boundary conditions for the velocity, and consider other boundary conditions below.

The first equation in (4.1) expresses Newton's 2nd law of conservation of momentum in vector form with ∇p the pressure force and $-\nu\Delta u$ the viscous force of a Newtonian fluid, and the second equation expresses conservation of mass in the form of incompressibility. Newton's 2nd law in component form reads

$$\dot{u}_i + \sum_{j=1}^{3} u_j u_{i,j} - \nu\Delta u_i + p_{,i} = f_i, \quad i = 1, 2, 3,$$

where $,j$ indicates differentiation with respect to x_j, or equivalently

$$\dot{u}_i + \sum_{j=1}^{3} (u_j u_i)_{,j} - \nu\Delta u_i + p_{,i} = f_i, \quad i = 1, 2, 3,$$

where we used the incompressibility of u: $\nabla \cdot u = \sum_{j=1}^{3} u_{j,j} = 0$.

For incompressible flow, the equation expressing conservation of total energy, that is the sum of kinetic energy and heat energy), is decoupled from the equations (4.1) expressing conservation of momentum and mass. We return below to the full model including the energy equation.

We note that the given data for NS is represented by (Ω, T, f, u^0) together with the viscosity ν, and $\hat{u} = (u, p)$ is the corresponding solution which we seek. The specification of the data (Ω, T, f, u^0) is usually clear, and we now comment on the determination of the viscosity ν, which may be much less clear.

4.2 What is Viscosity?

In fact, viscosity closely couples to turbulence and thus the viscosity in NS would rather represent a *turbulent viscosity* $\nu = \nu(u)$ with a possibly very complex dependence on the velocity u; with a non-constant ν the viscous term would take the form $-\nabla \cdot (\nu\nabla u)$. But if indeed ν depends on u and we cannot determine how, then the NS equations would seem to be useless for predictions, even using computational methods.

So how are we going to handle this problem? Well, first we recall that we focus on the case of *small viscosity*. The first idea that comes up is then of course to assume that the viscosity is so small that we can put it equal to zero. This leads to the *Euler equations*, which we present in the next section. This is an elegant solution: By assuming the viscosity to be zero there is no viscosity to specify as data. We shall below investigate how far this elegant solution can take us, and see that it is indeed quite far.

Next we assume that ν is non-vanishing, but still small, so that we are facing NS. We shall below see that solving NS computationally we have to use a mesh with a certain mesh size h, and we shall see that the computational method itself introduces an effect which can be viewed as a mesh

dependent *artificial viscosity* ν_h. Now, if $\nu_h > \nu$, then the true viscosity ν will be overshadowed by the artificial viscosity ν_h, which means that the precise value of ν becomes irrelevant. And the smaller ν is, the bigger is the chance that it will be overshadowed by the artificial viscosity ν_h, so that we do not have to determine ν accurately; it would be sufficient just to know that ν is (sufficiently) small.

Of course, we expect the solution $(u, p) = (u_\nu, p_\nu)$ to depend on ν, and in order for a computation with an artificial viscosity $\nu_h > \nu$ to have some predictive value, it is necessary that the *output* or *quantity of interest* from the solution (u_ν, p_ν) is not critically depending on the precise value of ν. We shall below see that this may indeed be true in many cases if the output is a mean value in space-time such as a *drag coefficient* $c_D(\nu)$ measuring the total force of a body moving through a fluid with viscosity ν. Thus, we shall see that $c_D(\nu)$ varies quite slowly with ν, which means that we do not have to know ν very precisely (which certainly helps when determining ν), or that we effectively can compute with an artificial viscosity ν_h and only need to know that $\nu < \nu_h$. Thus, the good news is that for turbulent flow with small viscosity, in many cases we do not need to specify the viscosity very precisely, which would be very difficult.

We shall also study cases with a critical dependence on (small) viscosity, including the so-called *drag crisis* reflecting that the resistance of e.g. a sphere of unit diameter and speed moving through a fluid, quite suddenly drops by 50% as ν decreases to about 10^{-6} to raise again for smaller ν.

As indicated, we shall see that simply assuming $\nu = 0$, in a case where we know that the viscosity is small but not exactly how small, will take us quite far. This follows the initial ingenious idea of Euler of studying ideal fluids with zero viscosity, but we shall see that to arrive at this peak, we will have to pass through the deep valley of d'Alembert's paradox.

To sum up: Turbulence occurs in fluids with small viscosity ν and typical outputs may have a weak dependence on ν. This means that we do not need precise information on ν; in many cases we may effectively set $\nu = 0$ following Euler, or knowing just one binary digit of ν may be enough. Thus turbulent flow is difficult because of its complexity, but may be easy because precise information on the viscosity is not needed. This is favorable for computation, because complexity is handled by brute computational power, while the viscosity advantage remains.

4.3 The Euler Equations

Setting the viscosity $\nu = 0$ in Navier–Stokes equations (4.1), we obtain the *Euler equations for incompressible inviscid flow*:

$$\begin{aligned} \dot{u} + (u \cdot \nabla)u + \nabla p &= f && \text{in } \Omega \times I, \\ \nabla \cdot u &= 0 && \text{in } \Omega \times I, \\ u \cdot n &= 0 && \text{on } \Gamma \times I, \\ u(\cdot, 0) &= u^0 && \text{in } \Omega, \end{aligned} \tag{4.2}$$

where n is the outward unit normal to Γ. Here we only prescribe the normal velocity $u \cdot n = 0$ on the boundary, while the tangential velocity $u \cdot \tau$ is free, where τ is a tangential direction. This is also referred to as a *slip* boundary condition, as compared to the *no-slip* Dirichlet boundary condition $u = 0$ in the NS boundary condition including $u \cdot \tau = 0$.

4.4 Friction Boundary Condition

We start our studies in Chapter 9 considering the Euler equations with slip boundary condition, following the historical development of fluid dynamics, to discover several surprising facts. Later we shall also discuss *friction* boundary conditions for the Euler equations with the tangential velocity $u \cdot \tau$ coupled to the tangential strain with a friction parameter, with slip corresponding to zero friction. We will view the friction boundary conditions as a simple so-called *wall model* for the flow in a *turbulent boundary layer* close to the boundary, with the friction parameter depending on the Reynolds number.

We will find that we may simulate flows with very large Reynolds number using the Euler equations with proper friction boundary condition, without computationally resolving the boundary layer. Computational solution of the Euler equations thus will become extremely useful all along Eulers original plans, which resurrects Eulers model after a long dark age of discredit caused by d'Alembert's Mystery.

4.5 Euler Equations as Einstein's Ideal Model

The Euler equations (with slip boundary conditions) is an example of the ideal mathematical model according to Einstein, that is, a model *without any parameter*. The only parameter in NS is the viscosity ν and setting $\nu = 0$, we obtain the Euler equations without any parameter. The advantage of a model without parameter, is that we do not need to feed in values of the parameter (like the viscosity) to make predictions. But is it really possible to make predictions about the flow of a fluid without knowing the

viscosity of the fluid, only knowing that the viscosity is small? In the book we shall show that this is possible, but not in the classical way that led to catastrophy assuming that the effect of viscosity was zero, but in a new non-trivial way building on the observation that outputs of turbulent flows may have a weak dependence on viscosity!

4.6 Euler and NS as Dynamical Systems

The Euler and Navier–Stokes equations are examples of a *dynamical system* of the general form of an initial value problem $\dot{u}(t) = g(u(t))$ for $t \in (0, T]$, $u(0) = u^0$, where $g(v)$ is a given function of v, u^0 is a given initial value, and $t \to u(t)$ is the solution defined on $[0, T]$. We say that the function $v \to g(v)$ expresses the *law of the dynamical system*. We also refer to a solution $t \to u(t)$ as a *trajectory* of the dynamical system. In a dynamical system of this form time changes continuously over an interval of time from an initial time 0 to a final time T. If g is bounded, then a solution $u(t)$ is continuous in time.

5
Triumph and Failure of Mathematics

The field of hydrodynamic phenomena which can be explored with exact analysis is more and more increasing. (Zhukovsky, 1911)

5.1 Triumph: Celestial Mechanics

In the famous treatise *Celestial Mechanics* in five volumes published during 1799-1825, Laplace formulated Newton's theory of gravitation in the form $-\Delta\phi = \rho$, where ϕ is the *gravitational potential* and ρ the *mass distribution*. Knowing the mass distribution, e.g. one heavy point mass representing the Sun, surrounded by lighter point masses representing the planets, that is, knowing $\rho(x)$ at a given time instant one can solve for $\phi(x)$ and obtain the gravitational force field $F(x) = \nabla\phi(x)$, from which the acceleration of the masses can be determined using Newton's Law $F = ma$, where m is the mass and a the acceleration. From the acceleration, the velocity and motion of the masses can then be determined. Laplace could thus summarize celestial mechanics in the differential equation $-\Delta\phi = \rho$, and in particular this way prove Newton's inverse square law, which Newton just assumed to be true. Laplace could thus, and also did, predict the positions of the planets many years ahead from knowing their present positions and velocities. This is probably the most important triumph of mathematics all times, and gave mathematics and science an enormous boost.

FIGURE 5.1. Isaac Newton (1643-1727), Pierre-Simon Laplace (1749-1827), and Jean Le Rond d'Alembert (1717-1783).

5.2 Failure: Potential Flow

The triumph for mathematics in celestial mechanics starting with Newton, stimulated mathematicians of the 18th and 19th centuries to try the same approach for fluid mechanics, with the hope of summarizing also this scientific discipline in the form $\Delta\phi = 0$, with ϕ now a *velocity potential* with $\nabla\phi$ representing the flow velocity. The prospects seemed really good: In this form one could represent a variety of ideal, *stationary* (time-independent), incompressible, *irrotational* flows as potential flows. We recall that a flow velocity u is irrotational if $\nabla \times u = 0$, which holds if $u = \nabla\phi$.

We know that potential flows had been studied already by d'Alembert in the mid 18th century and d'Alembert had published his paradox 1752: A body of any shape can move through a lightly viscous fluid like water without any drag! Of course nobody could believe this, which from start gave mathematical fluid mechanics a strange reputation among the many practitioners of hydraulical engineering, which probably has lasted into our days. The challenge is to change this unfortunate situation.

The same mathematical equation, Laplace's equation, which was so amazingly successful in celestial mechanics, thus was a complete failure in fluid mechanics, and evidently mathematics and fluid mechanics lived a long time with a very disturbing paradox. How could that be?

As indicated, we present below a new resolution of d'Alembert's Mystery to illustrate basics aspects of fluid flow, including stability and transition to turbulence.

6
Laminar and Turbulent Flow

Il y a toujours sur ma strophe ou sur ma page
un peu de l'ombre du nuage et de la salive de la mer;
ma pensée flotte et va et vient, comme dénouée par toute
cette gigantesque oscillations de l'infini. (Victor Hugo)

In my boyhood I had the advantage of the constant guidance of my father, also a lover of mechanics, and a man of no mean attainments in mathematics and its application to physics. (Reynolds)

6.1 Reynolds

The Navier–Stokes equations give an accurate description of a great variety of fluid flows including both *laminar flow* with ordered flow features and *turbulent flow* with unordered seemingly chaotic fluid dynamics.

The onset of turbulence in laminar flow was studied experimentally by Osborne Reynolds in the 1880s. By injecting dye in a flow through a transparent pipe of a certain length, Reynolds could trace streamlines of the flow through the pipe, and thus observe the straight streamlines of laminar inlet flow starting to fluctuate into irregular motion downstream. Reynolds thus could study *transition* from laminar to turbulent flow, see Fig. 6.1.

Reynolds tried to find a connection between transition and the *Reynolds number* $Re \equiv \frac{UL}{\nu}$, where U represents a characteristic flow velocity and L a characteristic length scale. Reynolds found that transition occurred if Re was large enough (usually in the range $10^2 - 10^3$), but his hope to determine a *critical value of* Re, above which transition would always occur

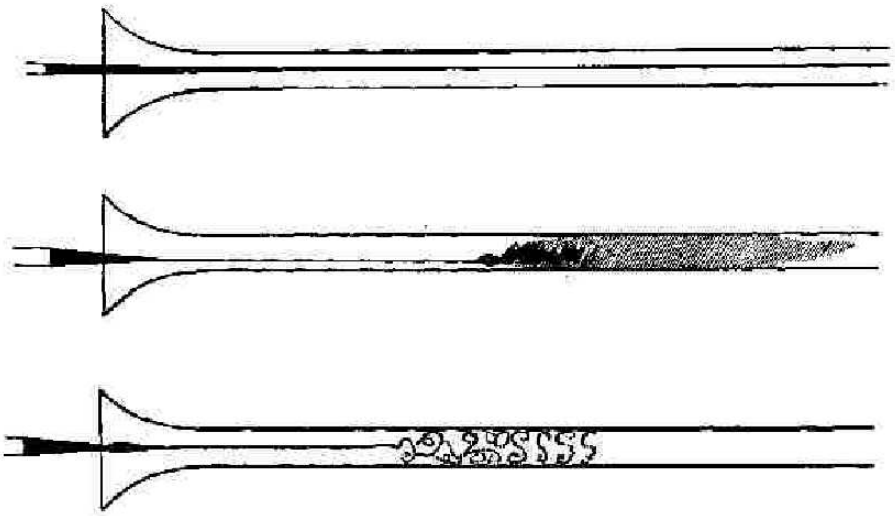

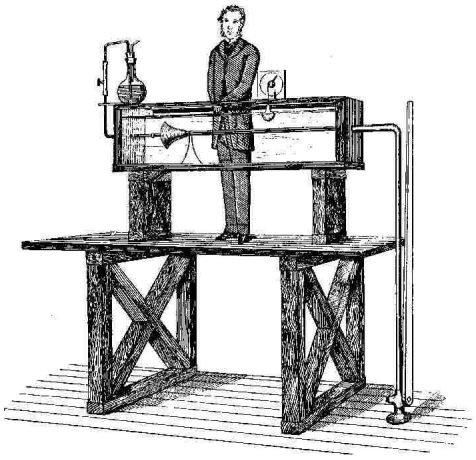

FIGURE 6.1. "This is a definite relation of the exact kind for which I was in search. Of course without integration the equations only gave the relation without showing at all in what way the motion might depend upon it. It seemed, however, to be certain, if the eddies were due to one particular cause, that integration would show the birth of eddies to depend on some definite value of UL/ν" (Osborne Reynolds, 1842-1912).

and never below, turned out to be elusive. We will explain in Chapter 34 below in a detailed study of transition, why this is impossible. In short, the reason is that transition occurs if a product of perturbation growth and perturbation level is above a certain threshold, and only the perturbation growth can be connected to Re. In Reynolds' experiments the perturbation level varied from one day to the other, and thus the transition clould occur at a certain Re one day, but not the next. Therefore Reynolds' idea of a critical value of Re for transition will have to be abandoned.

As a consequence, there is no precise value of Re indicating the presence of turbulence in a given flow, but most flows exhibit turbulent flow features for $Re \geq 10^3$, because perturbations are always present in both practice and controlled experiments, albeit on different levels. Kolmogorov conjectured in his famous 1941-articles [65, 66, 64] that turbulent flow features occur on a range of length scales down to a smallest scale, which may be estimated to be of size $Re^{-3/4}$, normalizing to $L = 1$. We can thus use the rough size of Re to indicate the qualitative nature of a given flow, such as the presence and scale features of turbulent flow.

6.2 Applications and Reynolds Numbers

Important applications concern fluid flow around *bluff bodies*, such as the flow of air around a car, a jumbo-jet at take off/landing or the sail of a sailing boat, or the flow of water around a super-tanker or a sailing boat, which all represent incompressible partly turbulent flows at large Reynolds numbers: $Re \approx 10^6$ for a car traveling at 60 mph, $Re \approx 10^8$ for a jumbo jet or a super-tanker at cruising speed, while $Re \approx 10^{10}$ might be relevant in meteorology. In bluff body flow, turbulence typically appears in a *boundary layer* close to the surface of the body, and in a *wake* attaching to the rear of the body, while the flow elsewhere is laminar, see Fig. 6.2. Typically the boundary layer is laminar on the body surface facing the flow, with streamlines following the surface, until *separation* away from the surface into recirculating turbulent flow. For very high Re ($\sim 10^6$) the boundary layer may undergo transition to turbulence before separation, resulting in a delayed separation of the boundary layer, corresponding to a drastically reduced volume of the wake, and thus also a reduction of the drag force, referred to as *drag crisis*.

In everyday life, we can observe separating laminar/turbulent bluff body flow around a boat, a stone in a river, or a car in the case of light rain or mist when the flow pattern becomes visible, see Fig. 6.2-6.3.

In this book we focus on flows with *medium* (say $Re \approx 10^2 - 10^4$) over *large* (say $Re \approx 10^4 - 10^6$) to *very large* (say $Re > 10^7$) Reynolds numbers involving both laminar and turbulent flow features, which appear in many important applications. For short we refer to such flows as *turbulent flows*.

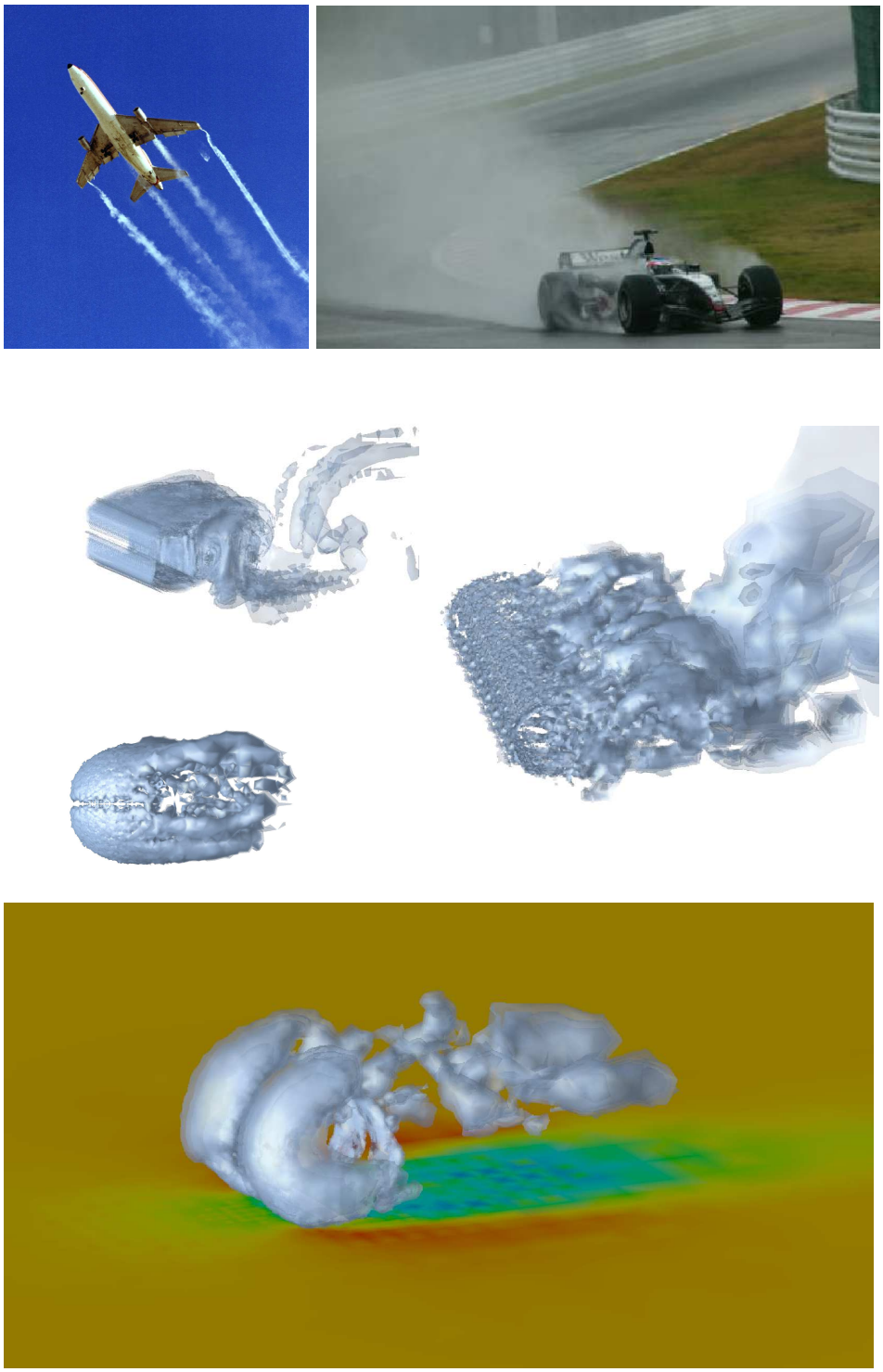

FIGURE 6.2. Lockheed L-1011 and F1 racing car (upper), vorticity in computations of flow past square and circular cylinders and a sphere, transversal velocities in a boundary layer computation, and in a computation of flow past cylinder rolling along ground (modeling a wheel).

Such flows typically have surfaces separating laminar and turbulent flow, see Fig. 6.2. For very large Reynolds numbers we use the Euler equations, formally corresponding to $Re = \infty$.

Normalizing to $U = L = 1$, we thus focus on flows with medium small viscosity ($\nu \approx 10^{-2} - 10^{-4}$), over small ($\nu \approx 10^{-4} - 10^{-6}$) to very small viscosity or zero viscosity ($\nu = 0$), that is, we focus on *small viscosity*. We shall see that the precise value of the small viscosity, or the large Reynold's number, in many cases is irrelevant. As indicated, this relieves us from the difficult (or simply impossible) task of determining a precise value of the viscosity ν to put into the NS equations.

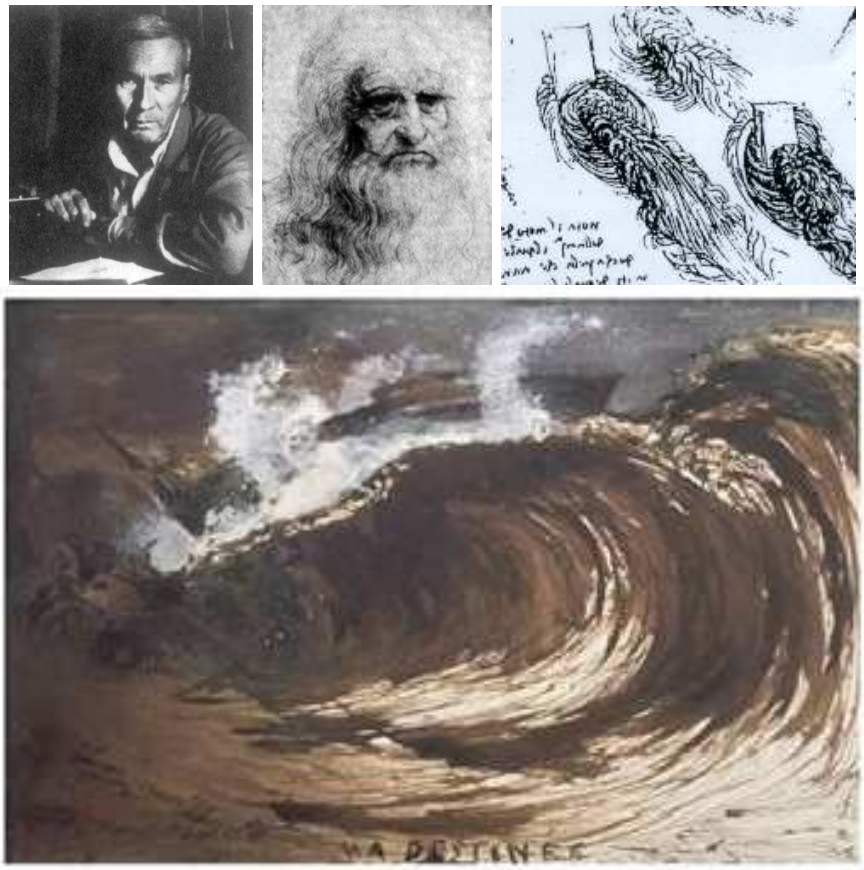

FIGURE 6.3. Andrey Nikolaevich Kolmogorov (1903-1987), and Leonardo da Vinci (1452–1519) with a sketch of turbulent wakes behind bluff bodies, and "My Destiny" by Victor Hugo. Inscription on the ship; FRACTA SED INVICTA.

7
Computational Turbulence

> The closer mutual approximation of the points of view of theory and practice brings most beneficial results, and it is not exclusively the practical side that gains; under its influence the sciences are developing in that this approximation delivers new objects of study or new aspects in subjects long familiar. In spite of the great advance of the mathematical sciences due to the works of the outstanding mathematicians of the last three centuries, practice clearly reveals their imperfection in many respects; it suggests problems essentially new for science and thus challenges one to seek quite new methods. And if theory gains much when new applications or developments of old methods occur, the gain is still greater when new methods are discovered; and here science finds a reliable guide in practice. (Chebyshev 1856)

7.1 Are Turbulent Flows Computable?

The main question addressed in this book is the following: Can we compute solutions to the NS or Euler equations in the case of turbulent flow? Or shorter: Are turbulent flows computable?

Recalling the dimensional analysis of Kolmogorov (1903-1987), it would appear that to pointwise resolve all the scales of turbulent flow in a *Direct Numerical Simulation DNS*, would seem to require of the order Re^3 mesh points in space-time, assuming the smallest scale in space and time is $Re^{-3/4}$ and $L = T = 1$. Thus, already a flow at $Re = 10^6$ would seem to require at least $Re^3 = 10^{18}$ mesh points in space-time for pointwise repre-

sentation, which is beyond the capacity of any foreseeable computer. Not to speak of Euler with $Re = \infty$!

Does this mean that we have to give up, and simply conclude that turbulent flows are not computable? The answer is yes if we ask for pointwise accurate computations in space-time. This not only because the number of mesh points would be overwhelming, but also because in fact pointwise values of a turbulent flow are not well defined, but fluctuate in a seemingly chaotic way. So even if we could compute with 10^{18} mesh points, we should not expect to be able to get pointwise accurate solutions for turbulent flow.

In fact, as we will see below, mathematical existence of pointwise solutions can neither be proved nor expected, and pointwise accurate computed solutions thus seem to be pure fiction. We may phraze this as an impossibilty of obtaining solutions $\hat{u} = (u, p)$ to the NS or Euler equations written in the form $R(\hat{u}) = 0$, with the *residual* $R(\hat{u})$ being zero pointwise in space-time. If true this would certainly be shocking to the large community of mathematicians trying to prove existence of pointwise solutions, but would not in principle disturb a computational mathematician familiar with the fact that computational solutions usually have non-zero residuals. However, we shall see that the pointwise residuals in computational simulations of turbulent flow usually are far from being small, and facing this evidence also many computational mathematicians should become nervous. In particular, these results challenge the traditional idea of DNS as a computation with small pointwise error.

The natural way out of this obvious dilemma is to ask for less, that is to seek to compute hopefully well-defined *mean values* in space-time, instead of ill-defined *point values*. This means that as *quantities of interest*, or *observables*, or simply *outputs*, we shift from pointwise to different mean value quantities.

We further introduce a quantitative quality measure in the form of a *tolerance* indicating the desired precision in a chosen output. We also measure *computational cost*, in terms of e.g. computing time and memory requirements on a certain system. The main problem addressed in this book can now be formulated as follows:

(P) What outputs of turbulent flows are computable to what tolerance to what cost?

We present answers to this problem, and in particular we show that we can compute outputs for turbulent flows of interest in a large variety of applications using the computational power of a PC on meshes with 100 000-500 000 mesh points. These results are new and should have important consequenses concerning the use of computational methods for simulation of fluid flow.

7.2 Typical Outputs: Drag and Lift

A typical quantity of interest may be the *drag coefficient* c_D or the *lift coefficient* c_L of a bluff body, which are mean values in time of the total fluid force acting on the body in the direction of the flow and perpendicular to the flow, respectively. The drag and lift coefficients thus represent global mean values in space-time. Some car manufacturers like to present the c_D of a certain car as an indication of fuel economy (for example $c_D < 0.3$). For a jumbo-jet a decrease in drag with one percent could save $400 million in fuel cost over a 25 year life span.

As a main contribution of this book, we show that mean values such as c_D and c_L are computable on a PC within a day (in 2006) up to a tolerance of a few percent.

We also show that as the mean values become more local in space or time, the computational work to reach the same tolerance increases, so that in particular point values are uncomputable.

7.3 Approximate Weak Solutions: G2

When we relax outputs to mean values, we open to relax to a *weak solution concept*, where we ask that $((R(\hat{u}), \hat{v})) \approx 0$, where $((\cdot, \cdot))$ is a scalar product in space-time and $\hat{v}$ varies over a a set of (smooth) *test functions*. We thus relax twofold from requiring *exact* satisfaction of $R(\hat{u}) = 0$ in a *pointwise* sense, to *approximate* satisfaction $R(\hat{u}) \approx 0$ in a *weak* sense, that is, $((R(\hat{u}), \hat{v})) \approx 0$ for all test functions $\hat{v}$ with the meaning of $\approx$ made precise below. Accordingly, we say that a function $\hat{u}$ satisfying $R(\hat{u}) \approx 0$ in a weak sense, is an *approximate weak solution*.

Our main problem can now be reformulated as follows:

(P1) What is the error in output of approximate weak solutions?

To answer this question amounts to finding the effect of a nonzero residual on the output error, which as we will see can be expressed as a question of *stability* of an associated *dual problem*.

In this book we compute approximate weak solutions using a Galerkin finite element method, where we seek an approximate solution $\hat{U}$ in a finite element space satisfying $((R(\hat{U}), \hat{v})) = 0$ for a set of finite element test functions $\hat{v}$. More precisely, we use a *General Galerkin method* with a certain *strong* control of the residual in a *weighted least squares* sense, which we refer to as G2. We may thus view a G2 solution $\hat{U}$ as an approximate weak/strong solution of the Navier-Stokes or Euler equations. We shall see that the weighted least squares control corresponds to an *automatic turbulence model*, relieving us from the (very difficult or probably in general impossible) task of finding a correct turbulence model.

7.4 G2 Error Control and Stability

In general terms, we will be able to estimate an output error of a G2 solution $\hat{U}$ by a product $S\epsilon$, where ϵ measures the size of the residual $R(\hat{U})$ in the weak sense and S is a *stability factor* which measures certain norms of the solution of the dual problem with data depending on the output. The computational goal is then to achieve $S\epsilon \leq TOL$, where TOL is the tolerance.

We shall see that for turbulent solutiopns the residual $R(\hat{U})$ of a G2 solution $\hat{U}$ may be small in the weak sense, while $R(\hat{U})$ is large in the pointwise sense, and the stability factor S may be of moderate size for a mean-value output like drag and lift. Altogether, we shall thus see that it is possible to satisfy the *stopping criterion* $S\epsilon \leq TOL$ with tolerances of practical interest and mesh sizes affordable on a PC.

An output with strong sensitivity will have a very large stability factor S, and one way of expressing the chaotic nature of a pointwise output of a turbulent flow is to say that the corresponding stability factor is so large that we can never make the residual so small that $S\epsilon \leq TOL$. Effectively we may say that this corresponds to $S = \infty$, and therefore it is impossible to choose $\epsilon > 0$ so that $S\epsilon \leq TOL$. In this case it does not help to choose $\epsilon = 0$, since $S\epsilon$ is not well defined if $S = \infty$ and $\epsilon = 0$. The result is that we have to give up the idea of a pointwise well defined solution to the NS equations in the case of turbulent flow.

Stability factors obviously play a central role in this book since they directly couple to errors in outputs, and a central theme of the book is accordingly the computation of stability factors. And we will be very happy to find that stability factors for mean-value outputs are of moderate size and not too large!!

7.5 What about Mathematics of NS and Euler?

The mathematician Jean Leray proved in 1934 existence of an exact weak solution to the NS equations satisfying $((R(\hat{U}), \hat{v})) = 0$ for all test functions $\hat{v}$ (corresponding to $\epsilon = 0$), by using methods from functional analysis. Leray referred to his weak solutions as turbulent solutions. This is still today the only analytical mathematical existence result for the general form of the NS equations! Leray did not prove any result on uniqueness of weak solutions of NS equations. Since uniqueness directly couples to stability, this means that effectively Leray did not consider the aspect of stability and in particular not the question of *output uniqueness*, which for turbulent flows has to replace pointwise uniqueness: We can estimate the difference in output of two approximate weak solutions by $S\epsilon$ if ϵ bounds the two residuals, so that the output will be unique up to $S\epsilon$.

For the Euler equations not even existence of an exact weak solution has been proved mathematically. Thus the analytical mathematics for the NS and Euler equations has remained severely incomplete over a long time, with little progress.

Our results indicate that approximate weak solution and output uniqueness are suitable concepts for the NS and Euler equations, while traditional analytical mathematical techniques working with exact weak solutions without output uniqueness, are not. We will discuss these aspects in more detail below when presenting the Clay Institute Millenium $1 million Prize Problem asking for existence and uniqueness of solutions to the NS equations.

7.6 When is a Flow Turbulent?

We will identify turbulence by the fact that the G2 least squares stabilization is not small signifying that the pointwise residual is large. Typically, this situation prevails under mesh refinement which reflects that the smallest scales of the physical flow are not computationally resolved, not even on the finest mesh.

7.7 G2 vs Physics

Changing from the classical setting with pointwise residuals and outputs to the new setting of global mean value outputs and G2 weak/strong residuals, suggests a new perspective on mathematical modeling of fundamental phenomena such as turbulent fluid flow. We remarked above that residuals of approximate weak solutions of the NS equations may be large pointwise but small in a mean value sense. We may view a pointwise large NS residual as a local violation of Newtons 2nd law and incompressibility, which we could view as a local non-equilibrium. An approximate weak solution would thus represent fluid dynamics in global equilibrium but local non-equilibrium.

Experimentally we would not be able to distinguish such "imperfect fluid dynamics" from "perfect fluid dynamics" in equilibrium pointwise, since we can only observe mean values. Mathematically we would be able to rationalize "imperfect fluid dynamics" by proving existence of weak approximate solutions, but probably not "perfect fluid dynamics" requiring exact solutions with pointwise vanishing residual. The scientific study of fluid dynamics would thus concern "imperfect fluid dynamics", while "perfect fluid dynamics" would belong to metaphysics. We add more substance to this picture below. In particular we propose a solution of the classical paradox of irreversibility in reversible systems based on finite precision computation.

The same type or reasoning may apply to other fundamental mathematical models of mechanics and physics such as the Schrödinger equation for the quantum mechanics of atoms and molecules. Solutions of the Schrödinger equation are called wave functions and have an incredibly rich structure with one separate copy of $\mathbb{R}^3$ for each electron and nucleus. It is impossible to experimentally or computationally determine this structure pointwise even for small clusters of atoms, and thus the existence of a world ruled by "perfect quantum mechancis" could again be questioned. This connects to the question of how it can be that an electron is smart enough to solve its own $\mathbb{R}^3$ version of the Schrödinger equation to determine what to do? Maybe the answer is that single electrons simply aren't that smart and thus leave large pointwise residuals, while clusters of electrons can do better and have small residuals in a mean value sense, all of which could be viewed to correspond to some kind of "imperfect quantum mechancis".

7.8 Computability and Predictability

Using the NS equations to simulate fluid flow, we obtain contributions to the error in output from the following sources: (i) computation, (ii) data and (iii) modeling. In this book we focus on output errors from computation and we also discuss errors from data, which includes Ω, f, u_0, ν, while we leave out errors from modeling related to the assumptions of incompressibility and constant density. In a forthcoming volume we consider compressible and variable density flows.

We will below connect the general concept of *predictability* to the quality of output based on the quality of given data, that is, predictability will connect to error in output resulting from error in data. Further, we will connect *computability* to output error from computation.

It is natural to expect that aspects of predictability and computability closely couple, because both connect to stability or *perturbation growth* in the model. Stability factors measure the sensitivity in output to perturbations from computation, data and modeling. Large stability factors indicate strong sensitivity.

We will further use the general concept of *reliability* to signify that the output error is below a certain *tolerance* TOL. We may thus indicate the reliability of a computation of a drag coefficient c_D by stating that $c_D = 1.5 \pm TOL$, or $|c_D - 1.5| \leq TOL$, where $TOL = 0.1$.

Using the NS equations to make predictions, it may be natural to speak of a total prediction error in output including errors from both data and computation. Usually however, we connect predictability to output error from data and computability to output error from computation.

We have indicated that in turbulent flow pointwise values in space-time of velocity-pressure are not predictable/computable to any tolerance of interest. The main question of this book thus concerns the predictability and computability of mean values in space-time of turbulent flow up to tolerances of interest.

7.9 G2 in Dolfin in FEniCS

The computational results presented in the book have been obtained on a PC on a 2 GHz single processor PC with 1 Gb memory with a typical computation taking a few days using meshes with up to 500.000 mesh points in space, using an implementation of G2 in the free software Dolfin developed by Johan Hoffman and Anders Logg as part of the FEniCS project (www.fenics.org). The goal of FEniCS is to set a new standard of Automation of Computatinonal Mathematical Modelling. FEniCS serves as the top software of the Body&Soul project (www.bodysoulmath.org) and also includes a mini-version of Dolfin named *Puffin* aimed at introductory education.

The reader is encouraged to down-load Dolfin and try its Navier–Stokes/Euler solver on some problems in the book, and of course other problems. There are many waiting to be solved.

8
A First Study of Stability

> ...do steady flow ever occur in nature, or have we been pursuing fantasy all along? If steady flows do occur, which ones occur? Are they stable, or will a small perturbation of the flow cause it to drift to another steady solution, or even an unsteady one? The answer to none of these questions is known. (Marvin Shinbrot in Lectures on Fluid Mechanics, 1970)

8.1 The linearized Euler Equations

As already indicated, a main theme of this book is the stability of fluid flow. Stability concerns the growth of perturbations in the flow. Since fluid flow is well described by the Euler and NS equations, stability concerns the growth of perturbations of solutions of the Euler and NS equations. Focussing here on Euler, suppose that $\hat{u}$ and $\hat{w}$ are two solutions to the Euler equations (4.2) with different initial data u^0 and w^0. We are interested in the difference $\hat{v} = (v, q) = \hat{u} - \hat{w}$ for time $t > 0$ knowing that $v^0 = u^0 - w^0$. Subtracting the two versions of the Euler equations, we obtain the following system, which we may refer to as the *linearized Euler equations*:

$$\begin{aligned} \dot{v} + (u \cdot \nabla)v + (v \cdot \nabla)w + \nabla q &= 0 && \text{in } \Omega \times I, \\ \nabla \cdot v &= 0 && \text{in } \Omega \times I, \\ v \cdot n &= 0 && \text{on } \Gamma \times I, \\ v(\cdot, 0) &= u^0 - w^0 && \text{in } \Omega, \end{aligned} \tag{8.1}$$

We may view this as a linear system for $\hat{v}$ with u a given convection velocity, and ∇w a given reaction coefficient. The growth properties of $\hat{v}(t)$ in time expresses the stability, and these properties directly couple to the reaction term $(v \cdot \nabla)w$ with ∇w as reaction coefficient in matrix form, while the convection term $(u \cdot \nabla)v$ intuitively does not seem to influence the growth of $\hat{v}$, since it just "shifts v around". We expect the eigenvalues of ∇w to connect to the growth properties of $\hat{v}$, with eigenvalues with positive real part corresponding to eigenmodes with exponential decay and with negative real part to eigenmodes of exponential growth. Because of the incompressibility, the trace of ∇w will be zero, and thus the sum of the eigenvalues will also be zero, and thus we normally have eigenvalues with real parts of both signs. Thus normally we expect to see some exponential growth, unless all the eigenvalues are purely imaginary or zero. We thus expect perturbations of Euler solutions to grow exponentially, and thus any Euler solution would be expected to be unstable! In particular, a stationary solution given by an analytical formula would be expected to be unstable.

We notice that the stability connects to the growth properties of $\hat{v}$ which may be studied assuming the perturbations to be small so that effectively we may choose $w = u$. To study the stability of a given solution $\hat{u}$, we would thus study the linearized Euler equations (8.1) with $w = u$.

We now proceed to give two basic examples illustrating basic features of the flow of an ideal fluid, which are also relevant for fluids with small viscosity. We thus present two analytical stationary solutions to the Euler equations, and we will of course discover that they are both unstable. We will kill any hopes of the reader by reminding that an unstable solution has no permanence, and thus will have no interest from practical point of view; it simply does not "exist"and cannot be observed. We would thus be led to the conclusion that making predictions about fluid flow based on an analytical solution of the Euler or NS equations (with small viscosity) would be impossible. This would seem to indicate pretty grim perspectives for analytical mathematics in fluid dynamics. We will give evidence below indicating that this is not overly pessimistic. Of course, we will counter by showing that on the other hand computational mathematics has excellent possibilities of generating information of value, by computational solution of the Euler or NS equations.

8.2 Flow in a Corner or at Separation

We consider the constant velocity $u(x,t) = (2x_1, -2x_2, 0)$ in the halfplane $\{x_1 > 0\}$, with streamlines according to Fig 8.1. We easily check that (u,p) solves the Euler equation, with $p = -2(x_1^2 + x_2^2)$. This is the potential solution for an incompressible ideal fluid in the corner of the quarterplane $\{x_1, x_2 > 0\}$, or at a separation point at the origin considering the halfplane

$\{x_1 > 0\}$, see Fig 8.2. We will explain below, why it is referred to as a potential solution. Incidently, this potential solution is also a solution to the NS equations for any viscosity, in particular for small viscosities.

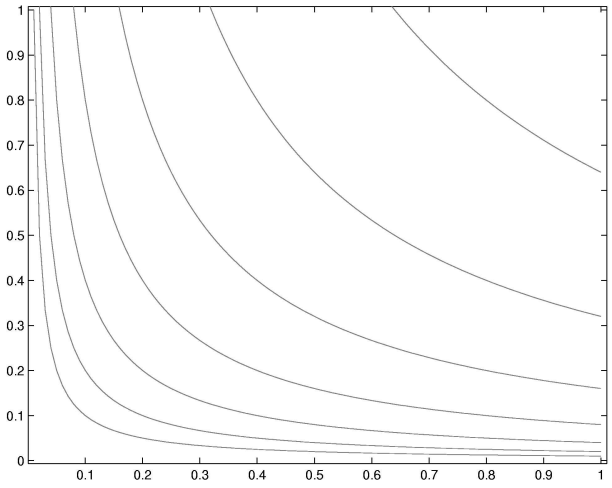

FIGURE 8.1. Potential solution at a corner.

To study the stability of this potential flow we study the perturbation equation (8.1) with $w = u$ and we are thus led to study the matrix ∇u, which we find to be diagonal with diagonal $(2, -2, 0)$, thus with one positive (stable) and one negative (unstable) eigenvalue. We conclude that the potential flow of an incompressible ideal fluid at a separation point is unstable, in fact exponentially unstable.

We will return to this observation below. Already here we can indicate some (far-reaching) consequences. Consider the flow around a body, e.g. a circular cylinder with axis along the x_3-axis in a flow in the direction of the x_1-axis. This could model the water flow around the pillar of a bridge standing on the bottom of a deep river. We could then imagine a stationary solution with streamlines around the pillar, e.g. according to Fig 8.3 (we will write down the corresponding analytical solution formula in Chapter 9 below). We notice that any such flow will necessarily have a separation point somewhere at the back of the cylinder, where the flow would look like the potential solution just given. Necessarily! We conclude that any such stationary flow will be unstable and hence would be impossible to observe. If we observe the flow around a pillar of a bridge, we must see something different. We will show what below.

Having now observed that the sum of the eigenvalues of the reaction coefficient in the linearized Euler equations is always equal to zero, we understand that most solutions to the Euler equations must be unstable! The flow at a separation point just studied was just one example. If someone

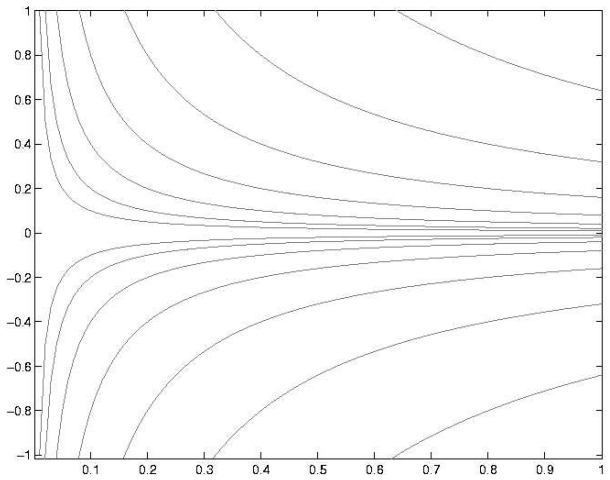

FIGURE 8.2. Potential solution at a separation point.

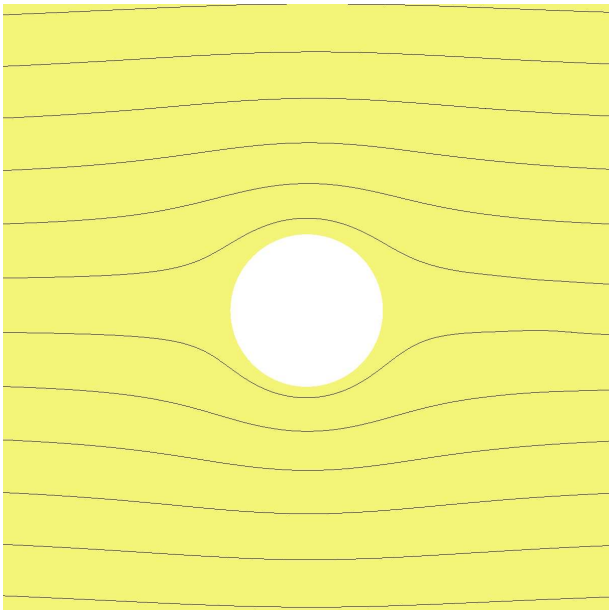

FIGURE 8.3. Streamlines for the potential solution of a circular cylinder.

comes to us with a formula for the analytical solution to the Euler equations, we would be able, with very high probability, to say that the solution must be unstable and thus can never be observed and thus would not have any predictive value. Right?

From this experience, we could be led to conclude that there is something seriously wrong with the Euler equations, so that we should never speak about this equation, and of course never try to find any solutions. We shall see below that this conclusion is wrong: We will see that the Euler equations is a very valuable model with lots of predictive value but we will have to qualify what we mean by *solving the Euler equations*. We shall see that this occupies an essential part of this book.

8.3 Couette Flow

Is there some flow velocity u with the eigenvalues of $\nabla u = 0$ all having zero real part? Yes, there is a basic flow pattern with this property, which is *Couette flow* given by $u(x) = (ax_2, 0, 0)$ and $p = 0$ with $a > 0$ a constant, which is a stationary solution of both the Euler and NS equations. It represents *parallell shear flow* in the x_1-direction, which may occur inside a flow or in a boundary layer along a boundary at $x_2 = 0$. The streamlines are parallell to the x_1-axis and the u_1 velocity increases linearly with x_2. The coefficient a controls the strength of the shear layer with the shear force given by $\nu\partial u_1/\partial x_2 = \nu a$. This is the simplest possible model solution to both the Euler and NS equations representing stationary parallell shear flow, see Fig. 8.4. Of course, for Euler, we would have $\nu = 0$, so the shear force would be zero. But $u(x)$ would anyway be a solution to the Euler equations.

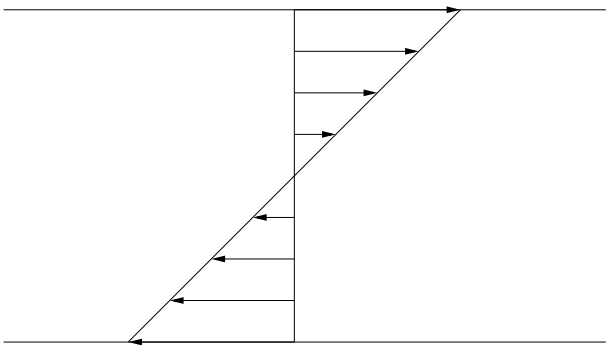

FIGURE 8.4. Couette flow: parallell shear flow.

Is Couette flow a stable solution to Euler? Well, we compute and find that $\nabla u = (0, a, 0; 0, 0, 0; 0, 0, 0)$ with the rows separated by semi-colon.

Obviously, the eigenvalues are all zero, so there are no exponentially unstable modes, but the presence of the off-diagonal coefficient a allows for linear growth in t with slope a. This is referred to as *non-modal growth*, occuring because the matrix ∇u is non-normal (in particular non-symmetric) with degenerate eigenmodes. More precisely, we expect to see that $v_1(t) \sim tav_2^0$. Now if a is large, then this will correspond to considerable growth of the perturbation $\hat{v}$, and thus would signify an unstable Couette flow. Now, in a boundary layer of thickness δ we would have $a \sim 1/\delta$, and we would thus conclude that Couette flow in a boundary layer would be unstable. The argument given also shows that Couette flow for NS with small viscosity is unstable. We will study this phenomenon in detail in Chapter 34 below.

Sommerfeld made the mistake to believe that without exponentially unstable modes, Couette flow would be stable, but then missed the large non-modal growth and got the wrong answer.

8.4 Reflections on Stability and Perspectives

We have presented two simple stationary analytical solutions to the Euler and NS equations, and we have shown that both solutions are unstable. From this experience we could easily be led to the suspicion that it would be hard to find *any* solution to the Euler/NS equations that is stable. In computations we will below see that if we initiate the flow with one of these simple solutions, then the flow will quickly develop into a completely different time-dependent, in fact turbulent, solution.

We see that the effect of the instability of solutions to the Euler/NS equations is the development of a fluctuating time-dependent turbulent solution. Since the flow is unstable, it will always have to change from one state to another; it simply cannot find any stable stationary configuration. It is like a flag in the wind, which is never in a flat stationary state, but is always changing from one state to another in a fluctuating seemingly chaotic way. It is clearly impossible to predict the exact position of a flag over a time interval which is not very short, yet there is some kind of repetitive behavior in the motion of a flag, but the motion is not periodic, rather sort of "turbulent".

We see similar phenomena in the evolution of the Weather; always changing in a way which is more or less predictable a couple of days ahead but not much more, but always with some mix of rain and sunshine and with certain mean values predictable over longer time. In fact, models for the weather look like the Euler/NS equations, and we will return to basic aspects of weather prediction below connecting to the Euler/NS equations.

We shall see that outputs from computed turbulent solutions fit with observations. We will in fact be able by a posteriori error estimation to assess the precision in the outputs. In the a posteriori error estimation

we solve (dual) linearized Euler or NS equations linearized at a computed solution and compute the relevant stability factors and find that these factors are not very large. We will thus be able to make accurate predictions of certain outputs by computing solutions to the Euler or NS equations, and thus we can reach our main goal: prediction by computation.

What we just said seems to contain a contradiction: We first said that the linearized Euler/NS equations seemed to be exponentially unstable, so that solutions would "blow up" exponentially, even when linearized at very simple basic solutions. On the other hand we claimed that we could solve the (dual) linearized Euler/NS equations without blow-up reflecting that stability factors are not very large, when linearized at a complex turbulent solution. How can this be? Exponential blow-up for simple solutions but no blow-up for complex turbulent solutions! We will discuss this remarkable phenomenon below and give some mathematical justification. Roughly speaking the secret reflects effects of *cancellation* in a fluctuating turbulent flow, which are not present in the case of the simple stationary solutions studied above. It is probable that this aspect of stability also is cruicial for phenomena in Nature to be functional and not completely chaotic and may explain why Nature is complex; simple solutions are unstable and only complex solutions can be realized and have some permanence!

We may thus say that it is the complexity that makes turbulent solutions to the Euler/NS equations computable. But the cancellation of perturbations in this complex flow is also some kind of "miracle", a miracle which gives permanence, stability and thus computability of certain outputs.

Below we will, in our discussion of d'Alembert's paradox, give more evidence that predictions from analytical solutions (without stability analysis) may be completely wrong. We spend some time and effort on this kind of "wrong mathematics" because it occupies an important part of the history of fluid dynamics, and because one can learn something even from completely wrong arguments, by proper understanding of exactly what is wrong.

9

d'Alembert's Paradox and Bernoulli's Law

In classical hydrodynamics the motion of nonviscous fluids is chiefly discussed. For the motion of viscous fluids, we have the differential equation (NS) whose evaluation has been well confirmed by physical observations. As for solutoins of this differential equation, we have, aside from unidimensional problems like those given by Lord Rayleigh, only the ones in which inertia of the fluid is disregarded (Stokes equations) or plays no important role. The bidimensional and tridimensional problems, taking viscosity and inertia into account (NS), still await solution. (Prandtl in *Motion of fluids with very little viscosity* 1904)

9.1 Introduction

We recall the Euler equations for incompressible inviscid flow:

$$\begin{aligned} \dot{u} + (u \cdot \nabla)u + \nabla p &= 0 && \text{in } \Omega \times I, \\ \nabla \cdot u &= 0 && \text{in } \Omega \times I, \\ u \cdot n &= g && \text{on } \Gamma \times I, \\ u(\cdot, 0) &= u^0 && \text{in } \Omega. \end{aligned} \tag{9.1}$$

We here set the volume force $f = 0$, and assume the non-homogeneous slip boundary condition $u \cdot n = g$, with n the outward unit normal to Γ, and g a given function. We assume that $\int_\Gamma g \, ds = 0$, so that the boundary condition is compatible with the incompressibility condition $\nabla \cdot u = 0$ in

Ω, in view of the divergence theorem stating that

$$\int_\Omega \nabla \cdot u \, dx = \int_\Gamma u \cdot n \, ds.$$

Let us first recall the derivation of the first of the Euler equations, the momentum equation, expressing a balance between fluid particle acceleration and the forces from the pressure gradient ∇p and f according to Newton's 2nd Law. We then consider a "fluid particle" following a trajectory $x(t)$ defined by

$$\frac{dx}{dt} = u(x(t), t) \quad \text{for } t > 0, \quad x(0) = x^0,$$

where x^0 denotes the position of the fluid particle at time $t = 0$, and $u(x, t)$ is the velocity of fluid particles at (x, t). The acceleration of the fluid particle is given by

$$\frac{d}{dt}u(x(t), t) = \dot{u}(x(t), t) + \nabla u(x(t), t) \cdot \frac{dx}{dt} = (\dot{u} + (u \cdot \nabla)u)(x(t), t),$$

where we used the chain rule. The acceleration should now be balanced by the force on the particle (assuming unit mass), that is $-\nabla p + f$, according to Newton's 2nd Law. This is because the force acting on a little volume V of fluid with boundary S is given by

$$-\int_S pn \; ds + \int_V f \, dx = \int_V (-\nabla p + f) \, dx,$$

where we again used the divergence theorem. We thus obtain the momentum equation

$$\dot{u} + (u \cdot \nabla)u + \nabla p = f$$

in the fluid domain, which expresses Newton's 2nd Law. We may thus view the Euler equations to model the flow of very many very small "fluid particles" interacting through a pressure force maintaining incompressibility.

It may seem natural to expect that the Euler equations model the flow of a fluid with very small viscosity (or very high Reynold's number). We shall below see that this statement is largely true, if interpreted in the right way. However, we shall now show that this idea has a serious flaw, if interpreted in the wrong way, which in particular was done during the initial mathematical studies of fluid mechanics by even the great masters of the 18th century.

9.2 Bernoulli, Euler, Ideal Fluids and Potential Solutions

The Euler equations were formulated by Euler in 1755 [30] building on Daniel Bernoulli's Hydrodynamik from 1738 and Johann Bernoulli's (father

of Daniel) Hydraulica, and thus predated the Navier-Stokes equations by almost 100 years.

In particular, Euler derived Bernoulli's Law for stationary incompressible inviscid irrotational flow from the Euler equations. We shall present Eulers derivation below.

An inviscid fluid ($\nu = 0$) is also said to be an *ideal fluid*. The initial studies by the Bernoullis and Euler thus concerned ideal fluids, with the terminology suggesting that these studies would be fundamental: In the ideal world there would be ideal fluids behaving in an ideal way. Of course, the hope was that the newly invented Calculus would be the ideal tool to uncover the secrets of this ideal World.

In particular, the interest focussed on stationary potential solutions with the velocity $u = \nabla\phi$, where the potential ϕ is a harmonic function satisfying Laplace's equation $\Delta\phi = 0$ in the domain of the fluid together with the Neumann boundary condtion $\frac{\partial\phi}{\partial n} = u \cdot n = g$. Obviously, such a velocity is both *irrotational* ($\nabla \times u = 0$) and divergensfree ($\nabla \cdot u = 0$). We show below that if $u = \nabla\phi$ with $\Delta\phi = 0$, then there is a pressure p such that (u, p) solves the stationary Euler equations. By solving Laplace's equation, one can thus construct stationary irrotational solutions to the Euler equations, and thus fluid mechanics seems to be open for exploration by Calculus, with all its capabilities of producing harmonic functions. Unfortunately for Calculus (but fortunately for Science, since potential solutions are pretty boring), these hopes were almost instantly ruined by the discovery that this type of ideal fluid theoretical predictions almost always were in complete disagreement with observations and thus had no scientific value.

FIGURE 9.1. Daniel Bernoulli (1700-1782), his father Johann Bernoulli (1667-1748), and Joseph-Louis Lagrange (1736-1813).

9.3 d'Alembert's Paradox

This was pointed out by d'Alembert in 1752 in his famous Paradox, comparing the Calculus prediction of zero drag/lift of an inviscid potential

solution, with the undeniable observations of non-zero drag/lift in very nearly inviscid fluids such as air and water. We shall present d'Alembert's Paradox below. We shall also propose a (new) solution to the Paradox: Briefly speaking, we will show that the zero drag/lift inviscid potential solution is not stable and instead a turbulent approximate solution develops, which has non-zero drag/lift. Our resolution of the Paradox is different from the standard solution by Prandtl from 1904, which claims that even the slightest viscosity changes the flow completely due to the presence of no-slip boundary layers. We will present more material further below to open for the reader to judge which solution of the Paradox may be closest to the thruth. Of course, we do not claim that boundary layers never influence the flow and the drag/lift, but we give evidence that for very small viscosity (very large Reynold's number), Prandtl's no-slip boundary layers may not be the true reason why non-zero drag/lift develops.

9.4 A Vector Calculus Identity

In our study of potential solutions we shall use the following identity, which may be verified by direct computation: If $u = (u_1, u_2, u_3)$ is differentiable, then

$$\frac{1}{2}\nabla|u|^2 = (u\cdot\nabla)u + u\times(\nabla\times u). \tag{9.2}$$

9.5 Bernoulli's Law

Let now $u = \nabla\phi$ with $\Delta\phi = 0$ in the domain Ω of the fluid together with the Neumann boundary condition $\frac{\partial\phi}{\partial n} = u\cdot n = g$ on Γ. Let us next define the pressure p by the equation

$$\frac{1}{2}|u|^2 + p = C \quad \text{in } \Omega, \tag{9.3}$$

where C is a constant. Taking the gradient of both sides of (9.3) and using (9.2) recalling that $\nabla\times u = 0$, we find that (u, p) satisfies

$$(u\cdot\nabla)u + \nabla p = 0, \quad \nabla\cdot u = 0 \quad \text{in } \Omega, \tag{9.4}$$

and we thus refer to (u, p) as a stationary *potential solution* to the Euler equations with $f = 0$, noting that by construction $u\cdot n = g$ on Γ. We have already remarked that a potential velocity is irrotational. We note further that the pressure in the Euler equations (with velocity boundary conditions) is only determined up to a constant, which explains the presence of the (arbitrary) constant C in Bernoulli's Law.

Conversely, we see that a stationary irrotational solution (u, p) of the Euler equations (9.1), also satisfies (9.3), which we refer to as *Bernoulli's*

Law. We thus see that for stationary potential solutions, the stationary Euler equations and Bernoulli's Law boil down to the same thing, all according to Euler. The same conclusion was reached by Lagrange, who showed that Bernoulli's Law is the exact differential of the Euler equations.

From Bernoulli's Law follows that for a potential solution (u, p), the pressure p is large where the speed $|u|$ is small, and vice versa.

9.6 Potential Flow around a Circular Cylinder

We consider now an infinitely long cylinder of diameter 1 oriented along the x_3 axis and immersed in an inviscid fluid filling $\mathbb{R}^3$ with velocity $(1, 0, 0)$ at infinity, see Fig. 9.2. We now construct a corresponding potential solution $u = \nabla\phi$ by using Calculus. We assume that $u_3 = 0$, and seek a function $\phi(x_1, x_2)$ which is harmonic outside the disc $x_1^2 + x_2^2 \leq 1$ occupied by the cylinder, such that $\frac{\partial\phi}{\partial n} = 0$ on the boundary of the disc.

We find that ϕ is equal to the real part of the analytic function $w(z) = z + \frac{1}{z}$ with $z = x_1 + ix_2$ and i the imaginary unit, that is,

$$\phi(x_1, x_2) = (r + \frac{1}{r})\cos(\theta), \tag{9.5}$$

where $(x_1, x_2) = (r\cos(\theta), r\sin(\theta))$ is expressed in polar coordinates (r, θ). We verify readlily that ϕ is harmonic outside the disc, because ϕ is the real part of an analytic function, and that $\frac{\partial\phi}{\partial n} = 0$ on the boundary of the disc. Further, one can show by a little more work that $\lim_{x_1^2+x_2^2\to\infty} \nabla\phi(x_1, x_2) = (1, 0, 0)$, so that the potential solution satsifies the uniform flow condition far away from the cylinder. In Fig 9.2 we plot the streamlines of u, which are the level curves of the imaginary part $(r - \frac{1}{r})\sin(\theta)$ of $w(z)$.

We have now constructed a potential flow solution around the cylinder, which intuitively looks quite convincing: the flow opens up to go around the cylinder and then closes, pretty much as one may naively expect. Right?

9.7 Zero Drag/Lift of Potential Flow

Let us now compute the drag of the potential flow around the cylinder, that is the net force on the cylinder in the x_1 direction from the pressure acting on the boundary of the cylinder. To this end we note that the flow speed $|u|$ evidently is symmetric with respect to both the x_1 and the x_2-axis, because the flow after/below the cylinder is evidently a mirror image of the flow before/above the cylinder. From Bernoulli's Law we then deduce that also the fluid pressure is symmetric before/after and above/below. This means that the pressure around the cylinder balances out to zero, that is, there is no net force from the flow on the cylinder: The drag is

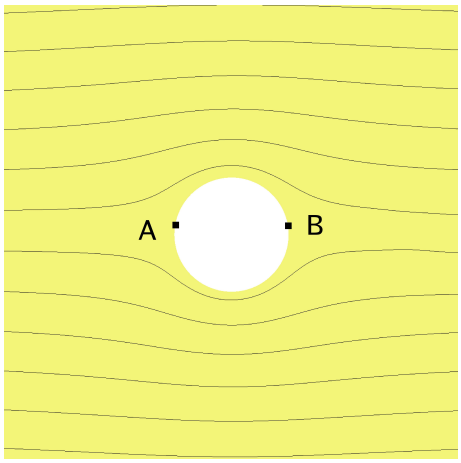

FIGURE 9.2. Potential flow around a cylinder

zero and evidently also the lift which is the net force in the x_2-direction. We see in particular that the pressure is high at the stagnation point A with zero speed opposing the flow, and that this high pressure is balanced by an equally large pressure in the opposite direction at the stagnation point B at the back of the cylinder. And so it goes for all symmetrically placed points on the boundary. One can easily generalize this result to a body of arbitrary (non-symmetric) shape, subject to potential flow which is uniform at infinity, we give the proof in the last section of this chapter.

This is d'Alembert's Paradox: Potential flow uniform at infinity has zero drag/lift. But massive experimental evidence indicates substantial non-zero drag even if the flow is very slightly viscous such as air and water. The first such experiments were performed by d'Alembert himself in order to present his Paradox. Further, with zero lift, flying would be impossible, again at variance with everybodys experience.

So how is science/mathematics to deal with d'Alembert's Paradox? Evidently, something must be wrong with the potential solution. But what? Is it the assumption about inviscid flow, which is essentially Prandtl's explanation? Or is there a different explanation? To find this out let us solve the Euler equations computationally using G2, instead of using analytical mathematics, and see what we get. Before we plunge into this adventure, let us give another highlight of Calculus appplied to the Euler equations, which is as misleading as the zero drag/lift of a potential solution.

9.8 Ideal Fluids and Vorticity

Taking the vorticity of the momentum equation in (9.1), we obtain with a direct computation using e.g. (9.2), the following equation for the vorticity

$\omega \equiv \nabla \times u$:

$$\dot{\omega} + (u \cdot \nabla)\omega - (\omega \cdot \nabla)u = 0 \quad \text{in } \Omega \times I. \tag{9.6}$$

This may be viewed as a linear convection-reaction equation for the propagation of the vorticity ω with the fluid velocity u being given. Multiplying by ω and integrating by parts with respect to x, we obtain

$$\frac{d}{dt}\int_\Omega \omega^2(x,t)\,dx + \frac{1}{2}\int_\Gamma u \cdot n\omega^2(s,t)\,ds \leq C\int_\Omega \omega^2(x,t)\,dx$$

if the velocity ∇u is bounded by the constant C, where Γ is the boundary of Ω. It follows that if ω vanishes in Ω at initial time $t = 0$, and no vorticity is convected into Ω through the boundary Γ where $u \cdot n < 0$, then $\omega(t)$ vanishes in Ω for all $t > 0$. We are thus led to the conclusion that in an ideal fluid with bounded velocity gradient, vorticity cannot be created. In the computational example with an ideal fluid which we now present, nevertheless vorticity seems to be generated. The only way out of this deadlock is that the assumption of bounded velocity gradient is not verified, that is, that the underlying Euler solution (u, p) is not a pointwise solution.

9.9 d'Alembert's Computation of Zero Drag/Lift

We recall d'Alemberts (erroneous) computation of zero drag: Suppose there is a stationary pointwise solution (u, p) to the Euler equations of inviscid incompressible flow around a bluff body in a horisontal channel oriented in the x_1-direction, with the velocity u irrotational, i.e., $\nabla \times u = 0$. Integrating the momentum equation over the domain, we obtain by partial integration, considering the first component

$$0 = \int_{\Gamma_b} pn_1\,ds + \int_{\Gamma_{in}} (u \cdot nu_1 + pn_1)\,ds + \int_{\Gamma_{out}} (u \cdot nu_1 + pn_1)\,ds$$

where Γ_{in} and Γ_{out} denote the inflow and outflow boundaries of the channel, and Γ_b denotes the boundary of the immersed body. Assuming now that the velocity is equal on in and outflow, which is natural if the channel is long, by Bernoullis law (stating that $|u|^2/2 + p$ is constant), the pressure will be as well, and thus the inflow and outflow terms will cancel and therefore the drag $\int_{\Gamma_b} pn_1\,ds$ will be zero.

Obviously, zero drag of a bluff body contradicts experience: All bluff bodies show substantial drag with the major contribution coming from the pressure distribution around the body with high pressure up front and low pressure in the back, and not from viscosity. In particular, we can attribute only a small part of the drag to viscosity and thus experience clearly indicates substantial drag for inviscid flow. But d'Alemberts computation shows zero drag.

We shall now in a concrete example see in Chapters 10-11 that the trouble with d'Alemberts computation of zero drag is that the pointwise laminar solution simply does not exist as a stable solution, which makes the computation meaningless. Instead a turbulent approximate solution develops and this solution has a substantial drag close to that for a solution of the NS equations with large Reynolds number.

9.10 A reformulation of the momentum equation

Using the identity (9.2) we can rewrite the Euler momentum equation as follows, assuming $f = 0$

$$\dot{u} - u \times \omega + \nabla(\frac{1}{2}|u|^2 + p) = 0, \tag{9.7}$$

a formulation which is sometimes used. In particular, we derive from this equation Bernoulli's Law for stationary irrotational flow.

10

Prandtl's Resolution of d'Alembert's Paradox

> By denying scientific principles, one may maintain any paradox. (Galileo Galilei)

10.1 Quotation from a Standard Source

To get the proper perspective, we present the standard view on the resolution of d'Alembert's Paradox as the one suggested by Prandtl in the short report *Motion of fluids with very little viscosity* read before the Third International Congress of Mathematicians at Heidelberg in 1904, in the form of some quotations from the standard source [77]:

"Ludwig Prandtl's discovery of the boundary layer is regarded as one of the most important breakthroughs in fluid mechanics of all time and has earned Prandtl the title of Father of Modern Fluid Mechanics."

"Before Prandtl's description of the boundary layer in 1904, there was no lack of interest in the dynamics of fluids due to the practical problems of nautical engineering, ballistics, and hydraulics. Throughout the 18th and 19th century the top physicists and mathematicians of Europe examined flows from a mathematical point of view. Much of this work was to construct potential flows, i.e., incompressible, irrotational flows, over bodies. Examples recognizable to most undergraduates are flows over circular cylinders and other flows involving source-sink superpositions. Although the mathematics was elegant and the flows aesthetically pleasing, it was recognized that such flows failed to mimic "real" flows seen in nature. Furthermore, it was known since the time of d'Alembert that potential flows

frequently resulted in zero drag; a prediction in clear contradiction with everyday experience!"

"What were these mathematicians to do? Thanks to Coulomb and Stokes, they were aware that a no-slip condition should be applied at solid bodies (we now realize that this condition holds at all fluid boundaries). However, standard external flow problems are ill-posed when the potential flow equations are combined with the no-slip condition. The correct approach would be to abandon the inviscid (small viscosity) approximation and solve the full Navier-Stokes equations. Stokes had done this himself for the problem of creeping flow around a sphere and derived a non-zero expression for the drag. However, the Stokes flow does not generate the large scale separation seen in most day-to-day flows and the predicted drag is always much less than what is measured for things like cannon balls and marbles in air and water. The reason for these discrepencies is the neglect of the fluid inertia in the creeping flow approximation. To include these terms is a daunting task, even today."

"Thus, as the 19th century came to a close, a universal and practical application of fluid mechanics seemed far off. Prandtl's contribution was to realize that we can view the flow as being divided into two regions. The bulk of the flow can be regarded as a potential flow essentially the same as that studied by the mathematicians. Only in a small region near the body do viscous effects dominate. This thin layer is known as the boundary layer. Conceptually, Prandtl's boundary layer is the reason the potential flow theory is compatible with the exact physics. Furthermore, certain details of the structure of the boundary layer are the key to understanding both flow separation and the physical mechanism behind the Kutta condition. That is, a proper understanding of the boundary layer allows us to understand how a (vanishingly) small viscosity and a (vanishingly) small viscous region can modify the global flow features. Thus, with one insight Prandtl resolved d'Alembert's Paradox and provided fluid mechanists with the physics of both lift and form drag."

10.2 Quotation from Prandtl's 1904 report

We follow up with some paragraphs from Prandtl's 1904 report which appeared in English translation as Technical Memorandum 452 of the National Advisory Committee for Aeronautics in 1928:

"It is known, however, that the solutions of the Euler equations generally agree very poorly with experience. I will recall only the Dirichlet sphere which, according to the theory, should move without friction."

"I have now set myself the task to investigate systematically the laws of motion of a fluid whose viscosity is assumed to be very small. The viscosity is supposed to be so small that it can be disregarded wherever there are

no great velocity differences nor accumulative effects. This plan has proved to be very fruitful, in that, on the one hand, it produces mathematical formulas. which enable a solution of the problem and, on the other hand, the agreement with observations promises to be very satisfactory."

"The most important aspect of the problem is the behavior of the fluid on the surface of the solid body, assuming that the fluid adheres to the surface and that, therefore, the velocity is either zero or equal to the velocity of the body. In the thin transition layer, the great velocity differences will then produce noticable effects in spite of the small viscosity."

"The most important practical results of these investigations is that, in certain cases, the flow separates from the surface at a point entirely determined by external conditions. A fluid layer, which is set in rotation by the friction on the wall, is thus forced into the free fluid."

"On the one hand, we have the free fluid, which can be treated as non-viscous, while, on the other hand, we have the transition layers on the solid boundaries, impart their characteristic impress on the free flow by the emission of turbulent layers."

"No. 7-10 show the flow around a cylindrical obstacle. No. 7 shows the beginning of the separation; Nos. 8-9, subsequent stages. No. 10 shows the permanent condition. The wake of turbulent water behind the cylinder swings back and forth, whence the momentary unsymmetrical apperance." (referring to the pictures in Fig. 10.2)

FIGURE 10.1. Ludwig Prandtl (1875-1953), called the father of modern aerodynamics.

10.3 Discussion of Prandtl's Resolution

The main point of Prandtl's resolution of the d'Alembert's Paradox is that boundary layers always exist at solid boundaries, even if the viscosity is

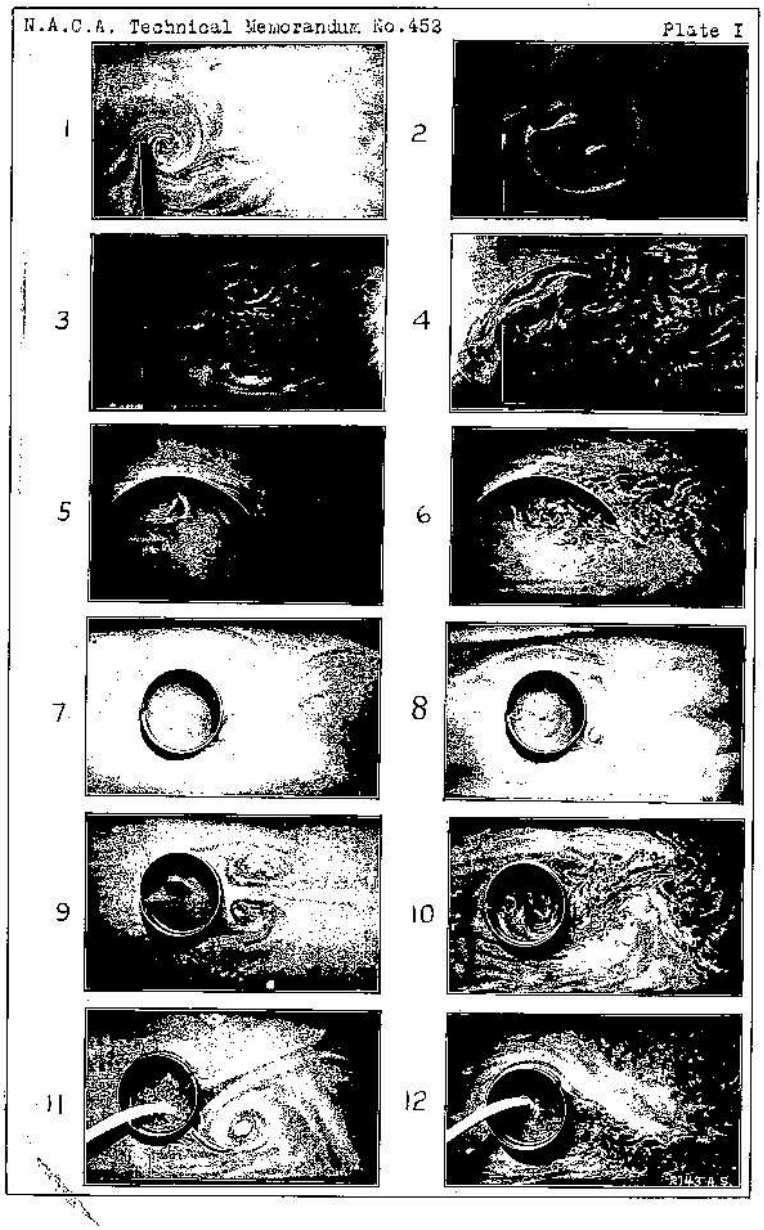

FIGURE 10.2. Pictures 1-12 from Prandtl's Technical Memorandum 452.

very small, and that by the strong velocity difference in the boundary layer, vorticity is created in the layer and is then ejected into the fluid. The important feature is the direction of the vortex generation according to Prandtl, which is parallel to the surface and perpendicular to the streamwise direction corresponding to "tripping" the flow by friction in the boundary layer. We refer to vorticity in this direction as *transversal vorticity*. The accepted resolution of the Paradox according to Prandtl is thus that transversal vorticity is generated in the boundary layer, even if the viscosity is very small, and this vorticity generation changes the global patterns of the flow, allowing non-zero drag to develop. Prandtl thus claims that the potential solution does not occur in practice, but instead a different (turbulent) solution develops from the generation of transversal vorticity in the bolundary layer.

We will below show that Prandtl's view on the potential solution is correct, but we will question his explanation by transversal vorticity generation by showing the importance of instead generation of vorticity in the streamwise direction reflecting the stability analysis in Chapter 8.

Another important aspect concerns the separation points: It is clear from Fig 5 and 6 that Prandtl believes that *there must be two* separation points, although his remark on No. 10 ("The wake of turbulent water behind the cylinder swings back and forth, whence the momentary unsymmetrical apperance."), indicates that he *can see only one* swinging back and forth. We will below show that with very small viscosity, there is in fact only one separation point (in each section perpendicular to the cylinder axis), which fits with Prandtl's experiment, but is contrary to Prandtl's analysis.

Altogether, we will thus present a resolution of the paradox, which is fundamentally different from the accepted resolution by Prandtl.

11

New Resolution of d'Alembert's Paradox

> How wonderful that we have met with a paradox. Now we have some hope of making progress. (Nils Bohr)

In this chapter we present a new resolution of d'Alembert's Paradox. We do this by showing computationally that the zero-drag potential solution is unstable, and will therefore not be realized physically, and instead a turbulent approximate solution with substantial drag develops. We show that the drag results from the low pressure inside tubes of vorticity in the streamline direction reflecting vorticity generation according to the stability analysis of Chapter 8 and Chapter 20. Our resolution is different from the accepted solution by Prandtl from 1904 based on boundary layer effects of vanishing viscosity. We believe our solution is more to the point in the case of vanishing (small) viscosity. We leave to the reader to judge which solution is more accurate.

11.1 Drag of a Circular Cylinder

We now show the results of a G2 computational simulation of the flow around a circular cylinder with axis oriented in the x_3-direction in a long channel oriented in the x_1-direction, subject to a uniform inflow velocity $(1, 0, 0)$ according to Fig. 11.1. This computation is presented in detail in Chapter 33. We choose the initial velocity equal to zero, and see a potential solution with almost zero drag developing in a couple of time steps, but if

we continue the computation we see that the potential solution undergoes transition to a turbulent solution with large drag and a lot of vorticity.

There is only one separation point (in each transversal section), see Fig. 11.2, which oscillates up and down, and we observe the generation of vortex tubes in the streamwise direction inside which the pressure is low generating substantial drag, see Fig. 11.3-11.6. In particular, we note that the transversal vorticity component ω_3 mainly develops downstream the cylinder, whereas the streamwise vorticity is generated at the separation point.

The main points in our resolution of d'Alembert's Paradox are thus:

1. No boundary layer prior to separation.
2. Only one separation point, which oscillates up and down.
3. Strong generation of vorticity in the streamwise direction at the separation point.

These features are completely different from those suggested by Prandtl based boundary layers before separation at two points and generation of transversal vorticity.

The stability analysis of Chapter 8 indicates that strong vorticity in the x_1-direction should be generated at the separation point, which is clearly observed in the computations, and which in particular reflects the instability of the potential solution. We study the instability in more detail in Chapter 20 below.

We sum up: the potential solution with zero drag is unstable and will not be realized in reality. Instead a turbulent solution develops with substantial drag. This is the resolution of d'Alembert's Mystery.

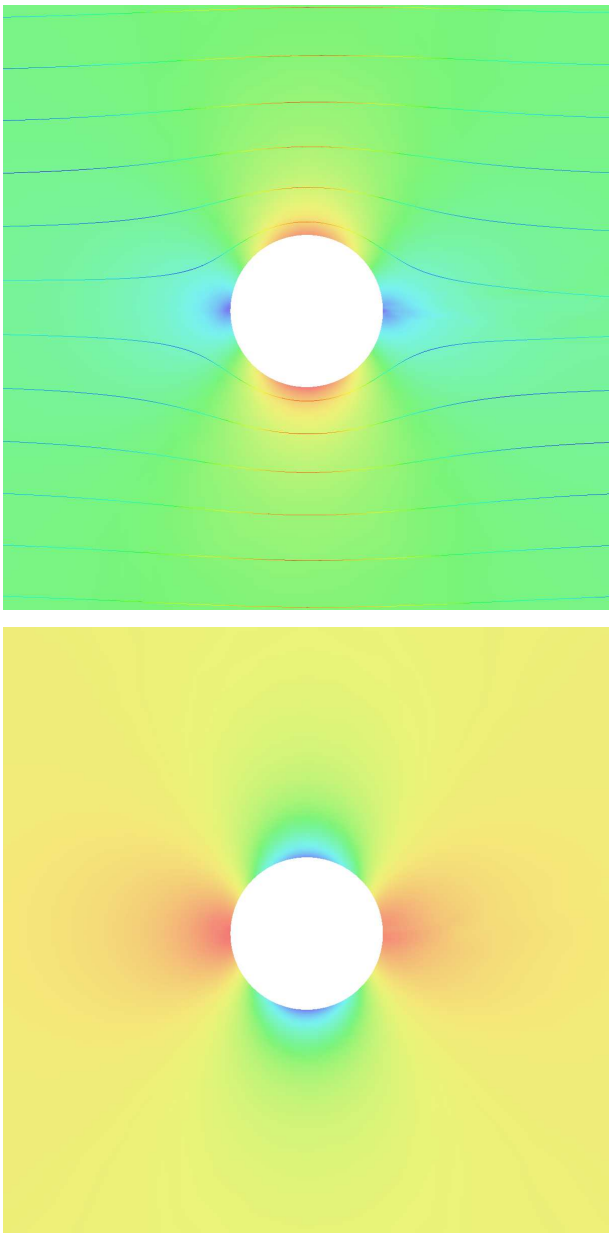

FIGURE 11.1. Flow past a circular cylinder; velocity (upper) and pressure (lower).

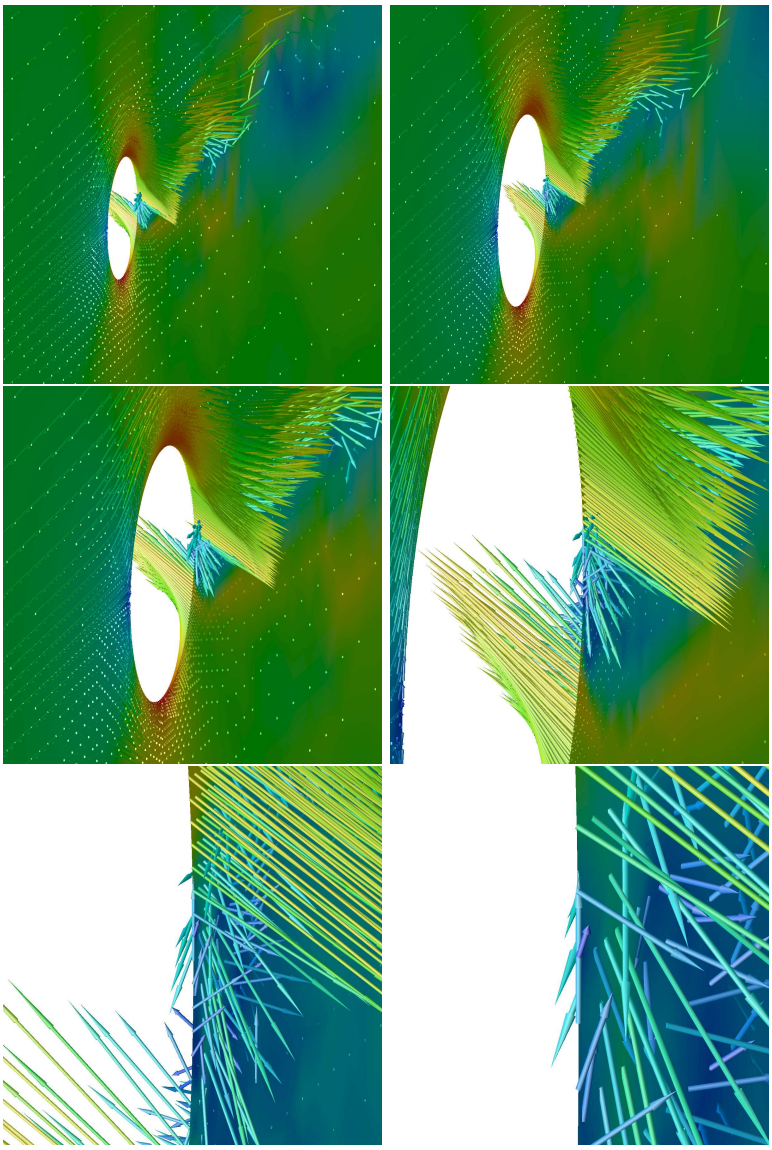

FIGURE 11.2. Snapshot of the velocity illustrating the single separation point.

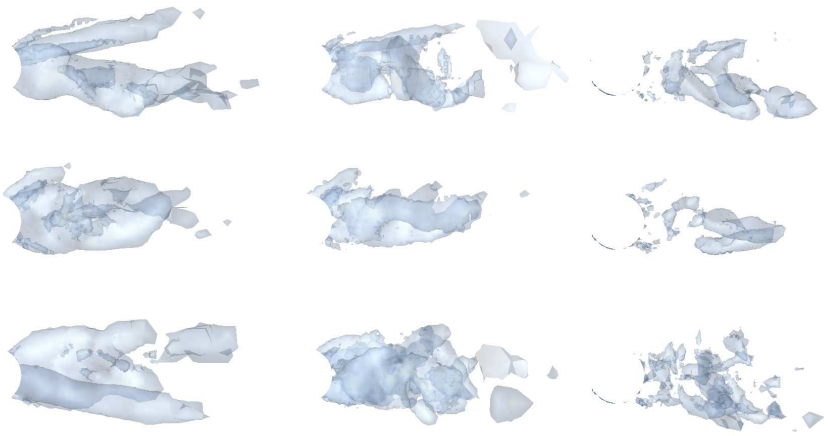

FIGURE 11.3. Isosurfaces for vorticity $\omega = (\omega_1, \omega_2, \omega_3)$: ω_1 (left), ω_2 (middle), and ω_3 (right), at three times $t_1 < t_2 < t_3$ (upper, middle, lower), in the x_1x_2-plane.

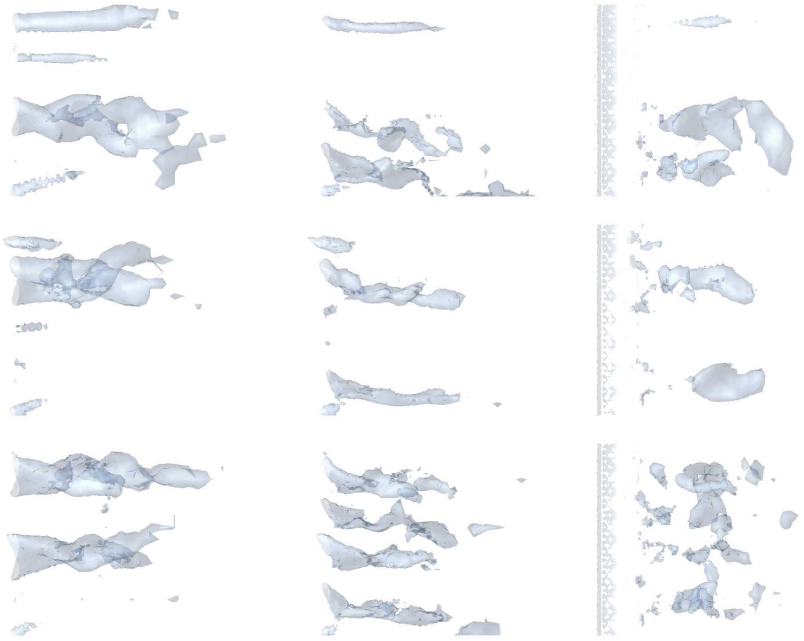

FIGURE 11.4. Isosurfaces for vorticity $\omega = (\omega_1, \omega_2, \omega_3)$: ω_1 (left), ω_2 (middle), and ω_3 (right), at three times $t_1 < t_2 < t_3$ (upper, middle, lower), in the x_1x_3-plane.

FIGURE 11.5. Isosurfaces for vorticity $\omega = (\omega_1, \omega_2, \omega_3)$: ω_1 (left), ω_2 (middle), and ω_3 (right), at three times $t_1 < t_2 < t_3$ (upper, middle, lower), in the x_2x_3-plane.

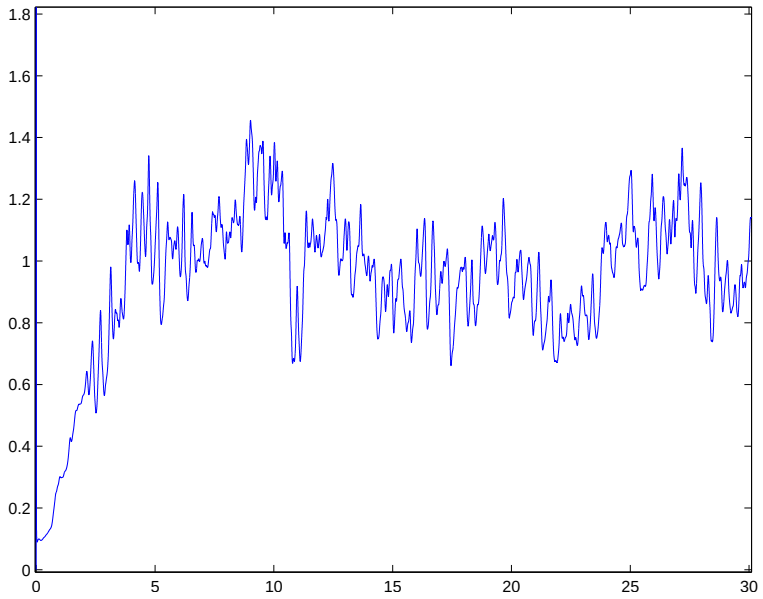

FIGURE 11.6. Time series of c_D for a G2 solution to the Euler equations.

12
Turbulence and Chaos

God does not throw dice. (Einstein)

We ought to regard the present state of the universe as the effect of its antecedent state and as the cause of the state that is to follow. An intelligence knowing all the forces acting in nature at a given instant, as well as the momentary positions of all things in the universe, would be able to comprehend in one single formula the motions of the largest bodies as well as the lightest atoms in the world, provided that its intellect were sufficiently powerful to subject all data to analysis; to it nothing would be uncertain, the future as well as the past would be present to its eyes. (Laplace)

12.1 Weather as Deterministic Chaos

In this chapter we approach some basic aspects of turbulent flow by connecting to the concept of *deterministic chaos* originating from the work of the meteorologist Edward Lorenz on the unpredictable nature of the weather, initiated in the early 1960s [71]. It is natural to make this connection because weather predictions are routinely made by computational solution of systems of differential equations similar to the NS equations modeling the turbulent motion of air and moisture in the atmosphere of the Earth.

We shall use the term *chaotic dynamical system* to describe dynamical systems for which pointwise values in space/time are very sensitive to perturbations and thus unpredictable, while certain mean values in space/time

are less sensitive and thus predictable. We shall see that the NS equations is an example of a chaotic dynamical system in this sense.

We recall that we consider dynamical systems of the form $\dot{u} = g(u)$, where the given function $u \rightarrow g(u)$ represents the law of the system. We thus consider *deterministic systems* following a deterministic law, and a chaotic dynamical system expresses deterministic chaos. The unpredictability of point values thus results from the strong sensitivity to perturbations, and not from any randomness in the given law. The law of a chaotic system is often of simple form, without any presence of randomness.

To illustrate the difference between pointwise values and mean values, we may consider the problem of predicting the weather, or more precisely the temperature, at a specific location in space. Guide books often present, for given locations, predictions of monthly mean temperatures for the different months of the year, but never 24h daily mean temperatures for all the days of the year. This indicates that monthly mean values are predictable to a tolerance of interest, while 24h daily mean values are not.

A daily mean value is an average over short time, which we may refer to as a pointwise value in time, while we may refer to a monthly mean value simply as a mean value. We may then say that mean values appear to be predictable to a tolerance of interest while point values are not.

It is a common observation that predictions of the daily weather more than 3-6 days ahead (depending on the general weather situation) are very unreliable. Lorenz connected the unpredictability to strong sensitivity to perturbations with the question: "Does the flap of a butterfly's wings in Brazil set off a tornado in Texas?" In predictions of daily weather it is observed that perturbations may double every 12-48 hour depending on the model, and thus make predictions over more than say a week unreliable because of the considerable uncertainty in both data and modeling.

Obviously, the size of the tolerance is an important aspect of predictability: To predict a July mean value up to 10°C is of little interest, while a tolerance of 1°C may be the best we can ever hope for. So, the difference between interest or no interest may be just one order of magnitude. We shall meet this aspect below when computing drag and lift coefficients.

To say that a daily mean temperature is unpredictable up to a tolerance of say 1°C, does of course not mean that the daily mean temperature a specific day of July at a specific location is not determined up to 1°C, but only that its value may effectively be anything between say 10°C and 30°C, and that we cannot predict more than a few days ahead what the actual value might be.

12.2 Predicting the Temperature in Målilla

As an illustration we focus on the little village Målilla in the county of Småland in southern Sweden, for which data are available from the Swedish Institute of Meteorology SMHI. In Fig. 12.1 we display daily, weekly, and monthly mean temperatures over the years 1988-1995, and we also show the yearly mean values of the temperature in southern Sweden for the period 1860-2003. We see that the variation of the daily temperatures is $\pm 10°$C, of weekly averages $\pm 7°$C, monthly averages $\pm 4°$C, and yearly averages $\pm 2°$C.

We may say that there are many possible daily temperature curves in Målilla which differ significantly ($\pm 10°$C), and it seems impossible to predict which curve the actual temperature in Målilla will follow a particular year.

On the other hand, the variation of monthly averages over the different daily temperature curves is significantly smaller, and seems predictable to a tolerance of $\pm 4°$C. Further, taking the monthly mean value of any of the many possible daily temperture curves will give a good approximation of the common monthly mean value for all the curves. To compute monthly averages is thus not necessarily a matter of statistics, where we would compute ensemble averages over many different daily temperature curves.

12.3 Chaotic Dynamical System

Lorenz connected the term chaos to strong pointwise sensitivity to perturbations, and noticed that many systems including pinball machines, planetary motion and the weather may show features of strong pointwise sensitivity to perturbations, and thus according to Lorenz show features of chaos. This is no surprize of course; everybody is familiar with the possibility that small perturbations may have large pointwise effects.

What made chaos to such a hot topic in the 1980s, was the seemingly paradoxical concept of *order in chaos*: in a system behaving pointwise in an irregular chaotic unpredictable manner, there may still be some aspects that are predictable. The challenge then becomes to identify these aspects, that is, to identify the order in the disorder or chaos.

The intriguing aspect of a chaotic system such as the weather, is that some quantities appear to be truely unpredictable, like a daily temperature, but there are also other quantities, such as a monthly average temperature, which may be predictable to a tolerence of interest.

We are thus led to identify a dynamical system as *chaotic* if the following two conditions are satisfied:

(1) Pointwise quantities are strongly sensitive to perturbations and therefore unpredictable.

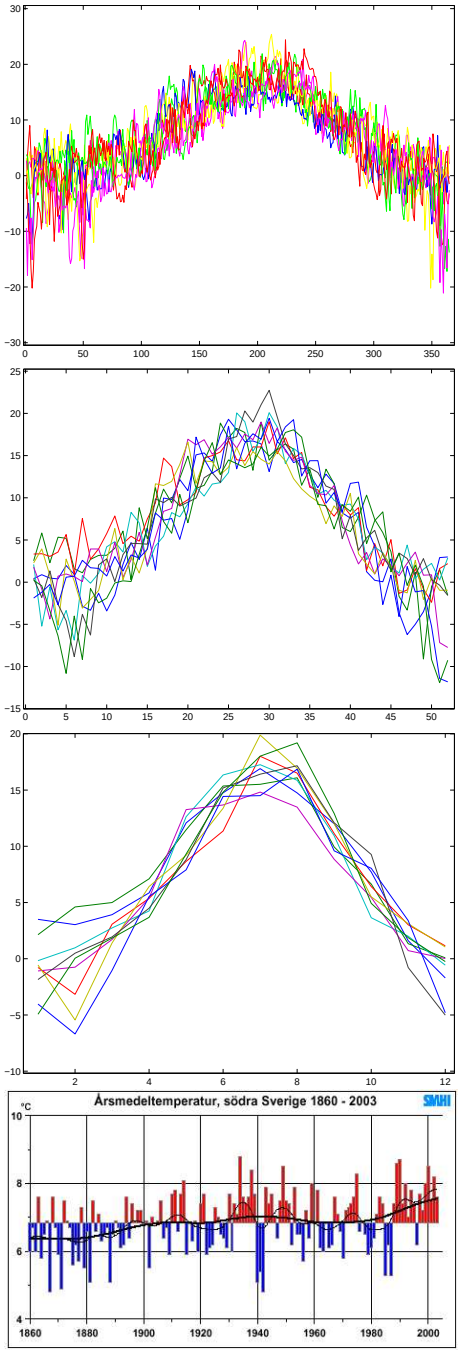

FIGURE 12.1. Mean temperatures for Målilla in Sweden over the years 1988-1995, 24 hour mean, weekly mean, monthly mean, and also yearly mean temperatures for southern Sweden over the years 1860-2003.

(2) Certain quantities of interest are moderatly sensitive to perturbations and thus predictable.

Typically, the quantities of interest are more or less local mean values in space-time of individual trajectories or solutions to the dynamical system, but may also be other quantities reflecting certain aspects of the solution.

The nature of the order in chaos of course is of prime importance. Much of the mathematical work on chaos has been geared towards global aspects such as *attractors* approached by all trajectories after long time. We focus on aspects of order in chaos that can be captured by mean values in space/time, which are not necessarily very long, like montly mean values of daily temperatures. We do this by computational methods which open new possibilites of identifying more precise expressions of order than analytical methods.

The main new contribution of this book is evidence that turbulent flow is chaotic in the above sense: pointwise quantities are unpredictable with strong sensitivity to perturbations, while certain mean value quantities in space-time of interest are predictable with moderate sensitivity to perturbations.

The notion of a chaotic system may seem to be paradoxical in the following sense: In a chaotic system (like the weather) individual trajetories are unpredictable (like the daily temperature in Målilla), yet certain mean values of interest of such unpredictable trajectories indeed may be predictable to tolerances of interest (like monthly mean value tempertures). We can also formulate the paradox: How can it be that certain mean values of a pointwise incorrect individual trajectory may be correct? If our daily trajectory is all wrong, how come that we are able to live normal lives over many years? We will unfold the paradox below, not as simple matter of statistics (because it is not), but as a subtle matter of cancellation.

We may express the essence of a chaotic system alternatively as follows: Each individual trajectory represents *one possible* trajectory out of *many possible* trajectories and we cannot predict which trajectory out of the many possible ones the system will actually follow. There are many possible developments of the daily weather over the next month and we cannot predict which possibility will be realized. However, certain mean value outputs vary little over the different possible trajectories, which effectively makes certain mean value outputs predictable. In Målilla there are many possible daily temperature variations, which are all very different, but their monthly mean values are all similar.

Another example: The trajectories of life for different human beings are all vastly different, but certain mean value quanties may have smaller variation (many human lifes are quite alike in certain aspects).

12.4 The Harmonic Oscillator as a Chaotic System

A basic model of physics is the harmonic oscillator with angular frequency $\omega > 0$:

$$\ddot{u}(t) + \omega^2 u(t) = 0 \quad \text{for } 0 < t \leq T,$$

with solution $u(t) = \cos(\omega t)$ satisfying the intial conditions $u(0) = 1$, $\dot{u}(0) = 0$. We claim that if ω is large, then this is a chaotic system. How can it be? Isn't the harmonic oscillator the most ordered, predictable and non-chaotic system that is thinkable? Well, let us consider the output $u(T)$ where T is the given final time. A change from T to $T + \delta T$ will change the output by the amount $\omega \delta T \sin(\omega T)$, which may be far from small even if δT is small, since ω is large. Thus the output $u(T)$ is strongly sensitive to perturbations in T, and thus unpredictable, so that the harmonic oscillator satisfies (1) in the requirement of a chaotic system, if ω is large.

Next, let us now for small positive τ consider the output

$$M_\tau(u) = \frac{1}{\tau}\int_{T-\tau}^{T} u(t)\,dt = \frac{1}{\tau\omega}(\sin(\omega T) - \sin(\omega(T-\tau)),$$

which is a mean value in time close to the final time T. Clearly, $|M_\tau(u)| \leq \frac{2}{\tau\omega}$, and thus $M_\tau(u) \approx 0$ if $\tau\omega$ is large, which does not change under perturbations of T. We conclude that if $\omega\tau$ is large, then the mean-value $M_\tau(u) \approx 0$ is not at all sensitive to perturbations in the data T and is therefore predictable, and thus also (2) is satisfied. Evidently, there is some order in the pointwise chaos of the harmonic oscillator at high frequency.

We conclude that the harmonic oscillator with large frequency may be viewed to be a chaotic system: The solution is pointwise unpredictable but a mean value in time is predictable. We understand that the reason for this effect is the oscillatory nature of the solution $u(t) = \cos(\omega t)$, creating substantial *cancellation* in the integral defining the mean value. We shall below meet the same crucial feature in turbulence.

We may say that the order of the harmonic oscillator is built into the law of the dynamical system itself: $\ddot{u} + \omega^2 u = 0$, which expresses Newtons 2nd law for a unit mass connected to the origin with a Hookean spring with spring constant ω^2. This is clearly a very simple law which should impose some order, and certainly does, although pointwise outputs evidently become unpredictable if the spring is stiff with ω large and the oscillation is fast. Similarly, the NS equations express Newtons 2nd law for a Newtonian fluid combined with incompressibility, and so we may expect some order in the chaos of turbulence as well.

12.5 Randomness and Foundations of Probability

One may attempt to describe a dynamical system to be *random* if only (1) is satsified but not (2). A random system would then be a system which deterministically would be fully unpredictable; not even mean values in space/time would be deterministically predictable. Knowing one solution trajectory of a random system would say nothing about other possible trajectories, not even about mean values. One might have the impression that the ideal objects of study in probability and statistics would be such deterministically unpredictable systems, but as we will see this does not appear to be a correct viewpoint.

As a possible example of a random system, let us consider the process of *coin-tossing*, which is studied with probabilistic methods in any text on probability or statistics. The assumption is that it is impossible to predict the outcome of head or tail of a single coin toss. As a compensation the notion of *probability* is introduced aimed at describing that tossing the coin *many times* will show approximately equal number of heads and tails (if there is nothing wrong with the coin). One would thus associate a probability of $1/2$ to both head and tail.

From a deterministic point of view the process of coin tossing may be described by the equations of motion for a rotating coin based on Newtons 2nd law, that is as a dynamical system based on a simple law as we have discussed. This system is very sensitive to perturbations in e.g. initial conditions, which makes it satisfy condition (1). A simplified model for coin tossing is the harmonic oscillator with the solution $u(t)$ describing the rotation of the coin during the tossing, with the outcome being say head if $u(T) > 0$ and tail if $u(T) < 0$, where T is the final time when the coin hits the table (and $u(T) = 0$ would correspond to the unlikely outcome that the coin ends up balancing vertically on its perimeter). We may here assume that we always initiate the coin with the same initial conditions $u(0) = 1$ and $\dot{u}(0) = 0$ say, and the unpredictable nature of the outcome of the tossing would then correspond to small perturbations in the choice of final time T, as in the above study of the harmonic oscillator. Viewing coin tossing this way would correspond to viewing it as a deterministic chaotic dynamical system with continuous time, for which a pointwise output in time would be unpredictable, but for which a mean value in time would be predictable. The predictability of the mean value in time would then result from carefully following one single coin toss and observing that half of the time of the toss the coin would have heads up.

However, in probability theory coin tossing is instead viewed as a process with discrete time, where the coin *jumps* from an initial state $u(0)$ at initial time 0 to a final state $u(T)$ at final time T. Here time appears to be *discrete* with only two values 0 and T, and the motion of the coin under a continuous change of time is not observed. It is like closing the eyes during the toss and to only open them at the end of the toss to observe the outcome. The

assumption is now made that it is impossible to say anything about a single coin toss, representing a jump from $u(0)$ to $u(T)$. To say anything about properties of the coin or the process of coin tossing, we would have to toss the coin many times corresponding to *ensembles of solutions* from which we can experimentally compute mean values and probabilities. Alternatively, for an *ideal coin* one could use probability theory based on (in this case very simple) combinatorics, noting that for an ideal coin head and tail represent 2 equally possible outcomes, to compute the the probability for each outcome to be 1/2. For a *real coin* (possibly a bit non-symmetric) tossed by real people, only the experimental method of tossing the coin many times would be seem to be available, and to determine any slight bias would require many thousands of coin tosses. In both practical experiments and probabilistic mathematics, we would then be working with *ensemble mean values* over many tosses and not mean values in time of a single toss.

The mathematical statistician Persi Diaconis [24] tried to get around costly experiments with real people tossing coins many times by instead recording the motion of a coin during a few tosses with a high-speed camera. From the video Diaconis could (somehow) predict that in 51 cases out of 100 the coin would land on the same side it started, a property of coin tossing which of course could be disputed. In any case, the methods contemplated by Diaconis as probabilist would either be expensive experiments with ensembles of many thousands of coin tosses, or expensive high-speed camera recordings of a few tosses and some kind of analysis (yet to be defined) of the video sequences.

Of course, using a deterministic approach, we would instead try computational simulation using a realistic model of a flipping coin based on Newtons 2nd law, with the advantage that it would be cheap and quick (if you have the software for the modeling and computation). Using computation we could thus be able to mimic Diaconis two methods, by either simulating the outcomes of many coin tosses with slightly different data and computing corresponding ensemble averages, or by carefully recording the motion of the coin in a few experiments and (somehow) drawing conclusions about the probability of head or tail by the very motion of the coin. In both cases we would view coin tossing as a deterministic chaotic dynamical system, rather than taking a probabilistic view. In particular, we would this way directly see a connection between ensemble mean values and time mean values: A time mean value at final time may be viewed either as a mean value in time over a discrete set of uniformly distributed quadrature points of a single coin toss, or as an ensemble mean value corresponding to randomly chosen quadrature points corresponding to randomly chosen final times, and the two mean values should be approximately the same. It would further seem natural to expect the randomly chosen final times to be smoothly distributed as a reflection of the strong sensitivity of the final time to perturbations in e.g. initial data. This would follow from the idea of Poincaré ([76]) that the scales of the initial data perturbations would

be larger than the very small scales of initial data resulting in different outputs reflecting the strong sensitivity. Of course, this idea connects to the idea of Leibniz and Laplace of "equally possible" outcomes.

Viewing coin tossing as deterministic chaos would connect to what is referred to as an *objectivist* point of view in probability theory advocated by Popper, where the probability of coin tossing with a certain coin would reflect the physics of that particular coin under tossing, or the *propensity* of the coin, also connecting to *single-case probability*. The experimental approch corresponds to the *frequentist* interpretation where the probability of head is the frequency of heads over ensembles of many tosses.

FIGURE 12.2. Gottfried Wilhelm von Leibniz (1646–1716): "I say therefore that the existent is the being which is compatible with most things, or the most possible being, so that all coexistent things are equally possible." Pierre-Simon Laplace (1749–1827): "The theory of chance consists in reducing all the events of the same kind to a certain number of cases equally possible...". Jules Henri Poincaré (1854–1912): "... it may happen that small differences in the initial conditions produce very great ones in the final phenomena."

Now, are there dynamical systems which are random but not chaotic? Assuming that a dynamical system is defined by some deterministic law, it would seem quite impossible that there would be no reflection whatsoever of this law as some kind of order in the variation in time of system trajectories. The only way we could get a random system would then be to build in the randomness into the law of the system, which would then no longer be deterministic. So maybe after all there are no dynamical systems based on deterministic laws which are random, but only chaotic systems with some order or fully deterministic systems with a lot of order?

Could it be that if we find some order in a system we believe is random, such as some ensemble mean values approaching some limit as the size of the ensemble grows, corresponding to a central limit theorem or law of large numbers in probability theory, this order in fact signifies that the system is chaotic instead of random. If we view space-time mean values as some kind of ensemble mean values, we may get support for such a suspicion. With this perspective the order in the randomness of coin tossing would

have the same origin as the order in coin tossing as a chaotic dynamical system, namely Newtons 2nd law underlying the process of coin tossing, which regulates the propensity of the coin.

If we observe pointwise unpredictable outputs of a certain system, and we do not search and find predictable mean value outputs, then we could come to believe that the system is random and not chaotic. If we then as probabilists observe some predictability of ensemble mean values of this system, then we would probably connect this to some (mysterious) *Law of Chance*. However, as non-probabilists we might instead from the observed order suspect that we are in fact dealing with a deterministic chaotic system based on some law, and we could then find motivation to search for a law defining the system. The observed order would then express the order built into the chaotic system by its law, rather than some (mysterious) Law of Chance.

12.6 NS chaotic rather than random

At any rate, the NS equations do not seem to represent a random dynamical system with solutions jumping around unpredictably like tossed coins in a probabilistic setting. Therefore, we avoid using probability theory and statistics in this book. We thus use a deterministic approach and not a probabilistic one. We do this not only because we do not master probabilistic methods, but also because we do not see any reasons to approach turbulence using such methods, because we are dealing with a dynamical system with a known simple law: Newtons 2nd law. We consider dynamical systems with pointwise outputs being unpredicable and certain space-time mean value outputs being predicatable and we do not have to proceed to ensemble mean values. This way we avoid the serious problem of obtaining input data needed in a statistical approach. The data we need is deterministic input data for the NS equations (f, u^0, Ω, T, ν), which we can regard as mean values, but not data on statistical distributions such as covariances, which may be extremely difficult to obtain.

To handle uncertainties in data we use a deterministic approach based on duality, where we compute sensitivites in output to perturbations in input, only requiring a rough estimate of the variance, thus again avoiding detailed statistics.

We sum up this discussion by pinpointing an important difference between a chaotic and a random system as follows: If we have access to only one trajectory of a chaotic dynamical system, we may still get correct information about certain mean values in space-time. In contrast, from knowing only one trajectory of a random system, we can conclude nothing. In the standard setting of discrete time it is impossible to draw some conclusion about the property of a coin by throwing it once. To get information from

a random system we need ensembles of many trajectories from which we can form ensemble mean values. We have to throw the coin many times to get statistical information concerning its properties.

This is a key point directly coupling to computational work. To compute information about a random system, we have to use *Monte Carlo simulation* corresponding to computing many trajectories and taking ensemble mean values. Alternatively, randomness may be modeled in a deterministic system with new independent variables, which is also computationally costly. In a chaotic system like turbulent flow, it may be sufficient to compute one trajectory and take mean values in space-time. Obviously the difference in amount of computational work may be enormous.

Computing solutions of a chaotic system generates seemingly random pointwise output from deterministic input, which could be viewed as some kind of a random number generation, and we could analyse the output using statistical methods. By computation we could thus generate data for statistics. We may say that computation is cheap while aquiring data by measurement in general is expensive, and thus computations could help tackle a main difficulty of statistics, namely how to collect statistical data.

As a final comment on chaotic vs random, we remind that the trajectory of the life of a certain person may be viewed to be chaotic in the sense that it is unpredictable pointwise, but this does not mean that it is random. In fact each life trajectory follows a certain logic (laws) and is far from being random (most of the time). A person taking all the time random decisions will not live long.

12.7 Observability vs Computability

The same questions of predictability/computability of mean values vs point values in space-time, seem to arise in connection with many basic mathematical models containing *macro*-states in the form of mean values of *micro*-states, such as the Schrödinger equations or Boltzmann's equations. In these cases the macro-states may correspond to *observables* such as energy levels or temperature, which are quantities which can be realiably measured and which represent mean values of micro-states in the form of point-valued wave functions or velocity distributions. In these models many different micro-states may produce the same mean value macro-state, and the pointwise values of the micro-states may not be observables nor predictable/computable. We may say that only God may have a correct knowledge about the micro-states, while we as human beings can only hope to observe/predict/compute macro-states. Or with another metaphor: We can never get full information about the thoughts of another person, but sometimes we may get some gross idea of the state of mind of that person and predict the action of that person (up to some tolerance of interest).

12.8 Lorenz system

Lorenz studied a dynamical system in the form of a 3×3 system $\dot{u} = f(u)$ of ordinary differential equations with

$$f(u) = (-10u_1 + 10u_2, 28u_1 - u_2 - u_1u_3, -\frac{8}{3}u_3 + u_1u_2).$$

One may view *Lorenz system* as a very simple model for the NS equations obtained by a Galerkin method with 3 trigonometric basis functions. One may thus view Lorenz system as a model for the evolution of the weather. Lorenz showed that solutions of the Lorenz system are very sensitive to perturbations, e.g. small perturbations in intial data, which makes it impossible to predict/compute the solution pointwise correctly over longer time. More precisely, using double precision it seems inpossible to accurately compute over a time interval longer than 50 time units. Lorenz thus in a very simple model problem gave an explanation of the observed impossibility of predicting the daily weather more than about 3-5 days ahead depending on the weather conditions.

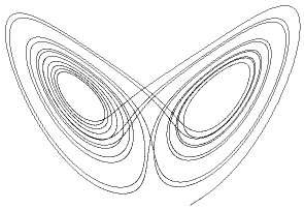

FIGURE 12.3. A Lorenz trajectory.

Lorenz system has a stationary point at the origin, which is unstable, and two slightly unstable stationary points P_1 and P_2 away from the origin. A trajectory of a solution to the Lorenz system repeatedly shifts from orbiting P_1 to P_2 and back again and the number of revolutions around each point seems to vary in an irregular "chaotic" way, see Fig 12.3. However, a plot of a solution trajectory is beautiful and partly very ordered, reflecting that there is some "order in chaos". A solution of the Lorenz system viewed as a weather model, may represent a succession of weather periods with alternating periods of high and low pressure with the lengths of the periods varying irregularly.

So what could then be the order of Lorenz system, other than that expressed by the beautiful "butterfly" order of a typical trajectory? One may expect that over long time the number of revolutions around P_1 and that around P_2 will be approximately the same. In Fig 12.4 we plot these numbers as functions of time for a trajectory computed over long time. Such a trajectory is not pointwise correct but would rather have to be viewed as an ensemble of trajectories over shorter time which are pointwise correct.

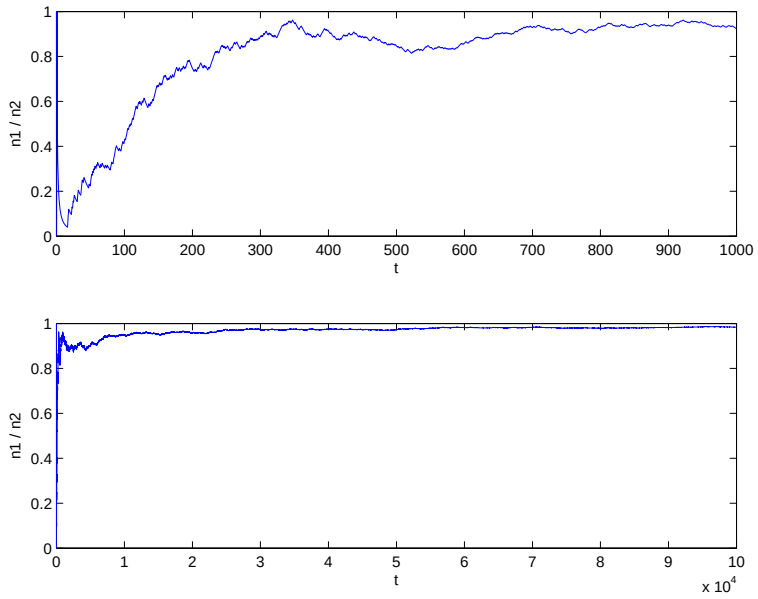

FIGURE 12.4. Number of rotations around P1 and P2 for a Lorenz trajectory (computations by Anders Logg, TTI Chicago).

At any rate we see that the number of revolutions around P_1 and P_2 are approximatey the same.

Summing up, turbulent flow shows features of chaos in the sense that pointwise quantities are not predictable/computable, which reflects strong pointwise sensitivity to perturbations, but certain mean values are predictable/computable, which reflects less sensitivity of mean values, and thus some "order in chaos".

Lorenz connected chaos to pointwise unpredictability, reflecting strong pointwise sensitivity to perturbations. However, Lorenz did not emphasize the other aspect of chaos which we are proposing, namely predictability of certain mean values reflecting moderate sensititvity to perturbations, which distinguishes a chaotic system from a random system.

12.9 Lorenz, Newton and Free Will

The reason Lorenz system attracted so much attention was the discovery that a seemingly innocent system of ordinary differential equations such as the Lorenz system with constant coefficients and quadratic non-linearities, could have pointwise unpredictable solutions. The interest came from the apparent contradiction with the Newtonian view of the Universe as a dynamical system governed by Laws of Nature like Newtons's Law of Grav-

itation, for which the future could be determined if the initial conditions were known to sufficient precision. The eternal philosophical question concerned the possible coexistence of Newtonian mechanics with the idea of a *free will*. If the future was determined by the past, there would be no free will. The Newtonian view now seemed to break down if not even in such a simple system like the Lorenz system, the future was well determined from the past.

Of course, the understanding that small causes could have a large effect is present in Newtonian mechanics, the simplest example being the inverted pendulum, which is very sensitive to small perturbations in an initial top position at rest. So, in fact, there is no contradiction between Newtonian mechanics and the free will: If a small cause can have a large effect, the future is not pre-determined (as we all know), but can be influenced by something like a free will.

Summing up, there are two seemingly paradoxical phenomena, which after all are not paradoxical, but perfectly normal and understandable: (i) A dynamical system expressing simple laws may have very complex pointwise chaotic solutions. (ii) There may be some order in the chaos generated by a dynamical system expressing simple laws.

The NS equations builds on simple laws, and have pointwise chaotic unpredicatable solutions, while some mean values seem to be predictable and ordered.

12.10 Algorithmic Information Theory

In algorithmic information theory one makes the distinction between the length of a computer program (list of instructions), and the length of the output of the program. A computer program for the solution of a dynamical system building on a simple law, like the NS equations, may be short, but the output in the form of a turbulent solution may be long, that is require a lot of memory to store pointwise, and thus require a lot of computational work to produce.

A chaotic system would then be a system with short instruction and long computation producing long pointwise output, from which reliable short mean value output could be obtained. A chaotic system would thus transform short input to short mean value output by passing through long pointwise output, obtained by long computation, following short instruction. Such a chaotic system requires little data and instruction but a lot of computation, which is favorable because data and instruction are both expensive in general, while computation is cheap. In contrast, a random system would require long data and/or instruction and thus would be expensive.

The basic mathematical models of mechanics and physics such as the equations by Schrödinger, Maxwell and Navier-Stokes, all combine short instruction/data with long computation, while mathematical models in biology and economics generally require long instruction/data. The "unreasonble effectiveness of mathematics in the natural sciences" according to Wigner, may be rooted in this difference.

12.11 Statistical Mechanics and Roulette

Boltzmann invented statistical mechanics in the scientific dead-lock caused by Loschmidt's Mystery of irreversibility in reversible Hamiltonian systems. Einstein in the later half of his life seriously questioned science based on microscopic games of roulette like statistical mechanics, as expressed in his famous "God does not play dice". Einstein was not stupid, but his critique was obviated by referring to senility, and statistical mechanics is today viewed as a basis of physics, including quantum mechanics with its probablistic "Copenhagen interpretation" of the Schrödinger wave function.

However, basing mechanics on microscopic games of roulette has a very high scientific price: First, it is impossible to experimentally verify the basic assumptions of microscopic statistics, because the microscopics is not open to inspection (by definition). Secondly, the basic idea of cause-effect in science, has to be given up: the microscopic particles are supposed to "jump" randomely without any cause.

As an alternative to statistical mechanics we propose a new basis of thermodynamics which we refer to as Euler/G2, that is a computational version of the basic laws of conservation of mass, momentum and energy. We can describe Euler/G2 as a model with *deterministic mean-value outputs* based on *determinsitic microscopics*, for which point value outputs are indeterminate. Thus in short, Euler/G2 models output mean-value determinism coupled with output pointwise indeterminism based on microscopic determinism. Euler/G2 thus may be viewed as a complex game of roulette in which pointwise outcomes are indeterminate but mean values are determinate.

In contrast, statistical mechanics is based on microscopic indeterminism. To simulate microscopic games of roulette it appears that one would need microscopics of microscopics, since a game of roulette necessarily is complex, which is against all logic. With this basic motivation we side up with Einstein in his scepticism of statistical mechanics (and he is not alone among famous scientists): Maybe after all, he was not senile when he so clearly expressed his doubts?

13
A $1 Million Prize Problem

> Leray viewed mathematics as a tool for modelling, and drew his inspiration from problems in mechanics and physics, such as fluid dynamics and wave propagation. He was fond of explaining how the road from mathematics to applications is twoway, and how a purely mathematical theorem (concering, for instance, the existence and uniquness of solutions of systems of partial differential equations) might have profound physical implications. (Ivar Ekeland on Jean Leray)
>
> Is it by accident that the deepest insight into turbulence came from Andrei Kolmogorov, a mathematician with a keen interest in the real world? (Uriel Frisch)
>
> Some proofs command assent. Others woo and charm the intellect. They evoke delight and an overpowering desire to say, "Amen, Amen". (John William Strutt (Lord Rayleigh) 1842-1919)
>
> A child, however, who had no important job and could only see things as his eyes showed them to him, went up to the carriage. "The Emperor is naked," he said. "Fool!" his father reprimanded, running after him. "Don't talk nonsense!" He grabbed his child and took him away. (HC Andersen 1805–1875)

13.1 The Clay Institute Impossible $1 Million Prize

At the 2000 Millennium shift, the *Clay Mathematics Institute* presented seven $1 million prize problems, as a reflection of the 23 problems for-

mulated by the famous mathematician Hilbert at the second International Congress of Mathematicians in 1900 in Paris. The prize problems represent open important problems of mathematics of today.

One of the prize problems concerns the *existence*, *uniqueness* and *regularity* of (pointwise) solutions to the Navier–Stokes equations for incompressible flow, that is, precisely the equations (4.1) at focus in this book.

This *Prize Problem* has resisted the attacks of the sharpest mathematical minds for many decades. Of course, with our experience from the previous chapters, it may be natural to connect the difficulty to the presence of turbulent solutions which are not pointwise well-defined in space-time. This was pointed out by Jean Leray, who in 1934 proved the *existence* of *weak solutions*, or *turbulent solutions* in the terminology used by Leray, which satisfy the Navier–Stokes equations in an average sense, that is with the residual tested against a suitable set of smooth test functions, as indicated above.

Proving uniqueness and regularity (which means that the solutions can be differentiated many times and satisfies the NS equations pointwise in space-time) of Leray's weak solutions, would give the $1 million prize. But nobody has been able to come up with such a proof. Leray himself probably did not even attempt to prove uniqueness nor regularity of his weak solutions, because turbulent solutions do not seem to have these qualities.

This leads to the suspicion that the Prize Problem is simply impossible to solve: The Navier-Stokes equations seem to have turbulent solutions and such solutions cannot be expected to be neither pointwise uniquely defined nor regular. So it appears that this is a safe formulation of the Prize Problem for which the prize will never have to be handed out, but this was probably not the intention by the Clay Institute.

We shall see below that the Euler equations in general lack pointwise as well as weak exact solutions, but admit approximate weak solutions, which carry important information.

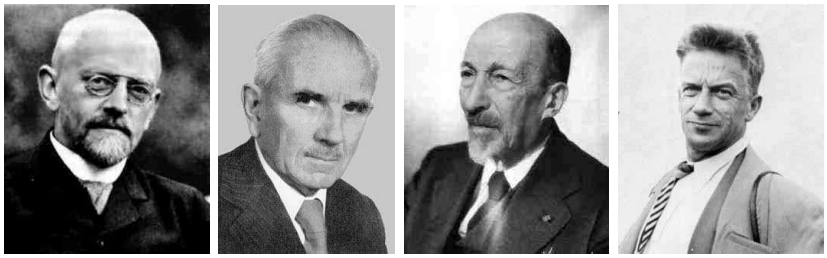

FIGURE 13.1. The famous mathematician David Hilbert (1862–1943), Jean Leray (1906–98) who proved existence of weak solutions, Jacques Salomon Hadamard (1865–1963) who first studied well-posedness of differential equations, and Sergei Lvovich Sobolev (1908-1989) who introduced many fundamental concepts in functional analysis underlying the study of partial differential equations.

13.2 Towards a Possible Formulation

We will now suggest a new formulation of the Prize Problem, which may not be impossible to solve. In this formulation we relax the uniqueness question to uniqueness of certain mean value outputs rather than pointwise uniqueness of solutions, and we do not request a proof of regularity.

To formulate the Prize Problem in this new setting, we will be led to extend the solution concept not only to Leray's weak solutions, but further to *approximate weak solutions* in quantitative form, as already indicated above.

The basic ideas follows a standard approach in *Functional Analysis* and can be concisely expressed as follows: Writing as above the NS equations in pointwise form as $R(\hat{u}) = 0$ with $\hat{u} = (u, p)$, we view $R(\cdot)$ as a *residual* vanishing pointwise for the solution $\hat{u}$. In this setting we seek a *strong solution* $\hat{u}$ which can be differentiated and thus satisfies the equation $R(\hat{u}) = 0$ pointwise in space-time.

We now first relax the requirements on $\hat{u}$, and define $\hat{u}$ to be a *weak solution* if

$$((R(\hat{u}), \hat{v})) = 0,$$

for all *test functions* $\hat{v}$ in a *test space* $\hat{V}$ with norm $\|\cdot\|_{\hat{V}}$ consisting of suitably pointwise differentiable functions, and $R(\hat{u})$ is assumed to belong to a space dual to $\hat{V}$, and $((\cdot, \cdot))$ denotes a duality pairing. Effectively this means that we relax the regularity requirements on the solution $\hat{u}$ and only ask the equation $R(\hat{u})$ to be satisfied in some average sense depending on the test space $\hat{V}$. Typically, $((\cdot, \cdot))$ corresponds to a L_2 inner product in space-time and $((R(\hat{u}), \hat{v}))$ is formally obtained by pointwise multiplication of $R(\hat{u})$ by the test function $\hat{v}$ and integration in space-time. It is the integration in space-time combined with the regularity requirements put on the test functions that relaxes the strong formulation $R(\hat{u}) = 0$ to the weak formulation $((R(\hat{u}), \hat{v})) = 0$ for all $\hat{v} \in \hat{V}$.

Next we relax further and define $\hat{u}$ to be an *ϵ-weak solution* if

$$|((R(\hat{u}), \hat{v}))| \leq \epsilon \|\hat{v}\|_{\hat{V}} \quad \forall \hat{v} \in \hat{V},$$

where ϵ is a (small) positive number. This means that for an ϵ-weak solution $\hat{u}$, we require the residual $R(\hat{u})$ to be smaller than ϵ in a weak norm which is dual to the strong norm of $\hat{V}$. Choosing $\epsilon = 0$ would then bring us back to Leray's concept of an *exact weak solution*. Note that we here do not specify precisely the space of functions where we seek the solution $\hat{u}$, but of course we require that $\hat{u}$ is such that $((R(\hat{u}), \hat{v}))$ is well defined for all $\hat{v} \in \hat{V}$, or that $R(\hat{u})$ belongs to the dual space of $\hat{V}$.

The final step is now to choose an output quantity of interest and seek to estimate the difference in output of two ϵ-weak solutions. This will lead us to introduce a certain linearized problem and measure its stability properties

by a certain stability factor S. The difference in output of two ϵ-weak solutions will then be estimated by $2\epsilon S$.

Before proceeding to present details of the new possible formulation of the Prize Problem, we connect to the concept of well-posedness according to Hadamard.

13.3 Well-Posedness According to Hadamard

The general question of uniqueness directly couples to a question about *well-posedness* of a set of differential equations, as first studied by the French mathematician Jacques Salomon Hadamard (1865–1963). A set of partial differential equations (like the Navier–Stokes equations) is *well-posed* if small variations in data (like initial data) result in small variations in the solution (at a later time). Hadamard stated that only well-posed mathematical models could be meaningful: if very small changes in data could cause large changes in the solution, it would clearly be impossible to reach the basic requirement in science of reproducibility.

The question of well-posedness may alternatively be viewed as a question of *sensitivity to perturbations*. A problem with very strong sensitivity to perturbations would not be well-posed in the Hadamard sense. Now Hadamard proved the well-posedness of some basic partial differential equations like the Poisson equation, but he did not state any result for the Navier–Stokes equations.

Of course, believing that solutions to the Navier–Stokes equations may be turbulent, and observing the seemingly pointwise chaotic nature of turbulence, we could not expect the Navier–Stokes equations to be well-posed in a pointwise sense: we would expect to see a very strong pointwise sensitivity to small perturbations. But, of course it would be most natural to ask if certain mean values may be less sensitive, so that the Navier–Stokes equations would be well-posed in the sense of such mean values. This is what we will do. The stability factor S may then be viewed to measure the well-posedness of certain mean values in the sense of Hadamard. Surprisingly maybe, this appears to be a new concept, which one may describe as *output uniqueness of approximate weak solutions* as compared to (nonexistent) pointwise uniqueness of strong solutions.

13.4 ϵ-Weak Solutions

We now define the concept of ϵ-weak solutions of the NS equations (4.1) in detail. We define for $\hat{v} = (v, q) \in \hat{V}$

$$\begin{aligned}((R(\hat{u}), \hat{v})) \equiv ((\dot{u}, v)) + (u(0), v(0)) + ((u \cdot \nabla u, v)) - ((\nabla \cdot v, p)) \\ + ((\nabla \cdot u, q)) + ((\nu \nabla u, \nabla v)) - (u^0, v(0)) - ((f, v)),\end{aligned} \tag{13.1}$$

where we choose

$$\hat{V} = \{\hat{v} = (v, q) \in H^1(Q)^4 : v = 0 \text{ on } \Gamma \times I\}$$

and $((\cdot, \cdot))$ is the $L_2(Q)^m$ inner product with $m = 1, 3$ (or a suitable duality pairing) over the space-time domain $Q = \Omega \times I$, and $(\cdot, \cdot)$ is the $L_2(\Omega)^3$ inner product. Here $H^1(Q)$ denotes the Sobolev space of functions defined on Q with first order derivates in space-time in $L_2(Q)$, and $H^1(Q)^2 = H^1(Q) \times H^1(Q)$ et cet. In order for all the terms in the definition of $((R(\hat{u}), \hat{v}))$ to be defined, we thus ask (for example) that $u \in L_2(I; H_0^1(\Omega)^3)$, $(u \cdot \nabla)u \in L_2(I; H^{-1}(\Omega)^3)$, $\dot{u} \in L_2(I; H^{-1}(\Omega)^3)$, $p \in L_2(I; L_2(\Omega))$, $f \in L_2(I; H^{-1}(\Omega)^3)$, where $H_0^1(\Omega)$ is the usual Sobolev space of vector functions being zero on the boundary Γ and square integrable together with their first order derivatives over Ω, with dual $H^{-1}(\Omega)$. As usual, $L_2(I; X)$ with X a Hilbert space denotes the Hilbert space of functions $v : I \to X$ which are square integrable, with norm $\|v\|_{L_2(I;X)} = (\int_X \|v(t)\|_X^2)^{1/2}$.

We note that we could have chosen $\hat{V}$ differently, asking for more or less smoothness; e.g. we may demand more smoothness and ask $\hat{V}$ to be a subset of the Sobolev space $H^2(Q)^4$ of vector functions with square integrable second order derivatives. The choice of $\hat{V}$ we made above fits into the G2 formulation to be given below.

We now define $\hat{u}$ to be an ϵ-weak solution if

$$|((R(\hat{u}), \hat{v}))| \leq \epsilon \|\hat{v}\|_{\hat{V}} \quad \forall \hat{v} \in \hat{V}, \tag{13.2}$$

where $\|\cdot\|_{\hat{V}}$ denotes the $H^1(Q)^4$-norm. We may here without loss of generality put in requirements on some smoothness of $\hat{u}$, e.g. that $\hat{u} \in \hat{V}$, or even the more stringent requirement that $R(\hat{u}) \in L_2(Q)^4$, with $R(\hat{u})$ the residual of (4.1). This is because we use a concept of approximate weak solution, which allows us to smooth an approximate weak solution with minimal smoothness requirements to get a smooth approximate weak solution. This reflects that for any function $v \in L_2(Q)$, there is a smooth function v_ϵ (e.g. in $H^1(Q)$), such that $\|v - v_\epsilon\| \leq \epsilon$, where $\|\cdot\|$ is the $L_2(Q)$-norm. We also note that the initial condition $u(0) = u^0$ is imposed approximately through the variational formulation (13.1).

We now finally define $\hat{W}_\epsilon$ to be the set of ϵ-weak solutions (in $\hat{V}$) for a given $\epsilon > 0$. Equivalently, we may say that $\hat{u} \in \hat{V}$ is an ϵ-weak solution if

$$\|R(\hat{u})\|_{\hat{V}'} \leq \epsilon,$$

where $\|\cdot\|_{\hat{V}'}$ is the dual norm of $\hat{V}$. This is a weak norm measuring mean values of $R(\hat{u})$ with decreasing weight as the size of the mean value decreases. Point values of $R(\hat{u})$ are thus measured very lightly. As indicated, we could go to an even weaker solution concept, for example by replacing H^1 by H^2.

We could also alternatively define $\hat{W}_\epsilon$ to be the set of functions $\hat{u}$ such that $((R(\hat{u}),\hat{v})) = \epsilon\|\hat{v}\|_{\hat{V}}$ for all $\hat{v} \in \hat{V}$, with $= \epsilon$, but we prefer here the first definition with $\leq \epsilon$.

Formally, we would obtain the equation

$$((R(\hat{u}),\hat{v})) = 0$$

by multiplying the NS equation by $\hat{v}$, that is, integrating in space-time the sum of the momentum equation multiplied by v and the incompressibility equation multiplied by q. Thus, a pointwise solution $\hat{u}$ to the NS equations would be an ϵ-weak solution for all $\epsilon \geq 0$, while an ϵ-weak solution for $\epsilon > 0$ may be viewed as an approximate weak solution, but not as an approximate pointwise solution, because its pointwise residual may be large as well as $\|R(\hat{u})\|_{L_2(Q)}$, while $\|R(\hat{u})\|_{\hat{V}'}$ is small.

Note that we may view an ϵ-weak solution $\hat{u}$ to be a pointwise defined solution, like a finite element solution, for which the residual $R(\hat{u})$ is small in the weak $\hat{V}'$-norm, but not in the $L_2(Q)$-norm.

13.5 Existence of ϵ-Weak Solutions by Regularization

There is a great variety of so called regularized NS equations for which it is possible to prove existence of pointwise solutions using standard methods of mathematical analysis. The regularization could be imposed by a higher-order diffusion term like the biLaplacian with a small coefficient acting on the velocity, or replacing the velocity-independent Newtonian viscosity ν by a viscosity $\hat{\nu}$ depending on the norm of the velocity gradient with e.g.

$$\hat{\nu} = \nu + h^2|\nabla u|^\alpha,$$

where $|\nabla u|^2 = \sum_i |\nabla u_i|^2$, $\alpha \geq 1$ and h acts as a (small) scaling parameter. For such regularized NS equations it is possible to prove the existence and uniqueness of solutions (see e.g [69, 39]).

The question is then if such regularized solutions would be ϵ-weak solutions, with an ϵ tending to zero with the regularization? In general we would be able to answer this question by yes, if we just use a sufficiently weak solution concept. The easiest case to analyze is regularization with the biLaplacian, corresponding to introducing the additional viscous term $((\kappa\Delta u, \Delta v))$ in the weak form of the NS equations, where $\kappa > 0$ is a small regularization parameter. We denote the corresponding regularized solution by $\hat{u}_\kappa$, which can be proved to exist by standard methods. By a basic energy estimate, we would have that $((\kappa\Delta u_\kappa, \Delta u_\kappa)) \leq C$, where C would depend only on data. Computing $((R(\hat{u}_\kappa),\hat{v}))$ we would get by Cauchy's inequality, assuming $C = 1$ for simplicity,

$$|((R(\hat{u}_\kappa),\hat{v}))| = |((\kappa\Delta u, \Delta v))| \leq \sqrt{\kappa}\|\hat{v}\|_{L_2(I;H^2(\Omega)^3)}$$

so that $\hat{u}_\kappa$ would be an $\sqrt{\kappa}$-weak solution with the norm of $\hat{V}$ including the $L_2(I; H^2(\Omega)^3)$-norm on the velocities.

Further, the original proof of Leray [68] produces a solution which is an ϵ-weak solution for $\epsilon = 0$, if we impose on $\hat{V}$ a slighly stronger norm on the velocities than $L_2(I; H^1(\Omega)^3)$, see [68, 69].

By introducing the notion of an ϵ-weak solution to the NS equations with a suitable choice of norms on the test functions, it is thus possible to prove existence of solutions using standard methods of mathematical analysis. Below, we shall computationally construct ϵ-weak solutions using the G2 finite element method (under a certain minor assumption). In general, for a computed G2 solution $\hat{U}$, we can by evaluating the residual $R(\hat{U})$ determine the corresponding ϵ.

To sum up, we may say that the question of existence of ϵ-weak solutions of the NS equations is easy to settle, analytically or computationally. By relaxing the requirements on the solution we have made the existence question easy to answer positively. We now turn to the real issue.

13.6 Output Sensitivity and the Dual Problem

Suppose now the quantity of interest, or output, related to a given velocity u is a scalar quantity of the form

$$M(\hat{u}) = ((\hat{u}, \hat{\psi})), \tag{13.3}$$

where $\hat{\psi} \in L_2(Q)$ is a given weight function, which represents a mean-value in space-time. In typical applications the output could be a drag or lift coefficient in a bluff body problem. In this case the weight $\hat{\psi}$ is a piecewise constant in space-time. More generally, $\hat{\psi}$ may be a piecewise smooth function corresponding to a mean-value output.

We now seek to estimate the difference in output of two different ϵ-weak solutions $\hat{u} = (u, p)$ and $\hat{w} = (w, r)$. We thus seek to estimate a certain form of *output sensitivity* of the space $\hat{W}_\epsilon$ of ϵ-weak solutions. To this end, we introduce the following linearized dual problem of finding $\hat{\varphi} = (\varphi, \theta) \in \hat{V}$ such that

$$a(\hat{u}, \hat{w}; \hat{v}, \hat{\varphi}) = ((\hat{v}, \hat{\psi})), \quad \forall \hat{v} \in \hat{V}_0, \tag{13.4}$$

where $\hat{V}_0 = \{\hat{v} \in \hat{V} : v(\cdot, 0) = 0\}$, and

$$\begin{aligned} a(\hat{u}, \hat{w}; \hat{v}, \hat{\varphi}) \equiv\ & ((\dot{v}, \varphi)) + ((u \cdot \nabla v, \varphi)) + ((v \cdot \nabla w, \varphi)) \\ & - ((\nabla \cdot \varphi, q)) + ((\nabla \cdot v, \theta)) + ((\nu \nabla v, \nabla \varphi)), \end{aligned}$$

with u and w acting as coefficients, and $\hat{\psi}$ is given data.

This is a linear convection-diffusion-reaction problem in variational form, with u acting as the convection coefficient and ∇w as the reaction coefficient, and the time variable runs "backwards" in time with initial value

$(\varphi(\cdot,T)=0)$ given at final time T imposed by the variational formulation. The reaction coefficient ∇w may be large and highly fluctuating, and the convection velocity u may also be fluctuating.

Choosing now $\hat{v}=\hat{u}-\hat{w}$ in (13.4), we obtain

$$((\hat{u},\hat{\psi}))-((\hat{w},\hat{\psi}))=a(\hat{u},\hat{w};\hat{u}-\hat{w},\hat{\varphi})=((R(\hat{u}),\hat{\varphi}))-((R(\hat{w}),\hat{\varphi})), \quad (13.5)$$

and thus we may estimate the difference in output as follows:

$$|M(\hat{u})-M(\hat{w})|\le 2\epsilon\|\hat{\varphi}\|_{\hat{V}}. \quad (13.6)$$

By defining the *stability factor* $S(\hat{u},\hat{w};\hat{\psi})=\|\hat{\varphi}\|_{\hat{V}}$, we can write

$$|M(\hat{u})-M(\hat{w})|\le 2\epsilon S(\hat{u},\hat{w};\hat{\psi}), \quad (13.7)$$

and by defining

$$S_\epsilon(\hat{\psi})=\sup_{\hat{u},\hat{w}\in\hat{W}_\epsilon} S(\hat{u},\hat{w};\hat{\psi}), \quad (13.8)$$

we get

$$|M(\hat{u})-M(\hat{w})|\le 2\epsilon S_\epsilon(\hat{\psi}), \quad (13.9)$$

which expresses output uniqueness of $\hat{W}_\epsilon$.

Clearly, $S_\epsilon(\hat{\psi})$ is a decreasing function of ϵ and we may expect $S_\epsilon(\hat{\psi})$ to tend to a limit $S_0(\hat{\psi})$ as ϵ tends to zero. For small ϵ, we thus expect to be able to simplify (13.9) to

$$|M(\hat{u})-M(\hat{w})|\le 2\epsilon S_0(\hat{\psi}). \quad (13.10)$$

Depending on $\hat{\psi}$, the stability factor $S_0(\hat{\psi})$ may be small, medium, or large, reflecting different levels of output sensitivity, with $S_0(\hat{\psi})$ increasing as the mean value becomes more local. Normalizing, we may expect the output $M(\hat{u})\sim 1$, and then one would need $2\epsilon S_0(\hat{\psi})<1$ in order for two ϵ-weak solutions to have a similar output.

Estimating $S_0(\hat{\psi})$ using a standard Grönwall type estimate of the solution $\hat{\varphi}$ in terms of the data $\hat{\psi}$, would give a bound of the form $S_0(\hat{\psi})\le e^{KT}$, where K a pointwise bound of $|\nabla w|$. In a turbulent flow with $Re=10^6$, we may have $K\sim 10^3$, and with $T=10$ such a Grönwall upper bound of $S_0(\hat{\psi})$ would be of the form $S_0(\hat{\psi})\le e^{KT}\sim e^{10000}$, which is an incredibly large number, larger than a *googol*$=10^{100}$. It would be inconceivable to have $\epsilon<10^{-100}$ and thus the output of an ϵ-weak solution would not seem to be well defined.

However, computing the dual solution corresponding to drag and lift coefficients in turbulent flow at $Re=10^6$, we find values of $S_0(\hat{\psi})$ which are much smaller, in the range $S_0(\hat{\psi})\approx 10^3$, for which it is possible to choose ϵ so that $2\epsilon S_0(\hat{\psi})<1$, with the corresponding outputs thus being well defined (up to a certain tolerance). We attribute the fact that $\hat{\varphi}$ and

derivatives thereof are not exponentially large, to cancellation effects from the oscillating reaction coefficient ∇w. We shall study this aspect in model form more closely below. However, the cancellation effects seem to be impossible to account for by analytical methods, because (i) knowledge of the underlying flow velocity u is necessary and (ii) the flow velocity has a complexity defying analytical description. The only way to get this knowledge is to compute the velocity, and introducing computation, we may as well compute the dual solution to get a computational hopefully reasonably accurate estimate of $S_0(\hat{\psi})$, instead of a using a Grönwall estimate of no value at all. In practice, there is a lower limit for ϵ, typically given by the maximal computational cost, and thus $S_0(\hat{\psi})$ effectively determines the computability of different outputs.

Note that we may view W_ϵ to be a set of *possible (ϵ-weak) solutions* sharing a similar output up to the corresponding stability factor.

13.7 Reformulation of the Prize Problem

We now consider a couple of different possible alternative formulations of the Prize Problem. One could simply be our formulations (P) or (P1) from Chapter 1. It seems that these problems could only be answered on a case by case basis, so the Prize would have to be reformulated as a collection of say 1000 $1000 prizes, one for each case. In this book we cover a certain number of these cases of key interest in applications.

We may compare with the following purely qualitative formulation which could fit into a tradition of "pure" mathematics dealing with exact solutions:

- (P2) What outputs of Leray's weak solutions are unique?

In this book we present evidence indicating that (P2) is impossible to answer, because of its purely qualitative nature. Instead we propose the quantitative formulaton (P1) involving approximate weak solutions. We could also formulate this problem as a problem of stability or sensitivity as follows:

- (P3) Determine output sensitivity of ϵ-weak solutions with $\epsilon > 0$, that is, estimate the stability factor $S_\epsilon(\hat{\psi})$ for $\epsilon > 0$ for different flows and different outputs (and different norms for the test functions).

We have seen above that the difference in output given by a function $\hat{\psi}$ of two ϵ-weak solutions is at most $2\epsilon S_\epsilon(\hat{\psi})$, which reflects the output sensitivity in quantitative form. We may thus answer (P1) by answering (P3). One may refer to (P3) as a question of *weak uniqueness* as a short for *output sensitivity of approximate weak solutions*.

We remind the reader again that a Leray weak solution corresponds to a ϵ-weak solution with $\epsilon = 0$. If $S_0(\hat{\psi}) < \infty$, one could in purely qualitative form argue that $\epsilon S_\epsilon(\hat{\psi}) = 0$ for $\epsilon = 0$, and output uniqueness of Leray solutions would follow. However, as we said above, if $S_0(\hat{\psi})$ is very large, this conclusion could be misleading, because multiplication of 0 by ∞ is ill defined. We thus would conclude that (P2) may not be a mathematically sound formulation, while the quantitative version (P3) should be.

In this book we thus only consider ϵ-weak solutions with $\epsilon > 0$. In fact the concept of an 0-weak solution does not make much sense, since already a weak solution is some kind of approximate solution in the pointwise sense. We may then as well choose $\epsilon > 0$, and refrain from the possibly "pathological" case $\epsilon = 0$!

In this book we address (P1), or (P3), using adaptive finite element methods with a posteriori error estimation. As indicated above the a posteriori error estimate results from an *error representation* expressing the output error as a space-time integral of the *residual* of a computed solution multiplied by *weights* which relate to derivatives of the solution of an associated *dual problem*. The weights express *sensitivity* of a certain output with respect to the residual of a computed solution, and their size determine the degree of computability of a certain output: The larger the weights are, the smaller the residual has to be and the more work is required. In general the weights increase as the size of the mean value in the output decreases, indicating increasing computational cost for more local quantities. The stability factor $S_0(\hat{\psi})$ is a certain space-time norm of the weights, and gives a scalar measure of the output sensitivity.

In the next chapter we present computational evidence in a bluff body problem that the drag coefficient c_D, which is a mean value in time of the drag force, is computable to a reasonable tolerance at a reasonable computational cost affordable on a PC, while the value of the drag force at a specific point in time appears to be uncomputable even at a very high computational cost.

13.8 The standard approach to uniqueness

The standard approach to uniqueness of NS solutions goes as follows: Suppose $\hat{u}$ and $\hat{w}$ are two classical pointwise solutions to the NS equations (4.1). Subtracting the two versions of the NS equations, we obtain the following equation for the difference $\hat{v} = (v, q) = \hat{u} - \hat{w}$:

$$\begin{aligned} \dot{v} + (u \cdot \nabla)v + (v \cdot \nabla)w - \nu\Delta v + \nabla q &= 0 && \text{in } \Omega \times I, \\ \nabla \cdot v &= 0 && \text{in } \Omega \times I, \\ v &= 0 && \text{on } \Gamma \times I, \\ v(\cdot, 0) &= u^0 - w^0 && \text{in } \Omega, \end{aligned} \tag{13.11}$$

Multiplying the momentum equation by v and integrating, we obtain for $t \in I$

$$\frac{1}{2}\frac{d}{dt}\|v(\cdot,t)\|^2 + \nu\|\nabla v(\cdot,t)\|^2 = -((v\cdot\nabla)w, v), \tag{13.12}$$

where $(\cdot,\cdot)$ and $\|\cdot\|$ denote the scalar product and norm in $L_2(\Omega)^m$ for $m = 1, 3$, and we used the fact that since $\nabla\cdot u = 0$, we have $((u\cdot\nabla v), v) = 0$. Estimating the right hand side by $K\|v\|^2$, where K as above is a pointwise bound for ∇w, we obtain by using a Grönwall estimate the following standard stability estimate:

$$\|v(\cdot,T)\| \leq \exp(KT)\|u^0 - w^0\|.$$

We noted above that this estimate is void of content from any practical point of view if K is large. Now, intense efforts over many years have been made to come up with alternative stability estimates involving only bounds on w and not ∇w. This is possible using various *Sobolev estimates* as e.g in [69], but will involve moving the derivative in $((v\cdot\nabla)w, v)$ instead to v and then require using the ν-term in (13.12) in a stability estimate, and thus bring in an exponential factor with exponent depending on negative powers of ν, which again will be very large for high Reynolds numbers corresponding to small ν.

There is a classical type uniqueness result of this form stating uniqueness if $w \in L_q(I; L_p(\Omega))$ with $\frac{3}{p} + \frac{2}{q} = 1$ [69]. Since one can actually guarantee that $w \in L_q(I; L_p(\Omega))$ with $\frac{3}{p} + \frac{2}{q} = \frac{3}{2}$, it would seem that uniqueness would lie around the corner, but again the presence of a very large exponential factor means that this is only an illusion.

The net result seems to be that any conceivable stability estimate of classical type based on norm estimation of the crucial term $((v\cdot\nabla)w, v)$, which does not use the oscillating character of the reaction coefficient ∇w, would necessarily involve very large stability factors and would thus be of no real value, according to our point of view. However, the Clay Institute does not seem to share our concern.

14
Weak Uniqueness by Computation

There's no sense in being precise when you don't even know what you're talking about. (John von Neumann)

Ces relations se déduisent d'ailleurs des équations de Navier–Stokes à l'aide d'intégration par parties...j'ai pu démontrer le suivant: les relations en question possédent toujours *au moins une solution*...Peut-être cette solution est-elle trop peu régulière pour posséder à tout instant des dérivées secondes bornées; alors elle n'est pas, au sense propre du terme, une solution des équations de Navier–Stokes; je propose de dire qu'elle en constitute *"une solution turbulente"* (Leray 1934).

14.1 Introduction

To compute approximations of a stability factor $S_\epsilon(\hat{\psi})$ defined by two ϵ-weak solutions $\hat{u}$ and $\hat{w}$ approximately, we replace both $\hat{u}$ and $\hat{w}$ as coefficients in the dual problem by a computed ϵ-weak solution $\hat{U}$, such as a finite element solution, and then compute an approximate dual velocity $\hat{\varphi}_h$ to get $S_\epsilon(\hat{\psi}) \approx S_h(\hat{U};\hat{\psi}) \equiv \|\hat{\varphi}_h\|_{\hat{V}}$. We may then study $S_h(\hat{U};\hat{\psi})$ as we refine the mesh size h, and we may extrapolate to $h = \nu$ to get an approximation of $S_0(\hat{\psi})$, assuming that $h = \nu$ would correspond to a small ϵ. If the extrapolated value is not too large, then we would have evidence of output uniqueness, and if the extrapolated value is very large, we would get indication of output non-uniqueness. As a crude test of largeness it may be natural to use $S_0(\hat{\psi}) >> \nu^{-1/2}$.

If the output is a mean value, then $\|\hat{\varphi}_h\|_{\hat{V}}$ will typically grow slowly with decreasing h. We may take this slow growth as evidence that it is possible to replace both $\hat{u}$ and $\hat{w}$ by $\hat{U}$ in the computation of the solution of the dual problem: a near constancy indicates a desired robustness to (possibly large) perturbations of the coefficients $\hat{u}$ and $\hat{w}$.

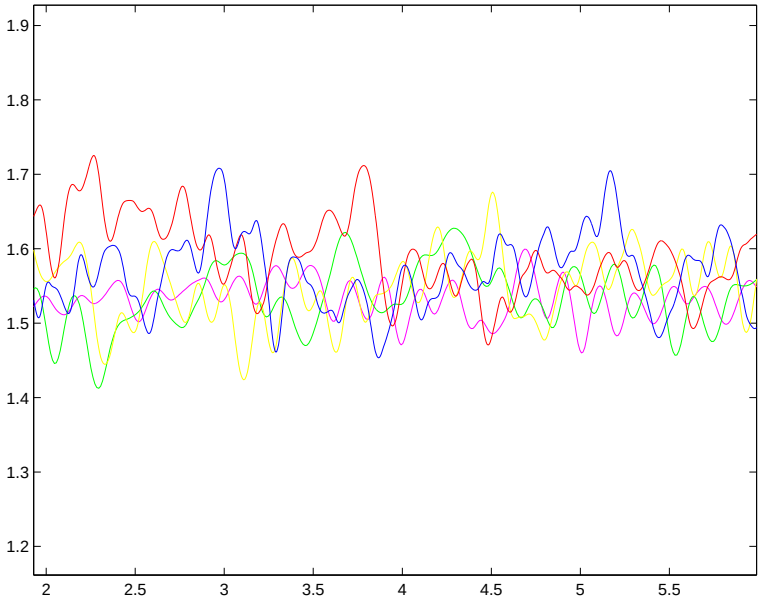

FIGURE 14.1. Drag $D(t)$ (normalized) for a surface mounted cube, as a function of time, for 5 computational meshes.

14.2 Uniqueness of c_D and c_L

The computational example is a bluff body benchmark problem, which is presented in more detail in Chapter 30. We compute the mean value in time of drag and lift forces on a surface mounted cube in a rectangular channel, from an incompressible fluid governed by the Navier–Stokes equations (4.1), at $Re = 40\ 000$ based on the cube side length and the bulk inflow velocity. We compute the mean values over a time interval of a length corresponding to 40 cube side lengths, which we take as approximations of c_D and c_L defined as (normalized) mean values over very long time.

The incoming flow is laminar time-independent with horse-shoe vortex upstream the cube and a laminar boundary layer on the front surface of the body, which separates and develops a turbulent time-dependent wake attaching to the rear of the body. The flow is thus very complex with a

combination of laminar and turbulent features including boundary layers and a large turbulent wake, see Figure 14.2.

The dual problem corresponding to c_D has boundary data of unit size for φ_h on the cube in the direction of the mean flow, acting on the time interval underlying the mean value, and zero boundary data elsewhere. A snapshot of the dual solution corresponding to c_D is shown in Figure 14.3, and in Figure 14.4 we plot $S_h(\hat{U};\hat{\psi})$ as a function of h^{-1} for a range of adaptively refined computational meshes, with h the smallest element diameter in the mesh.

We find that $S_h(\hat{U};\hat{\psi})$ shows a slow logarithmic growth, and extrapolating we find that $S_\nu(\hat{U};\hat{\psi}) \sim \nu^{-1/2}$. We take this as evidence of computability and weak uniqueness of c_D, and we obtain similar results for the lift coefficient c_L.

14.3 Non-Uniqueness of $D(t)$

We now investigate the computability and weak uniqueness of the normalized drag force $D(t)$ at a specific time t. In Figure 14.1 we show the variation in time of $D(t)$ computed on different meshes, and we notice that $D(t)$ for a given t does not appear to converge with decreasing h: The best we can say seems to be that $1.3 \leq D(t) \leq 1.7$.

We now choose one of the finer meshes corresponding to $h^{-1} \approx 500$, and we compute the dual solution corresponding to a mean value of $D(t)$ over a time interval $[T_0, T]$, where we let $T_0 \to T$. We thus seek to compute the point value $D(T)$.

In Figure 14.5 we find a growth of $S_h(\hat{U};\hat{\psi})$ similar to $|T - T_0|^{-1/2}$, as we let $T_0 \to T$. The results show that for $|T - T_0| = 1/16$ we have $S_h(\hat{U};\hat{\psi}) \approx 10\nu^{-1}$, and extrapolation of the computational results indicate further growth of $\tilde{S}_0(\hat{\psi})$, as $T_0 \to T$ and $h \to \nu$. We take this as evidence of non-computability and weak non-uniqueness of $D(T)$.

14.4 Stability of the dual solution with respect to time sampling

To get an idea of the dependence of stability factors on the primal solution $\hat{U}$ used to compute the dual solution, we sample the coefficients in the dual problem with different frequencies in time and compute the corresponding dual solutions. In Table 5.1 we display different norms of the dual solution $\hat{\varphi}_h$ and notice that different sampling frequencies give very similar stability factors, and in Fig. 14.6 we plot snapshots of different dual solutions, again very similar.

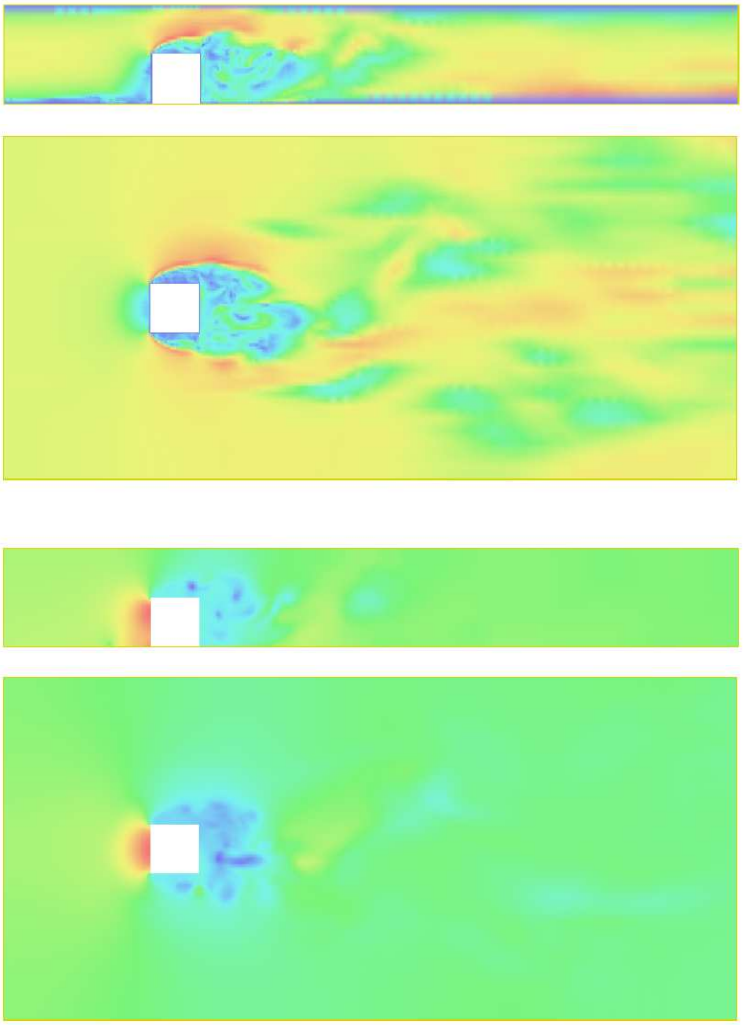

FIGURE 14.2. Surface mounted cube: velocity $|U|$ (upper) and pressure P (lower), in the x_1x_2-plane at $x_3 = 3.5H$ and in the x_1x_3-plane at $x_2 = 0.5H$.

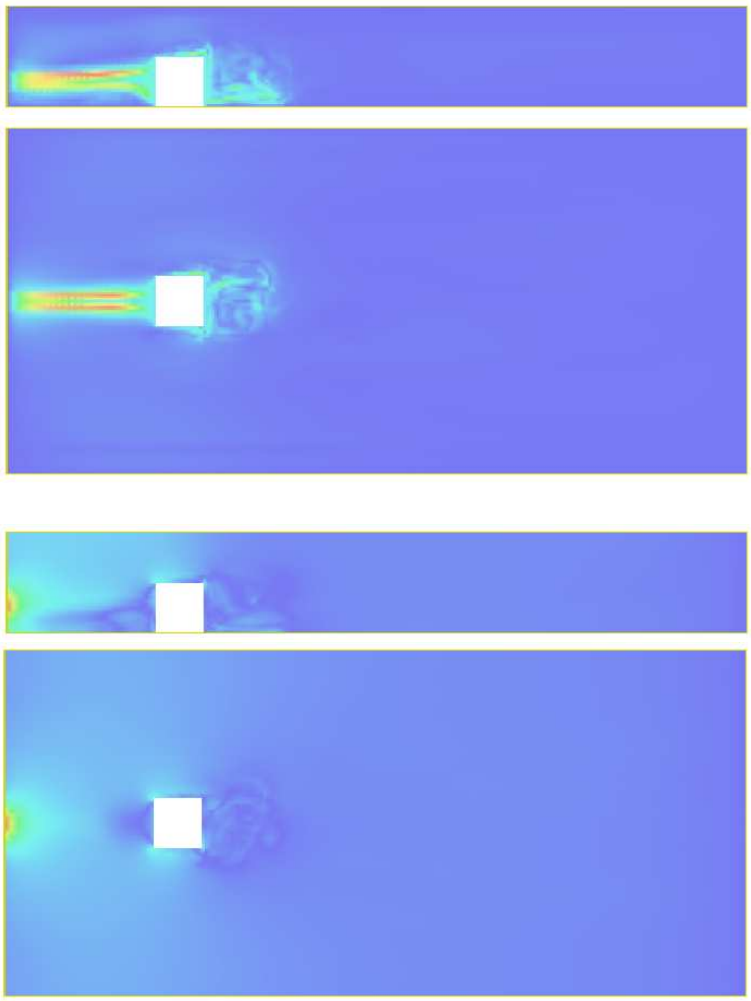

FIGURE 14.3. Surface mounted cube: dual velocity $|\varphi_h|$ (upper), and dual pressure $|\theta_h|$ (middle), in the x_1x_2-plane at $x_3 = 3.5$H and in the x_1x_3-plane at $x_2 = 0.5$H.

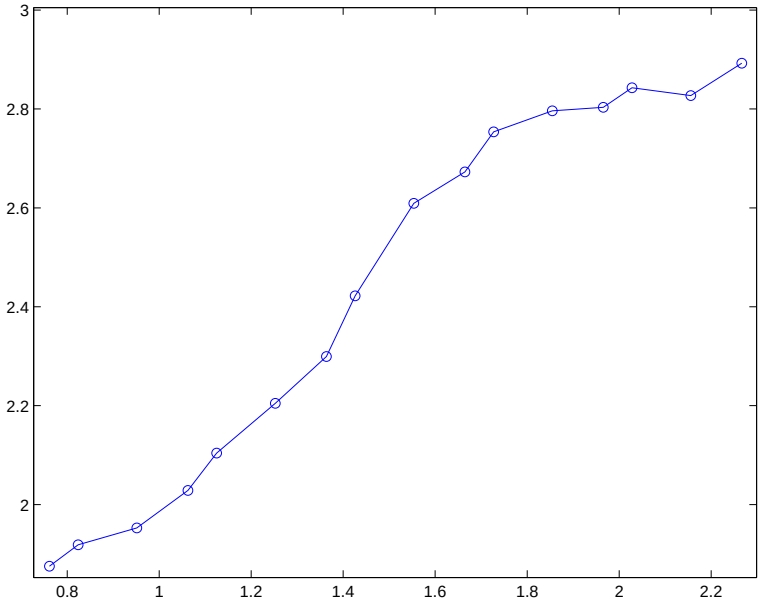

FIGURE 14.4. $\log_{10}$-$\log_{10}$-plot of $S_h(\hat{U};\hat{\psi})$ as a function of $1/h$.

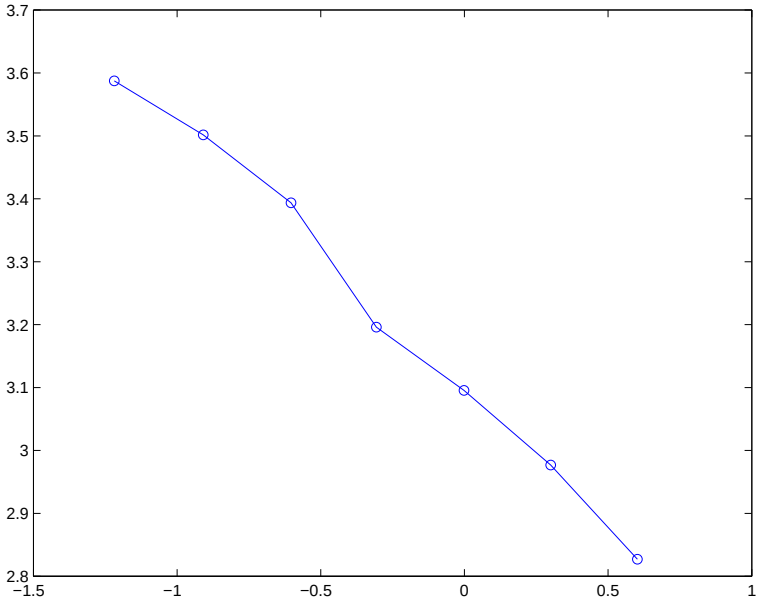

FIGURE 14.5. $S_h(\hat{U};\hat{\psi})$ corresponding to computation of the mean drag force (normalized) over a time interval $[T_0, T]$, as a function of the interval length $|T - T_0|$ ($\log_{10}$-$\log_{10}$-plot).

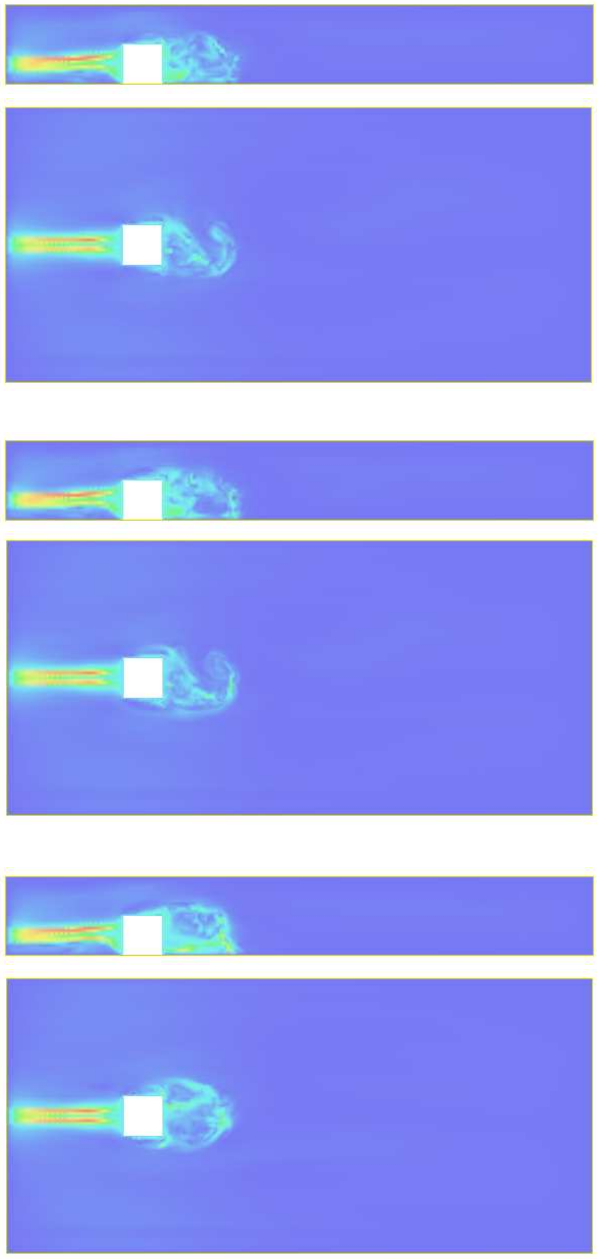

FIGURE 14.6. Surface mounted cube: snapshots of the dual velocity $|\varphi_h|$ sampled 4 times per time unit (upper), 2 times per time unit (middle), and once per time unit (lower), corresponding to "4", "2", and "1", in Table 14.1, in the x_1x_2-plane at $x_3 = 3.5$H and in the x_1x_3-plane at $x_2 = 0.5$H.

freq.	$\|\varphi_h\|$	$\|\nabla\varphi_h\|$	$\|\hat{\varphi}_h\|_{\hat{V}}$
8	7.99	646	652
4	8.04	658	663
4^*	8.14	679	684
2	8.23	693	698
1	8.35	744	749

TABLE 14.1. Surface mounted cube: Norms of the dual solution φ_h linearized at a primal velocity U sampled with different frequencies (normalized by the inflow velocity $U_\infty = 1$), with "4^*" being a translated sampling of "4" with the same frequency.

14.5 Conclusion

We have given computational evidence of weak uniqueness of mean values such as c_D and c_L and weak non-uniqueness of a momentary value $D(t)$ of the total drag. In the computations we observe this phenomenon as a continuous degradation of computability (increasing stability factor $S_0(\hat{\psi})$) as the length of the time interval underlying the mean value decreases to zero. Effectively we seem to be able to compute c_D and c_L up to a tolerance of roughly 0.05 taking mean valus in time of length 10, while the variation of a momentary value $D(t)$ may be almost a factor 10 larger. Thus the distinction between computability (or weak uniqueness) and non-computability (weak non-uniqueness) may in practice be just one order of magnitude in output error, rather than a difference between 0 and 1 (or ∞).

Of course, this is what you may expect to see in a quantified computational world, as compared to an ideal mathematical world. In particular, we are led to measure residuals of approximate weak solutions, rather than working with the exact weak solutions of Leray with zero residuals. A such quantified mathematical world is in fact richer than an ideal zero residual world, and thus may be more accessible.

15
Existence of ϵ-Weak Solutions by G2

> One may be tempted to believe that physical laminar flows correspond to smooth mathematical solutions (of the Navier–Stokes equations) and turbulent flows to non-smooth solutions (Oseen in Hydrodynamik ...).
>
> On peut vérifier en outre que l'énergie cinétique totale du liquide reste bornée; mais il ne semble pas possible de déduire de ce fait que le mouvement lui-même reste régulier; j'ai même indiqué une raison qui me fait croire à l'existence de mouvements devenant irréguliers au bout d'un temps fini; je n'ai malheuresement pas réussi à forger un exemple d'une telle singularité (Leray 1934).
>
> We will now discuss in a little more detail the Struggle for Existence.(Darwin)

15.1 Introduction

We now show that we may construct ϵ-weak solutions of the NS equations using stabilized Galerkin finite element methods in the form of G2. We do this in order to highlight a basic property of a G2 solution, which is designed so as to have a a small residual in a weak sense, and thus may pass as an ϵ-weak solution for a certain ϵ depening on the mesh size. We do not here give full details of the formulation of G2, e.g. concerning the use of continuous or discontinuous Galerkin for the time stepping, but focus on the basic role of the stabilization in G2, and give a complete description of G2 in Chapter 25.

In the discussion of the Clay Prize Problem we commented that an alternative way of proving existence of ϵ-weak solutions is to first prove existence for suitably regularized NS equations, which is possible using standard methods of mathematical analysis, and to then prove that a regularized solution passes as an ϵ-weak solution for some ϵ depending on the regularization, which tends to zero with the regularization.

15.2 The Basic Energy Estimate for the Navier–Stokes Equations

We start by deriving a basic stability estimate of energy type for the velocity u of the Navier–Stokes equations (4.1), assuming for simplicity that $f = 0$. This is about the only analytical a priori estimate known for the Navier–Stokes equations. We thus formally assume existence of a (pointwise) solution (u, p), and derive a bound for the velocity u in terms of given data.

Scalar multiplication of the momentum equation by u and integration with respect to x gives

$$\frac{1}{2}\frac{d}{dt}\int_\Omega |u|^2\,dx + \nu\sum_{i=1}^3\int_\Omega |\nabla u_i|^2\,dx = 0,$$

because by partial integration (with boundary terms vanishing),

$$\int_\Omega \nabla p\cdot u\,dx = -\int_\Omega p\nabla\cdot u\,dx = 0$$

and

$$\int_\Omega (u\cdot\nabla)u\cdot u\,dx = -\int_\Omega (u\cdot\nabla)u\cdot u\,dx - \int_\Omega \nabla\cdot u|u|^2\,dx$$

so that

$$\int_\Omega (u\cdot\nabla)u\cdot u\,dx = 0. \tag{15.1}$$

Integrating next with respect to time, we obtain the following basic a priori stability estimate for $T > 0$ in terms of the L_2-norm of the initial velocity u^0:

$$E_\nu(u) \equiv \frac{1}{2}\|u(\cdot,T)\|^2 + D_\nu(u,T) = \frac{1}{2}\|u^0\|^2, \tag{15.2}$$

where

$$D_\nu(u,T) = \nu\sum_{i=1}^3\int_0^T \|\nabla u_i\|^2\,dt,$$

and where $\|\cdot\|$ denotes the $L_2(\Omega)$-norm. This estimate gives a bound on the kinetic energy of the velocity with $D_\nu(u,T)$ representing the total *dissipation* from the viscosity of the fluid over the time interval $[0,T]$. We see

that the growth of this term with time corresponds to a decrease of the velocity (momentum) of the flow (with $f = 0$).

The characteristic feature of a turbulent flow is that $D_\nu(u,T)$ is comparatively large, while in a laminar flow with ν small, $D_\nu(u,T)$ is small. With $D_\nu(u,T) \sim 1$ in a turbulent flow and $|\nabla u|$ uniformly distributed, we may expect to have pointwise

$$|\nabla u_i| \sim \nu^{-1/2}. \tag{15.3}$$

15.3 Existence by G2

To generate approximate weak solutions of the NS equations, we use a finite element method of the form (assuming for simplicity $f = 0$): Find $\hat{U} \equiv \hat{U}_h \in \hat{V}_h$, where $\hat{V}_h \subset \hat{V}$ is a finite dimensional subspace of piecewise polynomial functions defined on a computational mesh in space-time of mesh size h, such that

$$((R(\hat{U}),\hat{v})) + ((hR(\hat{U}),R(\hat{v}))) = 0, \quad \forall \hat{v} \in \hat{V}_h, \tag{15.4}$$

where $R(\hat{w}) \equiv (R_1(\hat{w}),R_2(w))$, $\hat{w} = (w,r)$ and

$$\begin{aligned} R_1(\hat{w}) &= \dot{w} + U\cdot\nabla w + \nabla r - \nu\Delta w,\\ R_2(w) &= \nabla\cdot w, \end{aligned} \tag{15.5}$$

with elementwise definition of second order terms. We here interpret a convection term $((U\cdot\nabla w, v))$ as

$$\frac{1}{2}((U\cdot\nabla w, v)) - \frac{1}{2}((U\cdot\nabla v, w)$$

which is literally true if $\nabla\cdot U = 0$. With this interpretation we will have $((U\cdot\nabla U, U)) = 0$, which corresponds to (15.1), even if the divergence of the finite element velocity U does not vanish exactly. With this interpretation we obtain choosing $\hat{v} = \hat{U}$ in (15.4) (still assuming $f = 0$):

$$E_\nu(U) + ((hR(\hat{U}),R(\hat{U}))) \le \frac{1}{2}\|u^0\|^2. \tag{15.6}$$

The finite element method (15.4) is a stabilized Galerkin method with the term $((R(\hat{U}),v))$ corresponding to Galerkins method and the term $((hR(\hat{u}),R(\hat{v})))$ corresponding to a weighted residual least squares method with stabilizing effect expressed in (15.6). We also refer to this method as General Galerkin or G2, and we thus refer to $\hat{U}$ as a *G2-solution*. The existence of a discrete solution $\hat{U} \equiv \hat{U}_h \in V_h$ follows by Brouwer's fixed point theorem combined with the stability estimate (15.6).

We now return to the main objective of this chapter of showing the existence of ϵ-weak solutions to the NS equations. For all $\hat{v} \in \hat{V}$, we have


FIGURE 15.1. Richard Courant (1888-1972) was first to introduce the finite element method in 1922, in an existence proof of a version of the Riemann mapping theorem. Boris Grigorievich Galerkin (1871-1945), russian engineer who introduced the finite element method as a computational tool.

with $\hat{v}_h \in \hat{V}_h$ a standard interpolant of v satisfying $\|h^{-1}(\hat{v}-\hat{v}_h)\| \le C_i\|\hat{v}\|_{\hat{V}}$, using also (15.4),

$$\begin{aligned}((R(\hat{U}),\hat{v})) &= ((R(\hat{U}),\hat{v}-\hat{v}_h)) - ((hR(\hat{U}),R(\hat{v}_h))) \\ &\le C_i\|hR(\hat{U})\|\|\hat{v}\|_{\hat{V}} + M(U)\|hR(\hat{U})\|\|\hat{v}\|_{\hat{V}},\end{aligned} \tag{15.7}$$

where $M(U)$ is a pointwise bound of the velocity $U(x,t)$, and $C_i \approx 1$ is an interpolation constant. It follows that the G2-solution $\hat{U}$ is an ϵ-weak solution with

$$\epsilon = (C_i + M(U))\|hR(\hat{U})\| \le \sqrt{h}(C_i + M(U))\|u^0\|,$$

since from the energy stability estimate $\|\sqrt{h}R(\hat{U})\| \le \|u^0\|$.

Assuming now that $M(U) = M(U_h)$ is bounded with $h > 0$, and letting $C_i + M(U) \le C$, it follows that $\hat{U}$ is an ϵ-weak solution with $\epsilon = C\sqrt{h}$, assuming $\|u^0\| \le 1$. More generally, we may say that a G2 solution $\hat{U}$ is an ϵ-weak solution with $\epsilon = C\|hR(\hat{U})\|$.

We have now demonstrated the existence of an ϵ-weak solution to the NS equations for any ϵ, assuming that the maximum computed velocity is bounded (or grows slower than $h^{-1/2}$). More generally, we have shown that a G2-solution $\hat{U}$ is an ϵ-weak solution with $\epsilon = C_U\|hR(\hat{U})\|$ with $C_U = C_i + M(U)$. Computing $\hat{U}$, we can compute $\epsilon = C_U\|hR(\hat{U})\|$ and thus determine the corresponding ϵ.

We conclude that coming up with ϵ-weak solutions to the NS equations is easy, if we use G2 and a computer (and find that C_U grows slower than $h^{-1/2}$).

We now turn to the question of estimation of the error in output of G2-solutions, which of course as above will bring in the corresponding stability factor.

Remark. In estimating above $((R(\hat{U}),\hat{v}-\hat{v}_h))$ we did not properly account for the diffusion term $((\nu\nabla U,\nabla(v-v_h)))$. Doing so would introduce an

additional term which most easily can be estimated by a term of the form $C\sqrt{\nu}\|\hat{v}\|_{\hat{V}}$, and to bound this term as above we would need that $\nu \leq h$. Since ν often is smaller than 10^{-4} for the problems we focus on in this book, this would not be restrictive in most cases. For larger ν we can turn the argument around in a different way, but we do not here enter into details.

15.4 A Posteriori Output Error Estimate for G2

We now let $\hat{u}$ be an ϵ-weak solution of the NS equations and let $\hat{U}$ be a G2-solution, which we just showed can be viewed to be an ϵ_{G2}-weak solution, with $\epsilon_{G2} = C_U\|hR(\hat{U})\| >> \epsilon$.

As above we get the following a posteriori error estimate for a mean-value output given by a function $\hat{\psi}$:

$$|M(\hat{u}) - M(\hat{U})| \leq (\epsilon + C_U\|hR(\hat{U})\|)S_{\epsilon_{G2}}(\hat{\psi}), \tag{15.8}$$

where $S_{\epsilon_{G2}}(\hat{\psi})$ is the corresponding stability factor defined as above. Obviously the size of the stability factor $S_{\epsilon_{G2}}(\hat{\psi})$ is crucial for computability: the stopping criterion is evidently (assuming ϵ small):

$$C_U\|hR(\hat{U})\|S_{\epsilon_{G2}}(\hat{\psi}) \leq TOL,$$

where $TOL > 0$ is a tolerance. If $S_{\epsilon_{G2}}(\hat{\psi})$ is too large, or TOL is too small, then we may not be able to reach the stopping criterion with available computing power, and the computability is out of reach.

16

Stability Aspects of Turbulence in Model Problems

> Merkwürdig ist auch das Versagen der Eindeutigkeitsbeweise in drei Dimensionen. Diese Fragen sind immer noch nicht befriedigend erklärt. Est ist schwer zu glauben das die Anfangswertaufgabe zäher Flüssigkeiten für $n = 3$ mehr als eine Lösung haben könnte, und der Erledigung der Eindeutigkeitsfrage sollte mehr Aufmerksamkeit geschenkt werden. (E. Hopf)

16.1 The Linearized Dual Problem

We have seen that the predictability/computability of a given flow (solution $\hat{u} = (u, p)$ of the NS equations) is determined by the stability properties of the corresponding linearized dual problem. We may thus say that the secret of computational modeling of turbulent flow is hidden in the stability properties of the dual problem, which takes the following form when linearized around the given velocity u, if we for simplicity leave out the pressure part of the dual solution: Given ψ find φ such that

$$-\dot{\varphi} - u \cdot \nabla\varphi + \nabla u^\top \varphi - \nu\Delta\varphi = \psi \quad \text{on } [0,T), \quad \varphi(T) = 0,$$

where $(\nabla u^\top \varphi)_j = \sum_{i=1}^3 u_{i,j}\varphi_i$. This is a linear convection-diffusion-reaction problem with convection velocity u and reaction coefficient matrix ∇u and data ψ. We are interested in the stability properties of the dual problem which concern the size of the stability factor $S = \|\varphi\|/\|\psi\|$ where $\|\cdot\|$ represent some norms, usually different, for φ and ψ. The stability factor S expresses the sensitivity of an output related to ψ.

We now seek to estimate the size of the stability factor S for different data ψ corresponding to different outputs. We seek qualitative understanding and are thus ready to simplify. In reality, of course we just compute the stability factor S and we do not need to understand anything, but we here seek some rationale behind the computed values for S.

We then assume that the norm of $\|\varphi\|$, which typically involves derivatives of φ, can be reflected through the size of φ itself through the coupling to the viscous term in the dual equation. Effectively, we may then leave out the viscous term. Further, we note that the size of the dual solution φ does not seem to be much affected by the convection, since convection only shifts φ in space but does not change its size. In contrast, the reaction term with coefficient $\nabla u^\top$ obviously may change the size of φ, and thus may affect the size of S. We thus focus on the stability properties of the reaction problem:

$$-\dot{\varphi} + A\varphi = \psi \quad \text{on } [0,T), \quad \varphi(T) = 0,$$

where the matrix $A = \nabla u^\top$ depends on (x,t). We are interested in the size of the dual solution φ for different ψ. In a turbulent flow A may have large coefficients which may change rapidly with (x,t). In general we may expect that the growth properties of φ connect to the spectrum of A with exponential growth corresponding to eigenvalues with negative real part, exponential decay to eigenvalues with positive real part, and oscillations corresponding to the imaginary part of conjugate pairs of eigenvalues.

Let us now freeze x and let $\lambda_i(t)$, $i = 1,2,3$, be the eigenvalues of $A(x,t)$. By (approximate) incompressibility of u and the fact that the sum of the eigenvalues of a matrix is equal to the sum of its diagonal elements, we have that

$$\sum_{i=1}^{3} \text{Real part}(\lambda_i) \approx 0,$$

see Fig. 16.1, and thus we may expect that the exponential growth and decay from the real parts of the eigenvalues will balance with no net growth, if we let φ convect over different x with the convection velocity u.

It remains to understand the possible effect of the oscillating nature coupled to the imaginary part of the conjugate eigenvalues. We shall see that this connects to the observation that stability factors decrease as the length of the mean values in time increases, which we could address to cancellation in integrals of oscillating functions. We first present a model case with a pair of conjugate imaginary eigenvalues, in which case the dual problem for each x is just the harmonic oscillator.

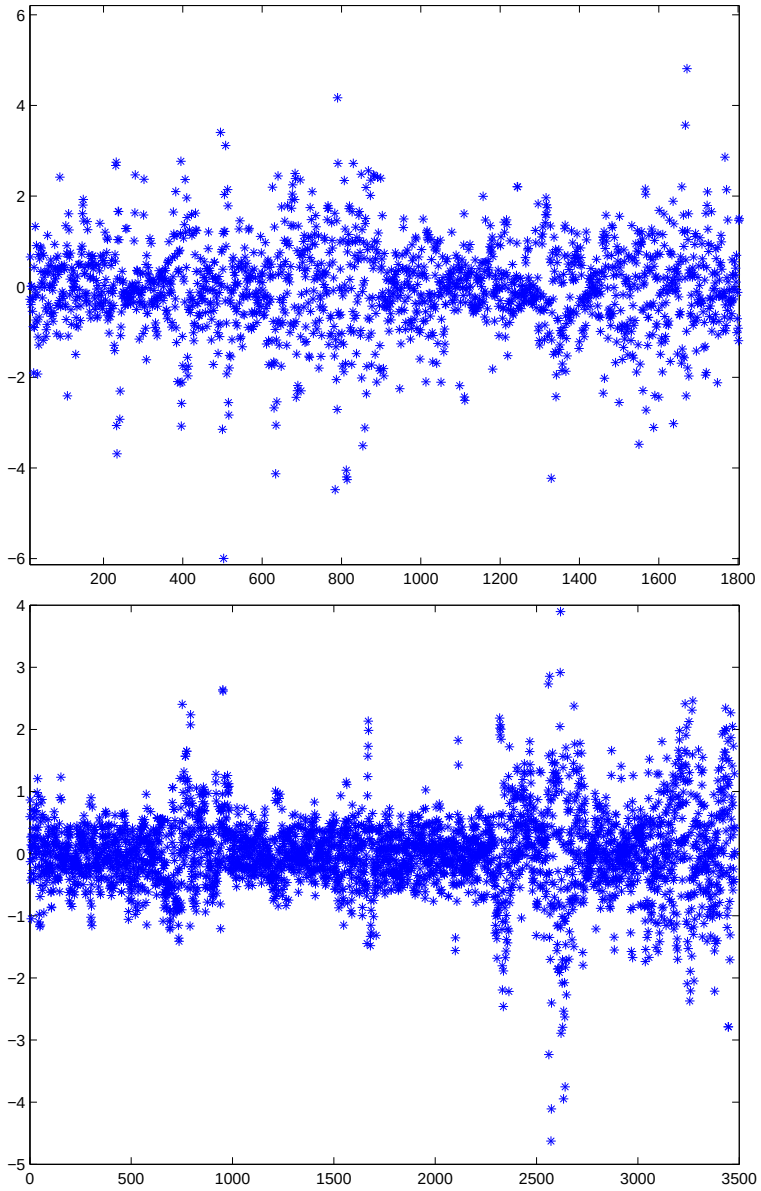

FIGURE 16.1. Sum of the real parts of the eigenvalues of ∇U, for G2 solutions $\hat{U}$ for a few thousand elements in the turbulent wake of a circular and a square cylinder, from computations presented in detail in Chapter 30.

16.2 Rotating Flow

We consider a flow corresponding to one rotating vortex tube oriented in the x_3-direction given by the stationary flow $\hat{u} = (u, p)$ such that

$$u(x) = \omega(-x_2, x_1, 0), \quad p = \frac{\omega}{2}(x_1^2 + x_2^2),$$

which satisfies the NS equations with $\nu = 0$ and $f = 0$, see Fig. 16.2. Here ω is a moderately large positive number which represents the angular rotational velocity of the vortex tube. We may think of the vortex tube having a diameter $1/\omega$, and we may, very loosely speaking, think of a turbulent flow as a collection of such rotating tubes. Recalling that the velocity gradient of a turbulent flow would be of size $\nu^{-1/2}$, or $h^{-1/2}$ in a computational simulation with smallest scale h, we could expect that $\omega \sim \nu^{-1/2}$ or $\omega \sim h^{-1/2}$.

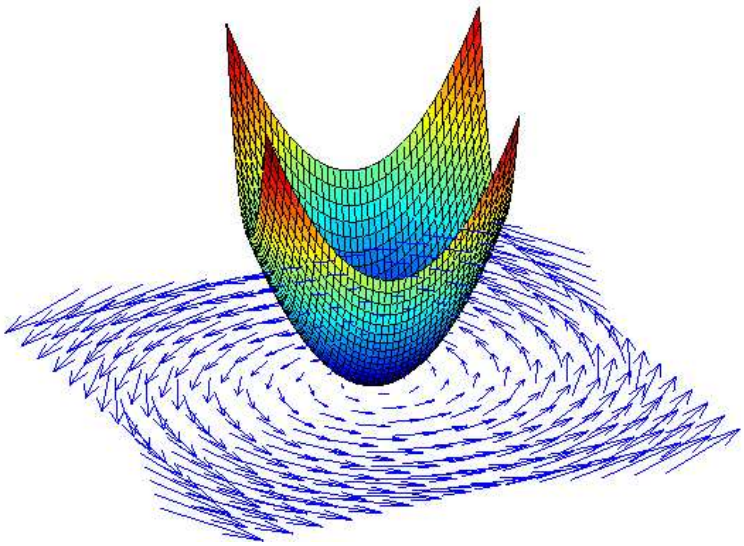

FIGURE 16.2. Rotational flow $u(x) = \omega(-x_2, x_1, 0)$, and $p = \frac{\omega}{2}(x_1^2 + x_2^2)$.

16.3 A Model Dual Problem for Rotating Flow

The dual problem corresponding to rotating flow takes the following form disregarding the convection term and the φ_3 component as well as the space

dependence:

$$\begin{aligned} \dot{\varphi}_1 + \omega\varphi_2 &= \psi_1 \quad \text{on } (0,T], \\ \dot{\varphi}_2 - \omega\varphi_1 &= \psi_2 \quad \text{on } (0,T], \\ \varphi_1(0) &= \varphi_2(0) = 0, \end{aligned} \tag{16.1}$$

where we for simplicity reversed time with the transformation $t \to T - t$. This is the model of a harmonic oscillator with frequency ω driven by the force (ψ_1, ψ_2). We choose $\psi_1(t) = 1/\tau$ for $0 \le t \le \tau$, $\psi_1(t) = 0$ for $\tau < t \le T$, and $\psi_2 \equiv 0$, which (before time reversal) corresponds to the output

$$M_\tau(u_1) = \frac{1}{\tau}\int_{T-\tau}^{T} u_1(t)\,dt, \tag{16.2}$$

which is a mean value in time of length τ.

Writing (16.1) in matrix form as $\dot{\varphi} + A\varphi = \psi$ on $[0,T]$, $\varphi(0) = 0$, where $\varphi = (\varphi_1, \varphi_2)$ and A has a pair of imaginary eigenvalues $\pm i\omega$, we can express the solution $\varphi(t)$ as a convolution of the data $\psi(t)$ with the the fundamental solution matrix $\exp(tA)$ of the homogeneous problem $\dot{\varphi} + A\varphi = 0$, as

$$\varphi(t) = \int_0^t \exp((t-s)A)\psi(s)\,ds.$$

Since $\exp(tA)_{11} = \cos(\omega t)$, we have for $t \le \tau$,

$$\varphi_1(t) = \frac{1}{\tau}\int_0^t \cos(\omega(t-s))\,ds = \frac{\sin(\omega t)}{\omega\tau},$$

and for $t > \tau$,

$$\varphi_1(t) = \frac{1}{\tau}\int_0^\tau \cos(\omega(t-s))\,ds = \frac{\sin(\omega t) - \sin(\omega(t-\tau))}{\omega\tau}.$$

We now study the dependence of the magnitude of $\varphi_1(t)$ as a function of the size τ of the mean value. We find that

$$\begin{aligned} |\varphi_1(t)| &\approx 1 \quad \text{for } \omega\tau \le 1, \\ |\varphi_1(t)| &\approx \frac{1}{\omega\tau} \quad \text{for } \omega\tau \text{ large}, \end{aligned}$$

and we have that $\varphi_1(t)$ increases from zero with slope $1/\tau$ as long as $t < \min(\tau, \frac{1}{\omega})$ and then levels off into oscillations, so that for $\omega\tau$ large, $\varphi_1(t)$ is much smaller than for $\omega\tau$ small, see Fig. 16.3. A short mean value output thus has a larger stability factor than a long mean value, which expresses that a short mean value is more sensitive to perturbations than a long mean value output.

Obviously, the reduction in size of the dual solution going from short to long mean value comes from considerable cancellation in the integral defining $\varphi_1(t)$ as a convolution of $\psi(t)$ with the oscillating integrand $\cos(\omega t)$, which starts coming into play when $\omega\tau > 1$ and becomes more pronounced as $\omega\tau$ grows larger.

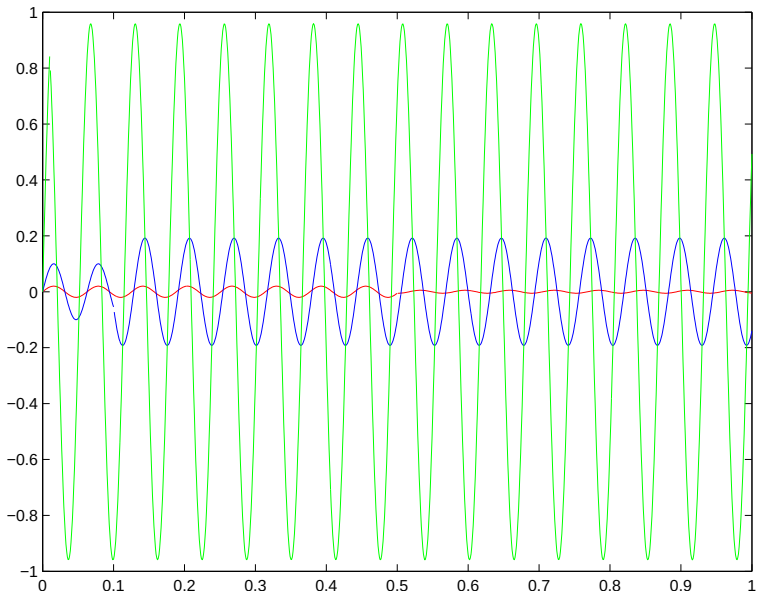

FIGURE 16.3. Model dual problem for rotational flow; $\omega = 100$, $\tau = 0.01, 0.1, 0.5$.

16.4 A Model Dual Problem for Oscillating Reaction

To model the effect of the real parts of the eigenvalues summing to zero we consider the scalar problem

$$-\dot{\varphi}(t) + \cos(t)\varphi(t) = 0, \quad \text{on } [0,T),$$

with solution

$$\varphi(t) = \exp(\sin(T-t))\varphi(T).$$

Clearly, the net effect of the oscillating reaction coefficient $\cos(t)$ is very small: $\varphi(t)$ neither grows nor decays.

16.5 Model Dual Problem Summary

The dual problem for the NS equations is a convection-reaction-diffusion problem in space-time of the form

$$-\dot{\varphi} - u\cdot\nabla\varphi + \nabla u^\top\varphi - \nu\Delta\varphi = \psi \quad \text{on } [0,T), \quad \varphi(T) = 0.$$

Disregarding the diffusion and following the streamlines defined by the convection, we can view this problem as a collection of reaction problems

in time of the form

$$-\dot{\varphi} + A\varphi = \psi \quad \text{on } [0,T), \quad \varphi(T) = 0,$$

where $A(t)$ is a 3×3 matrix which varies in time as $\nabla u^\top(x,t)$ varies along a streamline. The real parts of the eigenvalues of $A(t)$ sum to zero for each t, and the imaginary parts appear as complex conjugates. We have separately analyzed the stability properties of such a system as affected by (i) the real parts of the eigenvalues, and (ii) the imaginary parts of eigenvalues. Assuming the real parts to oscillate between negative and positive values, would give no net production. Finally the effect of the imaginary parts would by a cancellation effect make the dual solution decrease as the length of the mean value increases. The net effect would be that the stability factor is large for a small mean value output, and small for a large mean value output. We now proceed to check if we can see this type of qualitative behaviour by computing the dual solution for a turbulent flow.

16.6 The Dual Solution for Bluff Body Drag

In Fig. 16.4 we plot the dual solutions for mean values of the momentary drag $D(t)$ of the surface mounted cube for different lengths of the mean values. We see that these curves behave just like the ones we just presented for the model cases of the harmonic oscillator and the oscillating reaction coefficient problem, except for the fact that in the bluff body problem the dual solution is "swept out" of the computational domain after some time resulting in a decay to zero of the dual solution for larger times. Further, in the bluff body problem we measure derivatives of the dual solution and thus the stability factors are larger than in the model problem, but their relative size follow the pattern of the model.

16.7 Duality for a Model Problem

We illustrate the use of duality for error representation in the setting of a dynamical system $\dot{u} = f(u)$ on $[0,T]$, $u(0) = 0$, with $f : \mathbb{R} \to \mathbb{R}$. We consider two solutions $u(t)$ and $v(t)$ with different initial values $u(0)$ and $v(0)$. We want to analyze the difference in output $M_\tau(u) - M_\tau(v)$, where $M_\tau(u)$ is defined in (16.2), resulting from the difference $u(0)-v(0)$ in initial value, assuming we solve the dynamical system for $u(t)$ and $v(t)$ exactly.

By integration by parts we obtain the following representation

$$M_\tau(u) - M_\tau(v) = \varphi(0)(u(0) - v(0))$$

where the dual solution $\varphi(t)$ solves the linear problem

$$-\dot{\varphi} + f'(t)\varphi = \psi \quad \text{on } [0,T), \quad \varphi(T) = 0,$$

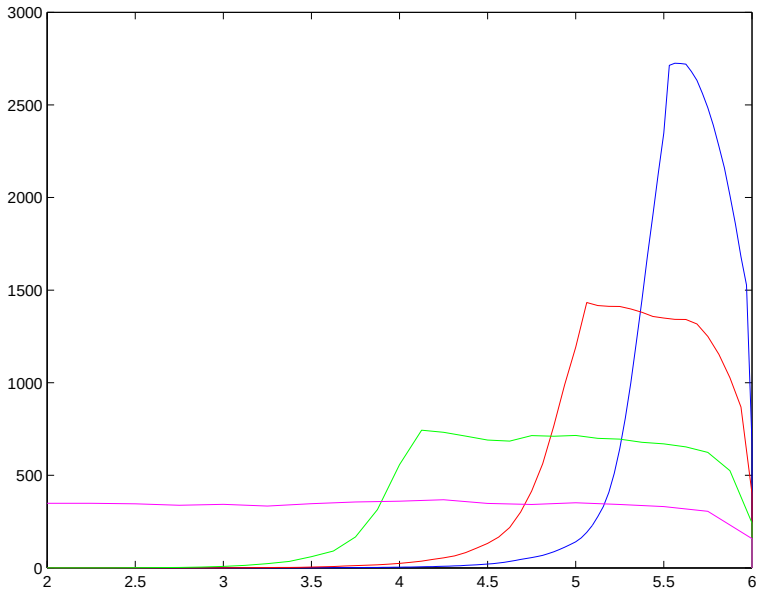

FIGURE 16.4. Surface mounted cube: time series of $\|\nabla\varphi\|$ (with the time running backwards), where the dual solutions corresponds to mean values of size 0.5,1,2,4.

with $\psi = 1/\tau$ on $[T-\tau, T]$ and $\psi = 0$ else, and

$$f'(t) = \int_0^1 \frac{d}{ds} f(su(t) + (1-s)v(t))\, ds.$$

Clearly $\varphi(0)$ is the stability factor expressing the sensitivity of the output mean value $M_\tau(u)$ to changes in input initial value $u(0)$. We can compute $\varphi(0)$ by first computing the two trajectories $u(t)$ and $v(t)$ forward in time, and then solving for the dual solution $\varphi(t)$ backwards in time to the initial time $t = 0$ to get $\varphi(0)$.

16.8 Ensemble Averages and Input Variance

Although we do not in this book consider statistical approaches to turbulence, we will make a comment on ensembles of solutions corresponding to ensembles of data. We do this to exhibit an aspect of the dual problem which is of key importance to understand that a mean value output may be moderatly sensitive to changes in input mean values, while it may be less sensitive to input variance. This means that if outputs are mean values, then we do not need information on input variance or the statistical distribution of input. This is crucial since usually information on input variance or distribution is lacking. The only thing we can hope for in such a case

is that a mean value output such as drag is relatively insensitive to input variance.

We consider two solution ensembles $u(t;i)$ and $v(t;i)$ with initial values $u(0;i)$ and $v(0;i)$, $i = 1, ...N$, in the setting of a dynamical system $\dot{u} = f(u)$ on $[0,T]$, $u(0) = 0$, with $f : \mathbb{R} \to \mathbb{R}$. For an ensemble $w(i)$, $i = 1, ..., N$, we introduce the mean value $\overline{w}$ and deviation $w'(i)$, $i = 1, ..., N$, defined by

$$\overline{w} = \frac{1}{N}\sum_{i=1}^{N} w_i, \quad w'(i) = w(i) - \overline{w},$$

assuming a uniform density for the ensemble. Using duality we have the following representation for the time mean value M_τ defined above:

$$\overline{M_\tau(u)} - \overline{M_\tau(v)} = \overline{\varphi(0)}\big(\overline{u(0)} - \overline{v(0)}\big) + \frac{1}{N}\sum_{i=1}^{N} \varphi'(0;i)(u'(0;i) - v'(0;i))$$

where for each pair $u(t;i)$ and $v_i(t;i)$ the dual solution $\varphi(t;i)$ solves the linear problem

$$-\dot{\varphi} + f'(t;i)\varphi = \psi \quad \text{on } [0,T), \quad \varphi(T) = 0,$$

with $\psi = 1/\tau$ on $[T-\tau, T]$ and $\psi = 0$ else, and

$$f'(t;i) = \int_0^1 \frac{d}{ds} f(su(t;i) + (1-s)v(t;i))\, ds.$$

Here $\overline{\varphi(0)}$ is the stability factor expressing the sensitivity of the output mean value M_τ to changes in input mean value. Further, the deviation $\varphi'(0;\cdot)$ expresses the sensitivity of the output mean value to input deviation. We pay particular attention to problems with $\overline{\varphi(0)}$ being of moderate size and the deviation $\varphi'(0;\dot{)}$ being at least one order of magnitude smaller. In such a problem output mean values would be (i) well determined from input mean values with (ii) little dependence on input deviation. In particular, (ii) signifies that the dual solution $\varphi(t;i)$ is relatively insensitive to the underlying trajectories $u(t;i)$ and $v(t;i)$.

In this book we give evidence that many cases of turbulent flow have the qualities (i) and (ii), see Chapter 14. Again, (ii) is important in order for stability aspects to be insensitive to individual trajectories. In the setting of NS equations, it is natural to view all the different solutions $u(t;i)$ (or $v(t;i)$) as members of the same set of approximate solutions W_ϵ for some $\epsilon > 0$, and we would then expect the individual outputs $M_\tau(u(\cdot;i))$ to be close to the mean value $\overline{M_\tau(u)}$. To compute the output it would then be sufficient to solve for only one trajectory. In this case it would not be necessary to enter into the statistics of solving for many trajectories $u(\cdot;i)$ and computing ensemble mean values.

Moreover, if (ii) is valid, then in fact all the $\varphi(0;i)$ are close to the mean value $\overline{\varphi(0)}$. We may thus expect to be able to compute a good approximation of $\overline{\varphi(0)}$, or any of the individual stability factors $\varphi(0;i)$, by solving the dual problem only once with some particular choice of linearization which would be representative.

17

A Convection-Diffusion Model Problem

How can it be that even if everything I do is pointwise wrong (according to my critics), yet my mean value comes out right? (Oscar Wilde)

17.1 Introduction

We discuss some basic aspects of G2 in the setting of a convection-diffusion model problem. We first comment on the fact that the residual $R(\hat{u})$ of an ϵ-weak solution $\hat{u}$ necessarily is pointwise large where the flow is turbulent and not fully resolved. In fact, a turbulent flow is characterized by the fact that the stabilization term is not small and thus the residual large pointwise. We then show that the least squares stabilization of G2 introduces an artificial viscosity acting as a turbulent diffusion on smallest scales only and therefore does not degrade the accuracy of mean value outputs.

17.2 Pointwise vs Mean Value Residuals

We have noticed above that even though the residual $R(\hat{u})$ of an ϵ-weak solution $\hat{u}$ of the NS equations is not small pointwise, its effect on a mean value output $M(\hat{u})$ may be small. We will now discover the same phenomenon in the following scalar linear constant coefficient stationary convection-

diffusion-reaction model problem with small viscosity ν:

$$u_{,1} + u - \nu\Delta u = f \text{ in } \Omega, \quad u = 0 \text{ on } \Gamma, \tag{17.1}$$

where $\Omega = (0,1)^2$ with boundary Γ, $u_{,1} = \frac{\partial u}{\partial x_1}$ and f is a given (smooth) function. The solution $u = u(x)$ in general has an outflow boundary layer at $x_1 = 1$ of width $\sim \nu$, and characteristic layers at $x_2 = 0$ and $x_2 = 1$ of width $\sim \sqrt{\nu}$. With an oscillating inflow value of $u(x)$ at $x_1 = 0$, the characteristic layers may fill Ω.

Let now V_h be the standard finite element space of continuous piecewise linear functions on a triangulation of Ω of mesh size h vanishing on Γ, and let $U \in V_h$ be a G2 solution defined by

$$(U_{,1} + U, v + hv_{,1}) = (f, v + hv_{,1}) \tag{17.2}$$

where $(\cdot,\cdot)$ is the $L_2(\Omega)$-norm, and we assume that $\nu << h$ so that the ν-term can be omitted in G2. Further, the stabilizing term was simplified from $h(v_{,1}+v)$ to $hv_{,1}$, as in the *streamline diffusion method* [27]. Choosing here $v = U$ gives the following basic energy estimate for U:

$$\|U\|^2 + \|\sqrt{h}U_{,1}\|^2 \leq (1+h)\|f\|^2 \approx 1$$

where $\|\cdot\|$ is the $L_2(\Omega)$-norm and we assume $\|f\| = 1$. We notice that in the case the exact solution u has layers, the stabilizing term $\|\sqrt{h}U_{,1}\|^2$ will not be small, because $U_{,1} \sim h^{-1}$ in an outflow layer of width $\sim h$, and $U_{,1} \sim h^{-1/2}$ in characteristic layers of width $h^{1/2}$.

Now, if $\nu << h$, then

$$R(U) \approx U_{,1} + U - f$$

and thus by choosing $v = U$ in (17.2)

$$-(R(U), U) \approx \|\sqrt{h}U_{,1}\|^2 >> 0,$$

which shows that $R(U)$ cannot be pointwise small everwhere in Ω: We will argue below that $R(U) \sim h^{-1}$ in outflow layers and $R(U) \sim 1$ in characteristic layers. Note that $\|\sqrt{h}U_{,1}\|^2$ not small signifies the presence of unresolved layers where $R(U)$ is not small, which mimics the fact that in the NS equations the stabilizing term and residual are not small in unresolved (turbulent) regions.

Now, if we in the model problem take as output $M(u) = (u, \psi)$, where ψ vanishes in the layers, that is we consider only output away from the numerical layers, then it follows by the analysis of G2 in [60], that if u is smooth outside layers then

$$|M(u) - M(U)| \sim h^{3/2},$$

which shows that the error in certain outputs may be small even though the residual $R(U)$ is large pointwise in certain parts of the domain. Of course, in the model problem this is fully understandable because by the nature of the convection in the positive x_1-direction and the smallness of the diffusion coefficients, effects in boundary layers are not propagated into the domain. Alternatively, we may as above in the case of the NS equations bound the output error in terms of

$$\|R(U)\|_{H^{-1}(\Omega)} \sim \|hR(U)\|,$$

which may be small ($\sim \sqrt{h}$), even though $R(U)$ is not small everywhere.

To understand more precisely why the residual $R(U)$ cannot be small in an outflow layer, we note that the exact solution u with f smooth there satisfies

$$u_{,1} + u - f = \nu\Delta u \sim \frac{1}{\nu} \tag{17.3}$$

if u varies between 0 and 1 in the layer, so that $R(u) = 0$ results from cancellation of the two terms $u_{,1} + u_1 - f$ and $\nu\Delta u$ both $\sim 1/\nu$. In the numerics this cancellation cannot be realized if $h >> \nu$, and the result is that $R(u) \approx 1/h$ in the numerical outflow layer: Roughly speaking, we have in an outflow layer

$$U_{,1} + U_1 - f \sim hU_{,11} \sim \frac{1}{h},$$

which is incompatible with (17.3) if $h >> \nu$, and thus necessarily $R(U) \approx 1/h$ in an outflow layer. A similar argument shows that we may have $R(U) \approx 1$ in a characteristic layer. We may say that the fact that $R(U)$ cannot be small in layers, is a necessary consequence of the underresolution with $h >> \nu$, which makes it impossible to numerically capture the cancellation of non-small viscous and non-viscous terms present in the continuous problem.

We sum up by noting that the underresolution with $h >> \nu$ makes it impossible for $R(U)$ to be pointwise small everywhere, while the fact that $\|R(U)\|_{H^{-1}(\Omega)}$ is small opens for the possibility that the error in a mean value output is small, if the dual solution is not too large.

17.3 Artificial viscosity from least squares stabilization

The least squares stabilization in (17.2) effectively introduces the term

$$(U_{,1} + U - f, hv_{,1})$$

which involves the artificial viscosity $(U_{,1}, hv_{,1})$. The stabilizing term is obviously small where $U_{,1} + U_1 - f$ is small, that is outside layers where

the solution is smooth. The net effect of the least squares stabilization thus is increased viscosity only in regions where the solution is non-smooth. Similarly the G2 stabilization in NS has the effect of a turbulent diffusion acting only on the smallest scales of the flow.

As a comparison we note that simply adding an artificial viscosity term $(U_{,1}, hv_{,1})$ without the compensating terms in $(U_{,1} + U - f, hv_{,1})$, introduces a perturbation of order h also to smooth parts of the flow, which significantly degrades the accuracy. Adding artificial viscosity in the form $(U_{,1}, hv_{,1})$ corresponds to the simplest version of the classical Smagorinsky turbulence model in NS.

The least squares stabilization in G2 thus may be viewed as a smart Smagorinsky model (see Chapter 20), effectively introducing diffusion only on the smallest scales of the mesh. The rationale is then that the actual size of the smallest scale of the diffusion is insignificant for certain mean value outputs, and thus that certain aspects of turbulent flow can be captured on computational scales which are (much) coarser than the actual physical scales. This reflects that our World would look the same even if the "fluid particles" were much bigger than particles on atomic scales.

18
Reynolds Stresses In and Out

[upon losing the use of his right eye] Now I will have less distraction.
(Leonhard Euler)

18.1 Introducing Reynolds Stresses

The traditional approach to mathematical modeling of turbulence is to seek modified NS equations satisfied by some mean value $(\bar{u},\bar{p})$ of the true velocity-pressure (u,p). In *Reynolds Averaged Navier–Stokes equations RANS* the mean value is an ensemble mean, or a time average taken over long time, while in *Large Eddy Simulation LES* the mean value is more local in space-time. The modified equations for the mean-values are sought by taking mean values of the NS equations to get the *Averaged NS equations*:

$$\begin{aligned} \tfrac{\partial \bar{u}_i}{\partial t} + \textstyle\sum_j (\bar{u}_j\bar{u}_i)_{,j} - \nu\Delta\bar{u}_i + \bar{p}_{,i} + \textstyle\sum_j \tau_{ji,j} &= \bar{f}_i, \\ \nabla\cdot\bar{u} &= 0, \end{aligned} \tag{18.1}$$

where

$$\tau_{ji} = \overline{u_j u_i} - \bar{u}_j\bar{u}_i$$

are the so-called *Reynolds stresses*. The idea is then to seek to model the Reynolds stresses in terms of the mean-values $(\bar{u},\bar{p})$ in a *turbulence model* (or *subgrid model*) to get a set of modified NS equations for the mean value $(\bar{u},\bar{p})$. Many turbulence models have been proposed in the literature, see e.g. [80], but all models only seem to cover the set of test problems they

were designed for, and thus lack the generality required to be able to model new problems and make predictions.

So, designing turbulence models of the Reynolds stresses seems to be a very difficult if not an unsurmountable problem. But do we really need to model the Reynolds stresses?

18.2 Removing Reynolds Stresses

Suppose that we are interested in some output $M(u,p)$ which itself is a mean value. Using a turbulence model we would then obtain the output $M(\bar{u},\bar{p})$ involving two mean value operations, to be compared with $M(u,p)$ with only one.

Now, averaging twice seems to be one too much, but what would be the evidence that we could live without Reynolds stresses? This would be possible if the effect of the Reynolds stresses on the output $M(u,p)$ would turn out to be small. Below we shall give computational evidence that this is true in many cases. More precisely, the computational model we use contains a stabilizing term, which may be viewed as a simple turbulence model, and we shall give evidence that the exact nature of this model has little effect on mean-value outputs. The net result is that very crude modeling of the Reynolds stresses seems to be sufficient in many cases of practical importance. We expand on this aspect in the next chapter. This means that we do not have to introduce any Reynolds stresses at all, nor model them, even if the flow is turbulent! The stabilizing term in the computational model will handle all that automatically! In particular, we settle directly for computing the mean value $M(u,p)$ and avoid introducing the double mean value $M(\bar{u},\bar{p})$.

Obviously, avoiding Reynolds stresses greatly simplifies computional turbulence modeling, since any chosen known turbulence model could be questioned on very good grounds.

19
Smagorinsky Viscosity In and Out

> The lateral transfer of momentum and heat by the non-linear diffusion, which parametrically is supposed to simulate the action of motions of sub-grid scale, accounts for a significant portion of the total eddy transfer. Although no direct comparison with the corresponding transfer in the real atmosphere is available, intuitively our small-scale diffusion appears to play too large a role. (Joseph Smagorinsky, 1963)

19.1 Introducing Smagorinsky Viscosity

The classical *Smagorinsky eddy viscosity* turbulence model [83] for the incompressible NS equations is obtained by replacing the given constant viscosity ν by the artificial *turbulent eddy viscosity*

$$\tilde{\nu} = \nu + Ch^2|\nabla\bar{u}|,$$

where $\tilde{u}$ is the velocity of the NS equations with viscosity $\tilde{\nu}$, h represents a smallest scale and $C \sim 0.01$. The Smagorinsky turbulence model thus introduces an additional non-linearity since $\tilde{\nu}$ depends on the velocity $\tilde{u}$. The model may also be formulated with $\epsilon(\tilde{u})$ replacing $\nabla\tilde{u}$, and the constant may be changed, possibly with feed back from $\tilde{u}$ in a *dynamical model*, see ([32]).

The energy estimate for the NS equations with the Smagorinsky turbulence model gives a bound for the term

$$\int_0^T Ch^2\|\nabla\bar{u}\|^3\,dt,$$

which indicates that in regions of turbulence $|\nabla\bar{u}| \sim h^{-2/3}$. This is consistent with a smallest scale $\sim h$ on which the change of $\bar{u}$ is $\sim h^{1/3}$, which fits with the Kolmogorov prediction that turbulent velocities are Hölder continuous with exponent $1/3$ [31]. Thus h would indeed represent the smallest scale of the turbulent velocity $\bar{u}$ in the Smagorinsky model. Effectively, the Smagorinsky turbulence model would thus change the smallest scale from $\nu^{3/4}$ without model to h, assuming $h > \nu^{3/4}$. Further, we may expect the turbulent viscosity $\tilde{\nu} \sim h^{4/3}$ in turbulent regions with local Reynold number $\sim h^{1/3}h/h^{4/3} \sim 1$.

The Smagorinsky model is the simplest turbulence model and as such seems to behave reasonably well, e.g. in the sense that it is consistent with the Kolmogorov estimates. The Smagorinsky model increases the effective viscosity in regions of turbulence and thereby removes the finest scales of the original flow, but it also affects coarser scales because of its action through a Laplacian. to minimize the action of Smagorinsky on coarser scales, variants of Smagorinsky may be contemplated with more focussed action only on smallest scales [57].

We recall that the shock-capturing artificial viscosity of G2 adds viscosity in the form $Ch^2|R(\hat{U})|$, which is very similar to Smagorinsky with $R(\hat{U})$ replacing ∇U in similarly increased viscosity in turbulent regions. This similarity is no coincidence, since Smagorinsky developed his model inspired by the work of von Neumann and Richtmyer on artificial dissipation for stabilization of numerical methods [63].

Now, numerical methods for the NS equations often are augmented by e.g. the Smagorinsky turbulence model, following the idea that the numerics alone will not be capable of modeling turbulence. Doing so the parameter h in the Smagorinsky model would correspond to the smallest mesh size in the numerics. In this approach turbulence modeling and stabilization of numerics are considered as separate issues, and thus the total artificial viscosity will have a contribution from Smagorinsky artificial vicosity and a contribution from the artificial viscosity needed to stabilize the numerics. The question of the relative size of these contributions then arises; if one dominates the other the dominated viscosity could be removed.

We will now advocate that the Smagorinsky artificial viscosity is too weak to stabilize the numerics, which effectively means that the artificial viscosity from least squares stabilization usually will dominate Smagorinsky, at least on the finest scales where dissipation is needed. Another way to see this is to recall that shock-capturing alone is not sufficient to stabilize the numerics very well; least squares stabilization is always needed, and shock-capturing

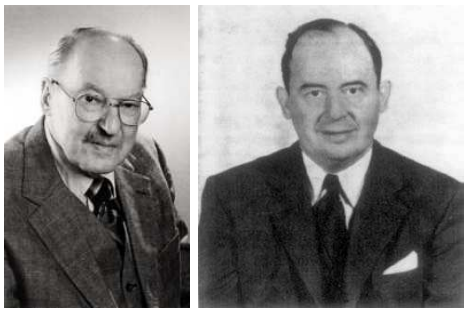

FIGURE 19.1. Joseph Smagorinsky (1924-2005) and John von Neumann (1903-1957).

only in extreme cases. The net result is that Smagorinsky has as little role to play in least squares numerics, and no role at all if the numerics is augmented with shock-capturing.

19.2 Removing Smagorinsky Viscosity

We have seen that Smagorinsky viscosity may be of size $h^{4/3}$, which should be compared with h in the least squares stabilization. The Smagorinsky viscosity thus seems to be dominated by the least squares viscosity, at least on the finest scales where the dissipation is needed.

As indicated, one may pose the question if Smagorinsky may replace the least squares stabilization, so that Smagorinsky alone would be enough to both model turbulence and stabilize the numerics. Following this line of thought we thus consider a method for solving the NS equations based on Galerkin combined with Smagorinsky. By the analysis of G2, leaving out the least squares term, we would then be led to estimate a term of the form $\|hR(\hat{U})\|$. Using the available stability from the Smagorinsky model we would end up with an esimate of the form $\|hR(\hat{U})\| \leq Ch^{1/3}$ to be compared with the corresponding G2 estimate with instead $h^{1/2}$. Thus, it would seem that Smagorinsky alone could work, but not as well as G2, the difference being a factor $h^{1/6}$. This may seem pretty small but may precisely be what is needed to get that one correct decimal in the computational output which is possible to get for turbulent flow. Changing from $h^{1/2}$ to $h^{1/3}$ would increase the required number of mesh points in space for the same accuracy from N to $N^{3/2}$, thus e.g. from 10^6 to 10^9, that is with a factor of 1000.

Our computational experience indeed shows that Smagorinsky alone is not sufficient to give good numerics, and that if good numerics such as G2 is used, then Smagorinsky has little role to play. The net result is that we see no reason to use Smagorinsky in conjunction with G2.

20
G2 for Euler

As an older friend I must advice you against it for in the first place you will not succeed, and even if you succeed, no one will believe you. (Planck to Einstein about the General Theory of Relativity)

Complex spatial structures have never been observed in numerical simulations of inviscid flow with smooth initial conditions. (Frisch in *Turbulence* 1995)

The well-posedness of the Euler equations is one of the most challenging questions of the present time for both the mathematician and the numerical analyst. (Saffman 1981)

Although this may seem a paradox, all exact science is dominated by the idea of approximation. (Bertrand Russel)

20.1 Introduction

We recall the Euler equations (4.2) for incompressible inviscid flow:

$$\begin{aligned} \dot{u} + (u\cdot\nabla)u + \nabla p &= f && \text{in } \Omega\times I,\\ \nabla\cdot u &= 0 && \text{in } \Omega\times I,\\ u\cdot n &= 0 && \text{on } \Gamma\times I,\\ u(\cdot,0) &= u^0 && \text{in } \Omega. \end{aligned} \tag{20.1}$$

The Euler equations are formally reversible: Changing the sign of time t and the velocity u, obviously leave the equations unchanged. In particular, if $\hat{u}$ is a solution to the Euler equations with initial velocity u^0 at time $t = 0$ and

final value $\hat{u}(T)$ at time $t = T$, then the function $\hat{v}(t) = (-u(T-t), p(T-t))$ satisfies Eulers equations for $t \in (0, T]$ with initial data $v(0) = -u(T)$ and final velocity $v(T) = -u(0)$. Thus, reversing the velocities $u(T)$ and letting time pass backwards, would bring back the velocities to $-u(0)$ from $-u(T)$.

The basic energy estimate (15.2) with $\nu = 0$ states that the total kinetic energy $\frac{1}{2}\|u(t)\|^2$ of a pointwise solution $\hat{u}$ of (20.1) with $\|\cdot\|$ the $[L_2(\Omega)]^3$-norm, stays constant if $f = 0$:

$$\frac{1}{2}\|u(T)\|^2 = \frac{1}{2}\|u(0)\|^2, \tag{20.2}$$

which follows by multiplication of the momentum equation by u and integration. Thus it appears that a system governed by the Euler equations allows the design of a *perpetuum mobile* by (somehow) reversing the velocity at $t = 0$ and $t = T$, corresponding to a system bouncing back and forth for ever. We conclude that if the Euler equations admit a pointwise solution with pointwise zero residual, then that solution would be reversible and represent a perpetuum mobile of the first kind, which is a machine running for ever without consuming any energy. On the other hand, NS would not allow such a design because kinetic energy would be lost to the ν-term in the energy balance (15.2), and turned into heat.

We further recall d'Alemberts Mystery stating that a bluff body, subject to inviscid flow described by the Euler equations, has zero drag. Both a perpetuum mobile and a bluff body with zero drag are at variance with observations, and something seems to be seriously wrong with the Euler equations. But what could it be, since they after all just express Newton's 2nd Law and incompressibility? Prandtl blamed the assumption of inviscid flow with $\nu = 0$, but we have instead pointed to the instability of any exact solutions of the Euler equations developing into turbulent approximate solutions. In particular, any conclusion made from an assumption of existence of an exact pointwise solution may be completely wrong, including the energy conservation (20.2) and d'Alembert's computations of zero drag.

We have claimed that non-existence of pointwise solutions of the Euler equations follows from the observation that solutions to the Navier-Stokes equations in general are turbulent if ν is small, and that it is unthinkable that these turbulent solutions could converge to a pointwise solution of the Euler equations as ν tends to zero. The reason is that as we let ν tend to zero, the corresponding Navier-Stokes solutions develop ever finer scales of turbulence which is incompatible with convergence to a pointwise solution of the Euler equations. If the Navier-Stokes solutions had stayed laminar as ν tends to zero, pointwise convergence would have been possible, but Navier-Stokes solutions invariably become turbulent if ν is small, and thus convergence simply cannot take place. We thus have clear evidence that in general pointwise solutions of the Euler equations are non-existent. For an

account of the analytical mathematical struggle to come to grips with the Euler equations, we refer to [23] and references therein.

20.2 Euler/G2 as a Model of the World

If now the Euler equations lack stable pointwise solutions, does it mean that we have to regard the Euler equations as useless? In fact not; we shall see that nevertheless G2 can compute approximate weak turbulent solutions, which may supply useful information in cases of very large Reynolds numbers. G2 will thus automatically compute turbulent solutions with stable mean value output, instead of unstable pointwise solutions without meaningful output.

An intriguing aspect of the Euler equations is that no physical constant is involved: In the NS equations the value of the viscosity ν has to be supplied, and the determination of ν either matematically or experimentally may be very difficult, while we simply put $\nu = 0$ in Euler, and we may assume the remaining data f, u^0, Ω and T to be known. We show below that nevertheless we can by G2 compute outputs of physical significance for Euler. This means that Euler/G2 may be viewed as a universal mathematical model of the World, which is fully self-contained, up to the mesh size parameter h in G2. Below we show that outputs like drag may have a weak dependence on h, if only h is small enough. This indicates that the self-contained mathematical model Euler/G2 could be identified with (a part of) the World, which may be viewed as the end goal of mathematical modeling following the spirit of the late Einstein. We remark that *Einstein's equations* contain a (unknown) "cosmological constant" possibly connecting to the "dark matter/energy", which physicists today seek to detect.

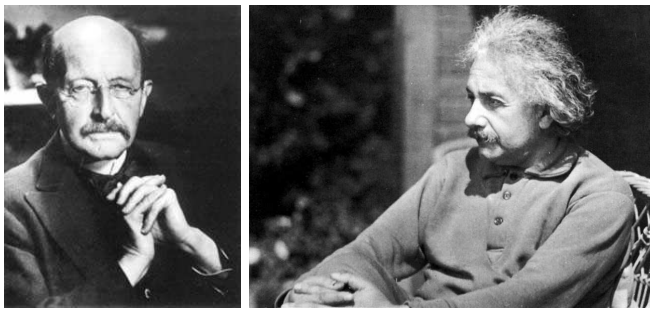

FIGURE 20.1. Max Karl Ernst Ludwig Planck (1858-1947) and Albert Einstein (1879-1955).

20.3 Solution of the Euler Equations by G2

G2 for the Euler equations takes the form (15.4) with $\nu = 0$ and changing the velocity boundary conditions in $\hat{V}_h$ from no-slip to slip boundary conditions (assuming also that $f = 0$). The basic energy estimate for the corresponding G2 solution $\hat{U}$ reads:

$$\frac{1}{2}\|U(T)\|^2 + \|\sqrt{h}R(\hat{U})\|_Q^2 = \frac{1}{2}\|U(0)\|^2, \tag{20.3}$$

where $\|\cdot\|_Q$ is the $L_2(Q)^4$-norm with $Q = \Omega \times I$. The least squares term $\|\sqrt{h}R(\hat{U})\|_Q^2$ corresponds to the the viscous term $D_\nu(u,T)$ in the energy estimate (15.2) for the Navier–Stokes equations. We shall see that in case of turbulence, the least squares term is not small, while it is for a laminar solutions.

Similarly, we may obtain an a posteriori error estimate for a certain output $M(\hat{U})$ such as drag or lift. Since an exact solution $\hat{u}$ is missing, we then estimate the difference in output of two different G2 solutions $\hat{U}$ and $\hat{W}$ on different meshes as follows:

$$|M(\hat{U}) - M(\hat{W})| \le S(\|hR(\hat{U})\|_Q + \|hR(\hat{W})\|_Q),$$

where h represents the mesh size of the corresponding residual respectively, and S represents a stability factor obtained by solving a dual problem. We can thus estimate the difference in output between two different G2 solutions in terms of their residuals multiplied with a certain stability factor. Below we compute bluff body drag for Euler, which is shown to be close to the drag for NS with large Reynolds number.

The evidence in G2 of non-existence of a pointwise Euler solution is that $\|R(\hat{U})\|_Q$ is not small, while $\|hR(\hat{U})\|_Q$ may be small. Typically, $\|R(U)\|_Q \sim h^{-1/2}$, reflecting that the least squares term $\|\sqrt{h}R(\hat{U})\|_Q$ has a significant contribution in the energy balance (20.3).

Notice that it is the combination of Galerkin and weighted least squares that produces a reasonable compromise in the case when a pointwise solution is impossible. Only least squares will not work because the residual cannot be small in the $L_2(Q)$-norm, and from only the knowledge that the residual is large nothing can be concluded. Further, only Galerkin will not work either because the residual control is too weak to produce any sensible output. It is only the combination of Galerkin and weighted least squares that works. The evidence of success is the presence of the factor h in the expression $\|hR(\hat{U})\|$ and the fact that by (15.6), we have $\|hR(\hat{U})\| \le \sqrt{h}$ if $\|u^0\| = 1$. In a pure least squares method the factor h in front of $R(\hat{U})$ would be missing, and in pure Galerkin one may have $R(\hat{U}) \sim 1/h$ and thus $\|hR(\hat{U})\| \sim 1$. Thus neither extreme case can work in general.

20.4 Drag of a Square Cylinder

As a basic example we consider the problem of computing the drag of a square cylinder of diameter $D = 0.1$ centered at $x = (0.5, 0.7, 0.2)$ and oriented in the x_3-direction in a channel of dimension $2.1 \times 1.4 \times 0.4$ oriented in the x_1-direction, subject to a uniform inflow velocity $(1, 0, 0)$. We use slip boundary conditions both on the cylinder and the channel walls. We use a locally refined tetrahedral mesh with 86 904 mesh points, shown in Fig. 20.2. The advantage of using a square cylinder, instead of the circular cylinder studied in Chapter 11 above, is that the separation points occur at the upstream corners and thus do not change position with decreasing viscosity or mesh size.

We first determine an (approximate) stationary irrotational solution, not by solving the Euler equations, but looking for a stationary velocity $u = \nabla\phi$ given by a potential $\phi(x_1, x_2, x_3)$, where $\phi = \phi(x_1, x_2, x_3)$ is constant in x_3 and solves Laplace's equation $\Delta\phi = 0$ in the domain of the fluid with $\nabla\phi \cdot n = 1$ at inflow, $\nabla\phi \cdot n = -1$ at outflow, and with homogeneous Neumann conditions $\nabla\phi \cdot n = 0$ on the channel walls and the cylinder, with n the outward unit normal. Such a velocity $u = (u_1, u_2, 0)$ is irrotational, and since the rotation of $(u \cdot \nabla)u$ vanishes (and by symmetry the circulation $\int_\Gamma u \cdot ds = 0$ with Γ the intersection of the cylinder with the $x_3 = 0$ plane), there is a pressure p such that $(u \cdot \nabla)u + \nabla p = 0$. In other words, $\hat{u} = (u, p)$ is a stationary laminar solution of the Euler equations with irrotational velocity u and with $u \cdot n = 0$ on the channel walls and the cylinder surface with approximately equal inflow and outflow velocities (since u_2 and u_3 are small on inflow and outflow). The drag of $\hat{u}$ is close to zero by the above argument.

Thus $\hat{u}$ represents a laminar solution with pointwise residual close to zero and with close to zero drag. By increasing the length of the channel, we can reduce the pointwise residual to any size. Alternatively, by taking the inflow velocity equal to that given by the potential ϕ, we have an exact solution to Euler equations with close to zero drag.

In practice we compute ϕ by solving $\Delta\phi = 0$ using piecewise linear finite elements in the three-dimensional fluid volume, and then associate a corresponding piecewise linear velocity $U^0 = \nabla\phi$ by interpolation of the piecewise constant $\nabla\phi$ to the nodes in the mesh. This produces an approximate potential solution $\tilde{U}^0$ with $R(\tilde{U}^0)$ being small pointwise except close to the edges of the cylinder.

We compute an approximate solution $\hat{U} = (U, P)$ to the Euler equations with initial velocity and inflow data given by $\tilde{U}^0$ using G2 in the form cG(1)cG(1) with continuous linear trial functions in space-time (see Chapter 25). We find that the computed velocity $U(t)$ remains equal to $\tilde{U}^0$ only for a few time steps, then develops non-symmetry in x_1 while maintaining two-dimensionality after which it successively develops into a fully three-dimensional turbulent solution which is far from irrotational.

This turbulent solution is similar to the turbulent solution of Navier-Stokes equations with small viscosity and with no slip boundary conditions on the cylinder presented in [51, 41]. For Euler we compute the drag coefficient to 2.2, which is close to the value 2.1 obtained for Navier-Stokes with viscosity $\nu = 10^{-6}$.

In Fig. 20.3-20.4 we plot (U, P) the solution for the first few time steps, using a very small time step of size 0.1 times the smallest element diameter in the mesh. We find that the instability of the the initial symmetric solution $U(0) = \nabla\phi$ is first expressed in a fluctuating pressure until a high pressure in front of the cylinder is established, which initializes the development of a non-symetric velocity eventually going turbulent.

In Fig. 20.5-20.9 we show results starting with zero initial velocity, using now time steps of the same size as the finest element diameter in the mesh. We find again the potential solution during the first few time steps with the same development into a turbulent solution.

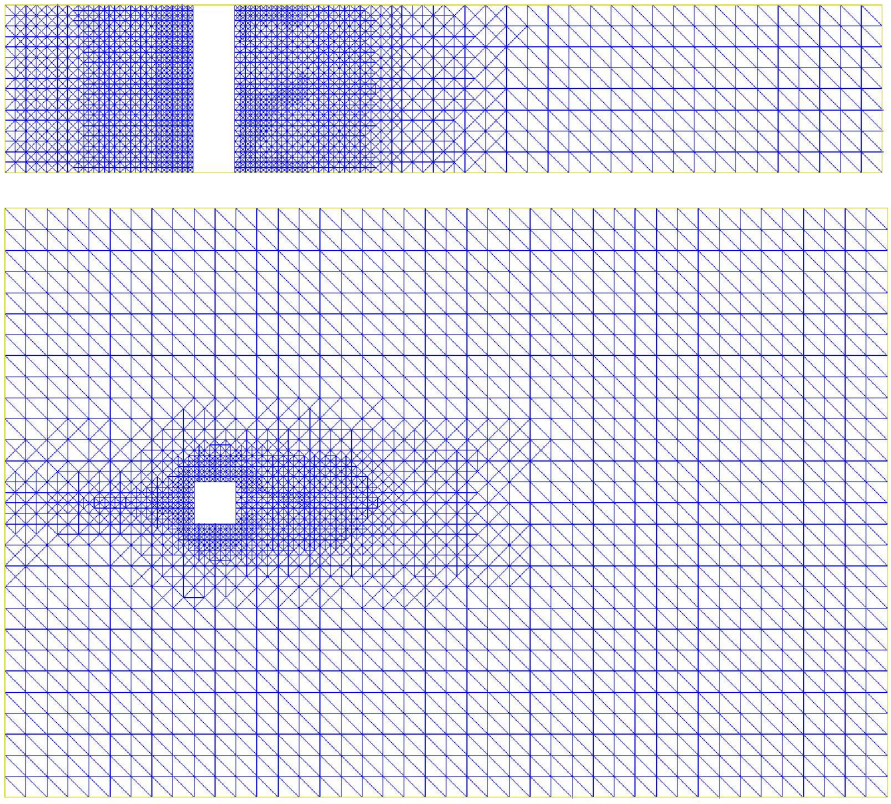

FIGURE 20.2. Computational mesh in the x_1x_2-plane (upper) and the x_1x_3-plane (lower).

20.5 Instability of the pointwise potential solution

We also illustrate the instability of the potential solution by solving the dual Euler equations, linearized at the potential solution and the developed turbulent flow respectively. We use as data to the dual problem a source term in the dual velocity equation being a characteristic function over a cube in space of side length 0.025 centered at (0.6,0.7,0.2), times 0.025^{-4}. The source term acts over a time interval of length 0.025 from the final time (start time in the dual equation), corresponding to the computation of a small space-time mean value at final time.

In Fig. 20.10 we find that the dual solution corresponding to linearization at the potential solution grows exponentially, whereas linearized at the turbulent solution the dual solution shows a slow growth followed by decay to zero. This reflects the instability of the potential solution, being extremely sensitive to perturbations at earlier times, and the destruction of information in the turbulent flow making the solution insensitive to perturbations with respect to the mean value output. We plot the two dual solutions in Fig. 20.11-20.12.

20.6 Temperature

The *total energy* e is the sum of the kinetic energy $\frac{1}{2}|u|^2$ and the *internal energy* i:

$$e = \frac{1}{2}|u|^2 + i, \tag{20.4}$$

where the internal energy i represents *heat*, which we may assume to be proportional to the *temperature*. Conservation of the total energy e is expressed by the conservation law

$$\dot{e} + \nabla \cdot (eu + pu) = 0 \quad \text{in } Q, \tag{20.5}$$

which we can also write:

$$D_u i = -D_u\big(\frac{1}{2}|u|^2\big) - \nabla p \cdot u \equiv E(u,p) \quad \text{in } Q, \tag{20.6}$$

where $D_u v = \dot{v} + (u \cdot \nabla)v$ is the convective derivative of v based on the velocity u. We note that for a pointwise solution (u,p) of (20.1) with $f = 0$, we have $E(u,p) = 0$, which follows by multiplication of the momentum equation by u. However, we know that (stable) pointwise solutions do not exist, so we cannot say that $E(u,p) = 0$.

Nevertheless, having computed $\hat{u} = (u,p)$ from the incompressible Euler equations, we can solve for the total energy e in the linear equation (20.5) with u and p given, to obtain the internal energy/temperature i from (20.4), assuming $i^0 = 0$. Alternatively, we can solve for the internal

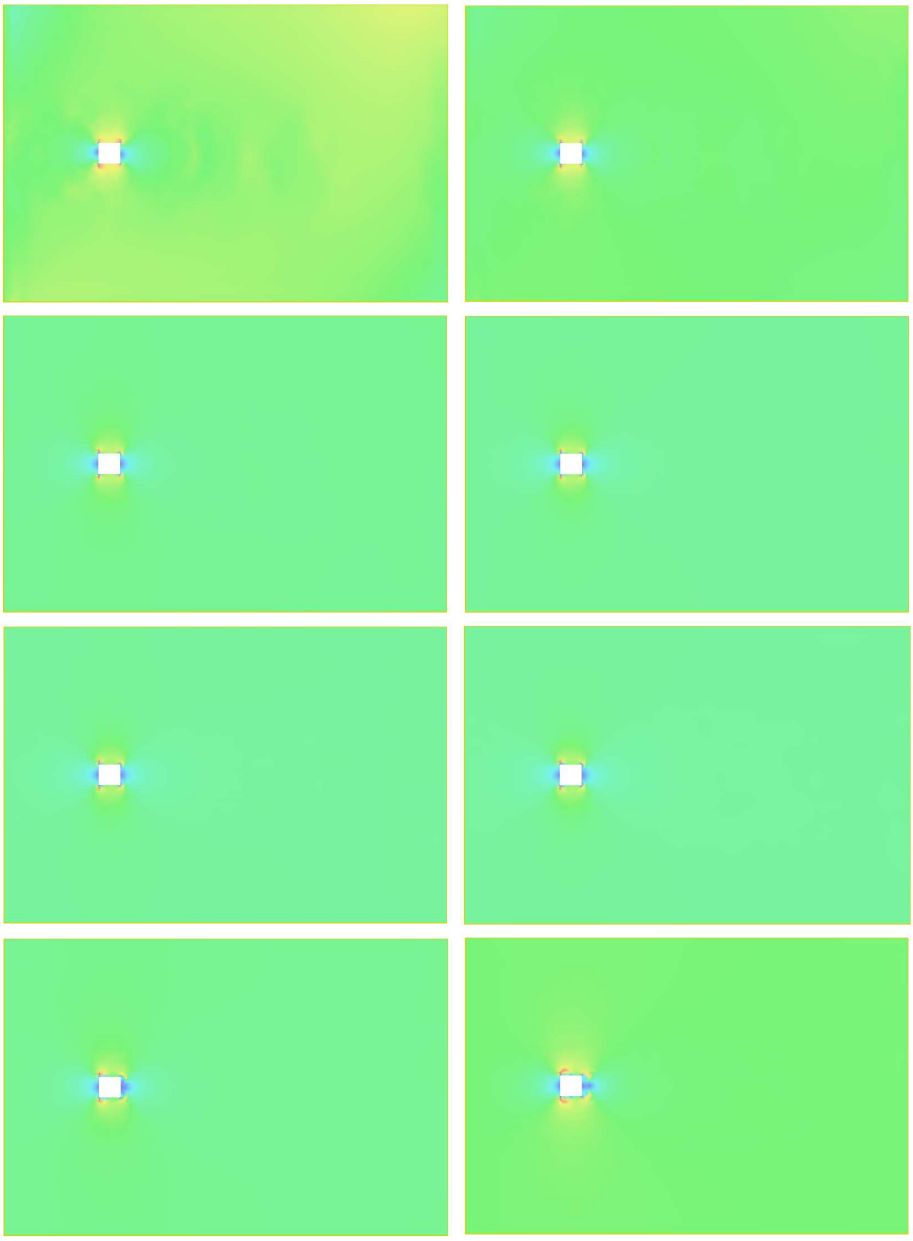

FIGURE 20.3. Magnitude of the computed velocity from initial data $U(0) = \nabla\phi$, for time steps no 1,2,4,5,6,7,20,37.

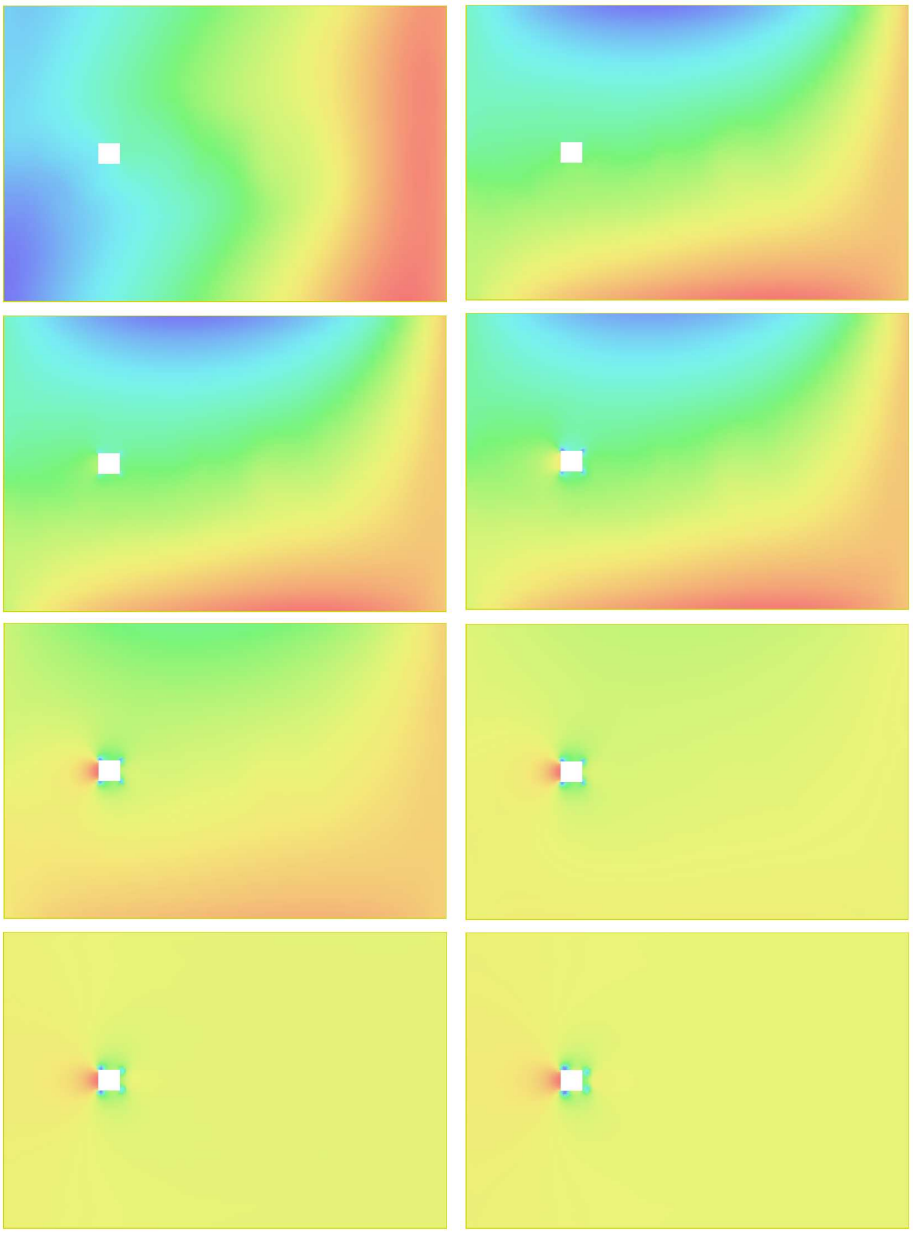

FIGURE 20.4. Computed pressure correspondig to the initial data $U(0) = \nabla\phi$, for time steps no 1,2,4,5,6,7,20,37.

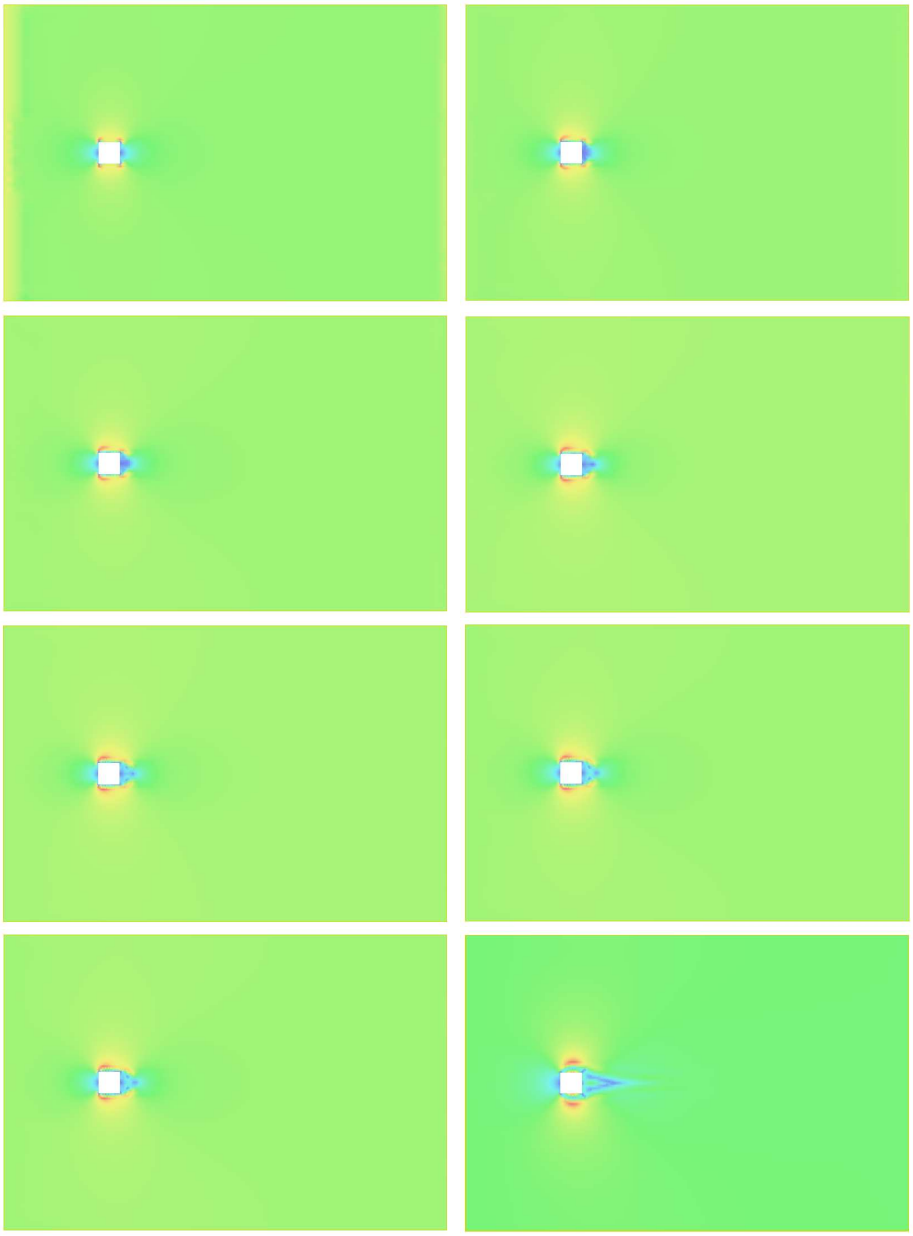

FIGURE 20.5. Magnitude of the computed velocity corresponding to zero initial data, for time steps 2,4,5,6,7,8,16,32.

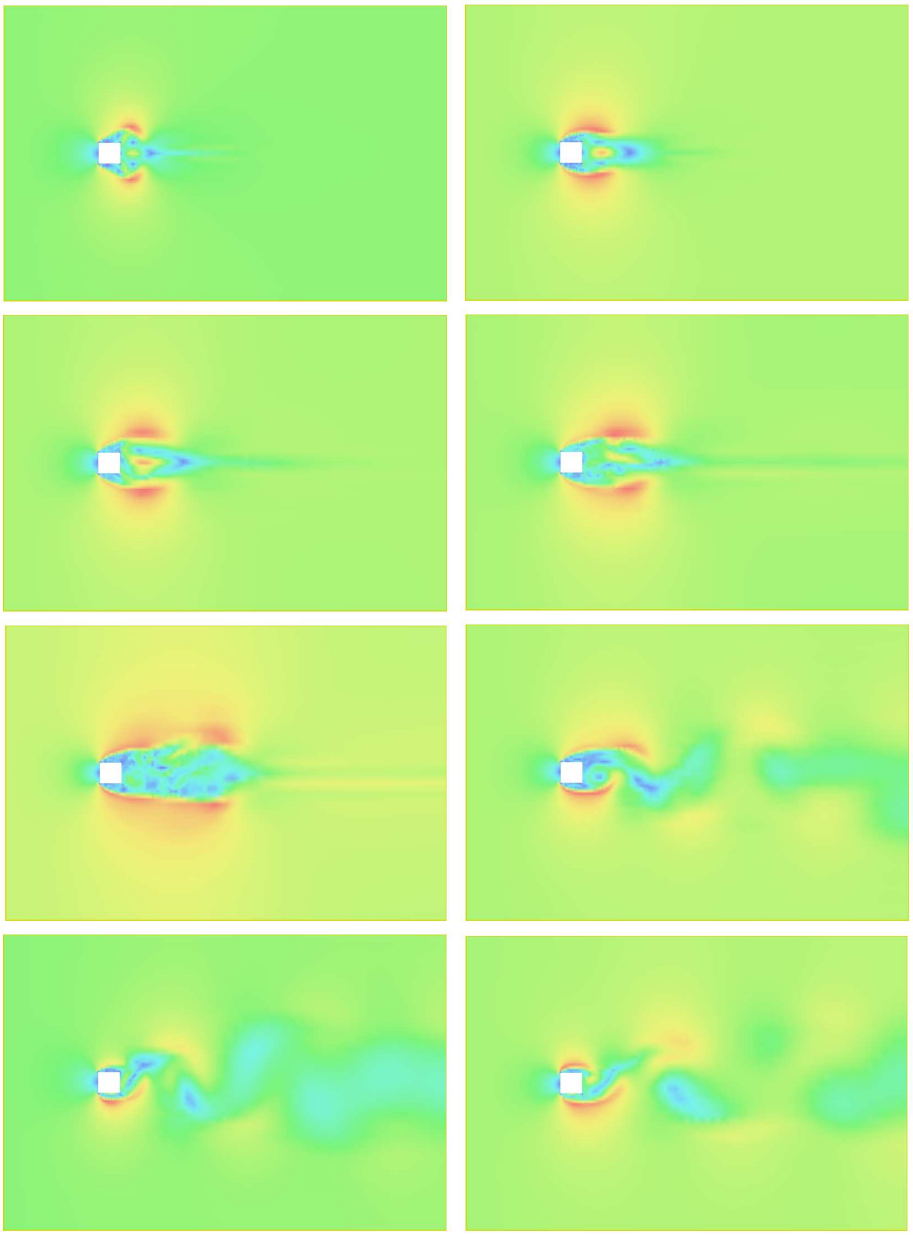

FIGURE 20.6. Magnitude of the computed velocity corresponding to zero initial data, for time steps 48,64,96,128,160,704,960,1024.

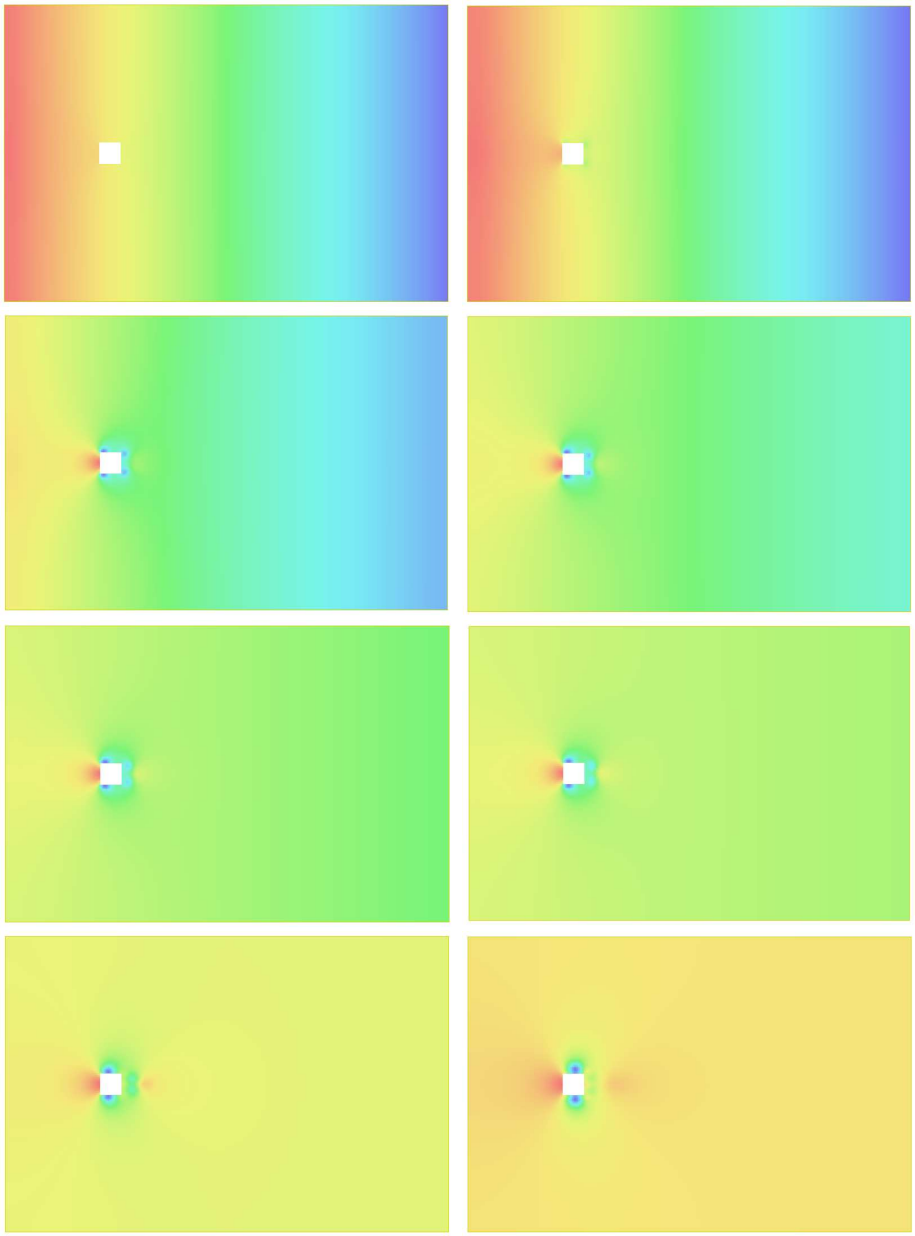

FIGURE 20.7. Pressure corresponding to zero initial data, for time steps 2,4,5,6,7,8,16,32.

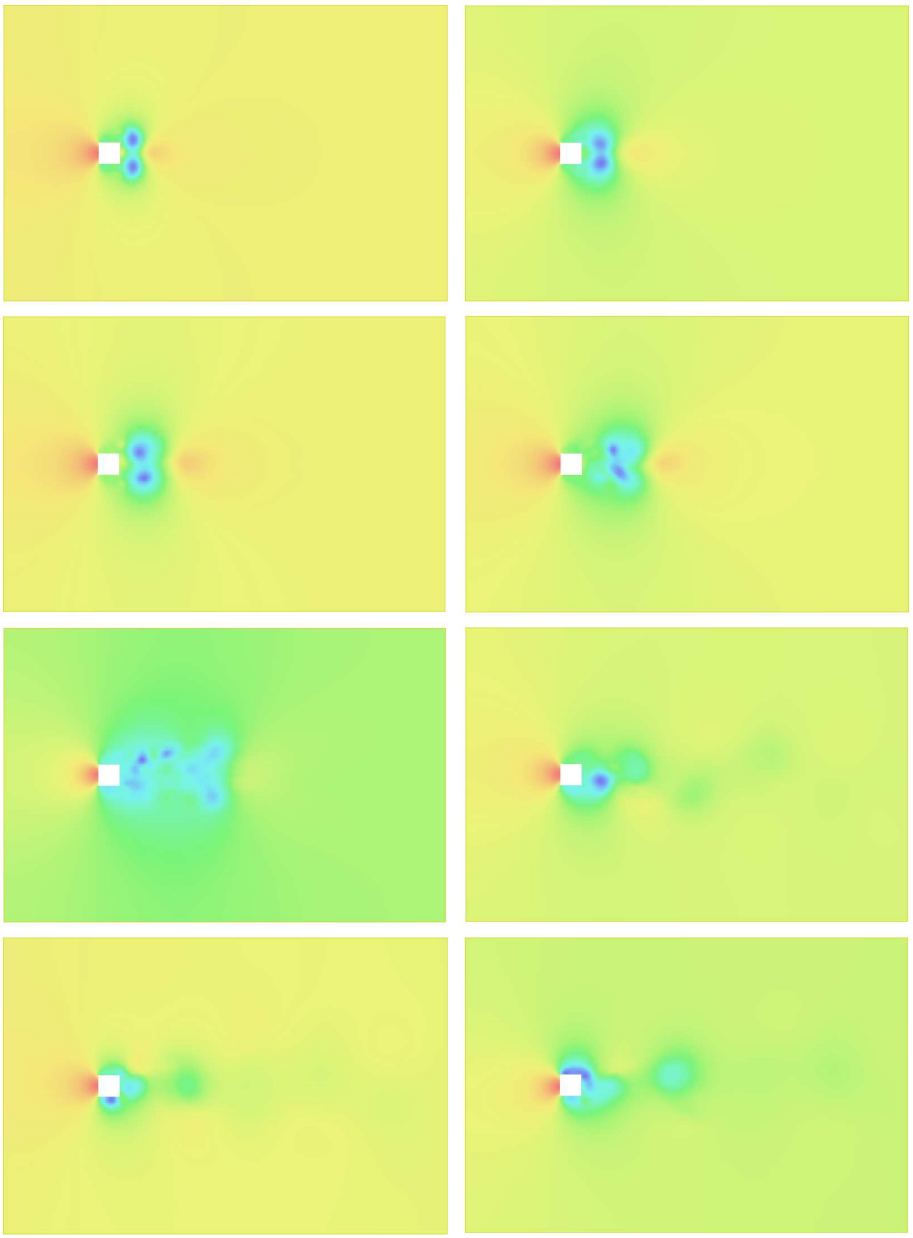

FIGURE 20.8. Pressure corresponding to zero initial data, for time steps 48,64,96,128,160,704,960,1024.

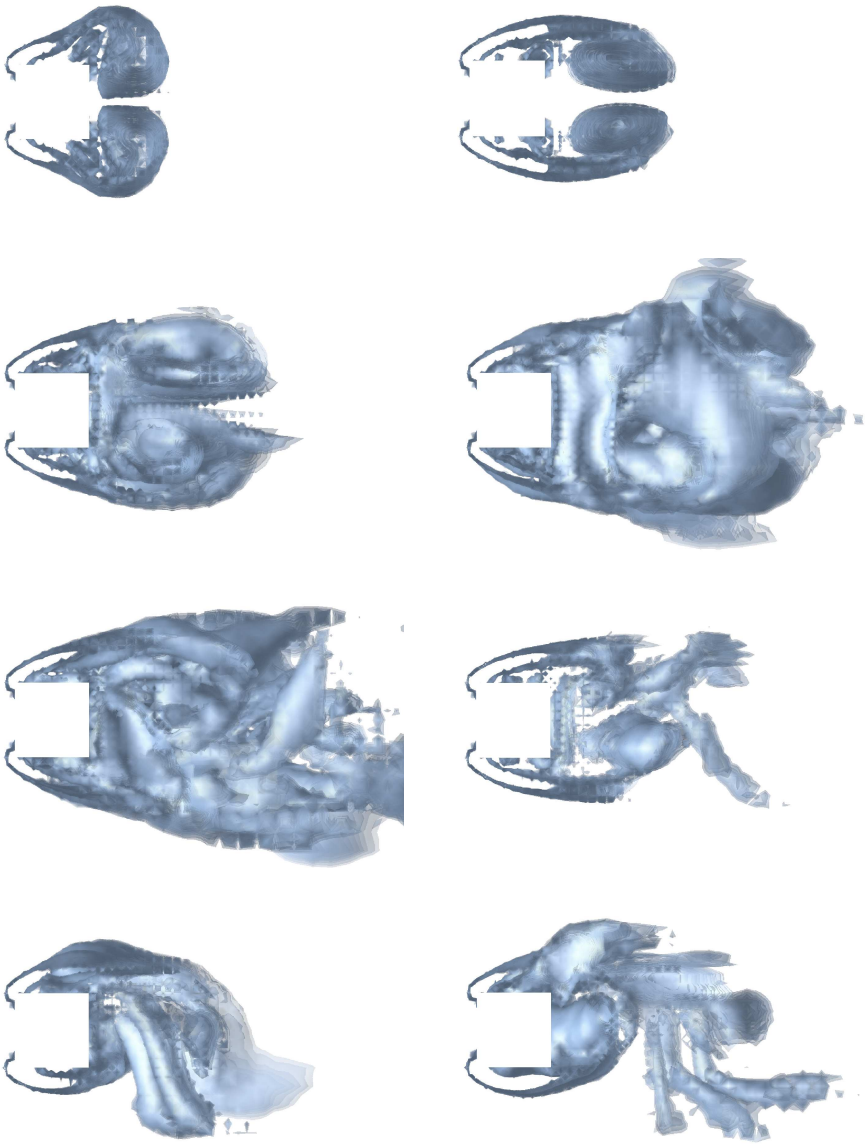

FIGURE 20.9. Magnitude of the vorticity corresponding to zero initial data, for time steps 48,64,96,128,160,704,960,1024.

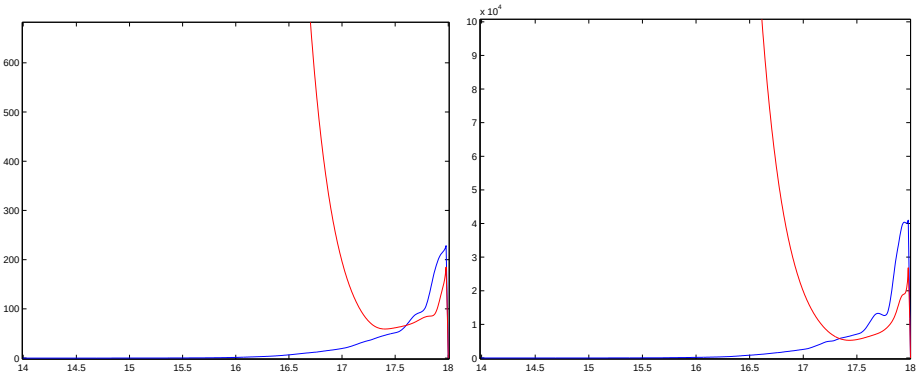

FIGURE 20.10. The L_2-norm of the dual velocity (left) and dual velocity gradient (right), linearized at $U(0) = \nabla\phi$ and turbulent flow respectively.

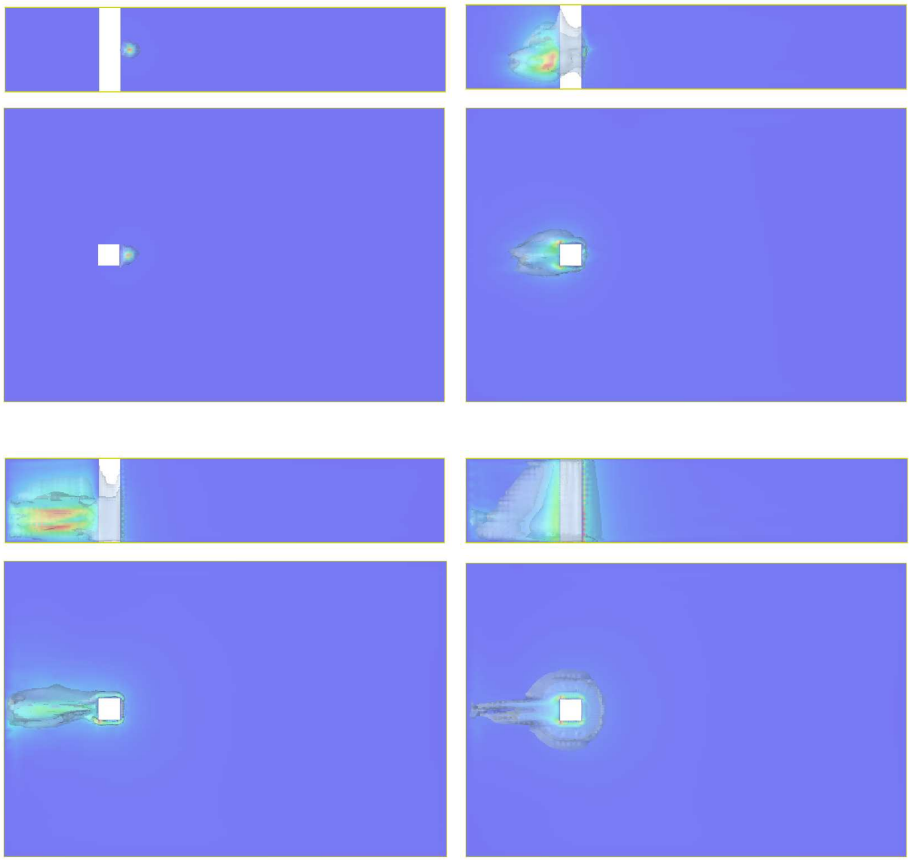

FIGURE 20.11. Dual velocity $|\varphi|$, linearized at $U(0) = \nabla\phi$, for time $t = 18, 17.75, 17.5, 17$.

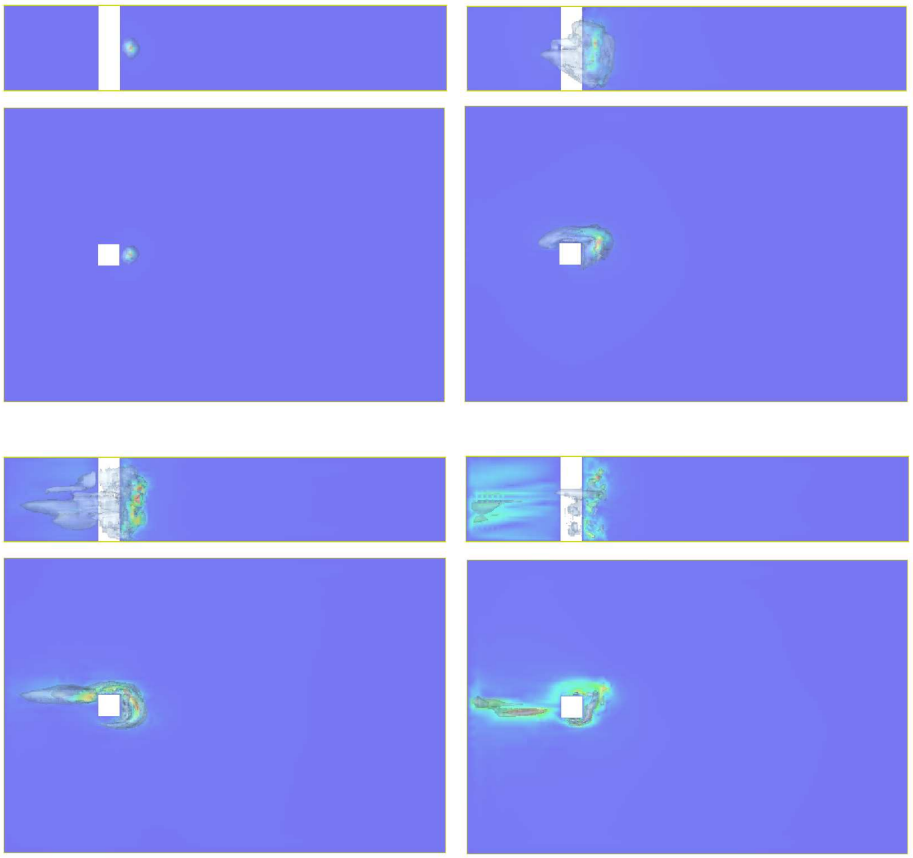

FIGURE 20.12. Dual velocity $|\varphi|$ linearized at turbulent flow, for time $t = 18, 17.75, 17.5, 17$.

energy i in (20.6) with the right hand side $E(u,p)$ given. In Fig. 20.13 we show the computed total energy, and in Fig. 20.14 we show the corresponding temperature starting from zero temperature at initial time and letting the inflow temperature be equal to zero. We notice that the temperature is elevated in the turbulent wake, with the heat being generated by the turbulent dissipation (represented by the weighted least squares term in G2). We notice that the generated heat is transported by the turbulent velocity u in a process of turbulent diffusion of heat, which most likely will dominate any molecular diffusion of heat (which we effectively set to zero in the computation). We are thus able to compute a temperature distribution in a turbulent flow with the only information that the coefficients of viscosity and molecular heat diffusion are very small. This is very good news since precise quantitative determination of very small viscosities or heat conductivitities is very difficult both theoretically and experimentally. From the computations we get the message that the precise values of these (small) quantities are irrelevant, if the quantities of interest are certain mean values.

20.7 G2 as Dissipative Weak Solutions

The computations above show that the internal energy i is non-negative, which we may connect to the sign of the right hand side $E(u,p)$ in (20.6): If $E(u,p) \geq 0$ in $\Omega \times I$, then necessarily $i \geq 0$ if $i^0 = 0$ in $\Omega \times I$. More precisely, (20.6) states that i can then only increase following the flow. So can we guarantee that a G2 approximate weak solution (U,P) satisfies (in a suitable weak sense)

$$E(U,P) \geq 0 \quad \text{in } Q?$$

Yes, we can prove that

$$\int_Q E(U,P)\phi \, dxdt \geq -C\sqrt{h}, \tag{20.7}$$

for any non-negative test function ϕ, where C is a positive constant depending on ϕ. We give a proof below.

The same question is similarly addressed by Duchon-Robert in [25], introducing the notion of a *dissipative weak solution* (u,p) to the Euler equations, which is a function (u,p) satisfying the Euler equations in a weak sense, and in addition satisfies the positivity condition $E(u,p) \geq 0$ in Q in a weak sense. The discussion starts from the observation that a strong (pointwise) solution (u,p) satisfies $E(u,p) = 0$ pointwise, as we remarked above. Further, the observation is made that a limit (u,p) of the Navier-Stokes solutions (u_ν, p_ν) as the viscosity ν tends to zero, will satisfy $E(u,p) \geq 0$ weakly, as a consequence of multiplying the momentum equation in Navier-Stokes by $u_\nu\phi$ with $\phi(x,t)$ a non-negative test function and integrating, to

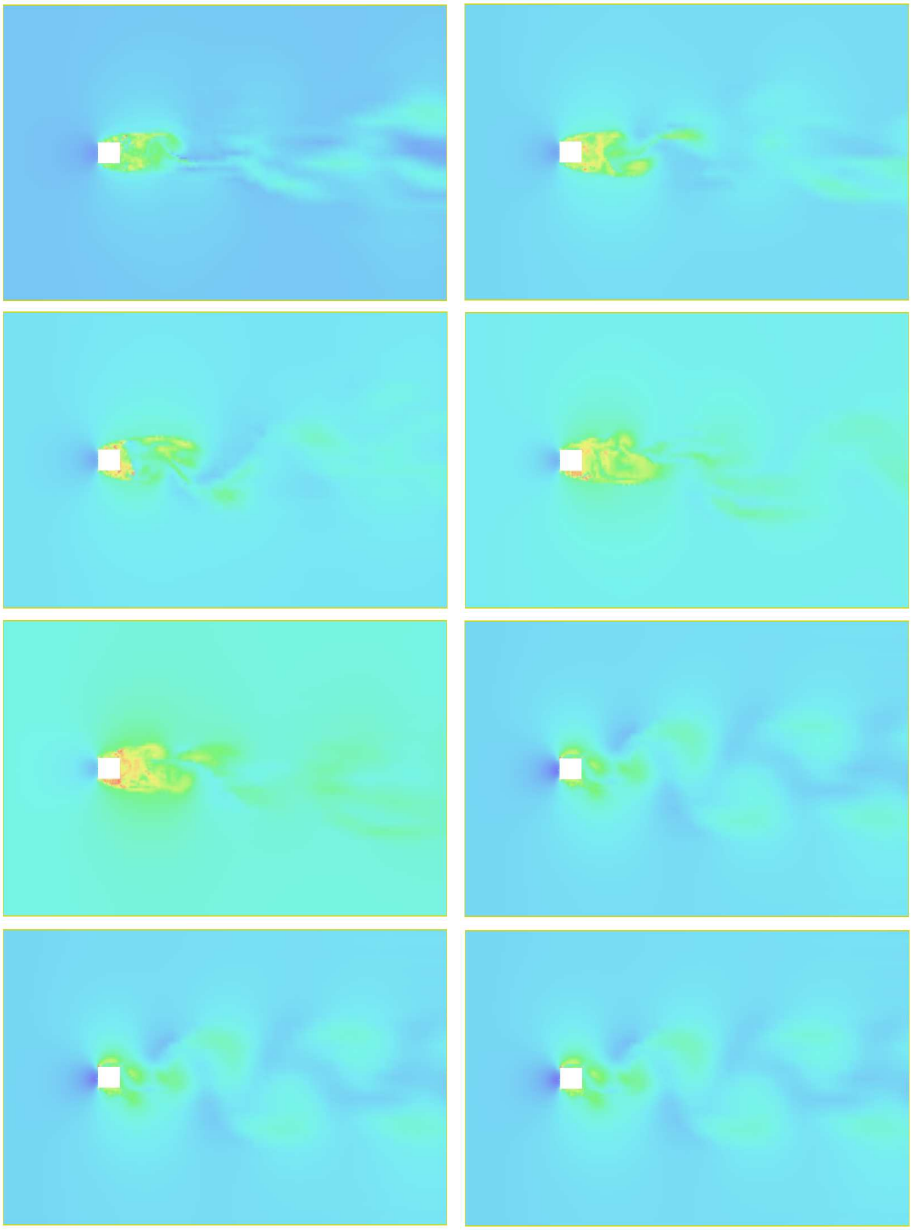

FIGURE 20.13. Total energy e, for time $t = 4, 4.5, 5, 5.5, 6, 11, 15, 16$.

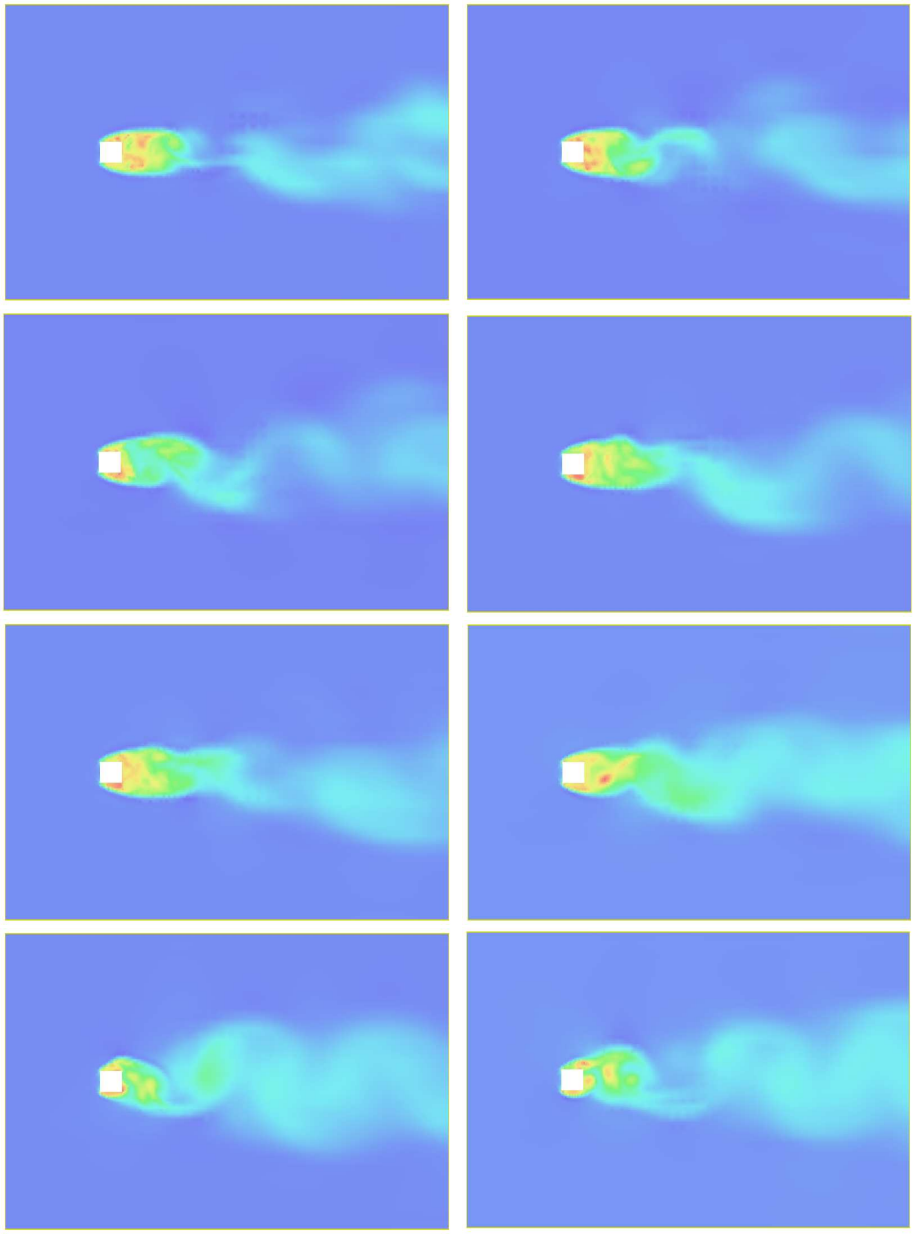

FIGURE 20.14. Internal energy $i = c_v\theta$, for time $t = 4, 4.5, 5, 5.5, 6, 11, 15, 16$.

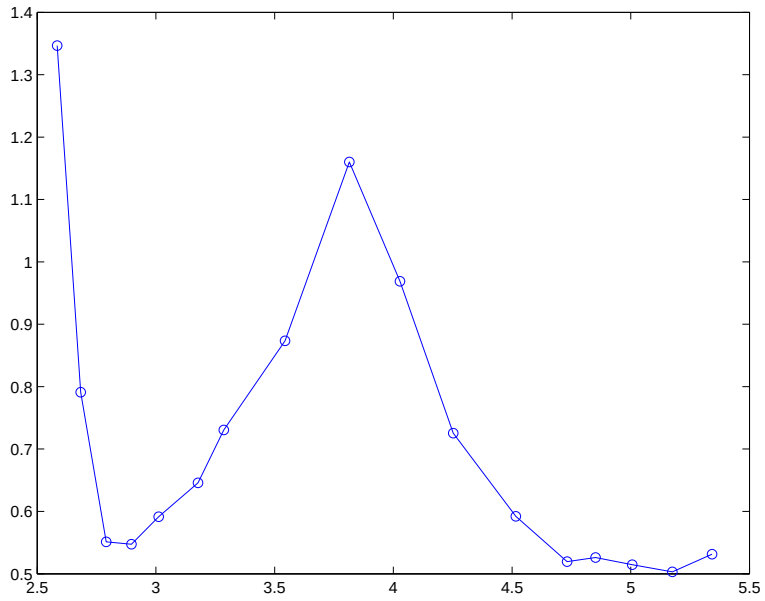

FIGURE 20.15. The mean value of the dissipation intensity of G2 in the turbulent wake of the flow around a surface mounted cube (see Chapter 30), vs $\log_{10}$ of the number of mesh points.

get

$$\int_Q E(u_\nu, p_\nu)\phi \, dxdt = \int_Q \nu|\nabla u|^2\phi \, dxdt + \sum_j \int_Q \nu u_j \nabla u_j \cdot \nabla\phi_j \, dxdt,$$

and noting that by the basic energy estimate (15.2)

$$\sum_j \int_Q \nu u_j \nabla u_j \cdot \nabla\phi_j \, dxdt \to 0,$$

as ν tends to zero. We thus have for small ν

$$E(u_\nu, p_\nu) \approx \nu|\nabla u|^2 \quad \text{in } Q, \tag{20.8}$$

that is, $E(u_\nu, p_\nu)$ is in fact approximately equal to the the *intensity of the viscous dissipation* $\nu|\nabla u|^2$. In particular, we expect that $E(u_\nu, p_\nu) > 0$ for a turbulent flow with substantial turbulent dissipation.

In this context, we recall Kolmogorov's conjecture that the intensity of the turbulent dissipation should have a finite limit as ν tends to zero. By computation we should be able to check if this is true; preliminary results indicate that Kolmogorov may be largely right, see Fig. 20.15.

So even if the existence of weak solutions to the Euler equations cannot be proved, Duchon-Robert propose that it may be reasonable to require a

weak solution (u, p) of Euler to satisfy $E(u, p) \geq 0$ in Q in a weak sense. The rationale is that limits of NS solutions satisfy this condition, as we just demonstrated, and therefore "physical solutions" should satisfy this condition. The proof below that G2 satisfies a variant of the same condition mimics the proof for NS just given. As indicated above, we have strong reasons to believe that (stable) weak solutions to the Euler equations do not exist, and thus that the notion of dissipative weak solution to Euler may not be useful, but the notion of approximate dissipative weak solution is.

20.8 Entropy, G2 and Physics

We can view $E(u, p) \geq 0$ to express an *entropy condition* stating that kinetic energy may be turned into internal energy, that is $D_u i \geq 0$, but internal energy cannot be converted back again, that is, we can never have $D_u i < 0$ with strict inequality. Once kinetic energy has been turned into internal energy it is "lost" and cannot be retrieved. This is a property of incompressible flow, where no energy can be stored by compression.

Using (20.8) we can reformulate the basic energy estimate for NS (15.2) as follows:

$$\frac{1}{2}\|u_\nu(T)\|^2 + \int_Q E(u_\nu, p_\nu)\,dx\,dt \approx \frac{1}{2}\|u^0\|^2, \tag{20.9}$$

indicating that for a dissipative weak Euler solution actually

$$\frac{1}{2}\|u_\nu(T)\|^2 < \frac{1}{2}\|u^0\|^2, \tag{20.10}$$

with substantial loss of total kinetic energy. A G2 solution will of course have the same property by the basic energy estimate (20.3), but satisfies the stronger more local positivity condition (20.7).

This reflects the general fact that kinetic energy can be turned into heat by (some kind of) friction, but cannot be (fully) retrieved. A stone dropped to the ground gets heated up, but cannot lift itself by cooling off.

The important observation is thus that an approximate G2 solution (U, P) to the Euler equations approximately satisfies the entropy condition $E(U, P) \geq 0$ in Q in a weak sense. We may interprete this as a statement that "G2 follows Physics". Below we will turn this around and ask if in fact instead "Physics follows G2?

We shall in a forthcoming volume on compressible flow meet the same question with a different notion of entropy.

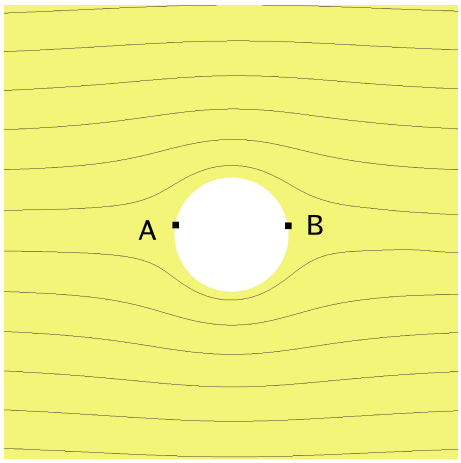

FIGURE 20.16. Streamlines for the potential solution of a circular cylinder.

20.9 Analysis of Instability of the Potential Solution

We have given computational evidence by G2 that the potential solution to the Euler equations is unstable. We shall now give analytical evidence of this instability in the model case of flow around a circular cylinder. We thus focus on the potential solution with velocity $u(x)$ given as the gradient of the real part $\phi(x_1, x_2) = (r + \frac{1}{r})\cos(\theta)$ of the analytic function $w = z + \frac{1}{z}$ with $z = x_1 + ix_2$, see Fig. 20.16. The stability is governed by (i) the linearized Euler equations (8.1), (ii) the dual linearized problem (13.4) with $\nu = 0$, or (iii) the vorticity equations (20.11):

$$\dot{\omega} + (u \cdot \nabla)\omega - (\omega \cdot \nabla)u = 0 \quad \text{in } \Omega \times I, \tag{20.11}$$

which we may view as a linear convection-reaction equation for the propagation of the vorticity ω with the fluid velocity u being given. In all cases (i)-(iii) the crucial term is the reaction term with $\pm\nabla u$ acting as coefficient in a linear convection-reaction problem. We now compute ∇u near the rear separation point B given by $z = 1$. We then write

$$w(z) = z - 1 + 1 + \frac{1}{z - 1 + 1} \approx 1 + (z - 1)^2$$

and thus have

$$\phi(x_1, x_2) \approx (x_1 - 1)^2 - x_2^2$$

and

$$u(x) \approx (2(x_1 - 1), -2x_2, 0)$$

and thus the vorticity equation takes the following approximate form close to B:

$$\begin{aligned} \dot{\omega}_1 + (u \cdot \nabla)\omega_1 &= 2\omega_1 \\ \dot{\omega}_2 + (u \cdot \nabla)\omega_2 &= -2\omega_2 \\ \dot{\omega}_3 + (u \cdot \nabla)\omega_3 &= 0 \end{aligned} \tag{20.12}$$

We see that ω_1 is exponentially increasing with rate $\exp(2t)$, which indicates that the potential flow solution is exponentially unstable.

The same analysis applies to the circular cylinder (without sharp corners) presented in Chapter 11.

20.10 Proof that Euler/G2 is a dissipative weak solution

Choosing $\hat{v} = (\phi\hat{U})_h \in \hat{V}_h$ in Euler/G2 according to (15.4), where ϕ is a positive test function and the index h indicates interpolation into $\hat{V}_h$, we get assuming $\hat{U}$ is bounded

$$\begin{aligned} \int_Q E(\hat{U})\phi \, dxdt &= ((h\phi R(\hat{U}), R(\hat{U})) + ((R(\hat{U}), \phi\hat{U} - \hat{v})) \\ &\quad + ((hR(\hat{U}), R(\phi\hat{U}) - R(\hat{v}))) + \tilde{R}, \end{aligned}$$

where $\tilde{R} \geq -C\sqrt{h}$ with $C > 0$ depending on first derivatives of ϕ and the max of $\hat{U}$. We now use so-called *superapproximation* to obtain

$$\|\phi\hat{U} - \hat{v}\| \leq Ch\|\hat{U}\|$$

with the notable feature that we gain one power of h without paying any first derivative price on $\hat{U}$. This is because $\phi\hat{U}$ is the product of a smooth function and a function in the finite element space $\hat{V}$. Combined with the basic energy estimate bounding $\|\sqrt{h}R(\hat{U})\|$, it follows that

$$\int_Q E(\hat{U})\phi \, dxdt \geq -C\sqrt{h}$$

which proves that G2 is a weak dissipative solution, as desired. This represents one of the most important proofs in the book. Notice that we assume $\hat{U}$ to be bounded but not derivatives of $\hat{U}$, which would make the proof meaningless.

21
Resolution of Loschmidt's Mystery

There are great physicists who have not understood it. (Einstein about Boltzmann's statistical mechanics)

There is apparently a contradiction between the law of increasing entropy and the principles of Newtonian mechanics, since the latter do not recognize any difference between past and future times. This is the so-called reversibility paradox (Umkehreinwand) which was advanced as an objection to Boltzmann's theory by Loschmidt 1876-77. (Translators foreword to Lectures on Gas Theory by Boltzmann).

21.1 Irreversibility in Reversible Systems

In this chapter we present a new approach to resolving Loschmidt's Mystery of irreversibility in reversible Hamiltonian systems. We base our solution on finite precision computation in the form of G2 instead of the standard approach of statistical mechanics, which we commented on in Chapter 12. We thus stay within a deterministic Hamiltonian framework and only add a restriction of finite precision G2 computation, and we do not use any form of statistics. A World governed by Hamiltonian mechanics combined with finite precision G2 computation, follows the laws of mechanics as far as possible taking the finite precision into account, but is not based on any microscopic game of roulette as statistical mechanics. The difference of scientific paradigm is fundamental.

21.2 Euler/G2 as a Model of Thermodynamics

As a model we consider the Euler equations for incompressible inviscid flow, which is a formally reversible Hamiltonian system expressing conservation of mass, momentum and energy. We thus consider G2 for the Euler equations (20.1) augumented with the energy equation (20.5) (assuming $f = 0$ and no heat conduction).

We recall from the previous chapter that a basic property of an Euler/G2 weak approximate solution $\hat{U}$ is that in a weak sense $E(\hat{U}) \geq 0$, which expresses the 2nd Law of Thermodynamics: Since by (20.6) we have in a weak sense

$$D_U I = E(\hat{U}) \geq 0$$

where here I is the Euler/G2 internal energy (heat energy), which expresses that internal energy once generated cannot be retrieved back into kinetic energy. For turbulent solutions we have $D_U I > 0$ with strict inequality, which means that in a turbulent flow necessarily internal energy is generated, which cannot be retrieved.

Euler/G2 thus gives a model for thermodynamics, where the 2nd Law is a a consequence of the basic laws of conservation of mass, momentum and energy. This is a model where the mystery of the 2nd Law has dissappeared! The reason time is moving foreward is that necessarily flows become turbulent and turbulent flows dissipate kinetic energy into internal heat energy which cannot be retrieved. We conclude that the reason a perpetum mobile cannot be constructed is the fact that inviscid flow *necessarly always* becomes turbulent with kinetic energy dissipating into heat, which cannot be retrieved.

We have thus resolved Loschmidt's Mystery in a Euler/G2 model of thermodynamics. We extend to compressible flow and kinetic gas theory in [53, 47, 48, 49, 50]. Altogether this gives a theoretical basis of thermodynamics where the crucial 2nd Law is a consequence of the 1st Law combined with G2 finite precision computation.

21.3 Euler/G2 vs Physics

Finite precision G2 computation of course appears in digital solution of the differential equations of deterministic mechanics, but it necessarily also has to appear in some form in the analog computation performed in the physics of the real World. We may analyze the consequences of finite precision computation of digital solution, and then seek to find G2 analogs in physics following the device of the computer scientist Dijkstra: "Originally I viewed it as the function of the abstract machine to provide a truthful picture of the physical reality. Later, however, I learned to consider the abstract machine as the *true* one, because that is the only one we can *think*; it is

the physical machine's purpose to supply a *working model*, a (hopefully) sufficiently accurate physical simulation of the true, abstract machine".

Notice that G2 is not just *any* model with finite precision, but a model with specific properties of satisfaction of the basic laws of Newtonian mechanics. This makes it more interesting to follow the idea of Dijkstra.

21.4 The World as a Clock with Finite Precision

This brings us back to a deterministic World as a giant Clock in the spirit of Laplace, but our Clock has G2 finite precision and that changes the game. In particular, it takes us out of the classical paradox of the existence of free will in a deterministic World. With finite precision computation, the future is no longer fully determined pointwise by the present, and there is room for something like a free will. And there are necessarily irreversible processess.

We now develop in some more philosophical aspects of Euler/G2 as a model of the World, which the reader may want to skip in a first reading, and instead go directly into Secrets.

21.5 Direction of Time

The origins of irreversibility in reversible systems is a main unsolved mystery of mechanics and physics. A Hamiltonian system is reversible in time and does not have a preferred (forward) direction of time: From a given configuration both the future and past are equally well determined. The reversibility follows from the invariance of a Hamiltonian system under a change of sign of time and velocity. It follows in particular that letting a Hamiltonian system evolve in time from an initial configuration to a final configuration and there reversing the velocity and changing the direction of time, will bring the system back to the initial configuration. As a result, one may in Hamiltonian mechanics construct a perpetuum mobile of the first kind, which is a machine that will run forever without consuming any energy. Both celestial mechanics and quantum mechanics are Hamiltonian and the motion of the planets in our Solar system as well as the electrons in an atom represent reversible perpetuum mobile of the first kind.

On the other hand, in the real World there is a preferred direction of time and we are all familiar with irreversible processess in which initial configurations cannot be recovered, and the impossibility of constructing a perpetuum mobile of the first kind, as well as of the second kind supposed to reversibly convert energy back and forth from heat to mechanical work without consuming any net energy. The irreversibility is expressed in the Second Law of Thermodynamics, which states that in an isolated system

a certain scalar quantity, named *entropy*, cannot decrease with time. As a consequence, an isolated system becomes irreversible if its entropy increases, since time reversal would correspond to decreasing entropy, which is impossible. In a Hamiltonian system the entropy is equal to minus the total energy being the sum of kinetic and potential energy, and energy conservation reflects reversibilty and entropy constancy. The observation that a perpetuum mobile of the second kind seems impossible, because converting mechanical energy into heat does not seem to be fully reversible, indicates the existence of real processes which are irreversible and thus not Hamiltonian. Dropping a stone to the ground will convert its potential energy into heat making the stone warmer, but the reverse process of the stone lifting itself by getting colder, is impossible. The question is why?

So if now the World ultimately is governed by reversible Hamiltonian (quantuum) mechanics, the scientific challenge thus becomes to explain how irreversibility may arise in systems based on reversible Hamiltonian mechanics. In the late 19th century when the existence of an Aether filling empty space was still contemplated, the irreversibilty was suggested to possibly result from some small viscosity of the Aether, but since no one could ever detect any Aether, this belief faded. Similarly, the idea of putting in just a tiny bit of friction (coming from somewhere) to explain irreversibility, is not convincing, since then the planets and electrons would be constantly retarding a little bit, but they don't seem to do that. And if there would be some friction in some system, the challenge would be to explain how friction can arise in a system governed by Hamiltonian reversible mechanics without friction. Thus the irreversibility paradox can be phrazed: How can there be friction in a system without friction?

The traditional way to resolve the paradox has been statistical mechanics, which is an expansion of Hamiltonian mechanics using concepts from statistics and probability. This expansion has a high scientific cost, since so many new (difficult) questions arise from the use of statistics. Accordingly statistical mechanics has been questionend by many famous scientists including Einstein, and still is.

Altogether, as far as we can understand, the true origins of irreversibility in reversible systems has not been given a scientifically convincing explanation. The literature is vast with contributions from mathematicians, physicists, chemists, engineers, philosophers, linguists, authors of science fiction and the general public.

21.6 Finite Precision Computation

We now focus on the new mode of explanation based on finite precision computation in the form of G2, which we advocate. The finite precision computation appears in two forms: First, it necessarily appears in digital

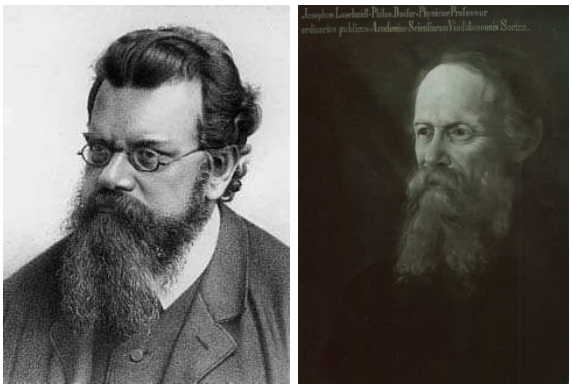

FIGURE 21.1. Ludwig Boltzmann (1844-1906) and Jan Josef Loschmidt (1821-1895).

solution of Hamiltonian equations using computers, which is the objective of our study. Secondly, it probably appears also in Natures evolution in time from one state to the next in some form of analog computation.

The solution of the paradox of irreversibility in reversible system based on finite precision computation, is not trivial in the sense that it may be blamed simply on something like round-off errors in digital computing or the inevitable approximations in solving differential equations numerically. This would be similar to explaining irreversibility as an effect of a slightly viscous Aether, a mode of explanation we have already rejected.

The solution of the paradox is much deeper and more fundamental and directly couples to computational turbulence as presented in this book. In short, the secret we uncover is the following: We consider a set of Hamiltonian equations describing the evolution in space/time of a certain system in Nature. We seek to solve the equations computationally using a numerical method implemented on a computer. Doing so we meet two different situations: In the first case, which is the simple standard case without surprise, the Hamiltonian equations have pointwise solutions which are computable, and if so we simply compute these solutions and find them to be reversible. A pointwise solution has a residual which is pointwise zero, obtained by inserting the solution in the equation, and we can compute approximate solutions with residuals being small pointwise. Such computed solutions are approximately reversible by the reversible nature of the equations they are approximately solving pointwise.

In the second case, which contains the secret, the Hamiltonian equations do not admit pointwise solutions, which means that there simply are no (stable) solutions with a residual being zero pointwise. This is the case with the Euler equations and reflects the appearance of turbulence. In this second case G2 cannot produce an approximate solution with small pointwise residual, and reacts by producing an approximate solution for

which the residual is small in a weak average sense combined with a certain weighted least squares control of the residual, which turns out to be possible to achieve. In the case the Hamiltonian equations do not admit pointwise solutions, which may correspond to the appearence of turbulence, G2 thus produces an approximate solution with the residual being small in a weak sense and with a certain weighted least squares control of the size of the pointwise residual, while the pointwise residual itself is not small.

We have remarked that this is about the best that can be done in the situation when the Hamiltonian equations do not admit pointwise solutions, and we have also seen that it is good enough if we as quantities of interest or output quantities choose certain mean values of the solution, rather than point values. In the case the Hamiltonian equations do not admit pointwise solutions, corresponding to turbulence/shocks, we can thus nevertheless by G2 compute certain mean value outputs accurately. From a physical point of view, we may say that even though the Hamiltonian equations cannot be satisfied pointwise, they can be satisfied in an average sense with the pointwise residual not being too large, and that may be enough for the system to evolve. The pointwise violation but average satisfaction of the Hamiltonian laws in this sense, corresponds to a physical system in pointwise non-equilibrium, but in average local equilibrium with some control of the pointwise non-equilibrium. In such a physical system the laws of physics serve as goals, which cannot be satisfied pointwise, and the search of satisfaction in a suitably approximate sense is what drives the evolution of the system. It is like the Law in our society, which is never followed pointwise by all citizens, only in some average sense, but yet has an important role to secure that society does not fall apart.

21.7 Dissipation

Now, the catch is that the weighted least squares control of the residual in G2 adds a dissipative term in an energy balance like (20.3), which effectively makes the system irreversible. This is like a fine or cost arising from not following the Law pointwise. It is thus the appearance of turbulent/shock small scales and the resulting impossibility of computing solutions with pointwise small residuals, which necessarily introduces the irreversibility. By necessity, a fine has to represent a positive cost; if we would get paid by breaking the Law, society would quickly collapse. Or if there would be a negative cost (gain) in changing currency, the monetary system would explode.

Facing the impossibility of pointwise solution, the system thus reacts by producing an approximate solution in which some of the energy is lost in a dissipative least squares term implying irreversibility. Moreover, the size of the dissipation and the energy loss does not decrease with increasing

precision: In turbulence the dissipation always occurs on the finest scales available, but the total amount of the turbulent dissipation (turning into heat), stays (approximately) constant under scale refinement. A shock in compressible flow has a similar nature. Mean value outputs thus may show an independence of the scale of resolution in the computation, while pointwise solution is impossible even if the computational scale is refined indefinitely. The more you refine, the more scales you find and there is no end to this process.

The basic idea is thus that in certain Hamiltonian processes necessarily small scale features in the form of turbulence/shocks appear, and when faced with these small unresolvable scales, which physically generate heat, the system reacts by introducing a dissipative least squares control of the residual, which implies irreversibility. Thus, in turbulence/shocks, large scale mechanical energy may be turned into small scale motion, corresponding to generation of heat, and this process is irreversible since the details of the small scales cannot be kept and thus cannot be recovered.

The key here is to realize that the dissipative damping (i) is necessary, (ii) is substantial, (iii) is not a numerical artifact which can be diminished by increasing the precision. The key new fact behind (i)-(iii) is the nonexistence of solutions to the Hamiltonian equations! The appearance of turbulence/shocks in inviscid compressible is an example of an irreversible process satisfying (i)-(iii), where inevitably and irreversibly energy is turned into heat. As is well known, a shock solution is a not pointwise solution to the Euler equations. As we will show below, neither does turbulence correspond to pointwise solution.

In G2 the irreversibility arises from the presence of the least squares control of the residual, which corresponds to a loss of the kinetic/potential energy which cannot be recovered in G2; reversing time and velocities at final time in G2 and computing backwards in time will bring in a new least squares term only adding to the losses already made in the forward computation. This reflects the difficulty of getting a refund of an already paid fine.

21.8 Coupling to Particle Systems

The Euler equations for incompressible inviscid flow may be viewed to model a very large collection of "fluid particles" following Newton's Second Law subject to a pressure force maintaining incompressibility.

The incompressible Euler equations represent a formally reversible system, which as we have seen in general lacks pointwise solutions. This is because the laminar pointwise solutions, which do exist, turn out to be unstable without physical realization, and because the turbulent solutions, which do appear, are not pointwise solutions but only approximate weak

solutions. Thus, both computation and Nature will have to go for suitable approximate solution of the Euler equations. Computation will then rely on G2, with presumably Nature resorting to something similar, which inevitable (because of the least squares residual control in G2) will introduce a dissipative effect implying irreversibility.

We have thus met a situation, where the equations we want to solve do not have exact pointwise solutions, (or if they have, then they are unstable), while the turbulent solutions which do exist in fact only are approximate weak solutions and not pointwise solutions, and moreover these approximate solutions necessarily have a dissipative character resulting in irreversibility. The paradox of irreversibility in a formally reversible Hamiltonian system is thus a consequence of the non-existence of a stable laminar pointwise (strong) solutions to the Euler equations, which would have been reversible if they had only existed, and the dissipative nature of the turbulent approximate weak solutions, which do exist computationally and and for which mean value outputs can be accurately computed.

We note that the non-existence of (stable) exact solutions, changes the way mathematics for the Euler equations can be presented: With non-existent exact solutions, the attention has to move to existing approximate solutions, and thus the computational aspect takes a prime position before analytical mathematics.

The non-existence of pointwise solutions to the Euler equations, which may be viewed as a failure of mathematics, in fact may be turned around into an advantage from a computational point of view: If there were an exact solution, one could always ask for more precision in computing this solution requiring finer resolution and higher computational cost, but if there is no exact solution, then we could be relieved from this demand beyond a certain point. A key feature in this situation is that the absolute size of the fine scales no longer are important, and this could save computational work. In turbulence this means that mean value outputs may be computed on meshes which do not resolve the turbulent vortices to their actual physical scale.

In order for a Hamiltonian system to develop turbulence, it has to be rich enough in degrees of freedom. In particular, the incompressible or compressible Euler equations in less than three space dimensions are not rich enough, even if the mesh is very fine. On the other hand, turbulence invariably develops in three dimensions once the mesh is fine enough. Our experience with turbulent solutions of the incompresible Navier-Stokes equations indicates that a mesh with 100.000 mesh points in space may suffice in simple geometries, while in more complex geometries millions, but not billions, of mesh points may be needed.

21.9 Imperfect Nature and Mathematics?

How are we to handle the fact that the Euler equations do not have pointwise solutions in general? Does this express an imperfection of mathematics? And what is the consequence in physics? Is Nature simply unable to satisfy the basic laws laid down in the form of e.g. Newton's Second Law? Does this mean that also Nature is imperfect? And if now both mathematics and Nature indeed are imperfect, what is the degree of imperfection and how does it show up?

We may make a parallel with the squareroot of two $\sqrt{2}$, which is the length of the diagonal in a square with side length 1. We know that the Pythagoreans discovered that $\sqrt{2}$ is not a rational number. This knowledge had to be kept secret, since it indicated an imperfection in the creation by God formed as relations between natural numbers according the basic belief of the Pythagoreans. Eventually this unsolvable conflict ruined their philosophical school and gave room for the Euclidean school based on geometry instead of natural numbers. Civilization did not recover until Descartes resurrected numbers and gave geometry an algebraic form, which opened for Calculus and the scientific revolution.

But how is the Pythagorean paradox of non-existence of $\sqrt{2}$ as a rational number handled today? Well, we know that the accepted mathematical solution since Cantor and Dedekind is to extend the rational numbers to the real numbers, some of which like $\sqrt{2}$ are called irrational, and which can only be described approximately using rational numbers. We may say that this solution in fact is a kind of non-solution, since it acknowledges the fact that the equation $x^2 = 2$ cannot be solved exacly using rational numbers, and since the existence of irrational numbers (as infinite decimal expansions or Cauchy sequences of rational numbers) has a different nature than the existence of natural numbers or rational numbers. The non-existence is thus handled by expanding the solution concept until existence can be assured.

We handle the non-existence of pointwise solutions to the Euler equations similarly, that is, by extending the solution concept to approximate solution in a weak sense combined with some control of pointwise residuals. Doing so we necessarily introduce a dissipation causing irreversibility. In this case, the non-existence of solutions thus has a cost: irreversibility. In the perfect World, pointwise solutions would exist, but this World cannot be constructed neither mathematically nor physically, and in a constructible World necessarily there will exist irreversible phenomena as a consequence of the non-existence of pointwise solutions. The non-existence of pointwise solution reflects the development of complex solutions with small scales, and thus the non-existence also relects a complexity of the constructible World. The perfect World would lack this complexity, so in addition to being non-existent it would also probably be pretty non-interesting. The World we live in thus does not seem to be perfect, but it surely is complex and interesting.

What is the reason that the resolution of the paradox we are proposing has not been presented before, if it indeed uncovers the mystery? We believe it can be explained by the Ideal Worlds that both mathematicians and physicists assume as basis of their science. In the Ideal World of mathematics, exact solutions to differential equations exist as well as infinite sets, not just approximate solutions and finite sets, and the World of physics is supposed to follow laws of physics exactly, not just approximately, unless a resort to statistics is made (which is a very strong medication with severe side effects). It thus appears that an imperfect World of mathematics or physics, where equations cannot be solved exactly or laws of physics cannot be exactly satisfied, classically is unthinkable at least as a deterministic World, and thus has recieved little attention by mathematicians and physicists with little background in computational mathematics. Yet, such an imperfect World seems to be a reality in both mathematics and physics, and thus should be studied.

21.10 A New Paradigm?

From philosophical point of view, we may say that the traditional paradigm of both mathematics and physics is Platonistic in the sense that it assumes the existence of an Ideal World, where equations/laws are satisfied exactly. We may say that this is an Ideal World of infinities because exact satisfaction of e.g. the equation $x^2 = 2$ requires infinitely many decimals. This is the mathematical Ideal World of Cantor, which represents a formalist/logicist school. In strong opposition to this school of infinities, is the constructivist school, which only deals with mathematicial objects that can be constructed in a finite number of steps. In the constructivists Constructible World, the set of natural numbers does not exist as a completed mathematical object as in Cantors Ideal World, but only as a never-ending project where always a next natural number can be constructed if needed, which follows the suggestions of e.g. Aristotle and Gauss. The Constructible World is finitary and thus inherently computational, while Cantors Ideal World is non-finitary and non-computational. In the educational project [1] and the pamphlett [54], we compare the two schools, and give our vote to the Constructible World, which today can be explored using the computer, and we question the existence an Ideal World as always a scientifically meaningful concept.

21.11 The Prize Problem Again

We have noted that one of the seven Clay Institute Millennium $1 Million Prize Problems asks for a proof of existence of a pointwise solution to the

Navier-Stokes equations for incompressible fluid flow, a formulation which fits into an Ideal World paradigm. We argue that the formulation of the Prize Problem is unfortunate, and propose instead a reformulation of the Prize Problem in constructive terms, since in general pointwise solutions do not exist, while turbulent approximate solutions do.

22
Secrets of Ball Sports

Football s not a matter of life and death. It is more important than that. (Bill Shankly)

If a player is not interfering with play or seeking to gain an advantage, then he should be. (Bill Shankly)

22.1 Introduction

Major ball sports such as football, golf, tennis, and baseball, gather millions of fans at stadiums and at the TV around the world every day. Can we understand the physics underlying the stunning performances of Ronaldinho, Tiger Woods, Roger Federer, Hideki Matsui and the others?

To investigate the physics of ball sports we here consider the flow of air past a sphere, and in particular we focus on the resulting forces on the sphere; that is drag and lift of the sphere, with drag being the force component in the opposite direction of the flow, and lift being the force in a direction perpendicular to the direction of the flow. Using a moving frame of reference centered at the sphere, a ball moving through air without any external wind load corresponds to a stationary sphere in a uniform flow in the opposite direction of the trajectory of the ball.

22.2 Dimples of a Golf Ball: Drag Crisis

Drag consists of the pressure drop over the sphere, referred to as *pressure drag*, and the viscous friction forces at the surface of the body, referred to as *skin friction*. We will see in Chapter 31 that the skin friction is decreasing with increasing Reynolds number, so that for high Reynolds numbers typically pressure drag is dominating. Pressure drag is connected to flow separation, see Chapter 32, where earlier separation in general leads to higher pressure drag.

The drag coefficient of a sphere for Reynolds numbers of the order $10^3 - 10^5$ is $c_D \approx 0.4$, with c_D a non dimensional normalization of the drag force F_D, defined by

$$c_D = \frac{1}{\frac{1}{2}\rho\, U_\infty^2 A} \times F_D, \tag{22.1}$$

with U_∞ a representative free stream velocity, A a representative area of the sphere, typically $A = \pi d^2/4$ with d the diameter of the sphere, and ρ is the density. The *dynamic pressure* p_{dyn} is defined as

$$p_{dyn} = \frac{1}{2}\rho\, U_\infty^2, \tag{22.2}$$

and thus the drag coefficient $c_D = F_D/(p_{dyn}A)$ is defined as the ratio of the drag force and the force produced by the dynamic pressure p_{dyn} times the area A.

At very high Reynolds numbers, of the order $10^5 - 10^6$, the boundary layer at the surface of the ball suddenly undergoes transition to turbulence, which leads to a delayed separation and a dramatic drop in c_D to about 0.1, referred to as *drag crisis*. It is the increased momentum near the boundary in a turbulent boundary layer that delay separation.

In golf we want to be able to drive the ball as far as possible, and thus we would like to minimize the drag of the golf ball. Now, in driving a golf ball we do not reach the critical Reynolds numbers leading to transition in the boundary layers, but it turns out that we can trigger transition at lower Reynolds numbers by introducing perturbations in the boundary layer, for example by adding the dimples on the surface. We discuss the role of the perturbations level for transition further in Chapter 34.

The skin friction of the boundary layer is decreasing with increasing Reynolds number, and we may model drag crisis by using G2 together with a skin friction boundary condition, see Chapter 32. Decreasing skin friction then leads to delayed separation, see Fig. 22.1.

22.3 Topspin in Tennis: Magnus Effect

In a number of ball sports we are familiar with the phenomenon that a spinning ball seems to experience a force in the direction of the rotation.

FIGURE 22.1. Vorticity for a sphere before (left) and after (right) drag crisis.

This is what we see in a topspin in tennis, or a curveball in baseball, and we refer to this phenomenon as the *Magnus effect*.

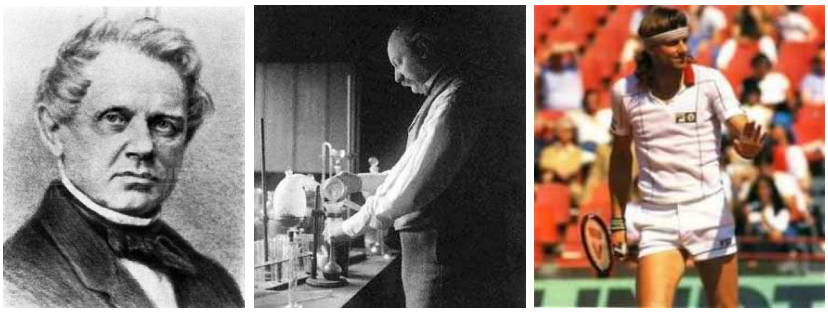

FIGURE 22.2. Heinrich Gustav Magnus (1802-1870), John William Strutt/Lord Rayleigh (1842-1919), and Björn Borg.

The notion of the Magnus effect goes back to Lord Rayleigh, who credited Heinrich Gustav Magnus for the first explanation of the lateral deflection of a spinning ball. But the phenomenon was studied already by Newton in 1672, who noted how a tennis ball is affected by spin, and by Robins who in 1742 showed that a transverse aerodynamic force could be detected on a rotating sphere (therefore also referred to as the "Robin's effect"). Lord Rayleigh showed that for a frictionless fluid the side force is proportional to the free stream velocity and the rotational speed.

The traditional explanation of the Magnus effect for a spinning sphere is based on Bernoulli's law, where the idea is that the fluid velocity on one side of the sphere is enhanced by the spin of the sphere, and the velocity on the opposite side is decreased, resulting in a pressure difference over the sphere, and thus a force, "the Magnus force", is created.

More recent studies agree on an explanation coupled to boundary layer separation, where the separation is delayed on the side of the sphere that is moving in the same direction as the free stream velocity, while the separation occurs prematurely on the side moving against the free stream flow, resulting in a shift of the wake toward the side moving against the free stream velocity, causing a deflection of the flow momentum and a resulting force in the opposite direction, by conservation of momentum.

In Fig. 22.3 we show a G2 solution of a rotating sphere, where we note the shifted wake, and also the low pressure on the side moving with the free stream velocity, consistent with Bernoulli's law predicting low pressure where the velocity is high. We also note the deflection of the flow due to the shifted wake, and thus we may rationalize the Magnus effect either by the pressure difference over the sphere, or by conservation of momentum and the deflection of the flow by the assymetric wake.

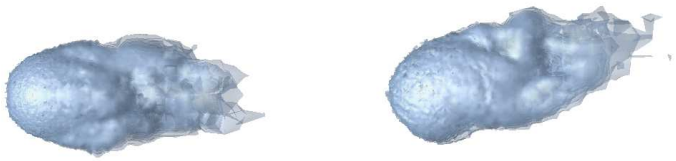

FIGURE 22.3. Vorticity for a still (left) and a rotating (right) sphere.

22.4 Roberto Carlos: Reverse Magnus Effect?

At certain conditions what is known as the *reverse Magnus effect* has been noted for smooth spheres, with a force acting in the opposite direction of the rotation of the sphere.

This appears to be caused by transition in the boundary layer on one side of the sphere only, the side with the highest relative velocity, which leads to a delayed separation on that side, resulting in a shift of the wake toward the opposite direction as for the "regular" Magnus effect.

For a typical shot in football (soccer), the Reynolds number is of the order 10^5, thus in the region close to drag crisis. It is speculated in the reverse Magnus effect being involved in the famous free-kick of Brazil's Roberto Carlos against France in 1997 [17], where the ball initially seems

to be moving around the defenders away from the goal, before curving back to end up behind the stunned French goalkeeper Barthez.

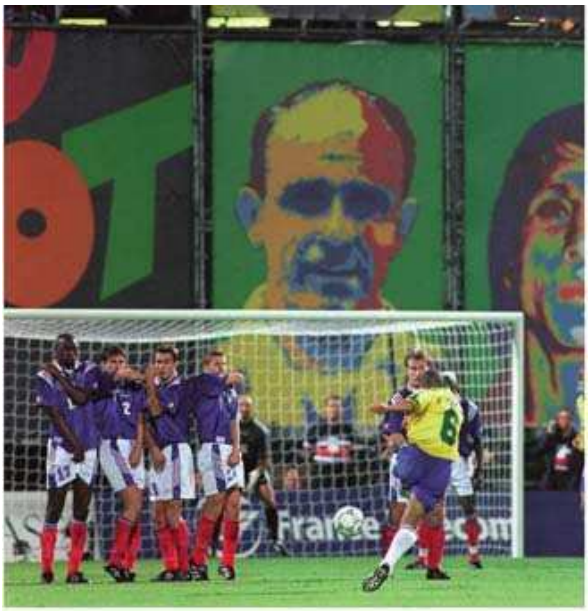

FIGURE 22.4. The Brazilian Roberto Carlos free-kick against France in 1997.

22.5 Pitch in Baseball

Baseball has received a lot of attention among fluid dynamicists, see e.g. [10, 5]. When the pitcher throws the ball, assuming no wind, the only forces acting on the ball in the air is gravity and the aerodynamic forces of lift and drag. Using different spins and velocities the pitcher has an arsenal of throws to challenge the batter.

For example, a *curveball* is thrown with a spin such that the axis of rotation is not perpendicular to the ground, rotating away from the pitcher, resulting in a Magnus force down and away from the batter.

A *knuckleball* is thrown with a very slow rotation and with a velocity corresponding to a flow near drag crisis. Transition to turbulence in parts of the boundary layer is triggered by the seams of the ball, whereas other parts of the boundary layer remain laminar, leading to slightly wobbling ball with a trajectory which is hard to predict by the batter.

23
Secrets of Flight

> The difficulties which obstruct the pathway to success in flying-machine construction are of three general classes: (1) Those which relate to the construction of the sustaining wings; (2) those which relate to the generation and application of the power required to drive the machine through the air; (3) those relating to the balancing and steering of the machine after it is actually in flight. (Wilbur Wright 1901)

In Fig. 23.1 we simulate take-off of an aircraft, by slowly increasing the angle of attack of a wing from 0 to 17 degrees, with stall at approximately 16 degrees. We clearly see the pressure difference over the wing leading to a lift force which increases with the angle of attack until the stall angle, where lift decreases for increasing angle of attack.

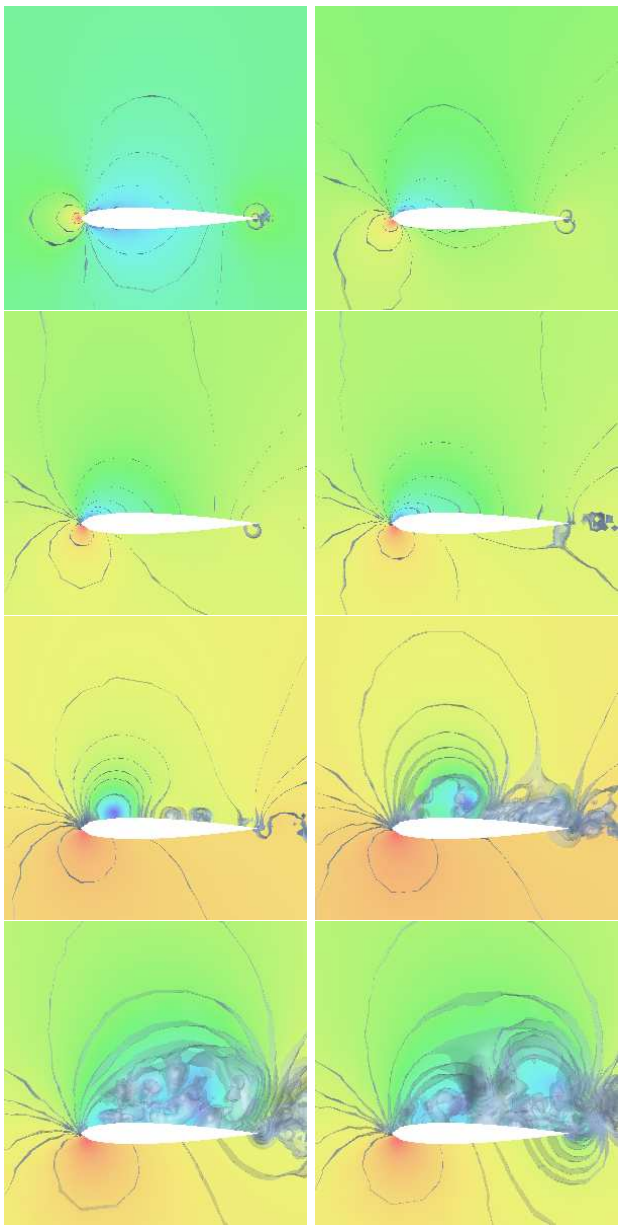

FIGURE 23.1. Simulation of take-off for a 3d wing using Euler/G2, with increasing angle of attack from 0 to 17 degrees.

24
Summary so far

My feeling is that many mathematicians and graduate students are intrigued by what they hear about problems of the mechanics of an incompressible fluid, but don't study them because they don't know enough physics and fear to make fools of themselves. What they don't know, I think, is how abysmally little we actually know about fluids, and how it would be hard to act more the fool than many have already done. I believe the difficulty arises first, over an inflated nomenclature that burdens the subject and, second, over a lack of understanding about how ignorant we can be in our technological society and how close to the surface many problems lie.... In spite of the profound mathematical methods we use to attack the problems, we know very little about fluids, we can tell the physicist almost nothing of what he wants to know, and interesting problems abound. (Marwin Shinbrot, 1973)

Our conciousness does not reflect the molecular chaos of the phenomena but exerts an integrating function with respect both space and time, from results the apparent homogeneity and continuity of the phenomena. (Weyl)

Blind fate could never make all the planets move one and the same way in orbs concentric. (Newton)

24.1 Outputs of ϵ-weak solutions

We have introduced the concept of ϵ-weak solutions to the NS equations. To estimate the difference in output of two ϵ-weak solutions $\hat{u}$ and $\hat{w}$,

$M(\hat{u}) - M(\hat{w})$, with $M(\hat{u}) \equiv ((\hat{u}, \hat{\psi}))$ defined by a function $\hat{\psi}$, we introduce a linearized dual problem with coefficients depending on u and w and estimate derivatives of the solution of the dual problem in a corresponding stability factor $S_\epsilon(\hat{\psi})$, to get

$$|M(\hat{u}) - M(\hat{w})| \leq 2\epsilon S_\epsilon(\hat{\psi}).$$

We next note that a G2-solution $\hat{U}$ is an $C_U\|hR(\hat{U})\|$-weak solution, and this way we obtain an a posteriori output error estimate of the form

$$|M(\hat{u}) - M(\hat{U})| \leq (\epsilon + C_U\|hR(\hat{U})\|)S_{\epsilon_{G2}}(\hat{\psi}),$$

with $S_{\epsilon_{G2}}(\hat{\psi})$ a corresponding stability factor, and $\epsilon_{G2} = C_U\|hR(\hat{U})\|$. Simplifying, assuming ϵ small (and $C_U \leq 1$), the a posteriori error estimate takes the form

$$|M(\hat{u}) - M(\hat{w})| \leq \|hR(\hat{U})\|S_0(\hat{\psi}), \tag{24.1}$$

and the corresponding stopping criterion would be

$$\|hR(\hat{U})\|S_0(\hat{\psi}) \leq TOL.$$

If the stability factor $S_0(\hat{\psi})$ is not too large and the tolerance TOL not too small, then we may be able to reach the stopping criterion with available computer power.

We have pointed out a basic feature of the a posteriori error estimate resulting from the properties of G2, namely the presence of the factor h multiplying the residual $R(\hat{U})$. If $S_0(\hat{\psi})$ is not too large, this means that we may reach the stopping criterion *without the residual* $R(\hat{U})$ *being pointwise small*. We may thus compute an accurate mean value output from a discrete solution with a pointwise large residual. In a turbulent flow we may expect (and actually see in computations) that pointwise $R(\hat{U}) \sim h^{-1/2}$. This evidence strongly indicates that the mere idea of a pointwise solution to a turbulent flow will have to be refuted. As already pointed out above, this is in direct opposition to the Clay Institute formulation of it's Prize Problem concerning existence, regularity and uniqueness of pointwise solutions to the NS equations.

24.2 Chaos and Turbulence

We have been led to the following essential aspects of a dynamical system with chaotic solutions such as the NS equations: (i) strong sensitivity of pointwise outputs, (ii) weak sensitivity of mean value outputs, and (iii) weak sensitivity of stability factors.

To identify these features for a given dynamical system, we would first compute one trajectory $u(t)$ pointwise. We would then solve the corresponding dual problem linearized at $u(t)$ with data corresponding to pointwise

output to find a large stability factor, and with data corresponding to a mean value output to find a stability factor which is not large. This would give evidence of (i) and (ii). In particular we would get the information that the mean value output would be insensitive to solution perturbations, and thus that we could expect to be able to compute the mean value output from only one solution trajectory.

There would be one piece of information missing, namely (iii) which represents insensitivity of the mean value stability factor to the choice of solution trajectory underlying the linearization in the dual problem. To get evidence of this insensitivity, we would have to compute a couple of different solutions $u(t)$ by introducing some perturbations and then solve the corresponding dual problems. The evidence would then be that the corresponding stability factors would be insensitive to the perturbations. In particular, we would get the signal that the more precise nature of the perturbations would be insignificant.

Below we will present evidence that turbulent flow has the features (i)-(iii) and thus carries the basic features of the type of chaos we suggest above.

The result is that a mean-value output may be observable/computable to a tolerance of interest under statistical perturbations of input of unknown nature, while a point value is not.

In a turbulent flow a lot of detailed information is destroyed in dissipation, which thermodynamically connects to a substantial increase of entropy. In order for a mean value in turbulent flow to be well defined, it cannot have other than a weak dependence on the destroyed information, and indeed we observe this to be a real phenomenon since we find mean value aspects of turbulent flow to be computable without resolving all details of the flow. Thus certain aspects of turbulent flows may be computable, in fact, sometimes more easily computable than laminar flows, which may show a stronger dependence on details.

This is in contrast to a conventional standpoint, where turbulent flow may seem to be uncomputable, without turbulence models which are difficult if not impossible to design. In this book thus we give concrete evidence that turbulent flow is computable, in fact often computable on a PC within hours.

We finally recall that we avoid introducing Reynolds stresses by avoiding taking mean values twice: Choosing a mean value output makes it unnecessary to average the NS equations. Avoiding Reynolds stresses also relieves us from modeling Reynolds stresses in turbulence models.

24.3 Computational Turbulence

We may say that the secret of computational turbulence is to understand how it may be possible to compute mean value outputs, while point-value outputs are not computable. We have noted that this can be exaplaind by the stability properties of the dual solution, which by cancellation effects is smaller for mean-value outputs than for point-values. Thus we may say that the secret lies in the cancellation in the dual problem, which may be observed to take place by simply computing the dual solution. We may also analyze the cancellation effect in simple model problems, but it seems impossible to mathematically analyze this cancellation effect in any realistic situation. Thus we may get a glimpse of the secret, but we seem to be unable to capture the whole truth by mathematical analysis. Our lifes may carry a similar secret: we may observe what we experience/compute as we go along and we may understand some aspects, but the full truth will remain hidden.

24.4 Irreversibility

We have unfolded the secret of irreversibility in reversible systems in the special case of incompressible inviscid flow governed by the Euler equations solved by G2. We have seen that the irreversibilty is a necessary consequence of the non-existence of stable pointwise solutions of the Euler equations and the dissipative nature of G2 when computing approximate solutions. We may phraze our result as a proof of the Second Law of Thermodynamics from the First Law (the Euler equations) combined with finite precision in the form of G2. We have remarked that Euler/G2 is a parameter-free mathematical model of (a part of) the World in the spirit of Einstein.

Part II

Computational Method: G2

25
G2 for Navier-Stokes Equations

> The scientist should listen to every reasonable suggestion, but judge objectively. He should not be biased by appearances; have a favorite hypothesis; be of a fixed school of thought; or have a master in matters of knowledge. He should remember constantly that the progress of knowledge if often hampered by the tyrannical influence of dogma. (G.A. Tokaty)

25.1 Introduction

We now proceed to present G2 applied to the NS equations in detail. G2 is a weighted least-squares stabilized Galerkin finite element method in space-time. G2 is adaptive with automatic choice of the mesh in space-time based on a posteriori error estimation of outputs with stability factors/weights obtained by solving linearized dual problems. The stabilization of G2 acts as an automatic turbulence model in the form of a generalized artificial viscosity model acting selectively on the smallest scales of the mesh.

G2 may be described as an *Adaptive DNS/LES* method, where adaptively the flow is resolved in DNS in certain parts of the domain and in other parts is underresolved in a LES with an automatic turbulence model. G2 may compute mean value outputs using LES in large parts of the domain such as the turbulent wake of a bluff body, and using DNS only to capture certain critical local flow features such as boundary layer separation and transition. The adaptive combination of LES and DNS in G2 opens for

a breakthrough in computational simulation of turbulent flow: With G2 Adaptive DNS/LES the number of mesh points may be orders of magnitude smaller than using non-adaptive or ad hoc refined meshes.

The a posteriori error estimation in G2 gives objective evidence that the basic idea of LES, which is to simulate turbulent flow on computational scales which are coarser than the actual physical scales using a relatively simple turbulence model, indeed is largely functional. The reason LES works couples to a cancellation effect in the associated dual problem allowing the residual of a G2 solution to be quite large in turbulent regions. Intuitively, LES may be motivated by the fact that the actual smallest scale of dissipation of turbulent energy may be insignificant for mean value outputs: it suffices to capture the correct level of the turbulent energy dissipation which can be done on coarser scales than the physical scales. Another signal to the same effect is that quantities such as drag may change very slowly with the Reynolds number over large intervals, which opens the possibility of correctly computing e.g. drag without fully resolving the flow thus computing with an effective Reynolds number which is smaller than the actual one.

Altogether, G2 offers a general flexible methodology for the discretization of the NS equations applicable to a great variety of flow problems from creeping viscous flow to slightly viscous turbulent flow, including free or moving boundaries.

25.2 Development of G2

Stabilized space-time finite element methods, including moving meshes, were developed by Hughes, Tezduyar, and Johnson, with co-workers, see e.g. [15, 56, 60, 36, 35].

A posteriori error estimation is traditionally done with respect to an *energy-norm*, naturally induced by the underlying differential operator, resulting in estimates in terms of computable residuals. For surveys and references on this approach we refer to [86, 4]. Although, in most applications the energy-norm does not provide useful bounds on the error in quantities of real physical interest. Another approach is to use duality arguments to obtain bounds on the error in other norms, such as the L_2-norm, or the error in various functionals of the solution, such as drag or lift forces for example. The idea of using duality arguments in a posteriori error estimation goes back to Babuška and Miller [6, 7, 8] in the context of postprocessing 'quantities of physial interest' in elliptic model problems.

A framework for more general situations has since then been systematically developed by Eriksson & Johnson and Becker & Rannacher, with coworkers, see e.g. [29, 27, 11, 12, 61, 62]. For an overview of adaptive finite element methods based on duality including references, we refer to the sur-

vey articles [27, 12, 34]. For incompressible flow, applications of adaptive finite element methods based on duality have been used to compute quantities of interest such as the drag force for stationary benchmark problems in [11, 33, 38, 14].

In [46] turbulent flow in 3d is first considered, and the extension of this framework to LES is investigated in [40]. The generalization to G2 for turbulent flow by Hoffman & Johnson is first presented in [51, 41, 52], with applications to flow around a surface mounted cube and a square cylinder, followed by other applications in [44, 42, 45, 43].

25.3 The Incompressible Navier-Stokes Equations

We start by recalling the incompressible Navier-Stokes (NS) equations expressing conservation of momentum and incompressibility of a unit density Newtonian fluid with constant kinematic viscosity $\nu > 0$ enclosed in a volume Ω in $\mathbb{R}^3$: Find $\hat{u} = (u, p)$ such that

$$\begin{aligned} \dot{u} + u \cdot \nabla u - \nu \Delta u + \nabla p &= f && \text{in } \Omega \times I, \\ \nabla \cdot u &= 0 && \text{in } \Omega \times I, \\ u &= w && \text{on } \partial\Omega \times I, \\ u(\cdot, 0) &= u^0 && \text{in } \Omega, \end{aligned} \tag{25.1}$$

where $u(x,t) = (u_i(x,t))$ is the velocity and $p(x,t)$ the pressure of the fluid at (x,t), and f, w, u^0, $I = (0,T)$, is a given driving force, Dirichlet boundary data, initial data and time interval, respectively. The quantity $\nu\Delta u - \nabla p$ represents the total fluid force (modulo the external force f), and may alternatively be expressed as

$$\nu \Delta u - \nabla p = \nabla \cdot \sigma(\hat{u}), \tag{25.2}$$

where $\sigma(\hat{u}) = (\sigma_{ij}(\hat{u}))$ is the *stress tensor*, with components $\sigma_{ij}(\hat{u}) = 2\nu\epsilon_{ij}(u) - p\delta_{ij}$, composed of the *stress deviatoric* $2\nu\epsilon_{ij}(u)$ with zero trace and an isotropic pressure: Here $\epsilon_{ij}(u) = (u_{i,j} + u_{j,i})/2$ is the *strain rate tensor*, with $u_{i,j} = \partial u_i/\partial x_j$, and δ_{ij} is the usual Kronecker delta, the indices i and j ranging from 1 to 3.

A Neumann type boundary condition, corresponding to the boundary stress being prescribed, takes the form $\sigma \cdot n = g$, where $(\sigma \cdot n)_i = \sum_j \sigma_{ij} n_j$ and $g = (g_i)$ is a given boundary stress with g_i the force component in the x_i-direction, and n is the unit outward normal to Γ.

We usually seek to normalize the reference velocity and length scale in (25.1) to be of unit size, in which case the Reynolds number $Re \approx \nu^{-1}$.

25.4 G2 as Eulerian cG(p)dG(q)

We now present G2 in the special case of Eulerian tensor product space-time meshes and extend below to Lagrangian and Arbitrary-Lagrangian-Eulerian (ALE) space-time meshes. We start by presenting G2 in the form cG(p)dG(q) with continuous polynomials of degree p is space and discontinuous polynomials of degree q in time.

Let $0 = t_0 < t_1 < ... < t_N = T$ be a sequence of discrete time steps with associated time intervals $I_n = (t_{n-1}, t_n]$ of length $k_n = t_n - t_{n-1}$ and space-time slabs $S_n = \Omega \times I_n$, and let $W_n \subset H^1(\Omega)$ be a finite element space consisting of continuous piecewise polynomials of degree p on a finite element mesh $\mathcal{T}_n = \{K\}$ on Ω of mesh size $h_n(x)$ with W_n^0 the functions in W_n vanishing on $\partial\Omega$. We introduce for $q \geq 0$ the following spaces of finite element functions defined on the slab S_n:

$$V_n^0 = \{v \in H^1(S_n)^3 : v(x,t) = \sum_{j=0}^{q} (t - t_n)^j U_j(x),\ U_j \in [W_n^0]^3\},$$

$$Q_n = \{q \in H^1(S_n) : q(x,t) = \sum_{j=0}^{q} (t_n - t_n)^j q_j(x),\ q_j \in W_n\},$$

and finally introduce the velocity space $V^0 = \prod_n V_n^0$ and the pressure space $Q = \prod_n Q_n$ defined on the union of space-time slabs.

We now define G2 for (25.1) with $w = 0$ in the form of cG(p)dG(q): Find $\hat{U} = (U, P) \in V^0 \times Q$, such that for $n = 1, 2, ..., N$,

$$(R(\hat{U}), \hat{v})_n + SD_\delta(\hat{U}; \hat{v})_n = 0, \tag{25.3}$$

for all $\hat{v} = (v, q) \in V_n^0 \times Q_n$, with the Galerkin term

$$\begin{aligned}(R(\hat{U}), \hat{v})_n \equiv &(\dot{U} + (U \cdot \nabla)U, v)_n - (P, \nabla \cdot v)_n + (q, \nabla \cdot U)_n \\ &+ (2\nu\epsilon(U), \epsilon(v))_n + ([U^{n-1}], v_+^{n-1}) - (f, v)_n,\end{aligned} \tag{25.4}$$

and the stabilizing weighted least squares term

$$SD_\delta(\hat{U}; \hat{v})_n \equiv (\delta_1(\bar{R}_1(U; \hat{U}) - f), \bar{R}_1(U; \hat{v}))_n + (\delta_2 \bar{R}_2(U), \bar{R}_2(v))_n, \tag{25.5}$$

where for $\hat{v} = (v, q)$

$$\begin{aligned}\bar{R}_1(w; \hat{v}) &= \dot{v} + w \cdot \nabla v + \nabla q - \nu\Delta v, \\ \bar{R}_2(w) &= \nabla \cdot w,\end{aligned} \tag{25.6}$$

with the Laplacian defined elementwise, $\delta_1 = \kappa_1(k_n^{-2} + |U|^2 h_n^{-2})^{-1/2}$ in the convection-dominated case $\nu < U h_n$ and $\delta_1 = \kappa_1 h_n^2$ otherwise, $\delta_2 = \kappa_2 h_n$

if $\nu < Uh_n$ and $\delta_2 = \kappa_2 h_n^2$ otherwise, with κ_1 and κ_2 positive constants of unit size, and

$$(v,w)_n = \int_{I_n} (v,w)\ dt,\ \ (v,w) = \sum_{K\in\mathcal{T}_n} \int_K v\cdot w\, dx,$$

$$(\epsilon(v),\epsilon(w)) = \sum_{i,j=1}^{3} (\epsilon_{ij}(v),\epsilon_{ij}(w)).$$

Further, $[v^n] = v_+^n - v_-^n$ is the jump across the time level t_n with $v_\pm^n$ the limit from right $(+)$ and left $(-)$ of $v(t)$ as $t \to t_n$, and we choose $U_-^0 \in V_1^0$ as an interpolant of u^0. In the case of Dirichlet boundary conditions the viscous term $(2\nu\epsilon(U),\epsilon(v))_n$ may equivalently occur in the form $(\nu\nabla U,\nabla v)_n = \sum_{i=1}^3 (\nu\nabla U_i,\nabla v_i)_n$.

25.5 Neumann Boundary Conditions

A Neumann boundary condition of the form $\sigma\cdot n = g$ on a part Γ_N of the boundary is implemented in variational form by restricting the functions in W_n^0 to vanish only where (homogeneous) Dirichlet conditions are imposed and supplementing the right hand side with an integral of $g\cdot v$ over Γ_N. This implements the Neumann boundary condition in weak form through the presence of the term $(-P,\nabla\cdot v)_n + (2\nu\epsilon(U),\epsilon(v))_n = (\sigma,\epsilon(v))_n$ on the left hand side, which when integrated by parts generates an integral over Γ_N of $(\sigma\cdot n)\cdot v$.

25.6 No Slip and Slip Boundary Conditions

The homogeneous Dirichlet velocity boundary condition $u = 0$ is referred to as a *no slip boundary condition* expressing that the fluid adheres to the boundary. A non homogeneous Dirichlet boundary condition, such as a given inflow velocity, is imposed in the velocity trial space for U, while the velocity test space is left unchanged with homogeneous Dirichlet boundary conditions.

A *slip boundary condition* corresponds to setting the normal component of the velocity $U\cdot n$ to zero at the boundary and models a boundary with neglible friction which the flow cannot penetrate.

25.7 Outflow Boundary Conditions

To simulate an outflow boundary condition we may use a Neumann condition with $g = 0$ corresponding to zero force at outflow as in outflow into

a large empty reservoir. If we let the viscous term appear variationally instead in the form $(\nu\nabla U, \nabla v)_n$, then the corresponding Neumann boundary condition (with $g = 0$) takes the form $\nu\nabla u \cdot n - pn = 0$. which acts as an approximate *transparent outflow boundary condition*, attempting to let the flow leave the domain with little obstruction (also referred to as a "do nothing" boundary condition [78]).

25.8 Shock Capturing

In extreme situations with very large velocity gradients, occuring e.g when a jet impinges on a wall, we may add residual dependent *shock-capturing artificial viscosity*, replacing ν by $\hat{\nu} = \max(\nu, \kappa_3|R(\hat{U})|h^2)$, where $R(\hat{U}) = \sum_{i=1}^4 R_i(\hat{U})$ with

$$\begin{array}{rcl} R_1(\hat{U}) & = & |\bar{R}_1(U;\hat{U}) - f|, \\ R_2(\hat{U}) & = & \nu D_2(U), \\ R_3(\hat{U}) & = & |[U^{n-1}]|/k_n \quad \text{on } S_n, \\ R_4(\hat{U}) & = & |\nabla \cdot U|, \end{array} \tag{25.7}$$

where

$$D_2(U)(x,t) = \max_{y\in\partial K}(h_n(x))^{-1}|[\frac{\partial U}{\partial n}(y,t)]| \tag{25.8}$$

for $x \in K$, with $[\cdot]$ the jump across the element edge ∂K, and κ_3 is a positive constant of unit size. $R_1(U,\hat{U}) + R_2(\hat{U})$ bounds the residual of the momentum equation, with the Laplacian term bounded by the second order difference quotient $D_2(U)$ arising from the jumps of normal derivatives across element boundaries. Note that $R_1(U,\hat{U})$ is defined elementwise and that with piecewise linears in space, the Laplacian ΔU is zero.

25.9 Basic Energy Estimate for cG(p)dG(q)

Choosing $\hat{v} = \hat{U}$ in (25.3), we obtain the following basic energy stability estimate for cG(p)dG(q) analogous to (15.2) (assuming $f = 0$):

$$\|U(\cdot,T)\|^2 + D_\nu(U,T) + \sum_{n=0}^{N-1}\|U_+^n - U_-^n\|^2 + SD_\delta(\hat{U};\hat{U}) = \|U^0\|^2. \tag{25.9}$$

If $q > 0$ then the term $SD_\delta(\hat{U};\hat{U})$ gives a weighted least squares control of the residual $R(\hat{U})$ of $\hat{U}$. In the case $q = 0$, the residual $R(\hat{U})$ is controlled by $SD_\delta(\hat{U};\hat{U})$ combined with the jump term giving weighted least squared control of the discrete time derivate $(U^n - U^{n-1})/k_n$. The momentum residual control is thus in the case $q = 0$ enforced by separatate control of a

discrete time derivative of U through the jump term combined with control of $(U \cdot \nabla U) + \nabla P - \nu \Delta U$ through the SD_δ-term.

Altogether, the basic energy estimate for cG(p)dG(q) gives control of $\|\sqrt{h}R(\hat{U})\|^2$ in terms of data, where h respresents the mesh size in space-time, which expresses a fundamental property of G2.

25.10 G2 as Eulerian cG(1)dG(0)

We now specialize to G2 in the form of cG(1)dG(0) with continuous piecewise linears in space ($p = 1$) and with piecewise constants in time ($q = 0$) corresponding to the backward Euler method for time-stepping. We thus seek an approximate velocity $U(x,t)$ such that $U(x,t)$ is continuous and piecewise linear in x for each t, and $U(x,t)$ is piecewise constant in t for each x. Similarly, we seek an approximate pressure $P(x,t)$ which is continuous piecewise linear in x and piecewise constant in t. Thus we seek $U^n \in V_n^0 = W_{0n}^3$ and $P^n \in Q_n = W_n$ for $n = 1, ..., N$, with

$$\begin{aligned} U(x,t) &= U^n(x) \quad x \in \Omega, \quad t \in (t_{n-1}, t_n], \\ P(x,t) &= P^n(x) \quad x \in \Omega, \quad t \in (t_{n-1}, t_n]. \end{aligned} \tag{25.10}$$

such that

$$\begin{aligned} &(\frac{U^n - U^{n-1}}{k_n}, v) + (U^n \cdot \nabla U^n + \nabla P^n, v + \delta_1(U^n \cdot \nabla v + \nabla q)) + (\nabla \cdot U^n, q) \\ &+ (\nu \nabla U^n, \nabla v) = (f^n, v + \delta_1(U^n \cdot \nabla v + \nabla q)) \quad \forall (v,q) \in V_n^0 \times Q_n. \end{aligned} \tag{25.11}$$

where $\delta_1 = \frac{1}{2}(k_n^{-2} + |U|^2 h_n^{-2})^{-1/2}$ in the convection-dominated case $\nu < U h_n$. Note that if $k_n \approx h_n/|U|$, which is a natural choice of time step respecting a CFL-condition, then $\delta_1 \approx h_n/|U|$. The stabilized form of the cG(1)dG(0) method is obtained by replacing v by $v + \delta_1(U^n \cdot \nabla v + \nabla q)$ in the terms $(U^n \cdot \nabla U^n + \nabla P^n, v)$ and (f^n, v). In principle, we should make the replacement throughout, but in the present case of the cG(1)dG(0), only the indicated terms get involved because of the low order of the approximations. The perturbation in the stabilized method is of size δ_1, and thus the stabilized method has the same order as the original method (first order in h if $k \sim h$).

Letting v vary in (25.11) while choosing $q = 0$, we get the discrete momentum equation:

$$\begin{aligned} &(\frac{U^n - U^{n-1}}{k_n}, v) + (U^n \cdot \nabla U^n + \nabla P^n, v + \delta_1 U^n \cdot \nabla v) \\ &+ (\nu \nabla U^n, \nabla v) = (f^n, v + \delta_1 U^n \cdot \nabla v) \quad \forall v \in V_n^0, \end{aligned}$$

and letting q vary while setting $v = 0$, we get the discrete pressure equation:

$$(\delta_1 \nabla P^n, \nabla q) = -(\delta_1 U^n \cdot \nabla U^n, \nabla q) - (\nabla \cdot U^n, q) + (\delta_1 f^n, \nabla q) \quad \forall q \in Q_n.$$

The backward Euler first order accurate time stepping in cG(1)dG(0) in general is too dissipative for time dependent flow at high Reynolds numbers, but may be used to solve stationary problems by time-stepping.

25.11 Eulerian cG(1)cG(1)

The cG(p)cG(q) method is a variant of cG(p)dG(q) using the continuous Galerkin method cG(q) in time instead of a discontinuous Galerkin method dG(q). With cG(1) in time the trial functions are continuous piecewise linear in time and the test functions piecewise constant in time. We now present G2 in the form of cG(1)cG(1) which is less dissipative than cG(1)dG(0), and which is the method used in for all problems presented in the book.

G2 in the form cG(1)cG(1) for (25.1) with $w = 0$ reads: For $n = 1, ..., N$, find $(U^n, P^n) \equiv (U(t_n), P(t_n))$ with $U^n \in V_0^n \equiv [W_0^n]^3$ and $P^n \in W^n$, such that

$$\begin{aligned}&((U^n - U^{n-1})k_n^{-1} + \bar{U}^n \cdot \nabla \bar{U}^n, v) + (2\nu\epsilon(\bar{U}^n), \epsilon(v)) - (P^n, \nabla \cdot v)\\ &+ (\nabla \cdot \bar{U}^n, q) + SD_\delta(\bar{U}^n, P^n; v, q) = (f, v) \quad \forall \hat{v} \in V_0^n \times W^n,\end{aligned} \tag{25.12}$$

where $\bar{U}^n = \frac{1}{2}(U^n + U^{n-1})$, and

$$SD_\delta(\bar{U}^n, P^n; v, q) \equiv (\delta_1(\bar{U}^n \cdot \nabla \bar{U}^n + \nabla P^n - f), \bar{U}^n \cdot \nabla v + \nabla q) + (\delta_2 \nabla \cdot \bar{U}^n, \nabla \cdot v). \tag{25.13}$$

This method corresponds to a second order accurate Crank-Nicolson time-stepping. We note that in the stabilizing SD_δ-term the time derivative $\dot{U}$ is missing, which is a consequence of the piecewise constancy of the test functions. This corresponds to a (small) inconsistency up to the term $\delta\dot{U}$. This inconsistency seems to be fully acceptable in the case of turbulent flow, since then the residual $R(\hat{U})$ anyway is not small.

25.12 Basic Energy Estimate for cG(1)cG(1)

To easily obtain an energy estimate for cG(1)cG(1), we assume that the nonlinear term $(\bar{U}^n \cdot \nabla \bar{U}^n, v)$ in fact appears in the form

$$\frac{1}{2}((\bar{U}^n \cdot \nabla \bar{U}^n, v) - (\bar{U}^n \cdot \nabla v, \bar{U}^n)),$$

which would be equivalent if $\bar{U}^n$ was divergence free. Choosing now $v = \bar{U}^n$ and $q = P$ on S_n in (25.12), we obtain (assuming $f = 0$):

$$\|U(\cdot,T)\|^2 + D_\nu(U,T) + SD_\delta(\hat{U};\hat{U}) = \|U^0\|^2. \tag{25.14}$$

As in the case of dG(0) the stabilizing term $SD_\delta(\hat{U};\hat{U})$ does not include the time derivative $\dot{U}$, but in this case there is no jump term to directly give control of $\dot{U}$. Instead we may obtain control of $\|\sqrt{h}\dot{U}\|^2$ in terms of $SD_\delta(\hat{U};\hat{U})$ by choosing $v = \dot{U}$ in the discrete momentum equation, and thus also cG(1)cG(1) includes the basic weighted least squares control of the residual $R(\hat{U})$ in G2.

25.13 Slip with Friction Boundary Conditions

Studied already by Navier [75] and Maxwell [73], the *slip with friction and penetration with resistance boundary condition* for a boundary Γ_{slfr} with normal n and two orthogonal tangential vectors τ_1, τ_2 takes the form

$$u \cdot n + \alpha\ n^T\sigma n = 0, \tag{25.15}$$

$$u \cdot \tau_k + \beta^{-1} n^T\sigma\tau_k = 0, \quad k = 1,2, \tag{25.16}$$

with the stress tensor $\sigma = \sigma(\hat{u})$, and where we use matrix notation with all vectors v being column vectors and the corresponding row vector is denoted v^T.

Here α is a penetration parameter and β is a friction parameter, both positive functions defined on the boundary. A no slip boundary condition corresponds to $(\alpha,\beta) \to (0,\infty)$, and a slip boundary conditions to $(\alpha,\beta) \to (0,0)$. By increasing β we increase the resistance at the boundary, and by increasing α we increase the penetration of the boundary.

We can implement (25.15)-(25.16) weakly by decomposing the test function v into components aligned with the normal and tangent directions:

$$v = (v \cdot n)n + \sum_{k=1}^{2}(v \cdot \tau_k)\tau_k, \tag{25.17}$$

see e.g. [58] for an algorithm for determining two linearly independent tangent vectors. We then have

$$\int_{\Gamma_{slfr}} (\sigma \cdot n) \cdot v\ ds = \int_{\Gamma_{slfr}} n^T\sigma n(v \cdot n) + \sum_{k=1}^{2} n^T\sigma\tau_k(v \cdot \tau_k)\ ds$$

$$= -\int_{\Gamma_{slfr}} \alpha^{-1}(u \cdot n)(v \cdot n) - \sum_{k=1}^{2} \beta(u \cdot \tau_k)(v \cdot \tau_k)\ ds. \tag{25.18}$$

The derivation of the weak formulation of (25.1) underlying the cG(1)cG(1) method (25.12) formally involves partial integration of (25.2), resulting in the term

$$(2\nu\epsilon(U^n),\epsilon(v)) - (P^n,\nabla\cdot v) = (\sigma(U^n,P^n),\epsilon(v)), \tag{25.19}$$

in the left hand side of (25.12), together with a surface integral

$$\int_{\Gamma_{slfr}} (\sigma(U^n,P^n)\cdot n)\cdot v\ ds. \tag{25.20}$$

This surface integral is zero in (25.12), since the test function $v \in V_0^n$ satisfies a homogeneous Dirichlet condition.

To implement the boundary conditions (25.15)-(25.16), we seek a solution $(U^n,P^n) \in [W^n]^3 \times W^n$ for $n = 1,...,N$, satisfying (25.12) for $(v,q) \in [W^n]^3 \times W^n$, with the surface integral (25.20) subtracted from the left hand side of (25.12). Substituting the surface integral by (25.18) then corresponds to a weak implementation of the boundary conditions (25.15)-(25.16). We here assume that there exists a unique solution to this problem.

We stress that one has to be careful when implementing this boundary condition; one needs to use normals and tangent vectors that are defined for each node in the mesh, not for each face (or edge in 2 dimensions). The reason is that in the case the boundary Γ_{slfr} is not a flat surface, the degrees of freedom in certain nodes will be forced to satisfy conditions in too many directions. For example, in the case of a slip condition with $(\alpha,\beta) = (0,0)$, the degrees of freedom in a node will be forced to satisfy a non penetration condition in several linearly independent directions, which may result instead in a no slip boundary condition.

By choosing $\hat{v} = \hat{U}$ in (25.12), we note that (25.18) corresponds to penalty terms for the L_2-norms of the normal and tangential components of the velocity at the boundary, with penalty parameters α^{-1} and β, and that the energy balance (15.6) is modified by adding the time integrals of the terms

$$\|\alpha^{-1/2}u\cdot n\|_{\Gamma_{slfr}} + \sum_{k=1}^{2} \|\beta^{1/2}u\cdot\tau_k\|_{\Gamma_{slfr}} \tag{25.21}$$

to the left hand side of (15.6).

We may also model friction with respect to a non zero velocity w at the boundary simply by changing $(u\cdot\tau_k)$ into $((u-w)\cdot\tau_k)$ in (25.18).

26
Discrete solvers

26.1 Fixed point iteration using multigrid/GMRES

To compute a G2 solution $\hat{U}$, we have to solve a nonlinear system of algebraic equations for each time-step. We now briefly discuss the solution of the nonlinear system of equations generated by cG(1)cG(1). We solve the system for (U^n, P^n) on slab S_n using fixed-point iteration with the convection velocity given by the previous iteration. Assuming the nodal values $(U^{n,j}, P^{n,j})$ in iteration j have been computed, we compute new nodal values $(U^{n,j+1}, P^{n,j+1})$ by solving a linearized version of G2 of the form:

$$\begin{aligned} AU^{n,j+1} + k_n BP^{n,j+1} &= k_n F^n, \\ -B^\top U^{n,j} + CP^{n,j+1} &= G^n, \end{aligned} \tag{26.1}$$

where $A = M_n + k_n N_n - k_n \nu \Delta_n$, where M_n is a mass matrix, the matrix N_n represents a discrete analog of the convection term with velocity $U^{n,j}$, Δ_n represents a discrete Laplacian, B is a discrete gradient, $B^\top$ a discrete divergence, $C = -\delta_1 \Delta_n$, and finally F^n and G^n represent terms given by data including U^{n-1}. We here first solve for $P^{n,j+1}$ in terms of $U^{n,j}$ in the second equation using a multigrid method, and then solve for $U^{n,j+1}$ in the first equation using GMRES. The resulting fixed point iteration converges under a CFL-condition (that is $\frac{U^n k_n}{h_n} < 1$ is small enough), and if also k_n/δ_1 is small enough. Since typically $\delta_1 \approx h_n/U^n$, convergence is thus achieved under a CFL-condition. In the typical applications of non-stationary high Reynolds number turbulent flow presented in this book,

convergence is usually obtained in a few iterations, assuming the CFL-condition is satisfied.

For further reading on solution algorithms for algebraic systems related to the discretization of NS equations, we refer to [85, 26].

27
G2 as Adaptive DNS/LES

> I came to realize that exaggerated concern about what others are doing can be foolish. It can paralize effort, and stifle a good idea. One finds that in the history of science almost every problem has been worked out by someone else. This should not discourage anyone from pursuing his own path. (Theodore von Kármán 1881-1963)

27.1 An a posteriori error estimate

We now derive an a posteriori error estimate for cG(1)cG(1) following the route layed out in Chapter 3 with a mean value output $M(\cdot)$ defined by a given function $\hat{\psi}$. Recalling (13.5) we can express the difference in output between two ϵ-weak solutions $\hat{u} = (u, p)$ and $\hat{w} = (w, r)$ as

$$M(\hat{u}) - M(\hat{w}) = ((R(\hat{u}), \hat{\varphi})) - ((R(\hat{w}), \hat{\varphi})), \tag{27.1}$$

where $((\cdot, \cdot))$ is a space-time inner product, $\hat{\varphi}$ is the solution to the dual problem (13.4) with data $\hat{\psi}$, and we define the output by

$$M(\hat{w}) \equiv ((\hat{w}, \hat{\psi})). \tag{27.2}$$

With $\hat{w} = \hat{U}$, where $\hat{U}$ is a cG(1)cG(1) solution given by (25.12), we may add (25.12) to (27.1), to get

$$M(\hat{u}) - M(\hat{U}) = ((R(\hat{u}), \hat{\varphi})) - ((R(\hat{U}), \hat{\varphi} - \hat{\Phi})) + \int_0^T SD_\delta(\hat{U}, \hat{\Phi})\, dt, \tag{27.3}$$

with $\hat{\Phi}$ a function in the test space of cG(1)cG(1), and the stabilizing form given by (25.13).

Assuming sufficient regularity of the dual solution $\hat{\varphi}$ to satisfy the requirements of Lemma 27.2 and Lemma 27.3 below, we obtain the following a posteriori error estimate of a space-time mean value output of the form (27.2):

Theorem 27.1 *If $\hat{U} = (U, P)$ solves (25.12), $\hat{u} = (u, p) \in \hat{W}_\epsilon$ is an ϵ-weak solution (with ϵ small), and $\hat{\varphi} = (\varphi, \theta)$ solves (13.4) with data $\hat{\psi}$, then we have the following error estimate for the output $M(\hat{u}) = ((\hat{u}, \hat{\psi}))$:*

$$
\begin{aligned}
|M(\hat{u}) - M(\hat{U})| \leq \epsilon S_\epsilon(\hat{\psi}) + \sum_{n=1}^{N} \{ & \int_{I_n} \sum_{K \in \mathcal{T}_n} |R_1(\hat{U})|_K \cdot \omega_1 \; dt \\
& + \int_{I_n} \sum_{K \in \mathcal{T}_n} |R_2(U)|_K \; \omega_2 \; dt + \int_{I_n} \sum_{K \in \mathcal{T}_n} R_3(U) \cdot \omega_3 \; dt \\
& + \int_{I_n} \sum_{K \in \mathcal{T}_n} |SD_\delta(\hat{U}; \hat{\varphi})_K| \; dt \; \}
\end{aligned}
$$

with the stability factor defined by $S_\epsilon(\hat{\psi}) \equiv \|\hat{\varphi}\|_{\hat{V}}$, and the strong residuals given by

$$
\begin{aligned}
R_1(\hat{U}) &= \dot{U} + (U \cdot \nabla)U + \nabla P - \nu \Delta U - f, \\
R_2(U) &= \nabla \cdot U, \\
R_3(U) &= \frac{1}{2} h_{n,K}^{-1/2} \max_{S \subset \partial K} (|[(\nu \nabla U)_1 \cdot n_S]|, ..., |[(\nu \nabla U)_3 \cdot n_S]|),
\end{aligned}
\tag{27.4}
$$

where $(M)_i$ denotes the i:th row of the matrix M, $SD_\delta(\cdot;\cdot)_K$ is a local version of the stabilizing form (25.13), and the dual weights are given by

$$
\begin{aligned}
\omega_1 &= C_{n,K}^k k_n |\dot{\varphi}|_{K,\infty} + C_{n,K}^h h_{n,K}^2 |D^2 \varphi|_K, \\
\omega_2 &= C_{n,K}^k k_n |\dot{\theta}|_{K,\infty} + C_{n,K}^h h_{n,K}^2 |D^2 \theta|_K, \\
\omega_3 &= C_{n,K}^k k_n h_{n,k}^{1/2} |\dot{\varphi}|_{\partial K \setminus \partial \Omega, \infty} + C_{n,K}^h h_{n,k}^2 |D^2 \varphi|_K,
\end{aligned}
$$

where $h_{n,K}$ is the diameter of element K in the mesh $\mathcal{T}_n$, D^2 measures second order derivatives with respect to x, and $C_{n,K}^h, C_{n,K}^k$ represent interpolation constants, $|w|_K \equiv (\|w_1\|_K, \|w_2\|_K, \|w_3\|_K)$ with $\|w\|_K = (w, w)_K^{1/2}$, and we let the dot denote the scalar product in $\mathbb{R}^3$.

The stability factor $S_\epsilon(\hat{\psi})$ and the dual weights ω_i here characterize output sensitivity of the output $M(\hat{u})$. In practise we approximate $S_\epsilon(\hat{\psi})$ and ω_i by computing solutions of the corresponding dual problem linearized at $\hat{U}$. Taking the linearization error into consideration, we should modify the definitions of $S_\epsilon(\hat{\psi})$ and ω_i by taking the maximum over all linearizations in the corresponding spaces of ϵ-weak functions.

In Chapter 30 we derive a posteriori error estimates for the error in computing a force acting on a body in a flow, which is a special case of Theorem 27.1 for a particular choice of weight function $\hat{\psi}$.

27.2 Proof of the a posteriori error estimate

To prove Theorem 27.1, we first use the definition of the ϵ-weak solution $\hat{u}$, to get

$$|((R(\hat{u}),\hat{\varphi}))| \leq \epsilon \|\hat{\varphi}\|_{\hat{V}}.$$

For the remaining terms in (27.3), we use partial integration to obtain a scalar product of the strong residuals (27.4) and an interpolation error in the dual solution. Integration by parts in the viscous term results in non zero boundary integrals over interior element boundaries $\partial K \setminus \partial\Omega$, for each t, since ∇U is piecewise constant in x over the elements, and thus discontinuous over interior element boundaries. This is not the case for the pressure term since the pressure is continuous in x over element boundaries, and so is the interpolation error $\varphi - \Phi$.

To estimate the element boundary integrals we use a standard finite element technique, where we first rewrite the sum of interior element boundary integrals as a sum of jumps of the form $[\nu\nabla U \cdot n_S]$ in normal derivative over all interior faces S in $\mathcal{T}_n$, with n_S being a globally defined unit normal vector associated with the face S. We then attribute half of the jump to each of the two elements sharing the face and rewrite the sum again over the elements $K \in \mathcal{T}_n$, to get

$$\begin{aligned}|M(\hat{u}) - M(\hat{U})| &\leq \epsilon S_\epsilon(\hat{\varphi}) + \sum_{n=1}^{N}\{|(\dot{U} + (U\cdot\nabla)U + \nabla P - \nu\Delta U - f, \varphi - \Phi)_n| \\ &+ |(\nabla\cdot U, \theta - \Theta)_n| + |\int_{I_n}\sum_{K\in\mathcal{T}_n}\int_{\partial K\setminus\partial\Omega}\frac{1}{2}[\nu\nabla U\cdot n_S]\cdot(\varphi-\Phi)\ ds\ dt| \\ &+ \int_{I_n}\sum_{K\in\mathcal{T}_n}|SD_\delta(\hat{U};\hat{\varphi})|\ dt\}.\end{aligned}$$

To estimate the interpolation error $\varphi - \Phi$ over the space-time domain $\Omega \times I_n$ we introduce $\bar{\varphi}$, a temporal average of φ over I_n, defined by

$$\bar{\varphi}(x) = \frac{1}{k_n}\int_{I_n}\varphi(x,s)\ ds. \tag{27.5}$$

Theorem 27.1 then follows from the following interpolation estimates:

27.3 Interpolation error estimates

Lemma 27.2 *For $(v,w) \in L_2(I_n;[L_2(\Omega)]^3 \times L_2(\Omega))$, $(\varphi,\theta) \in L_2(I_n;[H_0^2(\Omega)]^3 \times H^2(\Omega))$, with $(\dot\varphi,\dot\theta) \in \mathcal{C}(I_n;[L_2(\Omega)]^3 \times L_2(\Omega))$, and $(\Phi,\Theta) \in W_{0n}^3 \times W_n$ constant in time, we have*

$$|(v,\varphi-\Phi)_n| \le \int_{I_n} \sum_{K\in\mathcal{T}_n} |v|_K \cdot (C_{n,K}^k k_n |\dot\varphi|_{K,\infty} + C_{n,K}^h h_{n,K}^2 |D^2\varphi|_K)\ dt,$$

$$|(w,\theta-\Theta)_n| \le \int_{I_n} \sum_{K\in\mathcal{T}_n} |w|_K (C_{n,K}^k k_n |\dot\theta|_{K,\infty} + C_{n,K}^h h_{n,K}^2 |D^2\theta|_K)\ dt,$$

where $h_{n,K}$ is the diameter of element $K \in \mathcal{T}_n$, and D^2 measures second order derivatives with respect to x.

We prove the first inequality:

$$|(v,\varphi-\Phi)_n| \le |(v,\varphi-\bar\varphi)_n| + |(v,\bar\varphi-\Phi)_n| = I_1 + I_2.$$

Using the mean value theorem, with $\eta,\zeta \in I_n$, we get for $(x,t) \in \Omega \times I_n$ that

$$\varphi(x,t) - \bar\varphi(x) = \varphi(x,t) - \varphi(x,\zeta) = \dot\varphi(x,\eta)(t-\eta) \le C k_n \max_{\eta\in I_n} |\dot\varphi(x,\eta)|.$$

Cauchy-Schwarz inequality on each element gives

$$I_1 \le \int_{I_n} \sum_{K\in\mathcal{T}_n} |v|_K \cdot (C_{n,K}^k k_n \max_{\eta\in I_n} |\dot\varphi(\eta)|_K)\ dt.$$

For I_2, both $\bar\varphi$ and Φ are constant in time. We first use Cauchy-Schwarz inequality on each element, and then a standard interpolation estimate in x of the form $\|h_{n,K}^{-2}(\bar\varphi_i - \Phi_i)\|_K \le C\|D^2\varphi_i\|_K$, for each $t \in I_n$, to get

$$I_2 \le \int_{I_n} \sum_{K\in\mathcal{T}_n} |v|_K \cdot (C_{n,K}^h h_{n,k}^2 |D^2\varphi|_K)\ dt.$$

The proof of the second inequality in the lemma is similar to the proof of the first inequality.

Lemma 27.3 *For $w \in L_2(I_n;[L_2(\Omega)]^3)$, $\varphi \in L_2(I_n;[H_0^2(\Omega)]^3)$, $\dot\varphi \in \mathcal{C}(I_n;[H^1(\Omega)]^3)$, and $\Phi \in W_{0n}^3$ constant in time, we have*

$$\begin{aligned}
&|\int_{I_n} \sum_{K\in\mathcal{T}_n} \int_{\partial K\setminus\partial\Omega} w\cdot(\varphi-\Phi)\ ds\ dt| \\
&\le \int_{I_n} \sum_{K\in\mathcal{T}_n} |w|_{\partial K\setminus\partial\Omega} \cdot (C_{n,K}^k k_n |\dot\varphi|_{\partial K\setminus\partial\Omega,\infty} + C_{n,K}^h h_{n,k}^{3/2} |D^2\varphi|_K)\ dt,
\end{aligned}$$

where $h_{n,K}$ is the diameter of element $K \in \mathcal{T}_n$, and D^2 measures second order derivatives with respect to x.

We have

$$|\int_{I_n}\sum_{K\in\mathcal{T}_n}\int_{\partial K\setminus\partial\Omega} w\cdot(\varphi-\Phi)\ ds\ dt| \le |\int_{I_n}\sum_{K\in\mathcal{T}_n}\int_{\partial K\setminus\partial\Omega} w\cdot(\varphi-\bar\varphi)\ ds\ dt|$$
$$+|\int_{I_n}\sum_{K\in\mathcal{T}_n}\int_{\partial K\setminus\partial\Omega} w\cdot(\bar\varphi-\Phi)\ ds\ dt| = I_1+I_2.$$

For I_1 we use the Cauchy-Schwarz inequality for each element, then (27.6), to get

$$I_1 \le \int_{I_n}\sum_{K\in\mathcal{T}_n} |w|_{\partial K\setminus\partial\Omega}\cdot(C^k_{n,K}k_n\max_{\eta\in I_n}|\dot\varphi(\eta)|_{\partial K\setminus\partial\Omega})\ dt.$$

I_2 is estimated by the Cauchy-Schwarz inequality for each element, and the standard interpolation estimate $\|h_{n,K}^{-3/2}(\bar\varphi_i-\Phi_i)\|_{\partial K\setminus\partial\Omega}\le C\|D^2\varphi_i\|_K$, for each $t\in I_n$, to get

$$I_2 \le \int_{I_n}\sum_{K\in\mathcal{T}_n} |w|_{\partial K\setminus\partial\Omega}\cdot(C^h_{n,K}h^{3/2}_{n,k}|D^2\varphi|_K).$$

27.4 G2 as Adaptive DNS/LES

To formulate an adaptive algorithm for G2 for a given output, we start from the a posteriori error estimate given by Theorem 27.1 written in the form:

$$|M(\hat u)-M(\hat U)| \le \sum_{K\in\mathcal{T}_k}\mathcal{E}_K \equiv \sum_{K\in\mathcal{T}_k} e^K_{D,h}+e^K_{M,h} \equiv e_{D,h}+e_{M,h}, \quad (27.6)$$

where $e_{D,h}$ represents the discretization error from the Galerkin part of G2, and $e_{M,h}$ represents a modeling error from the stabilization in G2. We here assume that the error contribution from the ϵ-weak solution $\hat u$ is neglible compared to $e_{D,h}+e_{M,h}$.

The adaptive algorithm, which we refer to as *Adaptive DNS/LES*, can now be formulated as follows:

Algorithm 27.1. [Adaptive DNS/LES]. Given an initial coarse computational space mesh $\mathcal{T}^0$, start at $k=0$, then do

(1) Compute approximation to the primal problem using $\mathcal{T}^k$.

(2) Compute approximation to the dual problem using $\mathcal{T}^k$.

(3) If $\sum_{K\in\mathcal{T}_k}\mathcal{E}^k_K < \text{TOL}$ then STOP, else:

(4) Mark a fraction of the elements in $\mathcal{T}^k$ for refinement, based on the size of $\mathcal{E}^k_{K,h}$.

(5) Refine the mesh $\mathcal{T}^k$ using a standard mesh refinement algorithm, which gives a new refined mesh $\mathcal{T}^{k+1}$.

(6) Set $k = k + 1$, then goto (1).

By refining the mesh size h, also the time step k and the stabilization SD_δ are refined implicitly, since both k and δ depend on h. The stabilization may thus be thought of as being implicitly modified as we refine the mesh. But the a posteriori error estimates also allow for a direct adaptive modification of both the time step k and the stabilization SD_δ, by locally refining k and δ, respectively.

There are many potential optimizations of the adaptive algorithm, such as using dynamically changing meshes, adaptively refining the order of the approximation spaces in *hp-methods* [38], adaptively refined time steps, and using techniques of *multi adaptivity* [70], with adaptive choice of different time steps in different parts of the domain.

A pertinent question in this context is the choice of the parameter δ in the SD_δ-term. The rule is to choose $\delta(x) \sim h(x)$, but how do we know that this is correct? It is in fact possible to choose δ to be larger, at the expense of possibly having to refine more to decrease in particular the modeling error $e_{M,h}$. However, choosing δ smaller eventually makes the numerics explode and the discretization error $e_{D,h}$ becomes large. We are thus lead to adaptively choosing δ so that both $e_{D,h}$ and $e_{M,h}$ are small, or more generally to adaptively choose the form of the stabilization SD_δ, as a form of *adaptive modeling*.

Also, the efficiency of the algorithm depend on how large fraction of the elements that are refined at each step. If we refine few elements each iteration, we may expect to avoid unnecessary refinement in areas not so crucial for the output error, but on the other hand we risk to end up with an unnecessary large number of iterations. In the computations below we usually refine a fraction of about 5%-30% of the elements in each iteration.

27.5 Computation of multiple output

Often one is interested in several different output from one single computation. The objective is then to construct an adaptive method to control the errors in all the different output, and there are various ways to achieve this. Assuming we are interested in a number of different output $M_k(\hat{u}) \equiv ((\hat{u}, \hat{\psi}_k))$, with $k = 1, ..., N$, we first note that to evaluate the sum of the errors $\sum_k |M_k(\hat{u}) - M_k(\hat{U})|$, the straight forward way is to use the linearity of the dual problem (13.4) to compute solutions $\hat{\varphi}_k$ to the

corresponding N dual problems

$$a(\hat{u}, \hat{U}; \hat{v}, \hat{\varphi}_k) = ((\hat{v}, \hat{\psi}_k)), \quad \forall \hat{v} \in \hat{V}_0.$$

Although, with N large this could be quite expensive. A cheaper way is to instead compute the error $\hat{e} = \hat{u} - \hat{U}$ from the *error equation*

$$a(\hat{u}, \hat{U}; \hat{e}, \hat{w}) = ((R(\hat{U}), \hat{w})), \quad \forall \hat{w} \in \hat{V}_0, \tag{27.7}$$

with the $R(\hat{U})$ the residual defined by (4.1). The error equation (27.7) is independent of k, and we can then evaluate the error in each output M_k from the scalar product with the corresponding data $\hat{\psi}_k$, that is

$$M_k^{err} = M_k(\hat{u}) - M_k(\hat{U}) = M_k(\hat{e}) = ((\hat{e}, \hat{\psi}_k)).$$

For adaptive mesh refinement we need error indicators for each element individually, which is not possible to obtain only from the error M_k^{err}. Using the linearity of the dual problem we note that we obtain the sum of the output errors M_k^{err} as

$$\sum_k M_k^{err} = \sum_k M_k(\hat{u}) - M_k(\hat{U}) = ((R(\hat{U}), \hat{\varphi} - \hat{\Phi})) + \int_0^T SD_\delta(\hat{U}; \hat{\Phi})\, dt, \tag{27.8}$$

where $\hat{\varphi}$ is the solution to a dual problem with data $\sum_k \hat{\psi}_k$. Now, if we know the signs of the errors M_k^{err}, we may use this to avoid cancellation in (27.8) by using the linearity of the dual problem to get

$$\sum_k |M_k^{err}| = \sum_k (\text{sgn } M_k^{err}) M_k^{err} = ((R(\hat{U}), \hat{\varphi} - \hat{\Phi})) + \int_0^T SD_\delta(\hat{U}; \hat{\Phi})\, dt, \tag{27.9}$$

where $\hat{\varphi}$ now is the solution to a dual problem with data $\sum_k (\text{sgn } M_k^{err}) \psi_k$. One approach is then to solve the error equation (27.7), see [37], from which sgn M_k^{err} can be obtained.

27.6 Mesh refinement

In each step of the adaptive algorithm a certain fraction of the elements are marked for refinement. Depending on the geometry of the elements in the mesh, various algorithms are avaliable for refining the mesh.

For example, in the case of a tetrahedral mesh, one may choose to subdivide each marked tetrahedron into 8 new smaller tetrahedrons, which may correspond to subdividing each triangular element face into 4 new triangles. This type of regular subdivision is not unique, and there are different ways to choose which way to subdivide. In addition, to avoid so called *hanging*

nodes, one has to refine an additional number of tetrahedrons neighboring the marked elements.

The design and analysis of mesh refinement algorithms is an active area of research that we will not go into further in this book. The algorithms used for the computations in this book are described at the *FEniCS* homepage: (`http://www.fenics.org`).

28
Implementation of G2 with FEniCS

G2 methods for various differential equations, including the NS equations, are implemented in FEniCS.

FEniCS was initiated in 2003 by research groups at Chalmers University, University of Chicago and Toyota Technological Institute at Chicago including Johan Hoffman, Claes Johnson, Robert Kirby, Anders Logg, Ridgway Scott and others. FEniCS builds on the earlier DOLFIN project by Hoffman and Logg [55], and Analysa by Scott [9]. FEniCS can be freely downloaded from the project homepage: `http://www.fenics.org`.

FEniCS is organized as a collection of sub projects/components, with DOLFIN [2] being the C++ interface of FEniCS, providing a consistent PSE (Problem Solving Environment) for solving ordinary and partial differential equations. In addition, a Python interface PyDOLFIN is also available.

FEniCS currently hosts the following independent projects:

- *FFC* FEniCS Form Compiler: translates a differential equation in mathematical notation into efficient computer code for element stiffness matrices.
- *FIAT*: computes finite element basis functions.
- *FErari*: optimizes computation of element stiffness matrices.
- *Ko*: automates the simulation of mechanical systems.
- *Sieve*: data structures for parallel representation of meshes.

- *DOLFIN*: applications master program

Linear algebra in FEniCS uses *PETSc* [3].

Features of DOLFIN today include: a simple, consistent and intuitive object-oriented API, automatic and efficient evaluation of variational forms through FFC, automatic and efficient assembly of linear systems, support for general families of finite elements, including continuous and discontinuous Lagrange finite elements of arbitrary order on triangles and tetrahedra through FIAT, support for arbitrary mixed elements, including Taylor-Hood, high-performance parallel linear algebra through PETSc with simple C++ wrappers, triangular and tetrahedral meshes, including adaptive mesh refinement and mesh hierarchies, multi-adaptive mcG(q)/mdG(q) and mono-adaptive cG(q)/dG(q) ODE solvers, and support for a range of output formats for post-processing, including DOLFIN XML, MATLAB, Octave, OpenDX, GiD, Tecplot and Paraview/VTK.

The method cG(1)cG(1) presented in Chapter 25 is implemented in DOLFIN as a module, including demo examples.

We refer to the FEniCS homepage (`http://www.fenics.org`) for an up to date account of FEniCS and the various components.

29
Moving Meshes and ALE Methods

29.1 Introduction

The space-time formulation of G2 naturally opens the possibilty of allowing the space mesh to move in time in *Lagrangian* or *Arbitrary Lagrangian Eulerian (ALE)* methods, as generalizations of the Eulerian method presented in Chapter 25 with the space mesh being fixed in time. Letting the nodes of the space mesh move with the fluid velocity corresponds to a Lagrangian *Characteristic Galerkin method*, while moving the space nodes with a different velocity gives an ALE method. G2 as ALE thus includes both Eulerian and Lagrangian methods as special cases.

Lagrangian or ALE methods are useful to handle problems with free or moving boundaries where the geometry in space changes with time. In such problems the space-time mesh may change continuously in time by letting the boundary nodes move according to specification and letting the internal nodes follow in ALE using *mesh smoothing*, combined with occasional remeshing with projection into the new mesh to avoid too strong mesh distortion.

29.2 G2 formulation

We consider the incompressible NS equations on a general space-time domain $Q = \{(x,t) : x \in \Omega(t), t \in I = (0,T]\}$, with the space domain $\Omega(t)$

with boundary $\Gamma(t)$ occupied by the fluid at time t changing with t:

$$\begin{aligned} \dot{u} + (u\cdot\nabla)u - \nu\Delta u + \nabla p &= f && \text{in } Q,\\ \nabla\cdot u &= 0 && \text{in } Q,\\ u(\cdot,0) &= u_0 && \text{in } \Omega(0), \end{aligned} \tag{29.1}$$

combined with boundary conditions on $\Gamma(t)$ for $t \in I$ modeling a free boundary or a boundary with prescribed motion. We start by assuming $\Gamma(t)$ has a prescribed motion given by a prescribed velocity u on $\Gamma(t)$, and we return to the case of a free boundary below.

To define G2 for (29.1) let $0 = t_0 < t_1 < ... < t_N = T$ be a sequence of discrete time steps with associated time intervals $I_n = (t_{n-1}, t_n]$ of length $k_n = t_n - t_{n-1}$ and define the space-time slabs $S_n = \{(x,t) \in Q : t \in I_n\}$. Let $W_n \subset H^1(\Omega(t_{n-1}))$ be a finite element space consisting of continuous piecewise polynomials of degree p on a mesh $\mathcal{T}_n = \{K\}$ of mesh size $h_n(x)$. Let for a given velocity field β on S_n satisfying the velocity boundary condition, the particle paths $x(\bar{x},\bar{t})$ be defined by

$$\begin{aligned} \frac{dx}{d\bar{t}} &= \beta(x,\bar{t}) \quad \bar{t} \in I_n,\\ x(\bar{x},t_n) &= \bar{x}, \quad \bar{x} \in \Omega(t_{n-1}), \end{aligned} \tag{29.2}$$

and introduce the corresponding mapping $F_n^\beta : \bar{S}_n \to S_n$ defined by $(x,t) = F_n^\beta(\bar{x},\bar{t}) = (x(\bar{x},\bar{t}),\bar{t})$, where $x = x(\bar{x},\bar{t})$ satisfies (29.2), and $\bar{S}_n = \Omega(t_{n-1})\times I_n$. Define for a given $q \geq 0$, the spaces

$$\bar{V}_n^\beta = \{\bar{v} \in H^1(\bar{S}_n)^3 : \bar{v}(\bar{x},\bar{t}) = \sum_{j=0}^{q} (\bar{t}-t_n)^j U_j(\bar{x}),\ U_j \in [W_n]^3\},$$

$$\bar{Q}_n^\beta = \{\bar{q} \in H^1(\bar{S}_n) : \bar{q}(\bar{x},\bar{t}) = \sum_{j=0}^{q} (\bar{t}_n-t_n)^j q_j(\bar{x}),\ q_j \in W_n\},$$

together with their analogs in (x,t)-coordinates:

$$V_n^\beta = \{v : \bar{v} \in \bar{V}_n^\beta\}, \qquad Q_n^\beta = \{q : \bar{q} \in \bar{Q}_n^\beta\}, \tag{29.3}$$

where $v(x,t) = \bar{v}(\bar{x},\bar{t})$ and $q(x,t) = \bar{q}(\bar{x},\bar{t})$ and $(x,t) = F_n^\beta(\bar{x},\bar{t})$.

Defining finally $V^\beta \times Q^\beta = \prod_n V_n^\beta \times Q_n^\beta$, we can now formulate the G^2-method as a generalization of (25.3) as follows: Find $\hat{U} = (U,P) \in V^\beta \times Q^\beta$ satisfying the boundary conditions, such that for $n = 1, 2, ..., N$,

$$\begin{aligned} &(\dot{U} + (U\cdot\nabla)U, v)_n - (P, \mathrm{div}\, v)_n + (q, \mathrm{div}\, U)_n + (2\nu\epsilon(U), \epsilon(v))_n\\ &+ SD_\delta(\hat{U};\hat{v})_n + ([U^{n-1}], v_+^{n-1}) = (f,v)_n \quad \forall \hat{v} = (v,q) \in V_{0n}^\beta \times Q_n^\beta, \end{aligned} \tag{29.4}$$

where V_{0n}^β satisfies homogeneous Dirichlet boundary conditions, and

$$SD_\delta(\hat{U};\hat{v})_n \equiv (\delta_1(a(U;U,P) - f), a(U;v,q))_n + (\delta_2 \mathrm{div}\, U, \mathrm{div}\, v)_n \tag{29.5}$$

where $a(w;v,q) = \dot{v} + w \cdot v + \nabla q - \nu\Delta v$ with the Laplacian defined elementwise, $\delta_1 = \kappa_1(k_n^{-2} + |U|^2 h_n^{-2})^{-1/2}$ in the convection-dominated case $\nu < Uh_n$ and $\delta_1 = \kappa_1 h_n^2$ otherwise, $\delta_2 = \kappa_2 h_n$ if $\nu < Uh_n$ and $\delta_2 = \kappa_2 h_n^2$ otherwise, with κ_1 and κ_2 positive constants of unit size, and $(\cdot,\cdot)_n$ indicates integration over S_n.

The Eulerian version of G2 is obtained choosing $\beta = 0$, which means that the mesh does not move in time. G2 in the form of a *characteristic Galerkin method* is obtained by choosing $\beta = U$ which means that the mesh moves with the computed fluid velocity. Choosing β differently gives various ALE-methods, with the mesh and particle velocity being (partly) different; for example we may move the mesh with the particle velocity at a free boundary, while allowing the mesh to move differently inside the domain. In extreme situations with very large velocity gradients, we may add residual dependent shock-capturing artificial viscosity as in the Eulerian formulation (25.3). G2 for *Stokes equations* is obtained by omitting the nonlinear terms $(U \cdot \nabla)U$ and $(U \cdot \nabla)v$, and setting $\delta_1 = \kappa_1 h^2$, $\delta_2 = \kappa_2 h^2$.

Since in the local Lagrangean coordinates $(\bar{x}, \bar{t})$ on each slab S_n with $\beta = U$,

$$\frac{\partial \bar{U}}{\partial \bar{t}} \equiv \frac{\partial}{\partial \bar{t}} U(x(\bar{x},\bar{t}),\bar{t}) = \dot{U} + U \cdot \nabla U,$$

the convection term $U \cdot \nabla U$ effectively dissappears in the characteristic Galerkin method, when expressed in the characteristic coordinates $(\bar{x}, \bar{t})$, and thus the discrete equations on each time step effectively correspond to a Stokes problem, choosing $\delta_1 = \kappa_1 h_n^2$.

29.3 Free boundary

A *free boundary* $\Gamma(t)$ has homogeneous Neumann boundary conditions corresponding to zero boundary stress and moves with the velocity of the fluid. The velocity on a free boundary is thus not specified but free to vary in the variational formulation of G2. We also add a least squares stabilization of the discrete boundary stress to the left hand side of the G2 formulation (29.5), of the form

$$< \delta_3 \ \sigma(u,p) \cdot n, \sigma(v,q) \cdot n >_n, \tag{29.6}$$

where

$$< v, w >_n = \int_{I_n} \int_{\Gamma(t)} v \cdot w \ ds \ dt, \tag{29.7}$$

29.4 Laplacian Mesh Smoothing

In ALE methods with the mesh velocity and fluid velocity possibly being different, we may use various techniques of mesh modification to guarantee that the space mesh does not get tangled or too distorted with negative effects on conditioning of the discrete equations and on interpolation accuracy. In *mesh smoothing* the nodes of the mesh are moved in order to improve a certain mesh quality measure, without changing the connectivity of the mesh.

Laplacian mesh smoothing is based on solving a discrete Laplacian equation representing a spring model of the mesh, or on a diffusion model possibly with a variable diffusion coefficient. In its simplest form Laplacian mesh smoothing amounts to an iteration over the nodes in the mesh, where each node is moved to the geometric center of its neighbors.

Laplacian mesh smoothing is suitable when small deformations of the mesh suffice to improve the quality. In Section 29.6 we present a different mesh modification strategy which can handle the large deformations arising in the case of moving objects.

29.5 Mesh Smoothing by Local Optimization

We also present a mesh smoothing algorithm, where for each node we optimize the shape of the tetrahederons surrounding the node. A point $x = (x_1, x_2, x_3)$ in a tetrahedron E can be written as a linear combination of the coordinates $p = (p_1, ..., p_4)$ of the nodes $(N_1, ..., N_4)$ of E using *barycentric coordinates* $a = (a_1, ..., a_4)$, as follows

$$x = a_1 p_1 + ... + a_4 p_4, \tag{29.8}$$

with $a_1 + ...a_4 = 1$. We can express the barycentric coordinates a of x in the form

$$a = Ax + b, \tag{29.9}$$

where A is a 4×3 matrix. We now aim to minimize the cost functional $\mathcal{F}(N)$, given by

$$\mathcal{F}(N) = \sum_{E \in \mathcal{E}(N)} \kappa(A^T A), \tag{29.10}$$

for node N, where $\mathcal{E}(N)$ are the elements that contain the node N and $\kappa(A^T A)$ is the condition number of the 3×3 matrix $A^T A$. This loosely corresponds to minimizing the difference between the elements E and the equilateral reference element.

We now seek the entries of the matrix A. We denote by n_i the outward normal vector corresponding to the face opposite the local node N_i, given

by any pairwise vector product of edge vectors on this face. The following equality

$$(x - p_i) \cdot \frac{n_i}{c_i} = (1 - a_i) = \begin{cases} 0 & x = p_i, \\ 1 & x = p_j, j \neq i, \end{cases} \tag{29.11}$$

gives the entries of matrix A in (29.9) as

$$\begin{array}{l} a_1(x) = (-\frac{n_1}{c_1}) \cdot x + (1 + p_1 \cdot \frac{n_1}{c_1}), \\ a_2(x) = (-\frac{n_2}{c_2}) \cdot x + (1 + p_2 \cdot \frac{n_2}{c_2}), \\ a_3(x) = (-\frac{n_3}{c_3}) \cdot x + (1 + p_3 \cdot \frac{n_3}{c_3}), \\ a_4(x) = (-\frac{n_4}{c_4}) \cdot x + (1 + p_4 \cdot \frac{n_4}{c_4}), \end{array} \tag{29.12}$$

where

$$\begin{array}{l} c_1 = (p_2 - p_1) \cdot n_1, \\ c_2 = (p_1 - p_2) \cdot n_2, \\ c_3 = (p_1 - p_3) \cdot n_3, \\ c_4 = (p_1 - p_4) \cdot n_4. \end{array} \tag{29.13}$$

Based on the cost functional $\mathcal{F}(N)$ there are various ways to set up a minimization algorithm. For example, we may use the following algorithm: *For* $k = 0$ *and* $\mathcal{S} = \{$all free nodes in the mesh$\}$*, do*

(1) If $k =$ max no iterations *STOP, else*

(2) Find node $N \in \mathcal{S}$ *with largest cost functional* $\mathcal{F}(N)$

(3) Find coordinates of N *that minimize the cost functional* $\mathcal{F}(N)$

(4) Remove N *from* $\mathcal{S}$

(5) Goto (1)

To minimize $\mathcal{F}(N)$ we may use a Conjugate gradient method, where we, for example, use the QR-algorithm to find the eigenvalues of $A^T A$ in the evaluation of the cost functional $\mathcal{F}(N)$.

To illustrate the method we consider a simple example with a flat 3d object that we rotate slightly in a tetrahedral mesh, see Figure 29.1. We find that after only a few iterations the maximal condition numbers are reduced by a factor 10, through moving the nodes with the highest cost functional.

In Figure 29.2 we rotate the flat object $\pi/4$ radians, where we find that for this large deformation the Laplacian mesh smoothing is not enough to ensure geometric quality of the elements in the mesh. Again we find that a few iterations of the local smoothing algorithm significally improves the mesh quality.

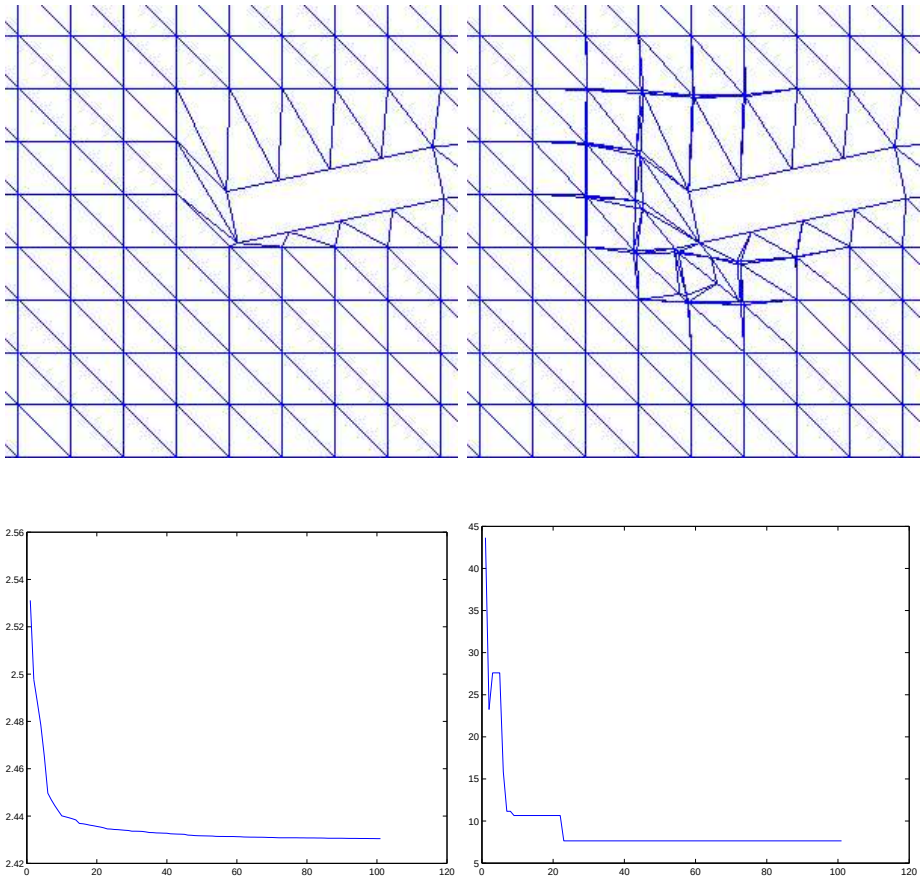

FIGURE 29.1. Locally distorted mesh before (upper left) and after (upper right), 100 iterations of the local optimization algorithm. The weighted l_2-norm (lower left) and the max-norm (lower right), of the square root of the condition numbers of $A^T A$ as functions of number of iterations.

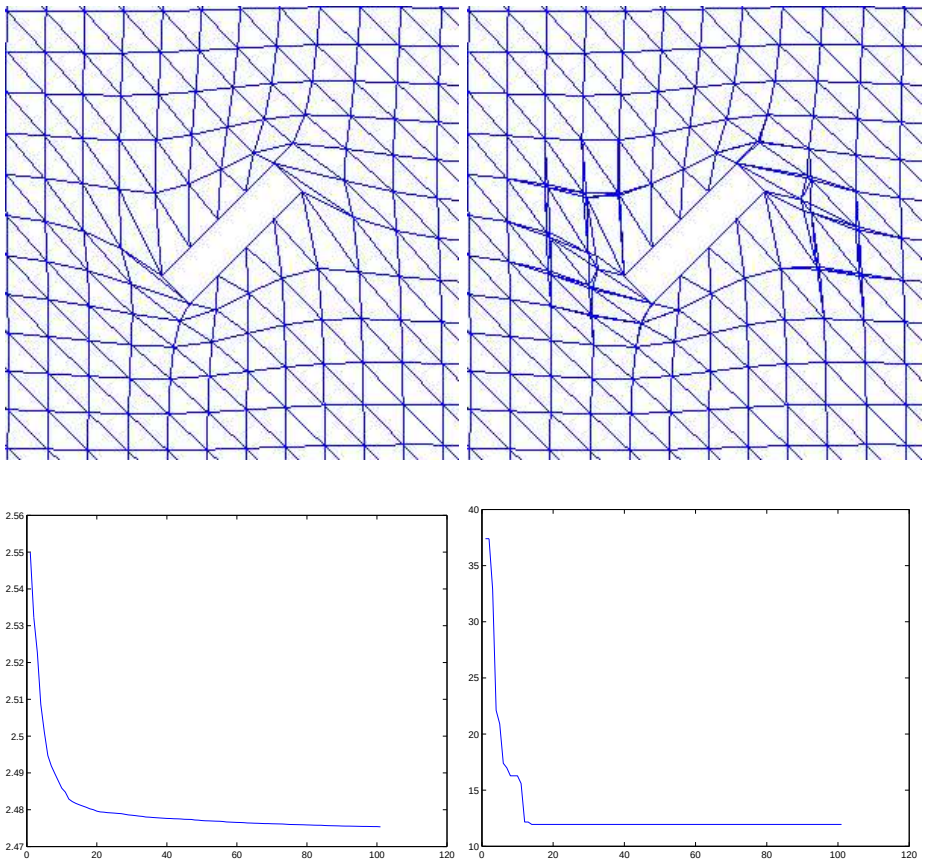

FIGURE 29.2. Rotated object mesh before (upper left) with Laplacian mesh smoothing, and after 100 iterations of the local optimization algorithm (upper right). The weighted l_2-norm (lower left), and the max-norm (lower right) of the square root of the condition numbers of $A^T A$ as functions of number of iterations.

29.6 Object in a box

The mesh smoothing techniques of the previous sections may be very efficient for small deformations of the mesh, but for a mesh undergoing large deformations these techniques may not be enough. We then need a strategy to handle large deformations of the mesh.

One common approach is to simply remesh (generate a new mesh) if the mesh deformation cannot be handled by standard mesh smoothing techniques. The downside of this approach is the cost of remeshing, as well as the loss of accuracy from projecting the solution from the old mesh to the new mesh.

We now present a mesh moving strategy for the case of an object moving through the mesh, which we refer to as *object in a box*, where the goal is to (i) allow for large deformations of the mesh while still keeping good mesh quality, and (ii) avoid remeshing.

The idea is that we split the computational domain $\Omega(t)$ into two parts: (i) a box $\Omega_b(t) \subset \Omega(t)$ that fits (ii) a regular background mesh that fills the rest of the domain $\Omega(t) \setminus \Omega_b(t)$. Within the box $\Omega_b(t)$ we may have an unstructured mesh around the object. When the object moves, the main part of the mesh deformation is handled by translation of the box, or $\pi/2$ radians rotation of the box, on the regular background mesh. The remaining deformation, which then is small, is taken by the mesh inside the box and is handled through regular mesh smoothing techniques such as the ones presented above.

The key ingredients are then the algorithms for translation and rotation of the box Ω_b, which we now describe.

We illustrate the box translation algorithm in Figure 29.3, where the moving object is a thin plate with dimension $0.25 \times 0.0625 \times 0.25$ in a cubic domain $\Omega = [0,1] \times [0,1] \times [0,1]$ that is moving in negative x_2-direction within a box $\Omega_b = 0.5 \times 0.5625 \times 0.5$. We find that as the plate is moving, the box Ω_b follows and the mesh outside the box is not deformed. Inside the box the small deformations are handled through Laplacian mesh smoothing, and good mesh quality is kept. The algorithm for translation of the box in direction x_i takes the following form:

Algorithm 29.1. *[Box translation in direction x_i] With a box $\Omega_b = [x_1^{min}, x_1^{max}] \times [x_2^{min}, x_2^{max}] \times [x_3^{min}, x_3^{max}]$, and with h_i^{reg} the mesh size of the regular background mesh outside the box, do*

(1) For all nodes in Ω_b: $x_i = x_i + h_i^{reg}$.

(2) For all object nodes: $x_i = x_i - h_i^{reg}$.

(3) For all nodes in Ω_b such that $x_i = x_i^{max} + h_i^{reg}$: $x_i = x_i - (x_i^{max} - x_i^{min} + h_i^{reg})$.

(4) For all nodes in the box: apply mesh smoothing.

(5) Update connectivity for Ω_b and the rest of the mesh.

In Figure 29.4 we illustrate box rotation using Algorithm 29.2, with Laplacian mesh smoothing, where now the box Ω_b is equal to the whole computational domain Ω.

Algorithm 29.2. *[Box rotation around axis e_i] With a box $\Omega_b = [x_1^{min}, x_1^{max}] \times [x_2^{min}, x_2^{max}] \times [x_3^{min}, x_3^{max}]$, and with h_i^{reg} the mesh size of the regular background mesh outside the box, do*

(1) Rotate the object $-\pi/2$ radians around the axis e_i, using mesh smoothing inside the box Ω_b.

(2) Rotate all nodes in Ω_b $\pi/2$ radians around the axis e_i.

(3) Update connectivity for Ω_b and the rest of the mesh.

The update of the connectivity after rotation takes some consideration to match the two parts of the mesh. The nodes typically match, but not the elements in general. For example, with rectangular elements there is no problem, but for tetrahedrons the element faces do not match.

There are several ways to approach this. We may use special matching elements at the box boundary, such as pyramids using tetrahedrons inside the box and rectangular elements in the rest of the structured domain. Another approach is to use a discontinuous method locally, allowing non matching element faces on the box boundary.

The global object in a box algorithm takes the form:

Algorithm 29.3. *[Object in a box] At time step k do*

(1) If the global translation coordinate ϕ_i^t for the object in the direction x_i is larger than the tolerance $TOL_i^t(h_i^{reg})$, then translate the box in that direction using Alogrithm 29.1.

(2) If the global rotation coordinate for the object ϕ_i^r around the axis e_i is larger than the tolerance TOL_i^r, then rotate the box in that direction using Alogrithm 29.2.

(3) Move the object according to given mesh velocity.

(4) Smooth the mesh inside the box.

(5) Solve the equations for time step k.

29.7 Sliding mesh

Variants of the object in a box method are possible. For example, computing the flow in a rotating turbine, a rotating cylinder may be used, which is referred to as a *sliding mesh* method.

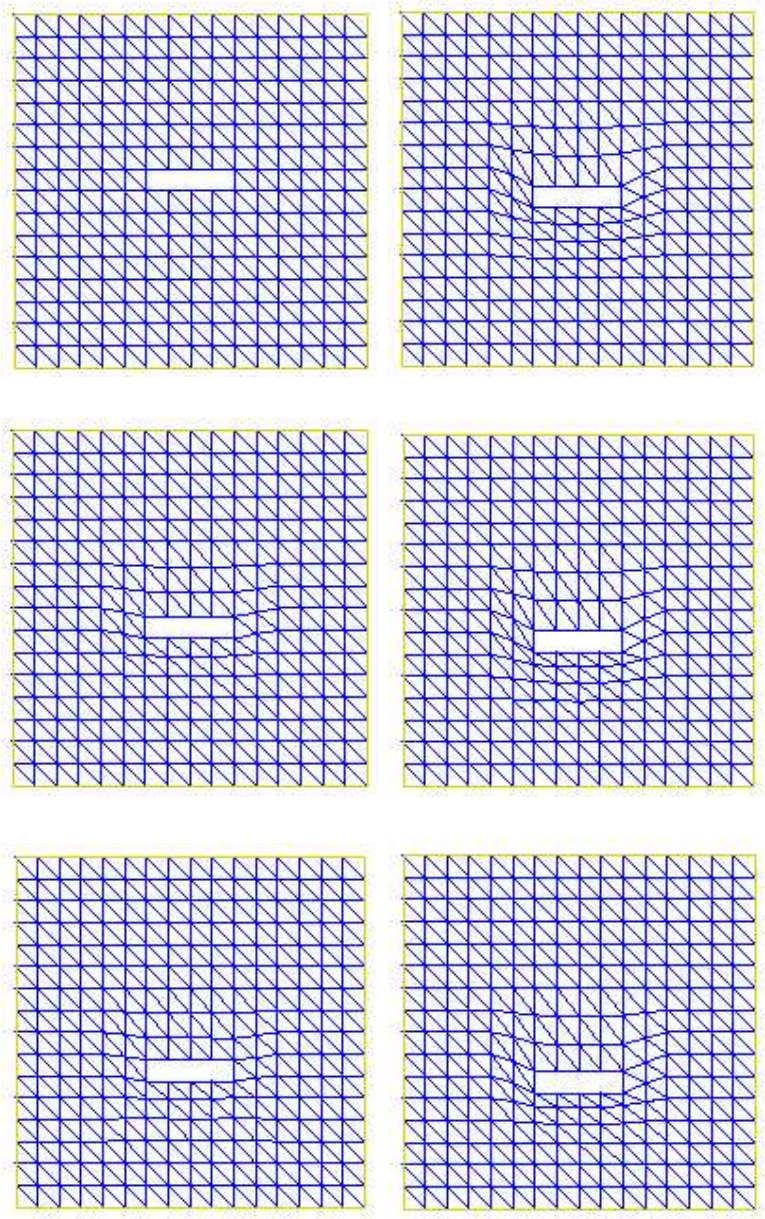

FIGURE 29.3. Box translation with Laplacian smoothing, for an $0.25 \times 0.0625 \times 0.25$ object inside a $0.5 \times 0.5625 \times 0.5$ box.

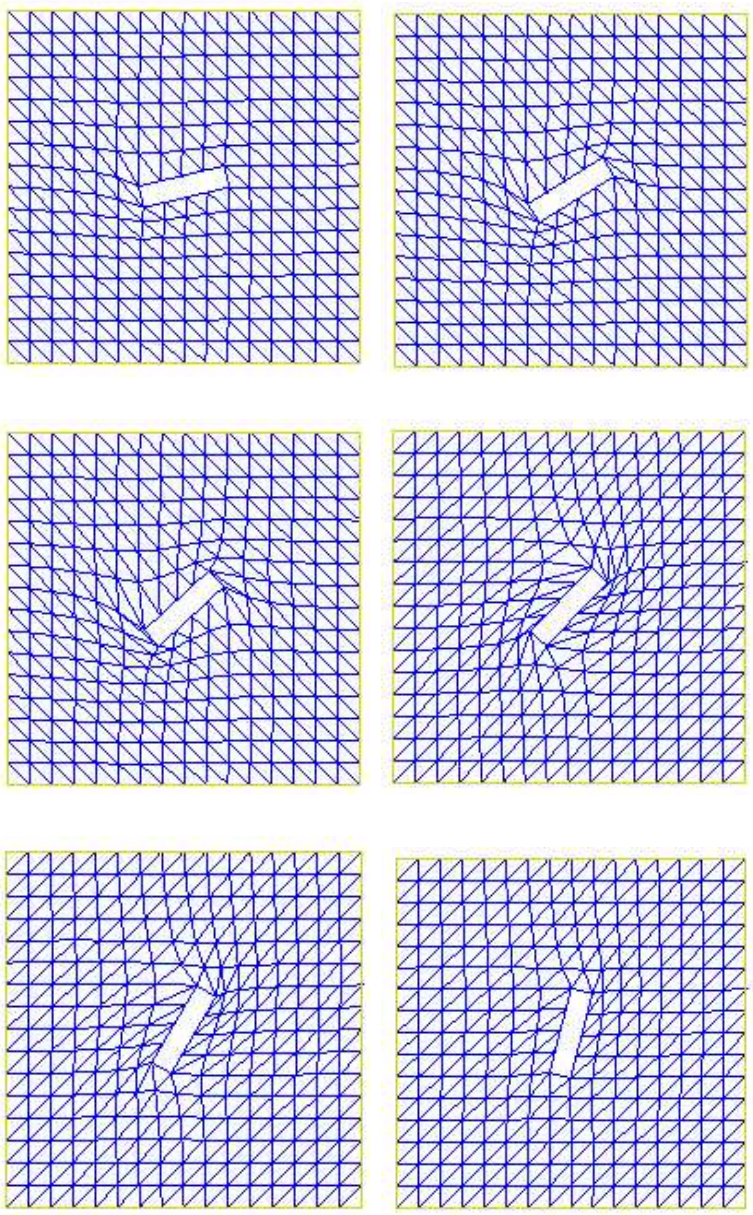

FIGURE 29.4. Box rotation with Laplacian smoothing, for an $0.25 \times 0.0625 \times 0.25$ object inside a $1 \times 1 \times 1$ box.

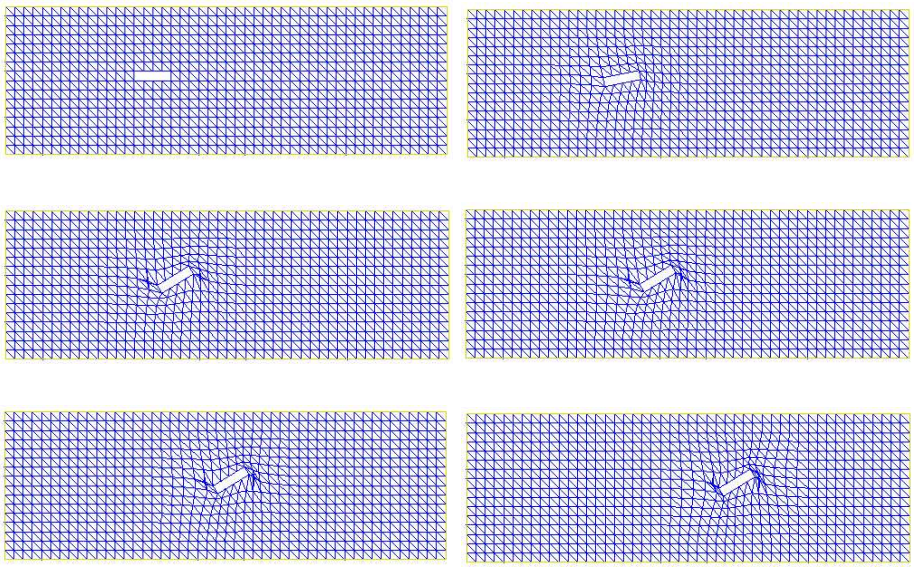

FIGURE 29.5. Mesh for moving $0.25 \times 0.0625 \times 0.25$ object inside a channel.

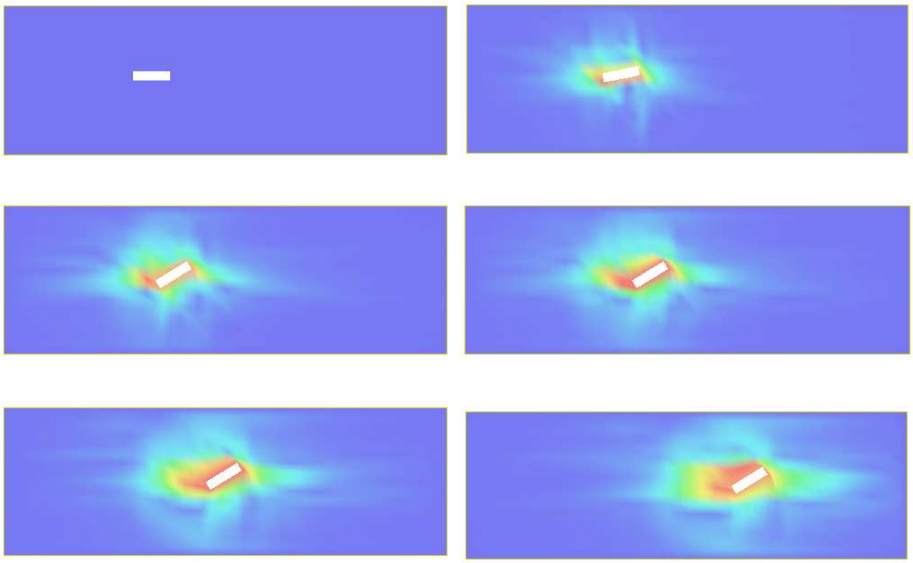

FIGURE 29.6. Magnitude of the velocity $|u|$ for moving $0.25 \times 0.0625 \times 0.25$ object inside a channel.

Part III

Flow Fundamentals

30
Bluff Body Flow

Flow visaulization has from early times played an important part in research, always yielding qualitative insight, and recently also quantitative results. (Milton Van Dyke)

30.1 Introduction

A basic flow of great practical importance is *bluff body flow*, occuring in a large number of situations including vehicles moving through air/water such as cars, boats and airplanes, or flow of air/water around bodies at rest such as buildings, bridges, off-shore structures or cables. One of the basic problems of bluff body flow is to compute the *drag coefficient* c_D, which is a normalized mean value in time of the momentary *drag force* at time t, which is the total force at time t acted upon the body by the fluid. Similarly, the *lift coefficient* c_L is a normalized mean value in time of the *lift* (force) acting in a direction perpendicular to the flow. The drag coefficient of a car or airplane directly couples to the fuel consumption, and the lift coefficient of an airplane to its load carrying capacity, both of which are of prime concern.

The flow around a bluff body at higher Reynolds numbers is turbulent in a *wake* attaching to the rear of the body. As the shape of the body gets more streamlined, the wake gets smaller and the drag decreases. A non-streamlined body like a T-Ford may have $c_D \approx 1$, a modern more streamlined car may have $c_D \approx 0.3$, and a streamlined airfoil at subsonic

speed may have $c_D \approx 0.01$. The drag has a contribution from the pressure distribution on the body surface, the *pressure drag* or *form drag*, and a contribution from the viscous forces, the *skin friction*. For a non-streamlined body skin friction is a small fraction of the total drag, while for an airfoil it may contribute up to 50 percent.

Bluff body flow exhibits basic phenomena such as *boundary layer flow*, *separation*, and *transition* from laminar to turbulent flow, to which we also devote separate chapters below.

In this chapter we present a set of benchmark problems for which experimental reference data are available, including a surface mounted cube, cylinders with square and circular cross sections and a sphere. The bluff body is placed in a channel with a given inlet flow, which may be viewed to model a wind tunnel test.

We first define the quantity of interest, drag or lift, then state an alternative expression for this quantity, and derive a corresponding a posteriori error estimate, and then we proceed to present computational results. The results indicate that the adaptive method is very efficient in terms of the number of mesh points needed to approximate the quantity of interest to an accuracy corresponding to the precision in experiments. For further details of the computations we refer to [51, 41, 44, 42].

30.2 Drag and Lift

We consider a body with surface Γ_0 placed in a horisontal channel and surrounded by a fluid flow $\hat{u} = (u, p)$ which we assume is satisfying the NS equations, to start with in a pointwise sense. The mean value in time over a time interval $I = [0, T]$ of the total fluid force acting on the body surface in a direction $\psi = (\psi_1, \psi_2, \psi_3)$, is given by

$$N(\sigma(\hat{u})) \equiv \frac{1}{|I|} \int_I \int_{\Gamma_0} \sum_{i,j=1}^{3} \sigma_{ij}(\hat{u}) n_j \psi_i \; ds \; dt, \tag{30.1}$$

where $\sigma(\hat{u})$ is the stress on Γ_0 given by $\hat{u}$. If ψ is directed along the channel in the direction of the flow, then $N(\sigma(\hat{u}))$ is a mean value in time of the drag force. If ψ is directed upwards, then $N(\sigma(\hat{u}))$ is a mean value in time of the lift force. The drag and lift coefficients are normalized versions of $N(\sigma(\hat{u}))$ over a long time interval.

30.3 An Alternative Formula for Drag and Lift

Below we will use an alternative expression for the force $N(\sigma(\hat{u}))$ which naturally fits with both a weak formulation and a G2 discretization, where

the boundary integral over Γ_0 is replaced by a volume integral over the volume Ω surrounding the body occupied by the fluid. To this end we extend ψ to a function Φ defined in Ω and being zero on the remaining boundary $\Gamma_1 = \Omega \setminus \Gamma_0$ of the fluid volume. Multiplying the momentum equation in (25.1) by Φ and integrating by parts, we get assuming a zero Dirichlet boundary condition on Γ_1,

$$\begin{aligned} N(\sigma(\hat{u})) &= \frac{1}{|I|}\int_I (\dot{u} + u\cdot\nabla u - f, \Phi) - (p, \nabla\cdot\Phi) \\ &\quad + (2\nu\epsilon(u), \epsilon(\Phi)) + (\nabla\cdot u, \Theta)\ dt, \end{aligned} \tag{30.2}$$

where we have also added an integral of $\nabla\cdot u = 0$ multiplied by a function Θ. Obviously, this representation does not depend on Θ, or the particular extension Φ of ψ. We note that the alternative expression (30.2) is more naturally defined for an ϵ-weak solution to the NS equations $\hat{u}$, than the original expression (30.1) involving derivatives of u on the boundary.

Similarly we define the drag force $N^h(\sigma(\hat{U}))$ correspondning to a computed G2 approximation $\hat{U} = (U, P)$ by

$$\begin{aligned} N^h(\sigma(\hat{U})) &= \frac{1}{|I|}\int_I (\dot{U} + U\cdot\nabla U - f, \Phi) - (P, \nabla\cdot\Phi) \\ &\quad + (2\nu\epsilon(U), \epsilon(\Phi)) + (\nabla\cdot U, \Theta) + SD_\delta(\hat{U}; \hat{\Phi})\ dt, \end{aligned} \tag{30.3}$$

where now Φ and Θ are finite element functions with $\Phi = \psi$ on Γ_0 and $\Phi = 0$ on Γ_1. Note in particular that we have here included the stabilization term SD_δ in (30.3) to make $N^h(\sigma(\hat{U}))$ independent of the choice of $\hat{\Phi} = (\Phi, \Theta)$ in the finite element test space.

30.4 A posteriori error estimation

We introduce the following dual problem: Find $\hat{\varphi} = (\varphi, \theta)$ with $\varphi = \psi$ on Γ_0 and $\varphi = 0$ on Γ_1, such that

$$\begin{aligned} -\dot{\varphi} - (u\cdot\nabla)\varphi + \nabla U\cdot\varphi - \nu\Delta\varphi + \nabla\theta &= 0, && \text{in } \Omega\times I, \\ \nabla\cdot\varphi &= 0, && \text{in } \Omega\times I, \\ \varphi(\cdot, T) &= 0, && \text{in } \Omega. \end{aligned} \tag{30.4}$$

For $\hat{u} \in \hat{W}_\epsilon$ an ϵ-weak solution to the NS equations, we derive a representation of the error $N(\sigma(\hat{u})) - N^h(\sigma(\hat{U}))$ by subtracting (30.3) from (30.2), with $\hat{\Phi} = (\Phi, \Theta)$ a finite element function in the test space of cG(1)cG(1), to get

$$\begin{aligned} &N(\sigma(\hat{u})) - N^h(\sigma(\hat{U})) = \frac{1}{|I|}\int_I (\dot{u} + u\cdot\nabla u, \Phi) - (p, \nabla\cdot\Phi) \\ &+ (2\nu\epsilon(u), \epsilon(\Phi)) + (\nabla\cdot u, \Theta) - ((\dot{U} + U\cdot\nabla U, \Phi) - (P, \nabla\cdot\Phi) \\ &+ (2\nu\epsilon(U), \epsilon(\Phi)) + (\nabla\cdot U, \Theta) + SD_\delta(\hat{U}; \hat{\Phi}))\ dt. \end{aligned} \tag{30.5}$$

With $\hat{\varphi}$ the solution to the dual problem (30.4), we also have, assuming Dirichlet boundary conditions for the velocity:

$$\begin{aligned}
&\frac{1}{|I|}\int_I (\dot{u} + u\cdot\nabla u, \varphi) - (p, \nabla\cdot\varphi) + (2\nu\epsilon(u), \epsilon(\varphi)) + (\nabla\cdot u, \theta)\\
&-((\dot{U} + U\cdot\nabla U, \varphi) - (P, \nabla\cdot\varphi) + (2\nu\epsilon(U), \epsilon(\varphi)) + (\nabla\cdot U, \theta))\ dt\\
&= \frac{1}{|I|}\int_I -(\dot{\varphi}, e) + (u\cdot\nabla e + e\cdot\nabla U, \varphi) - (p - P, \nabla\cdot\varphi) \qquad (30.6)\\
&+(2\nu\epsilon(e), \epsilon(\varphi)) + (\nabla\cdot e, \theta)\ dt = 0,
\end{aligned}$$

using partial integration with $\varphi(T) = e(0) = 0$, where $e = u - U$, and that $(u\cdot\nabla)u - (U\cdot\nabla)U = (u\cdot\nabla)e + (e\cdot\nabla)U$. By (30.5) and (30.6), we thus have that

$$\begin{aligned}
&N(\sigma(\hat{u})) - N^h(\sigma(\hat{U})) = \frac{1}{|I|}\int_I (\dot{U} + U\cdot\nabla U, \varphi - \Phi)\\
&-(P, \nabla\cdot(\varphi - \Phi)) + (\nabla\cdot U, \theta - \Theta) + (2\nu\epsilon(U), \nabla(\varphi - \Phi))\\
&-SD_\delta(\hat{U}; \hat{\Phi}) - ((\dot{u} + u\cdot\nabla u, \varphi - \Phi)\\
&-(p, \nabla\cdot(\varphi - \Phi)) + (\nabla\cdot u, \theta - \Theta) + (2\nu\epsilon(u), \nabla(\varphi - \Phi)))\ dt\\
&= \frac{1}{|I|}\int_I (R(\hat{U}), \hat{\varphi} - \hat{\Phi}) - SD_\delta(\hat{U}; \hat{\Phi}) - (R(\hat{u}), \hat{\varphi} - \hat{\Phi})\ dt,
\end{aligned}$$

adding and subtracting $(f, \varphi - \Phi)$, where we define

$$\begin{aligned}
(R(\hat{w}), \hat{v}) \equiv &(\dot{w} + w\cdot\nabla w - f, v) - (r, \nabla\cdot v)\\
&+ (\nabla\cdot w, q) + (2\nu\epsilon(w), \epsilon(v)),
\end{aligned} \qquad (30.7)$$

for $\hat{w} = (w, r)$ and $\hat{v} = (v, q)$.

We have now proved the following error representation, where we express the total output error as a sum of error contributions from the different elements K in space (assuming here for simplicity that the space mesh is constant in time), and we use the subindex K to denote integration over element K so that $(\cdot,\cdot)_K$ denotes the appropriate $L_2(K)$ inner product:

Theorem 30.1 *If $\hat{u} = (u, p)$ is an ϵ-weak solution to the Navier-Stokes equations, $\hat{U} = (U, P)$ is a cG(1)cG(1) solution, $\hat{\varphi} = (\varphi, \theta)$ is the dual solution satisfying (30.4), and $\hat{\Phi} = (\Phi, \Theta)$ is a finite element function in the test space of cG(1)cG(1) satisfying $\Phi = \psi$ on Γ_0 and $\Phi = 0$ on $\Gamma_1 = \partial\Omega\backslash\Gamma_0$, then*

$$N(\sigma(\hat{u})) - N^h(\sigma(\hat{U})) = \sum_{K\in\mathcal{T}_n} \mathcal{E}_K,$$

where $\mathcal{E}_K = e_D^K + e_M^K + e_\epsilon^K$, *with*

$$\begin{aligned} e_D^K &= \frac{1}{|I|}\int_I (R_K(\hat{U}), \hat{\varphi} - \hat{\Phi})_K \; dt, \\ e_M^K &= \frac{-1}{|I|}\int_I SD_\delta(\hat{U}; \hat{\Phi})_K \; dt, \\ e_\epsilon^K &= \frac{-1}{|I|}\int_I (R_K(\hat{u}), \hat{\varphi} - \hat{\Phi})_K \; dt, \end{aligned}$$

where $(R_K(\cdot), \cdot)_K$ *is a local version of* $(R(\cdot), \cdot)$, *defined by (30.7).*

We may here view e_D^K as a Galerkin error contribution from G2 on element K, e_M^K as a modeling error contribution from stabilization in G2, and e_ϵ^K as an error contribution from the ϵ-weak solution $\hat{u}$ characterizing the weak uniquness of $\hat{u}$.

From the error representation in Theorem 30.1, there are various possibilities to construct error indicators and stopping criterions for an adaptive algorithm. Using interpolation estimates of the type presented in Chapter 25, with $\hat{\Phi}$ a finite element interpolant of $\hat{\varphi}$, we may estimate e_D^K as follows

$$\begin{aligned} e_D^K \leq \frac{1}{|I|}\int_I \big((|R_1(\hat{U})|_K + |R_2(\hat{U})|_K) \cdot (C_h h^2 |D^2\varphi|_K + C_k k |\dot{\varphi}|_K) \\ + \|R_3(\hat{U})\|_K (C_h h^2 \|D^2\theta\|_K + C_k k \|\dot{\theta}\|_K) \big) \; dt, \end{aligned}$$

where the residuals R_i are defined by

$$\begin{aligned} R_1(\hat{U}) &= \dot{U} + U \cdot \nabla U - \nu \Delta U + \nabla P - f, \\ R_2(\hat{U}) &= \nu D_2(U), \\ R_3(\hat{U}) &= \nabla \cdot U, \end{aligned} \tag{30.8}$$

with

$$D_2(U)(x,t) = \frac{1}{h_n(x)} \max_{y \in \partial K} |[\frac{\partial U}{\partial n}(y,t)]|, \tag{30.9}$$

for $x \in K$, with $[\cdot]$ the jump across the element edge ∂K, D^2 denotes second order spatial derivatives, and we write $|w|_K \equiv (\|w_1\|_K, \|w_2\|_K, \|w_3\|_K)$, with $\|w\|_K = (w,w)_K^{1/2}$, and let the dot denote the scalar product in $\mathbb{R}^3$.

The next step involves replacing the exact dual solution $\hat{\varphi}$ by a computed approximation $\hat{\varphi}_h = (\varphi_h, \theta_h)$ obtained by, for example, G2 on the same mesh as we use for the primal problem. Doing so we are led to the following a posteriori error estimate (omitting the ϵ-term):

$$|N(\sigma(\hat{u})) - N^h(\sigma(\hat{U}))| \approx |\sum_{K \in \mathcal{T}_n} \mathcal{E}_{K,h}| \tag{30.10}$$

where $\mathcal{E}_{K,h} = e^K_{D,h} + e^K_{M,h}$ with

$$e^K_{D,h} = \frac{1}{|I|}\int_I \big((|R_1(\hat{U})|_K + |R_2(\hat{U})|_K)\cdot(C_h h^2|D^2\varphi_h|_K + C_k k|\dot{\varphi}_h|_K)$$
$$+ \|R_3(\hat{U})\|_K\cdot(C_h h^2\|D^2\theta_h\|_K + C_k k\|\dot{\theta}_h\|_K)\big)\ dt,$$
$$e^K_{M,h} = \frac{1}{|I|}\int_I SD_\delta(\hat{U};\hat{\varphi}_h)_K\ dt,$$

where we have replaced the interpolant $\hat{\Phi}$ by $\hat{\varphi}_h$. Again we may view $e^K_{D,h}$ as the error contribution from the Galerkin part of G2 on element K, and $e^K_{M,h}$ as the contribution from the stabilization in G2 on element K.

Note that we may view the ϵ-weak solution $\hat{u}$ as an approximate solution using maximal computational resources, and we may thus assume that $e^K_\epsilon << e^K_D + e^K_M$, and therefore drop e^K_ϵ. With this interpretation the term e^K_ϵ in Theorem 30.1 characterizes a best possible accuracy for the output $N(\sigma(\cdot))$ with the avaliable computational resources.

In the computations below we use $C_k = 1/2$ and $C_h = 1/8$ as constant approximations of the interpolation constants in Theorem 30.1. These values are motivated by a simple analysis on reference elements, using Taylor's formula. More detailed approximation of interpolation constants is possible using a computational approach for each element individually.

Non-Dirichlet boundary conditions, such as slip boundary conditions at lateral boundaries and transparant outflow boundary conditions, introduce additional boundary terms in the error representation in Theorem 30.1, but since the dual solution in the bluff body examples in this chapter is small at such non-Dirichlet boundaries, we neglect the corresponding boundary terms in the computations below.

We use Algorithm 27.1 for adaptive mesh refinement in space (with for simplicity the same space mesh for all time steps) based on the a posteriori error estimate (30.10).

30.5 Surface Mounted Cube

The flow past a surface mounted cube may serve as a very simple model of the flow of air around a moving car, or the flow past a building, for example. In this model the incoming flow is laminar time-independent forming a horse shoe vortex upstream the cube, and a laminar boundary layer on the front surface, which separates and develops a turbulent wake attaching to the rear face of the cube. The flow is thus very complex with a combination of laminar and turbulent features including boundary layers and a large turbulent wake, see Figure 30.1.

In the model problem the cube side length is $H = 0.1$, and the cube is centrally mounted on the floor of a rectangular channel of length $15H$,

height $2H$, and width $7H$, at a distance of $3.5H$ from the inlet. The cube is subject to a Newtonian flow governed by the NS equations with kinematic viscosity $\nu = 2.5 \times 10^{-6}$ and a unit inlet bulk velocity corresponding to a Reynolds number of 40 000, using the dimension of the cube as characteristic dimension. The inlet velocity profile is interpolated from experiments, we use no slip boundary conditions on the cube and the vertical channel boundaries, slip boundary conditions on the lateral channel walls, and a transparent outflow boundary condition.

30.5.1 The drag coefficient c_D

The drag coefficient c_D is a long-time mean value of a normalized drag force. We seek an approximate drag coefficient $\bar{c}_D$ over a finite time interval $I = [0, T]$ with fully developed flow $\hat{u}$, defined by

$$\bar{c}_D \equiv \frac{1}{\rho \frac{1}{2} U_\infty^2 A} \times N(\sigma(\hat{u})), \tag{30.11}$$

where $T = 40H$, $U_\infty = 1$ is a bulk inflow velocity, $A = H \times H = H^2$ is the cube area facing the flow, $N(\sigma(\hat{u}))$ is defined by (30.1), and we assume constant unit density $\rho = 1$. We compute an approximate drag coefficient

$$\bar{c}_D^h = \frac{1}{\rho \frac{1}{2} U_\infty^2 A} \times N^h(\sigma(\hat{U})), \tag{30.12}$$

with $N^h(\sigma(\hat{U}))$ defined by (30.3) and $\hat{U}$ a cG(1)cG(1) approximate solution. We use an adaptive algorithm based on a normalized version of the a posteriori error estimate (30.10).

In Figure 30.2 we display c_D^h as a function of the number of mesh points in space. We obtain $c_D^h \approx 1.55$, with the value seemingly being well captured up to ± 0.03 already using less than 10^5 mesh points. In each step of the adaptive process we refine roughly 30% of the space elements. The drag contribution from the stabilizing terms in (30.3) is notable on coarse meshes but decreases to less than 5% on the finer meshes. The a posteriori error estimate gives a tolerance of ± 0.3, which seems to be an over-estimate by a factor of 10, which can be attributed to the presence of absolute values in the error estimation.

30.5.2 Dual solution and a posteriori error estimates

Snapshots of the dual solution and the adaptively refined computational mesh are shown in Figure 14.3 and in Figure 30.3. The initial mesh is uniform and very coarse, 384 mesh points, and we find that the adaptive method automatically captures the turbulent wake and the horse-shoe vortex.

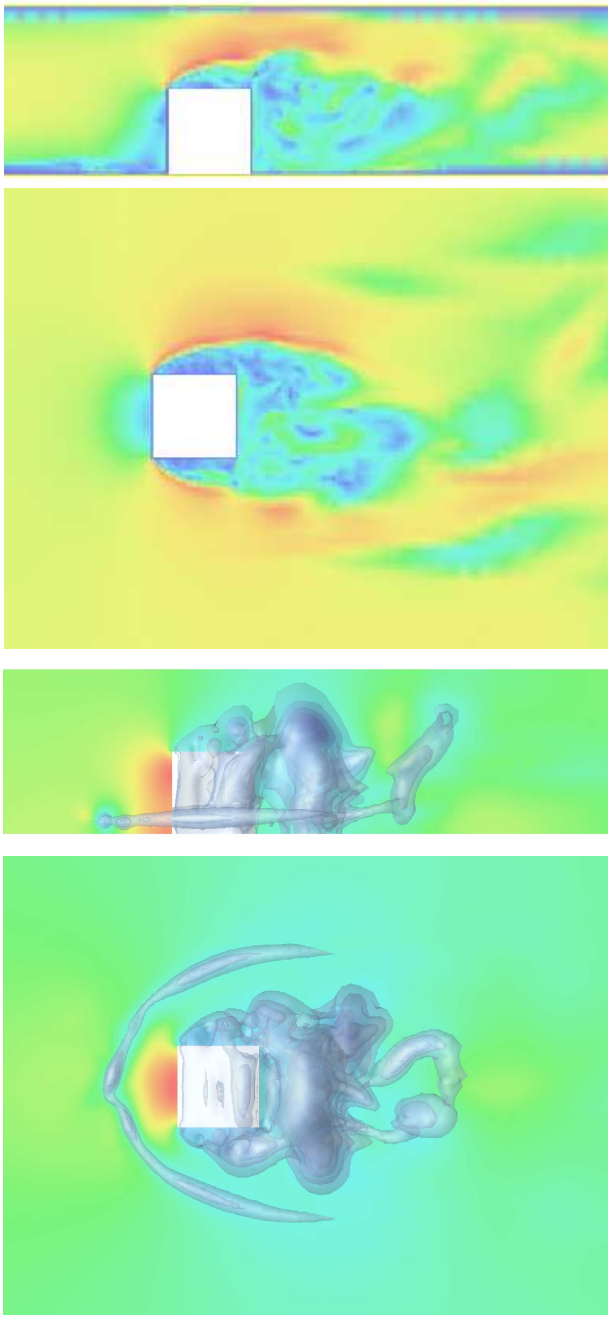

FIGURE 30.1. Surface mounted cube: Magnitude of velocity (upper), and pressure color map, with isosurfaces for negative pressure, illustrating the horse shoe vortex.

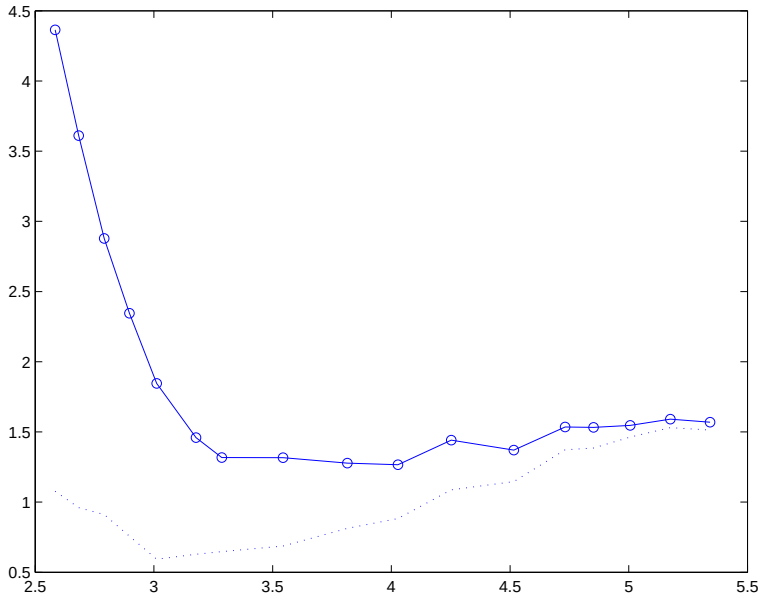

FIGURE 30.2. Surface mounted cube: $\bar{c}_D^h$ ('o'), and the corresponding approximations without the contribution from the stabilizing term (':'), as functions of the 10-logarithm of the number of mesh points.

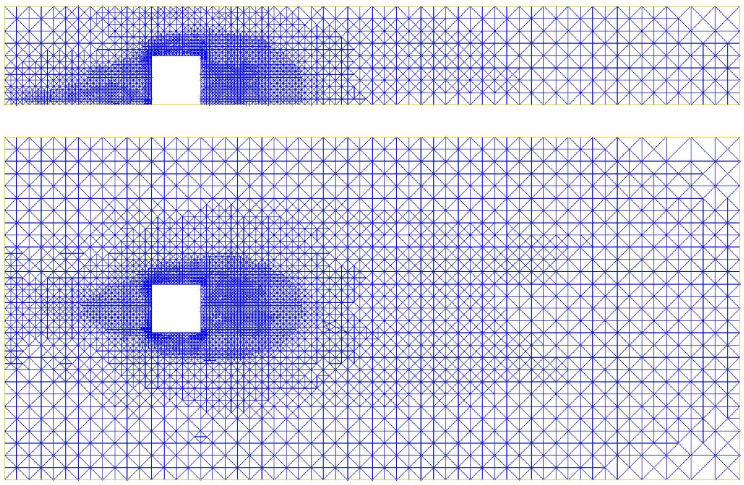

FIGURE 30.3. Surface mounted cube: computational mesh refined with respect to mean drag, in the x_1x_2-plane at $x_3 = 3.5H$ and in the x_1x_3-plane at $x_2 = 0.5H$.

In Figure 30.4 we plot the a posteriori error estimates $e_{D,h} = \sum_K e_{D,h}^K$ and $e_{M,h} = \sum_K e_{M,h}^K$ from (30.10), as well as the true error based on the computational approximation on the finest mesh. For the modeling error $e_{M,h}$ we use a conservative estimate where we have set the absolute values inside the sums in space and time.

We find that once the value for $\bar{c}_D^h$ is stabilized, the a posteriori error estimates indicate that it may be hard to further increase the precision in c_D, which couples to the discussion above of a lower bound on the tolerance.

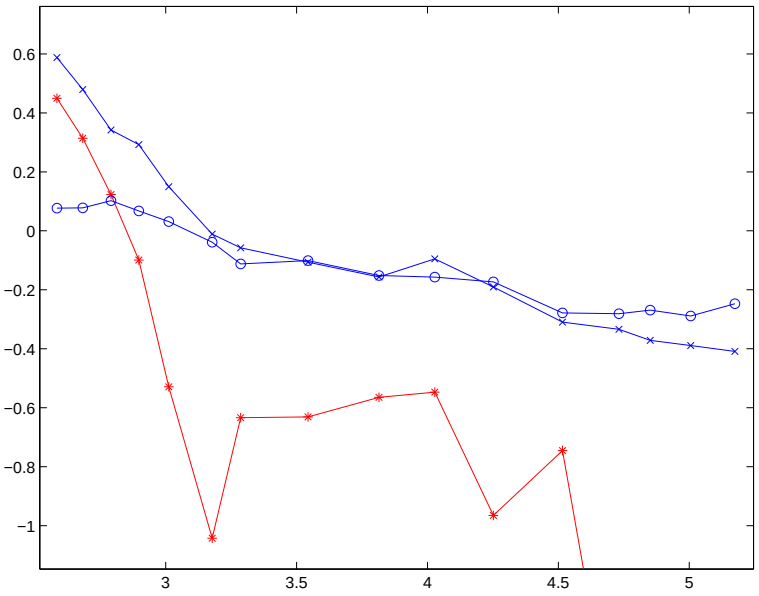

FIGURE 30.4. Surface mounted cube: $\log_{10}$-$\log_{10}$ plot of the a posteriori error estimates $e_{D,h}$ ('o') and $e_{M,h}$ ('x'), and the true error ('*') based on $c_D = 1.55$ (the solution on the finest mesh), as functions of the number of mesh points in space.

30.5.3 Comparison with reference data

We know of no experimental reference values of c_D, but in [16] a DNS using about 70×10^6 degrees of freedom gives $c_D \approx 1.42$ with the same data as in our computations using G2. The stabilizing terms in (30.3) is not used in the evaluation of c_D, and the result should thus be compared to the curve of somewhat lower values in Figure 30.2, resulting in a good agreement.

In [67] results using LES are reported where the computational setup is similar to the one we use here, except the numerical method, the length of the time interval, and the length of the channel. Using LES with different

meshes and subgrid models, approximations of c_D in the interval $[1.14, 1.24]$ are reported, thus significantly lower values.

We note that we reach the stable value of $c_D \approx 1.5$ using about 50 000 mesh points in space, which means that the adaptive method is very efficient in terms of the number of degrees of freedom, making the computations possible using a standard PC. In addition, we have an estimated accuracy from the a posteriori error estimates, and a set of results for a hierarchy of refined computational meshes reflecting convergence in output.

30.6 Square Cylinder

We now consider a square cylinder at Reynolds number 22 000, based on the cylinder diameter $D = 0.1$ and the unit inflow velocity in the streamwise direction. The computational domain is a channel of size $21D \times 14D \times 4D$ in the x_1-direction with the cylinder directed in the x_3-direction and centered at $(x_1, x_2) = (5D, 7D)$. We use no slip boundary conditions on the cylinder, slip boundary conditions on the lateral channel walls, and a transparant outflow boundary condition.

Characteristics of this flow are a turbulent wake of approximate diameter $1D$ attached to the trailing face of the cylinder, and two opposite shear layers periodically shedding vortices, see Figure 30.5. In addition, we have a cycle-to-cycle variation, so called *phase jitter*, due to turbulence and 3D instabilities in the shear layers, which is illustrated in Figure 30.6 as a time series of the vorticity showing the changing wake, with the shorter wake, with more pronounced vortex shedding, corresponding to high drag in Figure 30.7.

30.6.1 Computing mean drag: time vs. phase averages

We seek to compute the mean drag force $N(\sigma(\cdot))$ of the square cylinder, and we here choose an averaging time interval of length $100D$, starting at fully developed flow. The length of the time interval directly couples to computability and output uniqueness of $N(\sigma(\cdot))$, with a longer time interval resulting in a more well determined mean drag force which is cheaper to compute from an accuracy point of view. On the other hand, for a longer time interval the computational cost of course increases for each iteration of the adaptive algorithm.

Phase jitter complicate the computation of time averages, since the time averages are highly dependent of the size and location of the time interval, and thus a very long time interval is needed for a well determined mean drag force. This has lead to alternative ways to represent averages. For example, one may consider so called *phase averages*, where a number of shedding

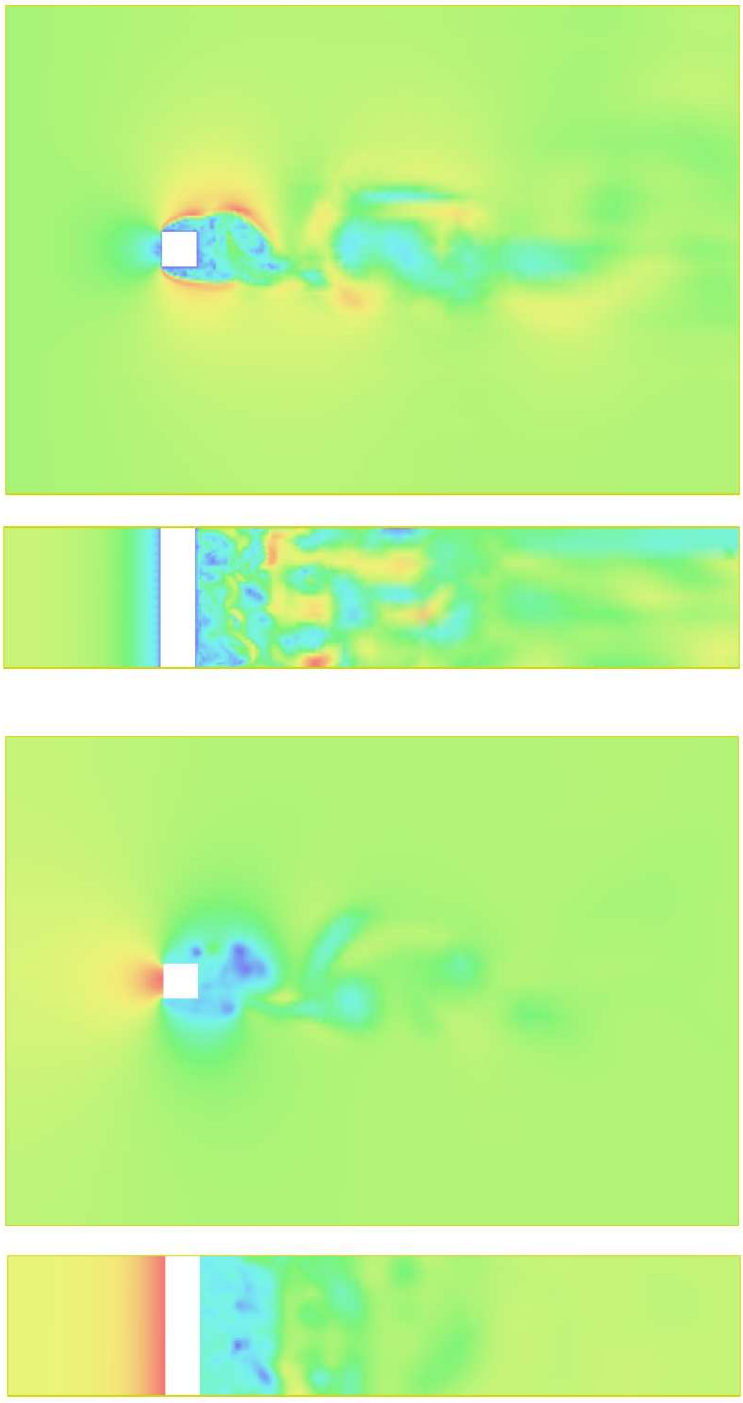

FIGURE 30.5. Velocity $|U|$ (upper), and pressure P (lower), in the x_1x_2-plane at $x_3 = 2D$.

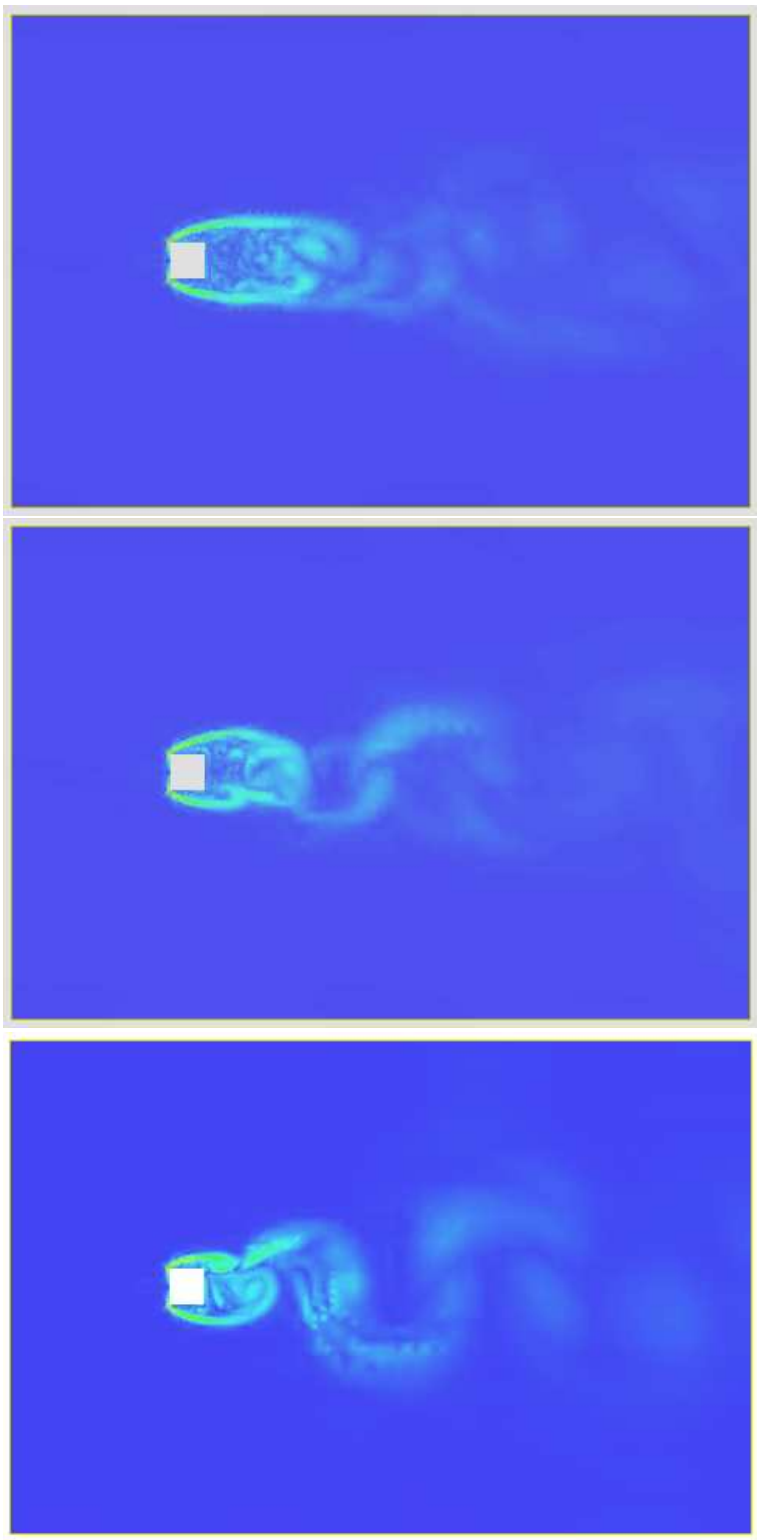

FIGURE 30.6. Time evolution of vorticity $|\nabla \times U|$, in the x_1x_2-plane at $x_3 = 2D$.

cycles are chosen as "typical" for the flow, over which mean values are computed.

We now seek the drag coefficient c_D, which we approximate by $\bar{c}_D$, defined by (30.11), with its computational version $\bar{c}_D^h$ given by (30.12), where we set $U_\infty = 1$ based on the inflow velocity, and the area $A = 4D \times D = 4D^2$. In Figure 30.7 we plot computed approximations $\bar{c}_D^h$ as we refine approximately 30% of the elements in the mesh each iteration, where we also include approximations without the stabilizing term in (30.3). For the finer meshes we get a $\bar{c}_D^h$ in the interval 2.0-2.4, and a value about 5% lower for the formulation without the stabilizing term. The large variation in $\bar{c}_D^h$ can be explained by effects of phase jitter and a relatively short time interval, as noted above. In Figure 30.7 we plot the trajectory of the normalized drag force for the finest mesh, where we notice the variations in amplitude and local mean of the drag.

30.6.2 Dual solution and a posteriori error estimates

A snapshot of the dual solution is shown in Figure 30.8. We note that the dual solution, with velocity boundary data on the cylinder in the streamwise direction, is of moderate size, and in particular is not exploding as pessimistic worst case analytical estimates may suggest, but rather seems to behave as if the net effect of the crucial reaction term (with large oscillating coefficient ∇U) is only a moderate growth. We also note that $\hat{\varphi}_h = (\varphi_h, \theta_h)$ is concentrated in space, thus significantly influencing the adaptive mesh refinement.

The resulting computational mesh after 9 adaptive mesh refinements is shown in Figure 30.9. The initial space mesh is uniform and coarse, and without the dual weights in the a posteriori error estimate the mesh would come out quite differently. We notice in particular that the adaptive method automatically captures the turbulent wake, which is essential for accurately computing drag.

In Figure 30.10 we plot the a posteriori error estimates $e_{D,h}$ and $e_{M,h}$ from (30.10), as well as an estimate of the true error based on the computational approximations on the finest meshes, suggesting that 2.2 may be a good candidate for a representative value of c_D. The modeling error $e_{M,h}$ consists of sums in space and time of integrals over the space-time elements, and in the evaluation of $e_{M,h}$ in Figure 30.10 we have set the absolute values inside the sums in space and time. The same goes for the discretization error, and thus error cancellation is not possible, leading to conservative error estimates.

30.6.3 Comparison with reference data

Various reference values for this problem are reported, including mean drag. Experimental reference values for c_D are reported in the interval 1.9-2.1,

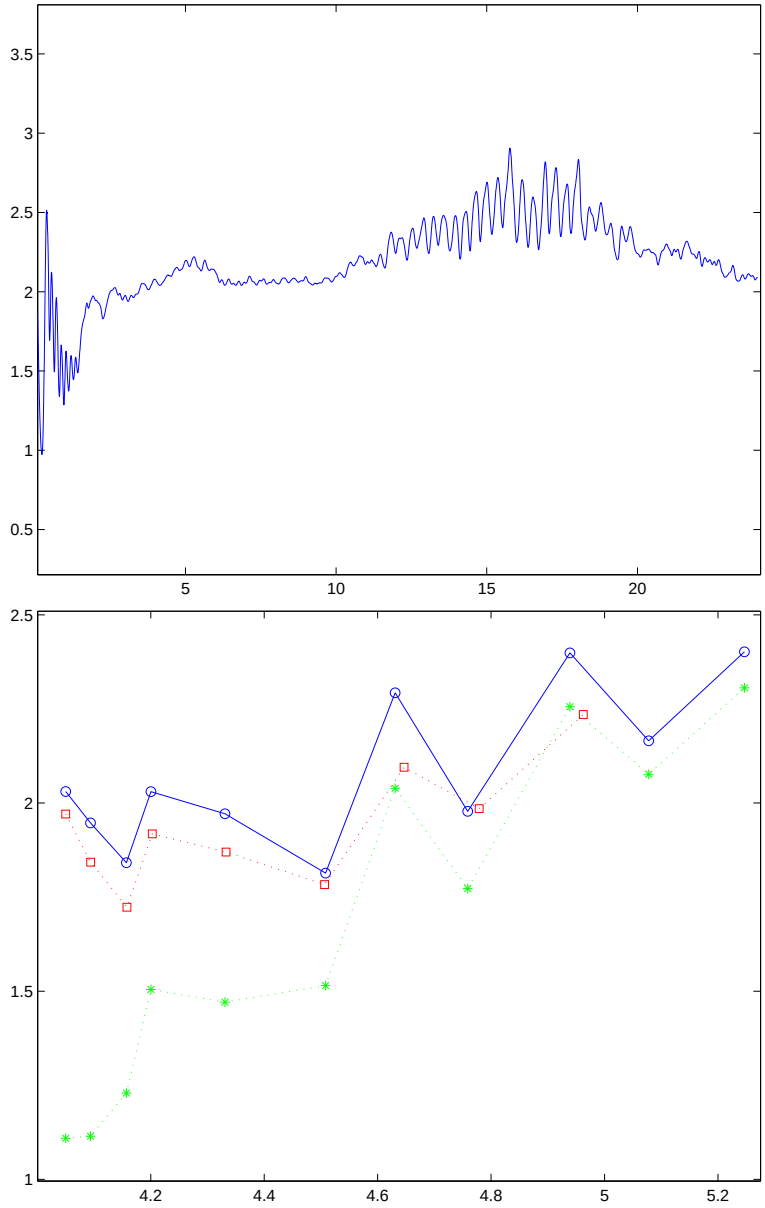

FIGURE 30.7. Square cylinder: Normalized drag force as a function of time after 9 mesh refinements (upper), and $\bar{c}_D^h$ ('o'), the corresponding approximations without the contribution from the stabilizing term in (30.3) ('*'), and the approximation with 2% white noise in inflow velocity ('□'), as functions of the 10-logarithm of the number of mesh points in space (lower).

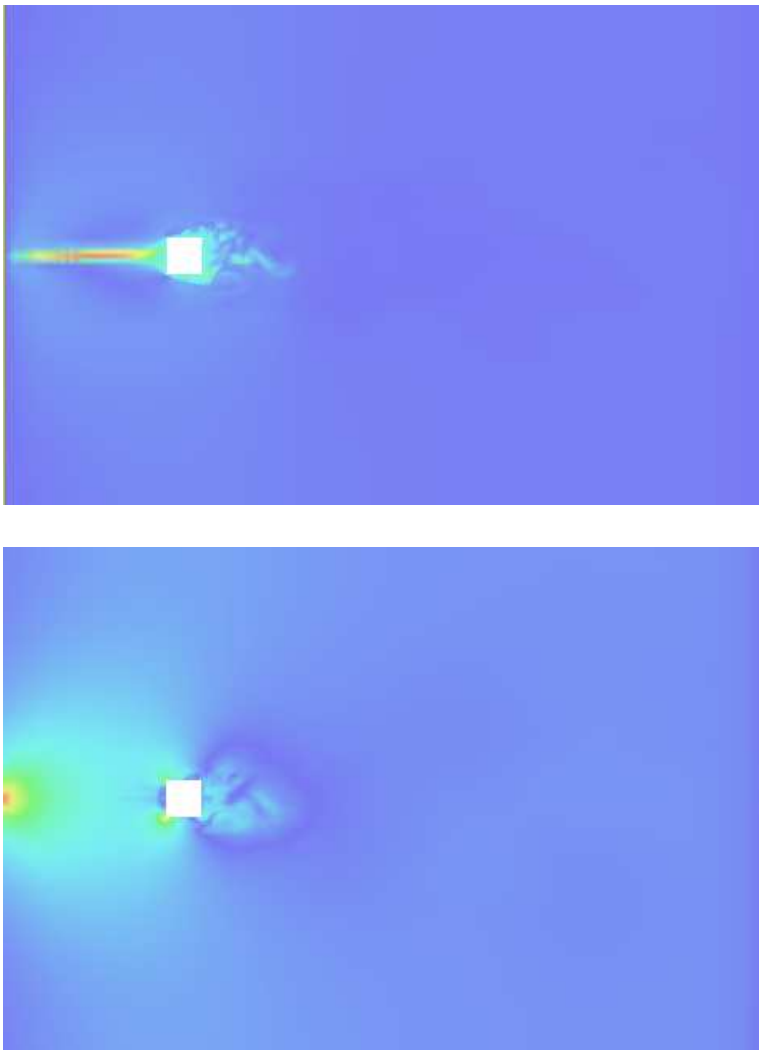

FIGURE 30.8. Square cylinder: dual velocity $|\varphi_h|$ (upper), and dual pressure $|\theta_h|$ (lower), in the x_1x_3-plane at $x_2 = 7D$ and in the x_1x_2-plane at $x_3 = 2D$.

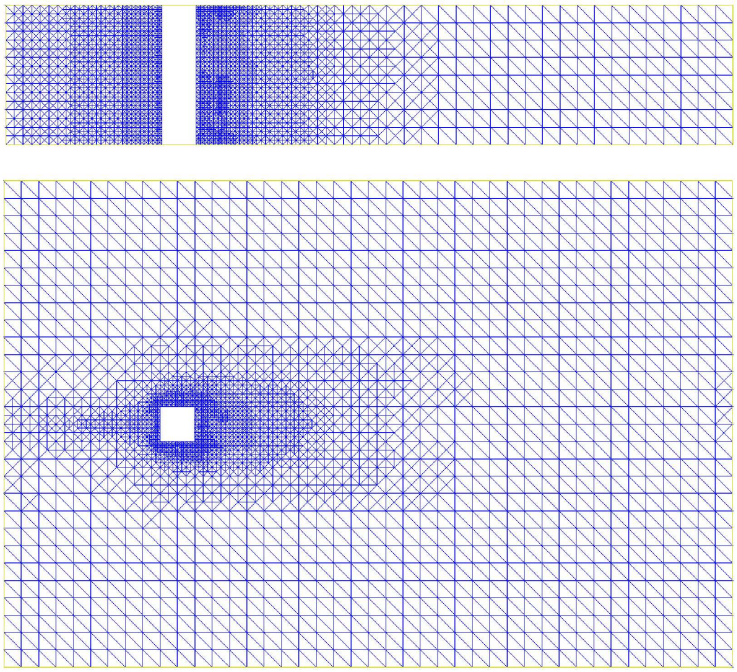

FIGURE 30.9. Square cylinder: computational mesh after 9 adaptive mesh refinements with respect to mean drag, in the x_1x_3-plane at $x_2 = 7D$ and in the x_1x_2-plane at $x_3 = 2D$.

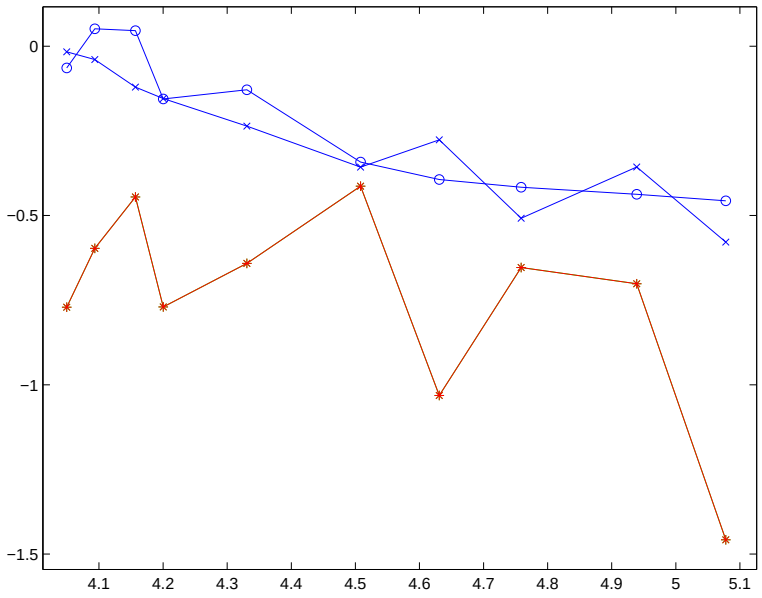

FIGURE 30.10. Square cylinder: $\log_{10}$-$\log_{10}$ plot of the a posteriori error estimates $e_{D,h}$ ('o') and $e_{M,h}$ ('x'), and the true error ('*') based on $c_D = 2.2$, as functions of the number of mesh points in space.

where the experiments are carried out under slightly different conditions than the computations, such as a slightly lower Reynolds number, a longer cylinder, and a turbulence level of 2% in the inflow velocity. In a collection of results from different research groups [79], LES results are reported in the interval 1.66-2.77, and RANS results in the interval 1.6-2.0.

To test the sensitivity in inflow data, we compare our results with a computation with 2% white noise added to the inflow velocity. These results are plotted in Figure 30.7, giving similar values for c_D, although somewhat lower, closer to the experimental results.

We find that apart from drag we are also able to capture the correct frequency of the oscillating wake, characterized by the *Strouhal number St*, defined as the dimensionless number

$$St = \frac{fL}{U_\infty}, \tag{30.13}$$

where f is the frequency, L is a length scale (here equal to the cylinder diameter: $L = D$), and U_∞ is a velocity scale (here $U_\infty = 1$).

In this study, the computation of c_D^h corresponds to the interval $[10, 20]$ in Figure 30.7. We can see that translating this interval suitably would result in a lower c_D^h, within the tolerance of the experimental reference values. We note that again we reach the targeted value for the drag coefficient using very few mesh points.

30.7 Circular cylinder

The flow past a circular cylinder is a classical problem of fluid dynamics. In our model we consider a circular cylinder of diameter D and length $4D$, in the direction of the x_3-axis, subject to a unit streamwise velocity inflow condition in a channel along the x_1-axis of length $21D$ and height $14D$. We use no slip boundary conditions on the cylinder, slip boundary conditions on the lateral walls of the channel, and a transparant outflow boundary condition at the end of the channel.

The flow past a circular cylinder depends on the Reynolds number. For Re very low (Re less than 4-5) we have *creeping flow* without separation and with high viscous drag. Inreasing the Reynolds number the flow separates to form a steady, symmetric wake of recirculating flow, and further increasing Re beyond 30-48 leads to the onset of an oscillation of the wake that periodically sheds alternating vortices gradually developing downstream, a so called *von Kármán vortex street*. Theodore von Kármán in 1911 investigated the stability of two rows of vortices, showing that such vortices are generally unstable with respect to small perturbations and that the only stable arrangement is that with $h/l = 0.281$, with h and l being the vertical and streamwise distances between the center of the vortices, see Fig. 30.11.

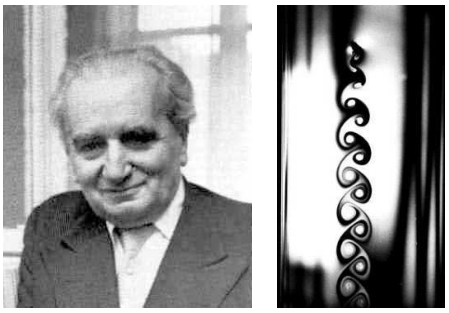

FIGURE 30.11. Theodore von Kármán (1881-1963), and a von Kármán vortex street for $Re = 100$.

The flow for higher Reynolds numbers is characterized by transition to turbulence in different parts of the flow. First the wake undergoes transition, then the shear layers, and finally the boundary layers. The different regimes are characterized by different separation and different shedding frequencies. For $Re < 100$, c_D is proportional to Re^{-1}, for $100 < Re < 10^5$ we have $c_D \approx 1$, while for $Re > 10^5$ we find that the c_D first drops significantly and then rises back again. The drag reduction near $Re = 10^5$ is commonly referred to as *drag crisis*, where the boundary layer undergoes transition, leading to a delayed separation with a smaller wake, corresponding to a drastic reduction of the drag. We come back to the problem of simulating drag crisis in Chapter 32.

A G2 approximation of the flow past a circular cylinder is plotted in Fig. 30.12 for $Re = 100$. We find that the flow is two dimensional for this low Reynolds number, and we clearly see the vortex shedding. For $Re = 3900$, we find in Fig. 30.13 that we still have vortex shedding, but now the flow is three dimensional, and we have a large turbulent wake attached to the cylinder, see Fig. 30.14.

30.7.1 Comparison with reference data

The flow past a circular cylinder at various Reynolds numbers is probably the most well documented bluff body flow, with an extensive amount of experimental and computational results avaliable, see e.g. [87, 81].

In Fig. 30.15 we plot computational approximations of the drag coefficients using G2 for Reynolds numbers 100 and 3900, where we refine 10% and 5% of the elements in each iteration, respectively. The normalization is now $U_\infty = 1$ and $A = 0.1 \times 0.4 = 0.04$. For $Re = 100$ we get a $\bar{c}_D^h$ somewhat lower than 1.5, which is within the tolerance of experimental results, and for $Re = 3900$ we have $\bar{c}_D^h$ slightly less than 1.0, which is consistent with experiments. We also capture the correct Strouhal numbers, with $St \approx 0.16$ for $Re = 100$ and $St \approx 0.22$ for $Re = 3900$, where we average over a time interval $I = 35D/U_\infty$.

We study the surface pressure on the cylinder as a function of an angle starting from the upstream stagnation point of the cylinder, in the form of a *pressure coefficient* c_p, defined by

$$c_p = \frac{p - p_\infty}{\rho \frac{1}{2} U_\infty^2}, \tag{30.14}$$

where U_∞ and p_∞ are the *free stream velocity* and the *free stream pressure*, respectively, and we assume constant unit density $\rho = 1$.

The normalization of c_p in (30.14) couples to *Bernoulli's Law*, stating that for an incompressible irrotational inviscid fluid at steady state, we have

$$\frac{1}{2}|u|^2 + p = C, \tag{30.15}$$

with C an constant. If Bernoulli's law is valid, we then have $c_p = 0$ in the free stream, and $c_p = 1$ at the upstream stagnation point with zero velocity. Typically, upstream the cylinder the flow is almost steady, and thus Bernoulli's law should be valid for ν small. On the other hand, for ν large, corresponding to small Reynolds numbers, Bernoulli's law may not be valid, and thus c_p may differ from 1. In Figure 30.16 we plot the pressure coefficients for $Re = 100$ and $Re = 3900$, both matching experimental results.

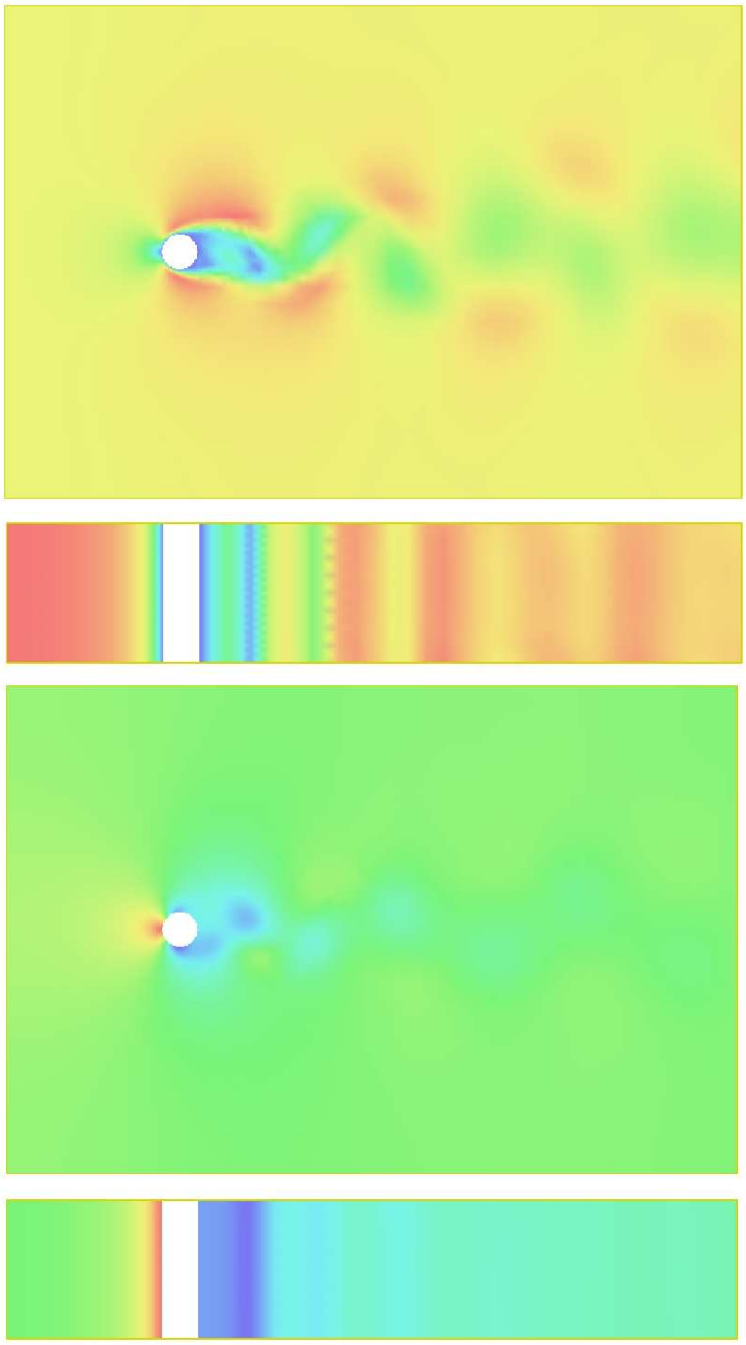

FIGURE 30.12. Circular cylinder at $Re = 100$: magnitude of velocity $|U|$ (upper), and pressure P (lower).

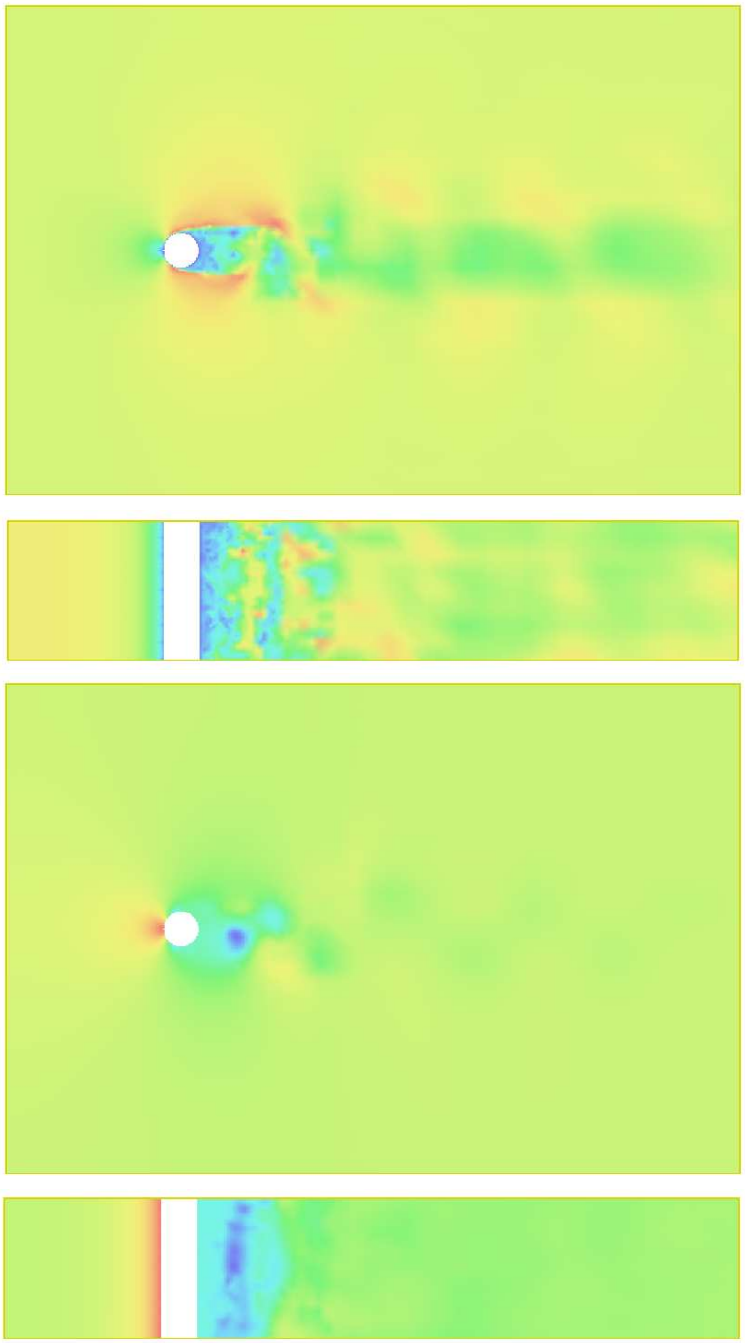

FIGURE 30.13. Circular cylinder at $Re = 3900$: magnitude of velocity $|U|$ (upper), and pressure P (lower).

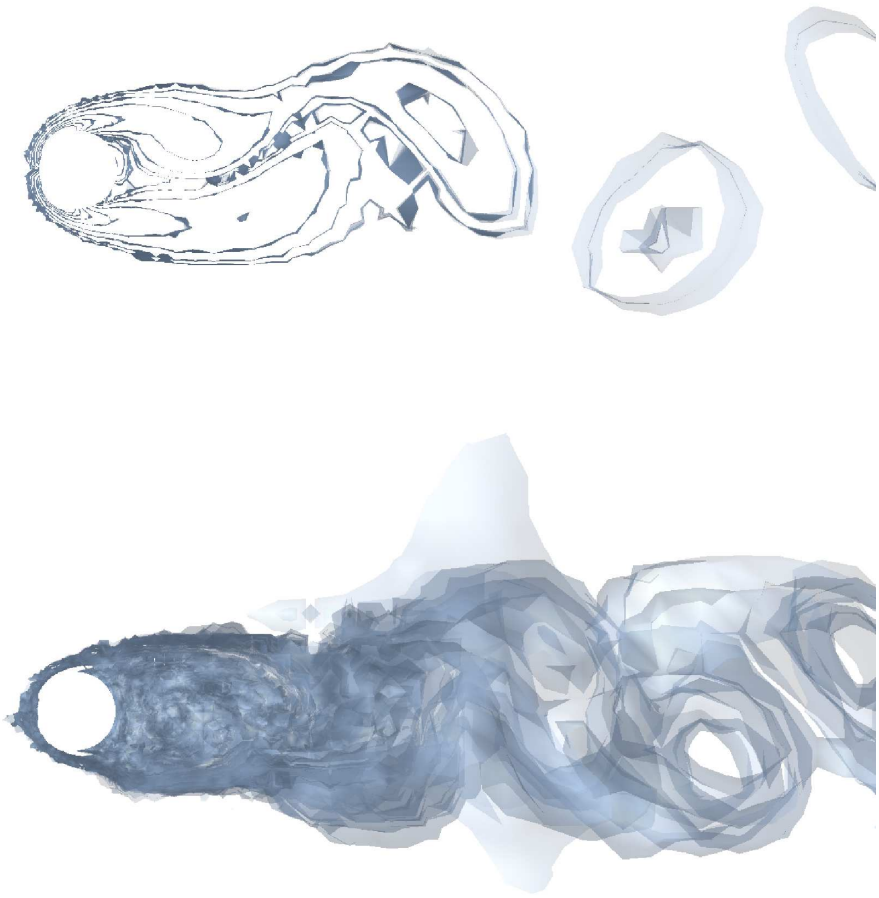

FIGURE 30.14. Magnitude of vorticity isosurfaces for 3,5,10,20,...,100, for a circular cylinder at $Re = 100$ (upper), and $Re = 3900$ (lower).

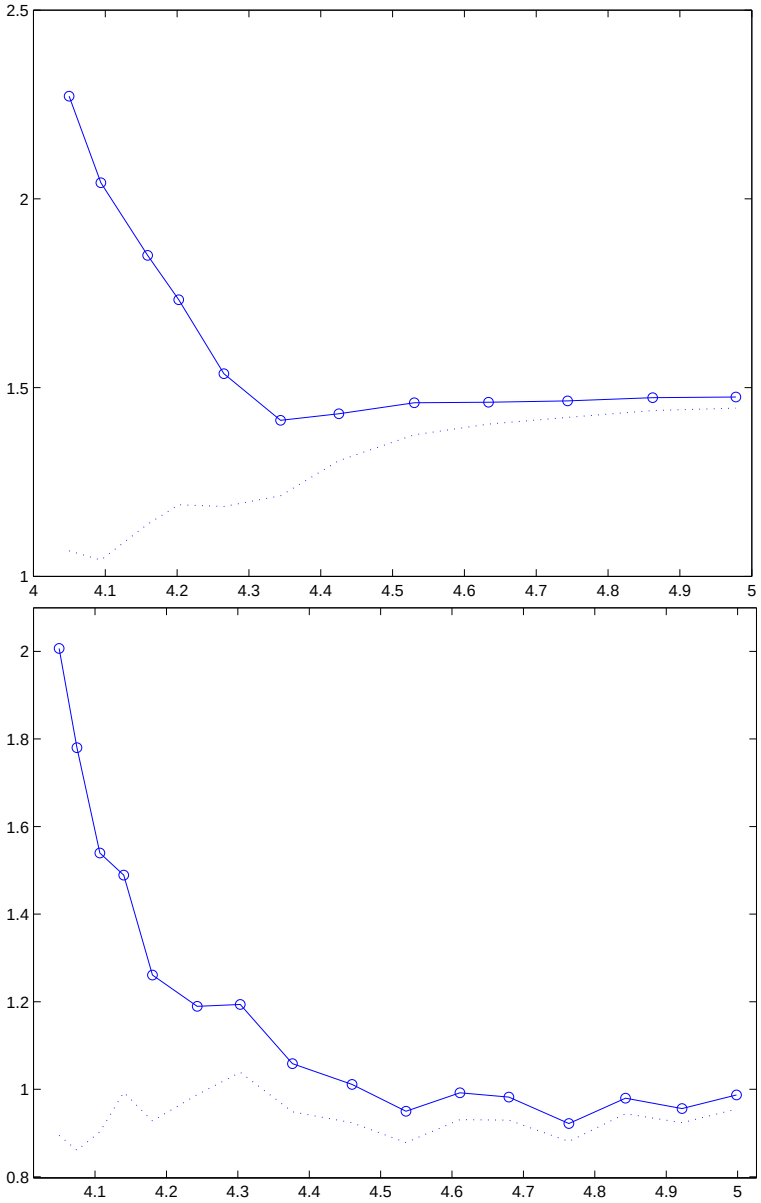

FIGURE 30.15. Circular cylinder: approximative drag coefficient as a function of the 10-logarithm of the number of mesh points in space, for $Re = 100$ (upper) and $Re = 3900$ (lower).

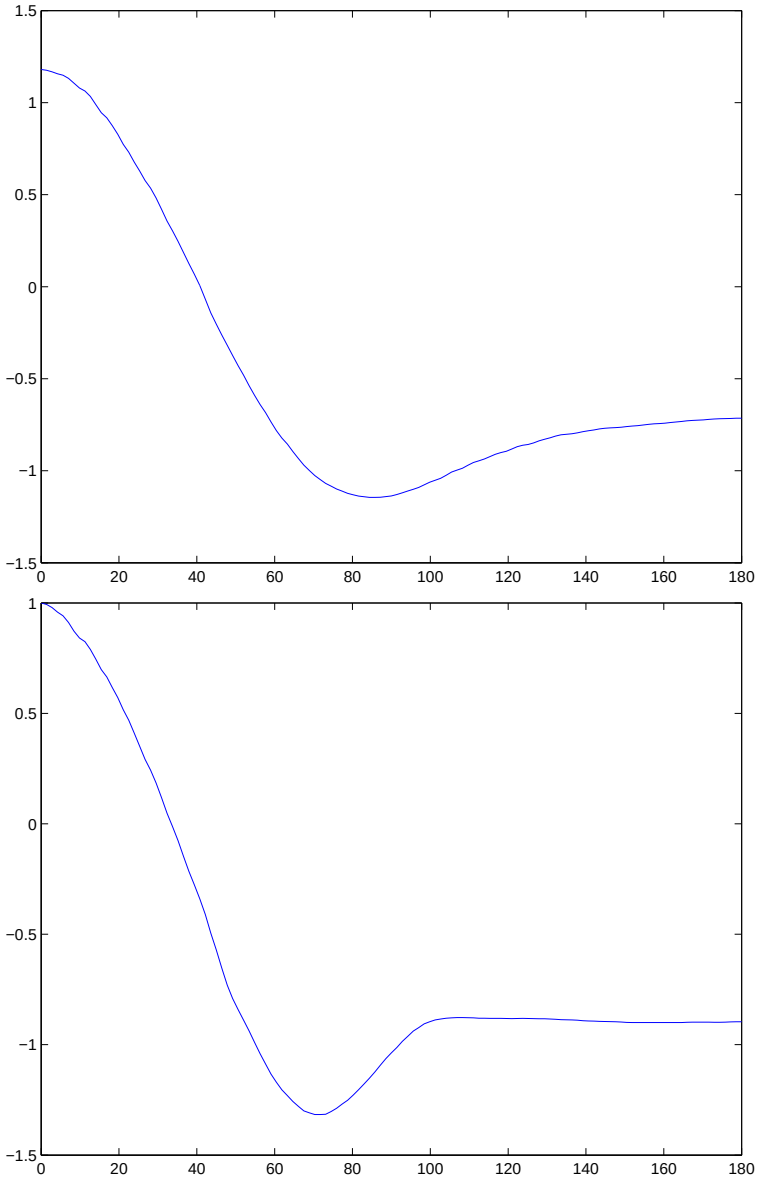

FIGURE 30.16. Circular cylinder: Pressure coefficient c_p as a function of an angle starting at the stagnation point, for $Re = 100$ (upper) and $Re = 3900$ (lower).

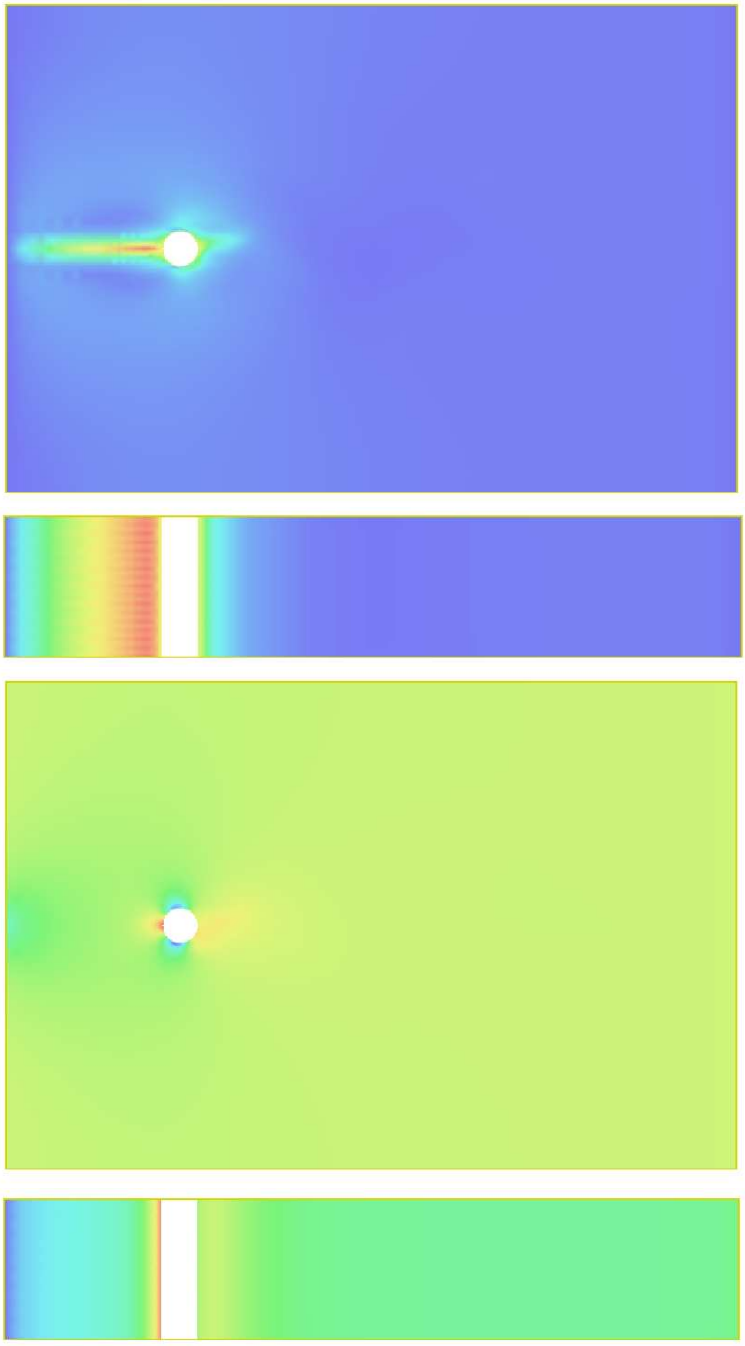

FIGURE 30.17. Circular cylinder at $Re = 100$: magnitude of dual velocity $|\varphi_h|$ (upper), and dual pressure $|\theta_h|$ (lower).

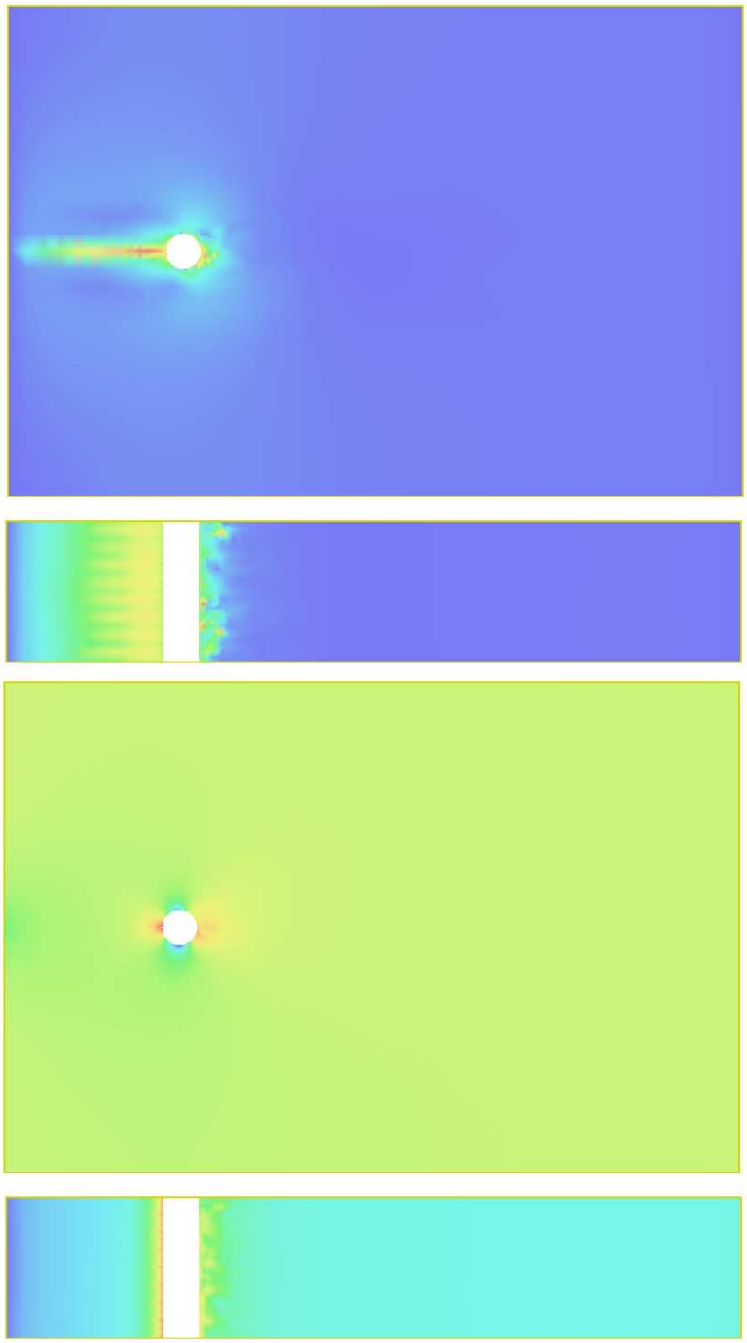

FIGURE 30.18. Circular cylinder at $Re = 3900$: magnitude of dual velocity $|\varphi_h|$ (upper), and dual pressure $|\theta_h|$ (lower).

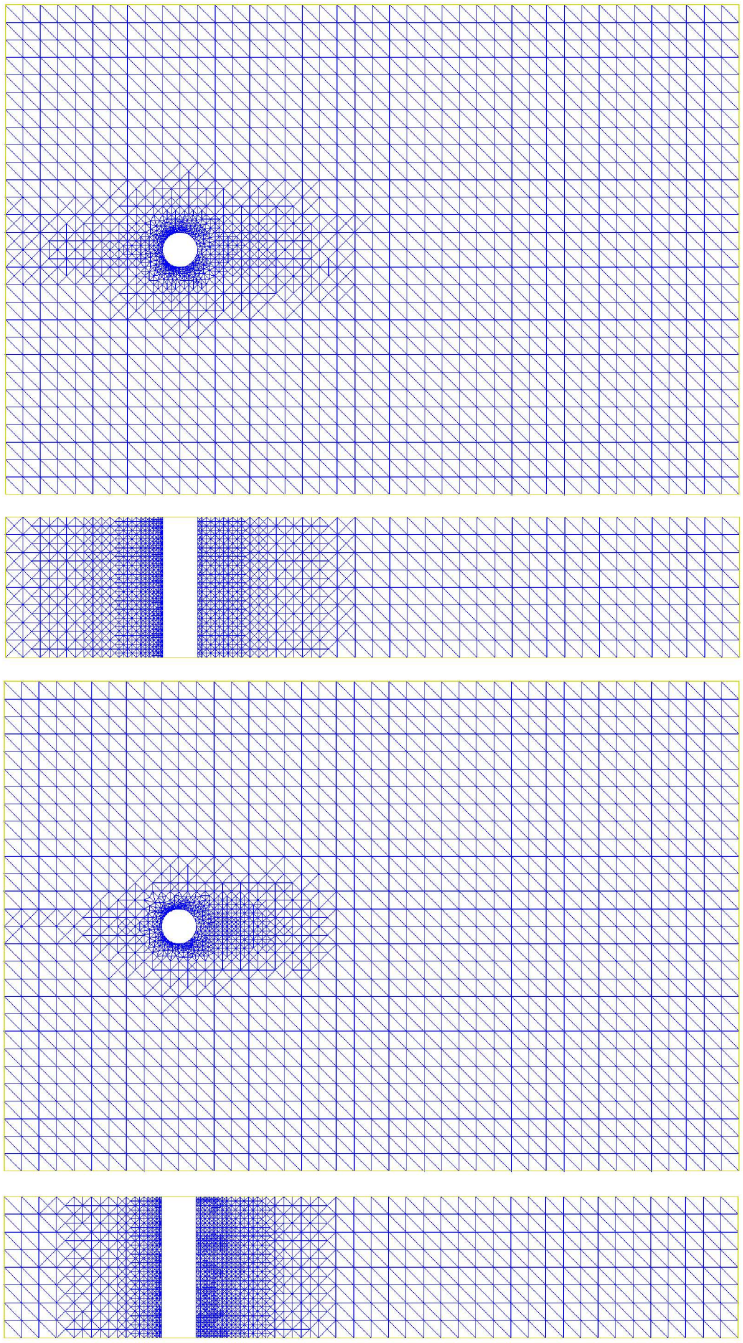

FIGURE 30.19. Circular cylinder: Computational mesh for $Re = 100$ (upper), and $Re = 3900$ (lower).

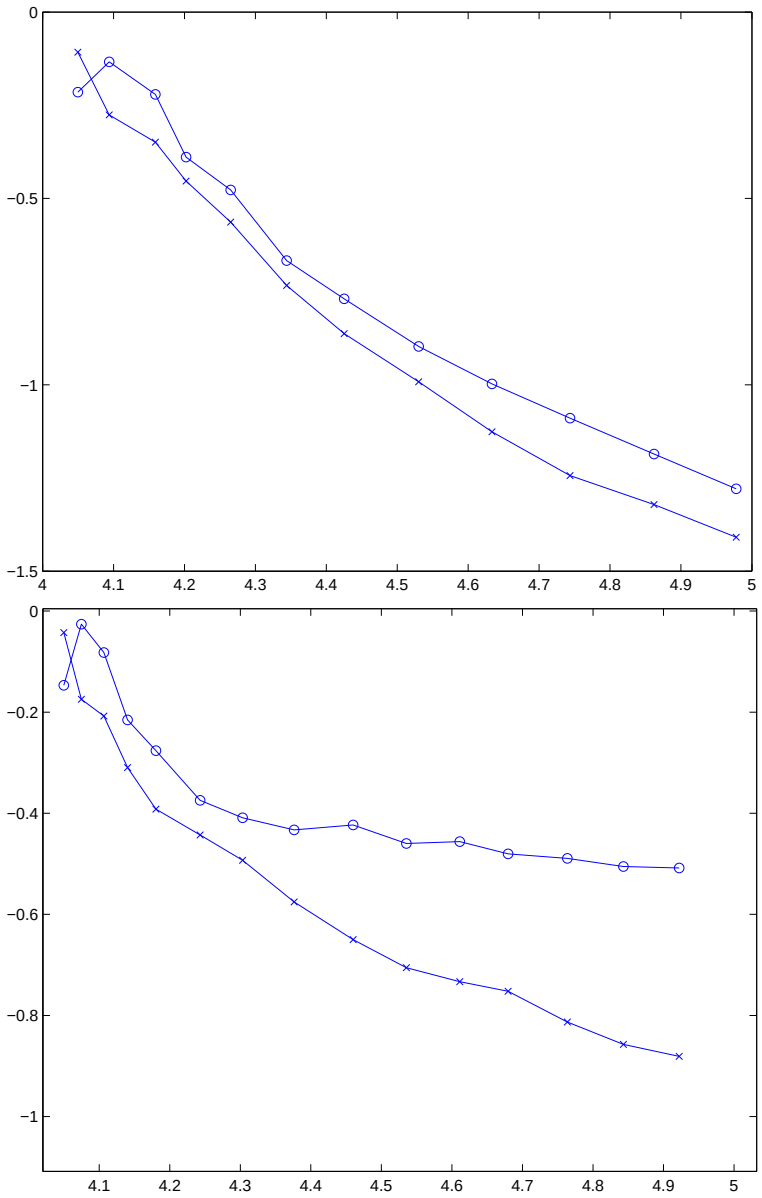

FIGURE 30.20. Circular cylinder: A posteriori error estimates e_D ('o') e_M ('x'), for $Re = 100$ (upper) and $Re = 3900$ (lower).

30.7.2 Dual solution and a posteriori error estimates

In Fig. 30.17-30.18 we plot the dual solutions corresponding to approximation of drag, and in Fig. 30.19 we plot the resulting computational meshes.

Studying the different meshes, we note that the mesh corresponding to $Re = 100$ is almost symmetric in the streamwise direction, and that the mesh refinement is spread wider vertically for this laminar flow than for the turbulent flow corresponding to $Re = 3900$. For $Re = 3900$, the mesh refinement is concentrated to the boundary layer of the cylinder and to the turbulent wake.

Overall, the mesh refinement is more localized for the higher Reynolds number, which is consistent with the dual problem being convection dominated, whereas the dual problem for the lower Reynolds number is more viscous and thus spreads the data more. For example, this results in a larger sensitivity to boundary conditions for low Reynolds numbers than for large.

In Fig. 30.20 we plot the a posteriori error estimates, where we find that the convergence rate is faster for $Re = 100$ than for $Re = 3900$, in particular the convergence with respect to the discretization error is slower for $Re = 3900$.

30.8 Sphere

The next example is the flow around a sphere with diameter $D = 0.1$, centered at $(5.5D, 7.5D, 7.5D)$, in a channel of dimension $10D \times 15D \times 15D$. We use no slip boundary conditions on the sphere, unit streamwise inflow velocity, slip boundary conditions on the lateral walls, and a transparant outflow boundary condition at the end of the channel.

A typical benchmark problem for turbulent flow in the literature concerns the case of $Re = 10\ 000$, and here the experiences from using G2 is very much the same as for the circular cylinder. We plot the solution in Fig. 30.22, and in Fig. 30.21 we plot the approximation of c_D as we refine 5% of the elements in each iteration of the adaptive algorithm.

For the sphere we have $c_D \approx 0.40$, which thus is less than half the drag of the cylinder, and in Fig. 30.22 we find that the wake behind the sphere is smaller than for the cylinder, consistent with lower drag.

30.8.1 Comparison with reference data

Using less than 30 000 nodes we capture the experimental reference value $c_D \approx 0.40$, and for the finer meshes using less than 10^5 nodes we capture the correct frequency $St \approx 0.20$. Compared to LES computations with *ad hoc* mesh refinement [20, 19, 21], G2 is about a factor 10-40 times cheaper in terms of the number of mesh points.

30.8.2 Dual solution and a posteriori error estimates

In Fig. 30.22 we plot snapshots of a dual solution and in Fig. 30.23 we plot the resulting computational mesh, where we note that again mesh refinement is concentrated to the boundary layers and the turbulent wake.

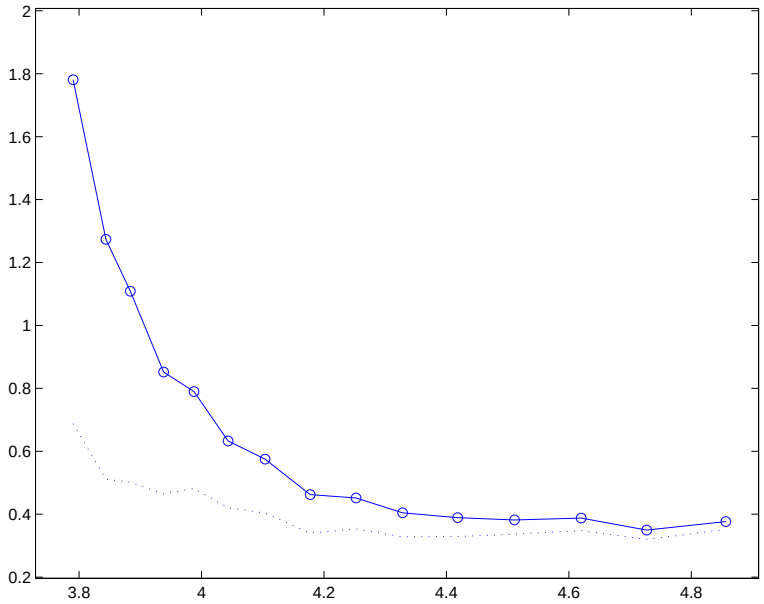

FIGURE 30.21. Sphere: approximative drag coefficient as a function of the 10-logarithm of the number of mesh points in space.

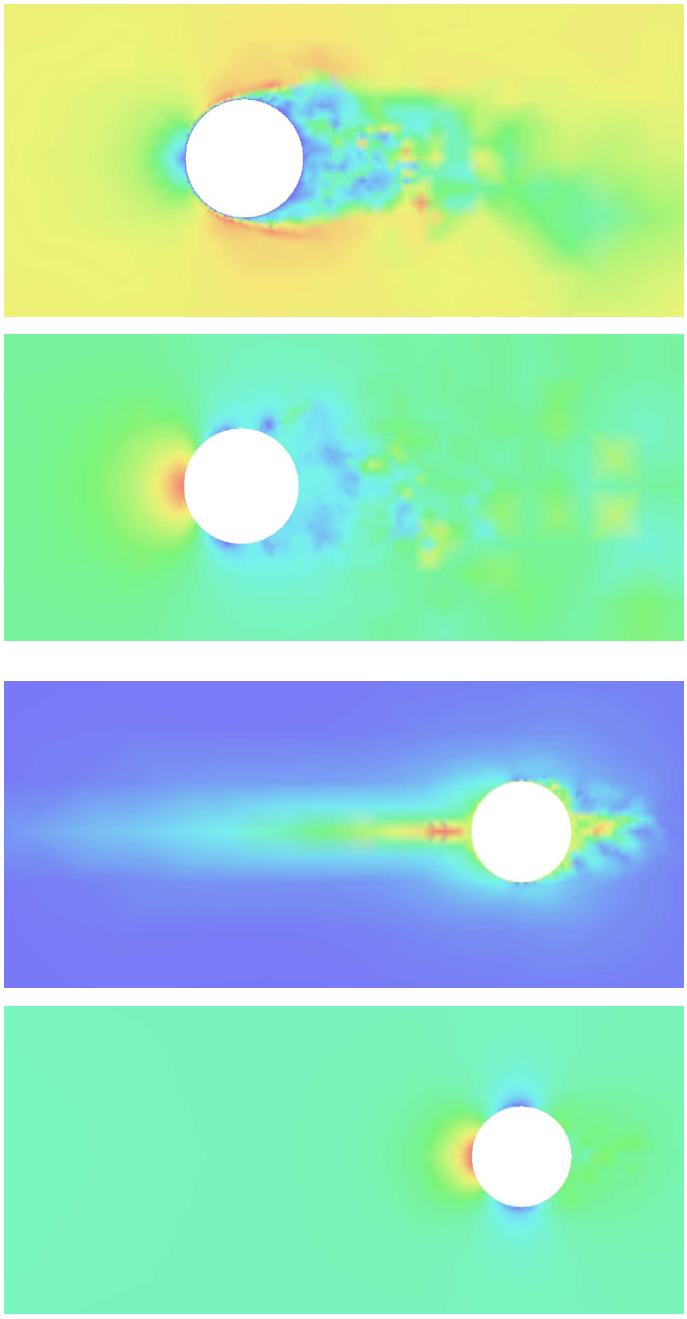

FIGURE 30.22. Sphere: magnitude of velocity and pressure (upper), and magnitude of dual velocity and pressure (lower).

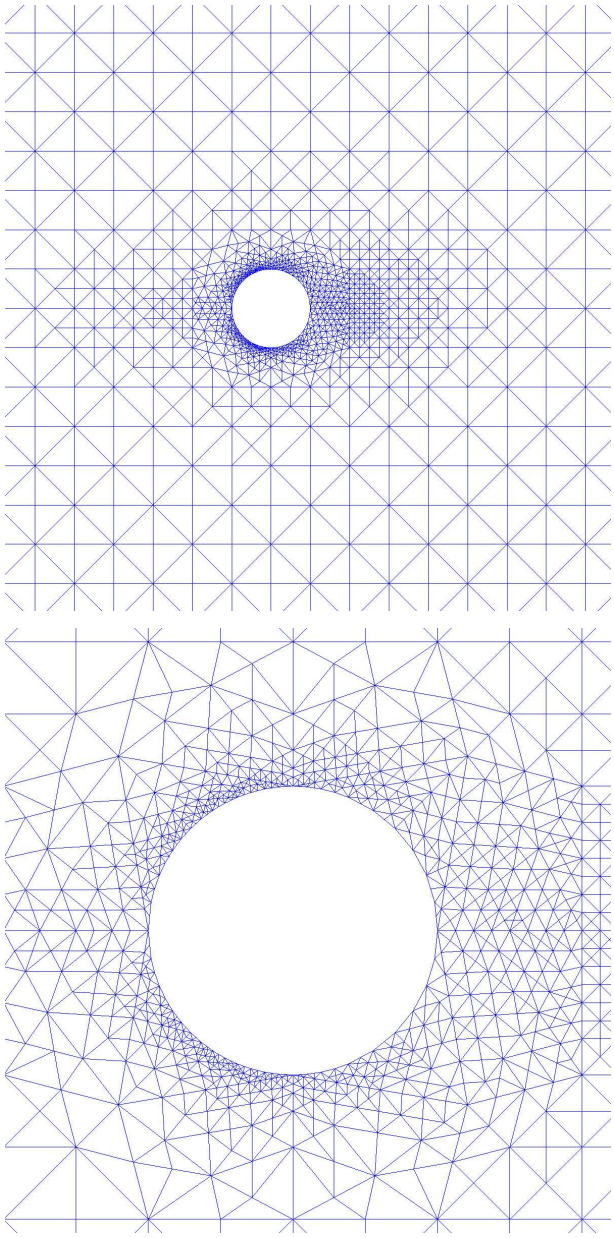

FIGURE 30.23. Sphere: computational mesh refined with respect to drag.

31
Boundary layers

> "Prandtl's contribution of the boundary layer was to realize that we can view the flow as being divided into two regions. The bulk of the flow can be regarded as a potential flow essentially the same as that studied by the mathematicians. Only in a small region near the body do viscous effects dominate." (On Ludwig Prandtl 1875-1953)

A common feature of fluid flow is the appearance of *boundary layers*, which are thin regions adhering to the boundary where the tangential fluid velocity rapidly changes from being zero at the boundary to taking on a non-zero value inside the fluid volume. Boundary layer flow represents *shear flow*, notably with strong shear because the tangential velocity gradient is large in the direction normal to the boundary. In Chapter 34 we shall see that laminar flows with strong shear are unstable and turn turbulent in a process of *transition* from laminar to turbulent flow. This process takes some time and therefore a boundary layer may stay laminar over some distance in the direction of the flow before transition. Boundary layers thus may be laminar or turbulent and the precise location in space-time for transition may be sensitive to surface roughness or inflow perturbations.

The generic model case of boundary layer flow is represented by flow over a (horisontal) flat plate with no-slip velocity boundary conditions. In this chapter we briefly recall some of the material concerning this model problem usually presented in texts on fluid dynamics based on heuristics of qualitative dimensional analysis or experiments. A goal of this heuristics has been to design *wall models* which can be used in conjunction with the NS equations instead of no-slip conditions to model the flow in turbulent

boundary layers without resolving the flow. The design of wall models is a part of turbulence modeling and carries the same difficulties, see [80] for an overview.

We compare the heuristics with some computational results using G2 without using any wall model. We find that we can simulate the transition in the boundary layer from laminar to turbulent flow on a PC, and we are able to compute the correct drag in the turbulent boundary layer found in experiments.

For bluff body flow, the contribution to drag from skin friction of the boundary layer is small, since drag is dominated by the pressure drop. However, the general flow pattern including the size and form of the turbulent wake and the location of boundary layer separation may significantly influence the drag. In Chapter 30 we found that we were able to compute the coorect drag and capture the large scale features of the flow, such as the separation, without resolving the boundary layers to their physical width.

Although, the problems in Chapter 30 are all flows with laminar separation, that is the boundary layer stays laminar before separation. For very high Reynolds numbers the boundary layer undergoes transition to turbulence before separation, which delays the separation of the boundary layer. We discuss this phenomenon further in Chapter 32, where we offer a solution with a very simple wall model, based on a friction boundary condition. Transition to turbulence is further discussed in Chapter 34.

31.1 Flat plate laminar boundary layer

We consider fluid flow of viscosity ν over a flat horisontal plate with a leading edge facing a constant inflow velocity U_∞. We estimate the thickness δ of a laminar boundary layer at a distance l from the leading edge assuming balance of the inertia and viscous forces estimated by

$$\begin{aligned} F_{viscous} &= |\nu\Delta u| \approx \frac{\nu U_\infty}{\delta^2}, \\ F_{inertia} &= |u\cdot\nabla u| \approx \frac{U_\infty^2}{l}, \end{aligned} \tag{31.1}$$

which gives $\delta \sim (\nu l/U_\infty)^{1/2}$, or more precisely with a heuristic constant,

$$\delta = 5\sqrt{\frac{\nu l}{U_\infty}}. \tag{31.2}$$

We see that qualitatively speaking, the boundary layer thickness increases as the viscosity and the distance from the leading edge increase, and decreases as the inflow velocity increases.

31.2 Skin friction for laminar boundary layers

We noted in Chapter 30 that a bluff body drag force has a contribution from *skin friction*, which is the friction force from the viscous stresses at the boundary, and from *pressure drag*, which relates to the pressure drop over the bluff body. For a flat horisontal plate the pressure does not contribute to the drag, and the drag is then equal to the skin friction, which we normalize to a *skin friction coefficient* c_f by dividing by $1/2 \times \rho A U_\infty^2$, with constant unit density $\rho = 1$, and $A = bl$ the area of the plate with b the width and l the length. We note the difference compared to Chapter 30, where we normalized the bluff body drag coefficient c_D by an area based on the cross section of the object normal to the flow.

The shear stress τ_0 on the plate is given by

$$\tau_0 = \nu \left(\frac{\partial u_1}{\partial x_2} \right)_0 \tag{31.3}$$

with x_2 the direction perpendicular to the plate, and u_1 the streamwise velocity component. Estimating $(\partial u_1/\partial x_2)_0 \sim U_\infty/\delta$, we obtain $\tau_0 \sim \nu\, U_\infty/\delta$, and using (31.2) we get

$$\tau_0 \sim \sqrt{\frac{\nu U_\infty^3}{l}}. \tag{31.4}$$

The total drag force D on the plate is then $\tau_0 bl$, which, with b the width of the plate, would then be

$$D \sim b\sqrt{\nu U_\infty^3 l}, \tag{31.5}$$

with the total drag being proportional to b, $\nu^{1/2}$, $U_\infty^{3/2}$ and $l^{1/2}$. For the skin friction coefficient (or drag coefficient) for laminar boundary layer flow, we then obtain with a heuristic constant

$$c_f = \frac{D}{\frac{1}{2}\, bl\, U_\infty^2} = 1.328\, \sqrt{\frac{\nu}{U_\infty l}}. \tag{31.6}$$

31.3 Skin friction for turbulent boundary layers

There are various attempts to derive models for the boundary layer thickness and skin friction for turbulent boundary layers, where the models are typically based on assumptions on the turbulent mean velocity profile and fit to experimental data.

For a flat plate, one may introduce a type of Reynolds number

$$Re_l = U_\infty l/\nu, \tag{31.7}$$

which is based on the length of the plate l, and typically one finds in experiments that the skin friction c_f for a turbulent boundary layer is proportional to $Re_l^{-0.2}$ [81], that is a very weak dependence on Re_l.

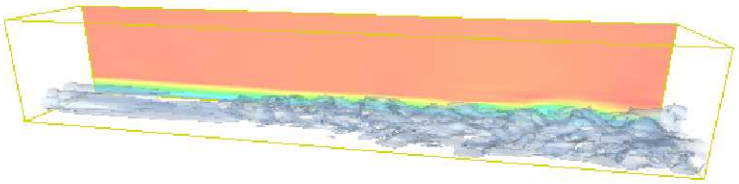

FIGURE 31.1. Transition to turbulence in a boundary layer computation, introducing Taylor-Görtler type perturbations (see Chapter 34) of amplitude 0.1 at the inflow.

31.4 Computing skin friction by G2

As an example, we consider a flow over a flat plate with $U_\infty = 1$, $b = 1$, and $\nu = 10^{-4}$. We assume a laminar boundary layer thickness $\delta = 0.2$, which corresponds to

$$l = \left(\frac{\delta}{5}\right)^2 \frac{U_\infty}{\nu} = \left(\frac{0.2}{5}\right)^2 \frac{1}{10^{-4}} = 16, \tag{31.8}$$

using (31.2), corresponding to a Reynolds number $Re_l = 1 \times 16/10^{-4} = 1.6 \times 10^5$. The corresponding skin friction of the laminar boundary layer would be

$$c_f = 1.328\sqrt{\frac{10^{-4}}{1 \times 16}} \approx 3.3 \times 10^{-3}.$$

We note that this is orders of magnitude lower than the drag for the bluff body problems in Chapter 30, for which the pressure drop dominates. For a turbulent boundary layer, one finds in experiments that c_f at $Re_l \approx 10^5$ is about 5×10^{-3} [81].

We now compute a boundary layer flow in a channel of dimension $12 \times 1 \times 1$ using G2. We initialize the computation with a linear streamwise velocity profile in a boundary layer of thickness 0.2 at the floor of the channel, given by initial and inflow data. The mesh is of dimension $129 \times 33 \times 33$ nodes, with 21 nodes vertically for $0 < x_2 \leq 0.2$ and 12 nodes vertically for $0.2 < x_2 \leq 1$. We introduce small rotational perturbations of size 0.1, and notice transition from laminar to turbulent flow at a certain distance from the inlet. Perturbations of this type are referred to as *Taylor-Görtler* type perturbations. We will come back to the problem of transition to turbulence in more detail in Chapter 34.

We now use the techniques of Chapter 30 to compute the drag (equal to skin friction) over the floor of the channel viewed as a plate. Using (30.3) to approximate drag gives a drag force $D \approx N^h(\sigma(\hat{U}))$, and normalizing with the relevant plate area, we have

$$c_f \approx \frac{N^h(\sigma(\hat{U}))}{\frac{1}{2}U_\infty^2 bl}, \tag{31.9}$$

where we get $c_f \approx 3 \times 10^{-3}$ for the laminar part of the boundary layer and $c_f \approx 5 \times 10^{-3}$ for the turbulent part, thus in accordance with experimental findings [81].

31.5 Summary

We have in this chapter given a glimpse into laminar/turbulent boundary layer flow including transition from laminar to turbulent flow. Using G2 we were able to simulate transition to turbulence in a flat plate boundary layer, where we found that our approximations of the skin friction coefficient c_f was in accordance with experimental data, both in the case of a laminar and a turbulent boundary layer.

32
Separation

The scientist describes what is; the engineer creates what never was.
(Theodore von Kármán 1881-1963)

Separation in a boundary layer occurs where the tangential flow velocity changes sign and *recirculation* occurs. Similarly, a separated flow may *reattach* where the tangential velocity changes sign in the opposite direction. Alternatively, we may define separation/reattachment to occur where the streamwise shear stress at the boundary changes sign. Separation is caused by a positive pressure gradient in the streamwise direction, resulting in a force opposing the flow with a retarding effect. If the opposing pressure force is strong enough over a sufficiently long time, the tangential velocity may change sign and separation will occur. We note that there is no separation in a flow over a flat plate, since the streamwise pressure gradient is negative.

In bluff body flow the drag depends critically on the location of separation, with an earlier separation (following the direction of the flow) increasing the drag because of a lower pressure in the wake and a larger pressure drop over the body. If the boundary layer undergoes transition to turbulence before separation, the separation is delayed, corresponding to *drag crisis*, with a significant reduction of the drag.

Separation is also connected to the *Magnus effect* causing a tennis ball with top spin to curve down (as skillfully exploited by Björn Borg).

32.1 Drag reduction for a square cylinder

For the bluff body problems with sharp corners in Chapter 30, the surface mounted cube and the square cylinder, the flow separates at the sharp leading edge of the body, to form a large turbulent wake resulting in high drag, as compared to the rounded geometries of the circular cylinder and the sphere with smaller wakes. For the surface mounted cube we have $c_D \approx 1.5$ and for the square cylinder $c_D \approx 2.2$.

But why is the drag so much lower for the surface mounted cube than for the square cylinder? One main difference between the two is the no-slip boundary condition on the channel floor for the surface mounted cube, implying that the difference in drag should connect to the presence of a boundary layer upstream the surface mounted cube, which has no equivalent for the cylinder. The presence of the boundary layer leads to separation and the formation of a horse-shoe vortex upstream the surface mounted cube, with less pressure build-up on the leading face of the cube compared to the cylinder.

To check the validity of this explanation of the difference in drag, we artificually introduce a boundary layer ahead of the square cylinder flow by inserting a horisontal plate in front of the cylinder. As expected the plate makes the flow separate ahead of the cylinder, causing c_D to drop from 2.2 to 1.4, see Fig. 32.1-32.2. The plate also causes the frequency in the wake oscillation to increase from $St \approx 0.14$ to $St \approx 0.16$.

32.2 Drag crisis

In Fig. 32.3 we plot the drag coefficient c_D of a circular cylinder as a function of Reynolds number, as obtained from experimental results presented in the literature. We note that for $Re < 100$, c_D is proportional to Re^{-1}, for $100 < Re < 10^5$ we have $c_D \approx 1$, while for $Re > 10^5$ we find that c_D first drops significantly and then rises back again. The drag reduction near $Re = 10^5$ is commonly referred to as *drag crisis*, which is related to transition to turbulence in the boundary layers causing a delayed separation. Simulation of drag crisis is a major challenge of turbulence simulation.

To resolve the very thin boundary layer of a high Reynolds number flow is too expensive, and thus many different wall-models have been proposed to capture the effect of the boundary layer without resolving it to its physical scale, see [80] for an overview.

Assuming the main effect of the boundary layer on the flow is the skin friction, we propose in [43] a simple approach to model the effect of the unresolved boundary layer, based on a slip with friction boundary condition, see Chapter 25, which may be viewed as a very simple wall-model. The problem is then to choose a suitable friction coefficient β. We now go on to

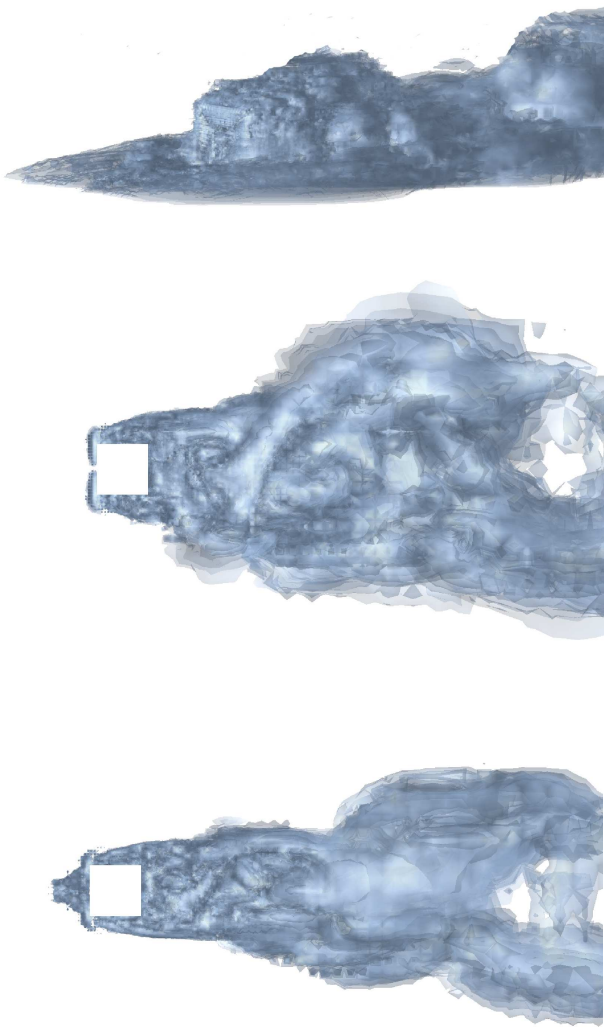

FIGURE 32.1. Isosurfaces for the magnitude of the vorticity for the cube (upper), the cylinder (middle), and the cylinder with a plate (lower).

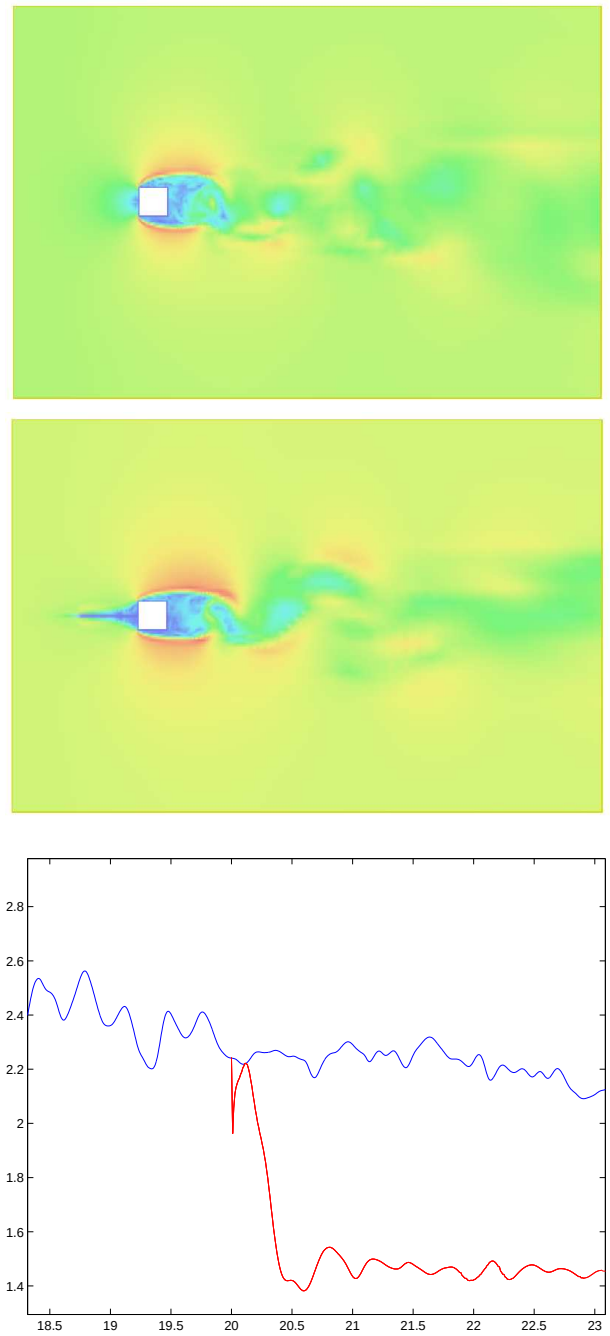

FIGURE 32.2. Magnitude of the velocity for the cylinder with and without the plate (upper), and a time series of the corresponding (normalized) drag forces when introducing the plate (lower).

present results from [43] using friction boundary conditions for simulating drag crisis.

In [58, 59] such a boundary condition is used to study reattachement of a low Reynolds number flow past a surface mounted cube in 2d and 3d as a function of the friction parameter β, and it is found that the reattachement is delayed with decreasig friction, as could be expected.

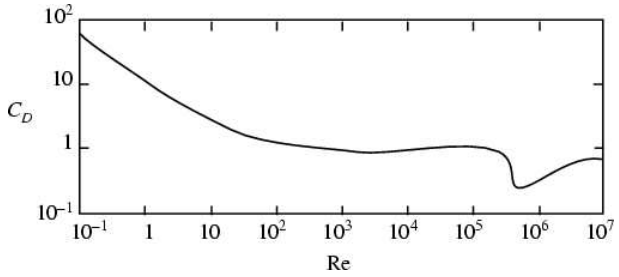

FIGURE 32.3. c_D for a circular cylinder as a function of Reynolds number.

32.3 Drag crisis for a circular cylinder

We now turn to the issue of modeling drag crisis for a circular cylinder of diameter D and length $4D$, with the cylinder in the direction of the x_3-axis, subject to a unit streamwise velocity inflow condition (in the x_1-direction) in a channel of length $21D$, width $4D$, and height $14D$. We use slip boundary conditions on the lateral walls of the channel, and a transparant outflow boundary condition at the end of the channel.

For very high Reynolds numbers the viscous ν-term in the computational method (25.12) is neglible if we do not resolve the finest scales of the flow, and may be dropped from the equation, corresponding to a cG(1)cG(1) method for the Euler equations. Apart from the boundary conditions, the dissipation in the flow is then only due to the stabilizing term in (25.12), with the energy dissipation expressed in (15.6).

The main computational challenge that remains is to capture the correct separation of the flow and the correct dissipation in the boundary layer. Flow separation is determined by the force balance in the momentum equation, where an adverse pressure gradient in the flow direction results in a force in the opposite direction which reduces the momentum. When this retarding force has reduced the momentum to zero near the boundary the flow separates. The skin friction of the boundary layer is reducing the momentum near the boundary, and thus high skin friction leads to an earlier separation. And conversely, when the skin friction decreases with the Reynolds number, the separation is delayed since the momentum near the boundary increases.

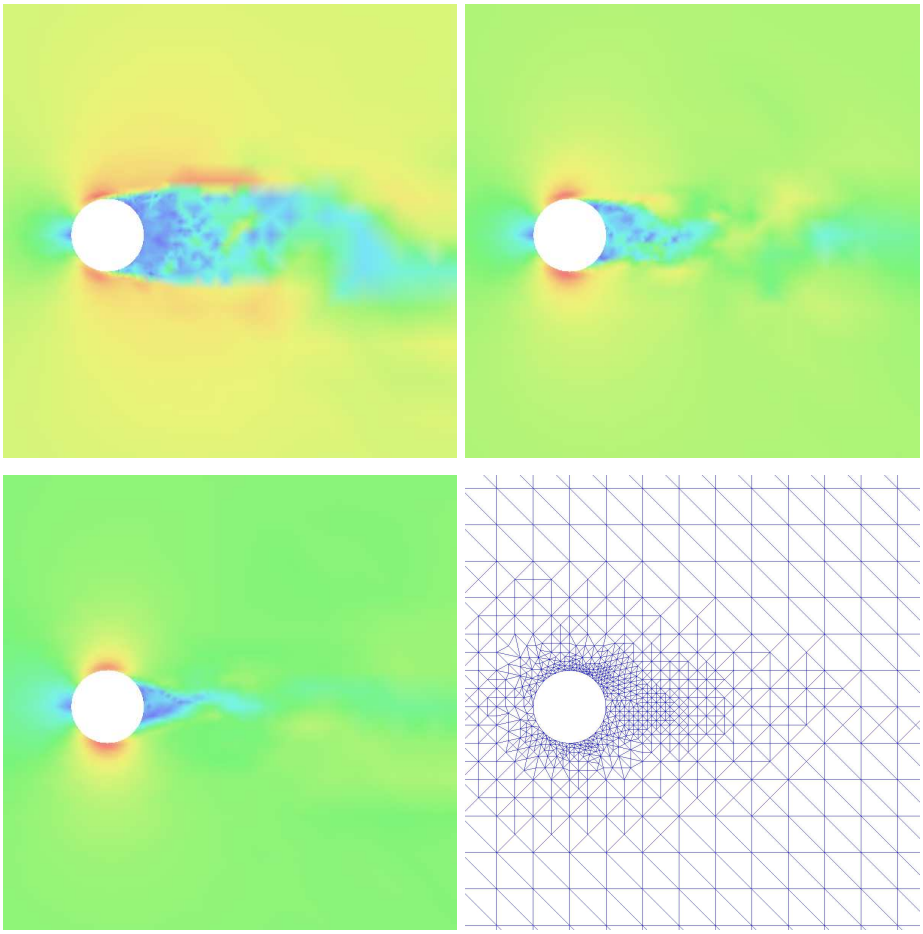

FIGURE 32.4. Drag crisis: magnitude of the velocity for G2 solutions for $\nu = 0$; $\beta = 2 \times 10^{-2}$ with $c_D \approx 0.7$ (upper left), $\beta = 1 \times 10^{-2}$ with $c_D \approx 0.5$ (upper right), $\beta = 5 \times 10^{-3}$ with $c_D \approx 0.45$ (lower left), and the mesh with 80 000 mesh points (lower right), in the x_1x_2-plane for $x_3 = 0.2$.

The idea underlying the model of the boundary layer is here that for flow separation, the important characteristic of the boundary layer is skin friction, and thus that it should be possible to capture a correct separation of the boundary layer as long as we have correct skin friction.

For the problems in Chapter 30 the flow separates from a laminar boundary layer, corresponding to a relatively high skin friction, where it is possible to capture the separation using no slip boundary conditions (corresponding to $\beta = \infty$).

The criterion for choosing β should be that the skin friction in the computation should be the same as in the physical problem. In Chapter 31 we found that experimental results indicate that skin friction has a very weak dependence on the Reynolds number, proportional to $Re^{-0.2}$ in the case of a flat plate, and thus a certain value for β should be characteristic for a rather wide range of Reynolds numbers. Experimental results also indicate that once we have drag crisis the separation is again rather stable for a range of Reynolds numbers. The exact Reynolds number for when the separation point starts to move downstream seems to be hard to determine, which is probably due to its relation to the transition to turbulence in the laminar boundary layers, which in turn depends on the level of perturbations in the boundary layer, which is very hard to determine in a realistic problem, see Chapter 34. Thus, there is a range of Reynolds numbers, close to where transition in the boundary layers occur, for which the separation of the flow is very hard to predict. From an engineering point of view it is then important to take both the sub-critical and the super-critical scenario into account.

Our model is here a cG(1)cG(1) method for the Euler equations together with a slip with friction boundary condition. Letting the friction parameter β go from large to small values, we find that the separation point is moving downstream. For $\beta = 10^{-2}$ we are able to capture the delayed separation of a drag crisis with $c_D \approx 0.4$, see Fig 32.4.

32.4 The Magnus effect

We consider the circular cylinder, now rotating counter-clockwise with an angular velocity corresponding to a unit magnitude of the velocity at the surface. The result of a computation using 62 000 nodes is shown in Fig. 32.5, where we clearly see an asymmetric separation of the flow, and an asymmetric pressure distribution, resulting in a downward force component, with $c_L \approx -1.5$ and $c_D \approx 1$.

This phenomenon of a rotation resulting in a transversal force, is referred to as the *Magnus effect*. The Magnus effect has been given different explanations, with the traditional one being that the velocity at the surface of the cylinder is enhanced on one side of the cylinder and decreased on the

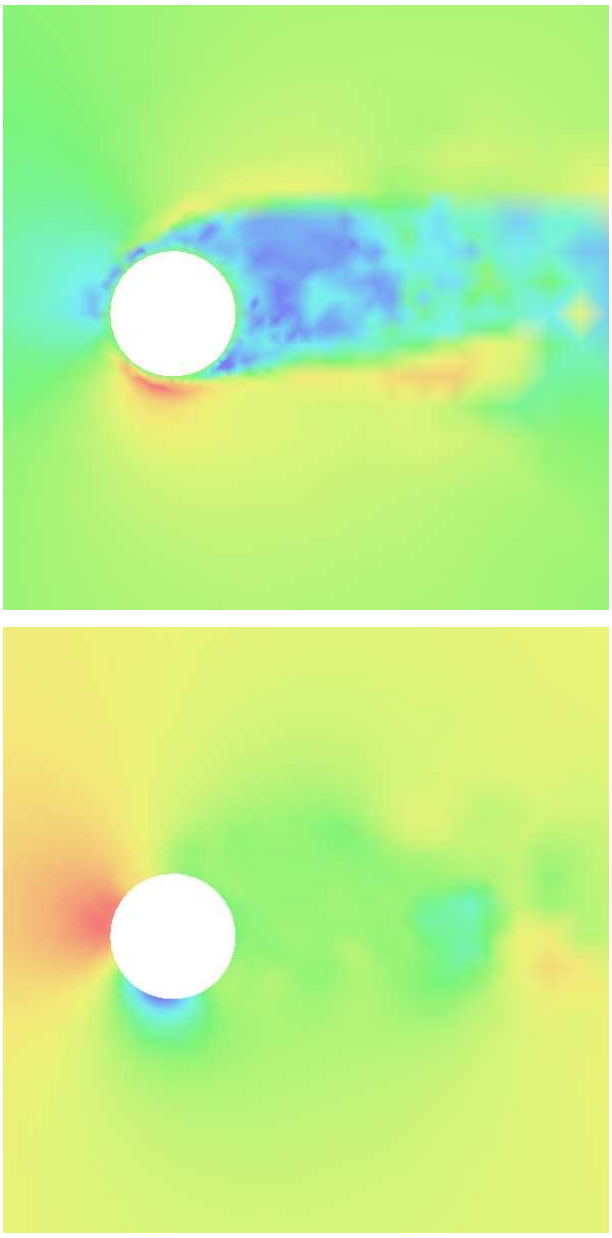

FIGURE 32.5. Asymmetric separation of a rotating cylinder (with the rotation counter-clockwise).

other side, which by Bernoulli's law leads to an assymetric pressure and a resulting transversal force. A more recent explanation is based on an assymetric boundary layer separation, where the separation is delayed on the side which rotates in the same direction as the free stream velocity, and an earlier separation on the opposite side. The resulting asymmetric wake is then redirecting flow momentum downstream the cylinder, resulting in a corresponding momentum on the cylinder in the opposite direction due to the law of conservation of momentum. Of course, also in this mode of explanation we can envoke Bernoulli's law for the resulting velocity to explain the transversal pressure difference.

Observations of a *reverse Magnus* effect are reported for high Reynolds numbers, where the resulting transversal force acts in the opposite direction. An explanation of this phenomenon is a transition to turbulence in the boundary layer on one side only, the side with the largest relative velocity, which leads to a delayed separation on that side resulting in an assymetric wake, now in the other direction.

32.5 Flow due to a cylinder rolling along ground

We now consider the problem of computing the flow due to a cylinder rolling along ground. A typical application comes from the automotive industry, where the flow of air past the wheels of a car or other vehicle is of much concern, since the drag of the wheels is a significant part of the total drag.

In [45], we use a computational model where we assume uniform rotation of a circular cylinder on flat ground, with the length of the cylinder being equal to it's diameter. In a coordinate frame moving with the constant speed of the centre of the cylinder, the problem is to determine the flow past a uniformly rotating circular cylinder with a fixed centre and in contact with the ground moving with the same velocity as the oncoming free stream of the fluid. The Reynolds number based on the free stream velocity and the cylinder diameter is set to $Re = 10\ 000$. We compare our results with a stationary cylinder on a stationary surface in a free stream, modeling a stationary wheel in a wind tunnel. In Fig. 32.7-32.9 we plot the solutions, the adaptively refined meshes, and the approximations of the drag coefficients as we refine the mesh, with $c_D \approx 1.3$ for the rotating cylinder and $c_D \approx 0.8$ for the stationary cylinder.

We note that since the ground is moving with the same speed as the flow for the rotating cylinder, we have no boundary layer, and thus no separation of the flow upstream the cylinder, which makes the flow very different from the flow past the stationary cylinder, where we have separation upstream the cylinder due to the presence of a boundary layer, similar to the flow around a surface mounted cube. We also have an earlier separation of the flow for the rotating cylinder, coupling to the Magnus effect. These

differences have important practical implications, illustrating limitations of wind tunnel testing.

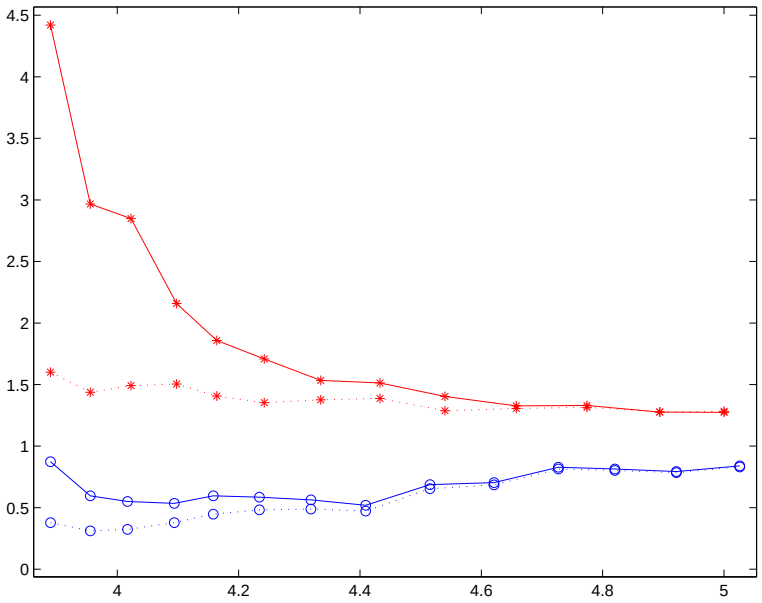

FIGURE 32.6. $\bar{c}_D^h$ vs $\log_{10}$ # nodes for the rotating ('*') and the stationary ('o') cylinder.

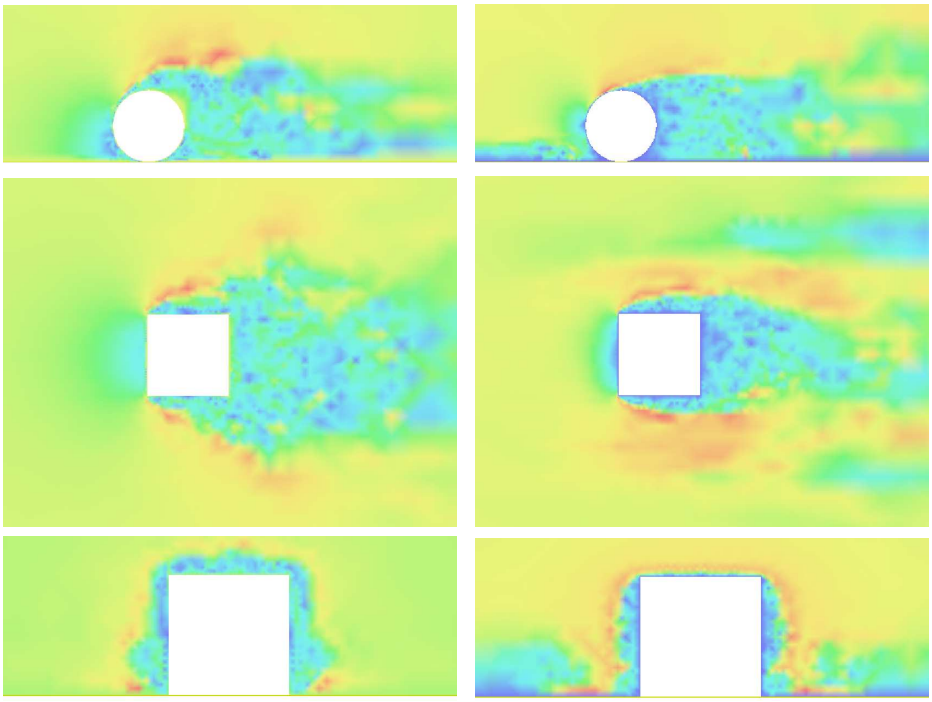

FIGURE 32.7. Snapshots of magnitude of velocity, for rotating (left) and stationary (right) cylinder, in the x_1x_2-, x_1x_3-, and x_2x_3-planes, through the center of the cylinder.

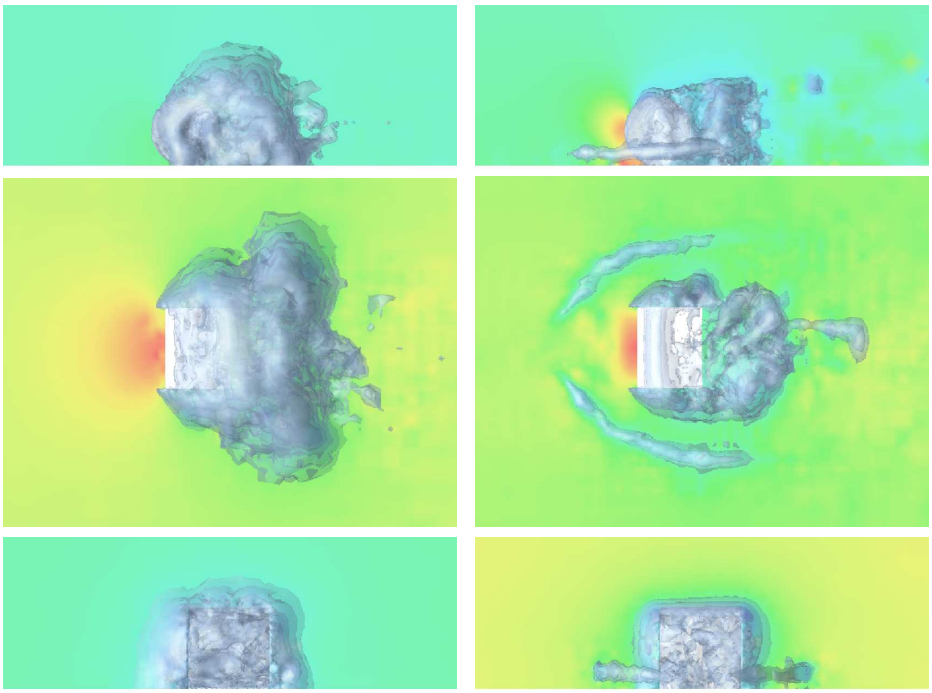

FIGURE 32.8. Snapshots of pressure and isosurfaces of negative pressure, for rotating (left) and stationary (right) cylinder, in the x_1x_2-, x_1x_3-, and x_2x_3-planes, through the center of the cylinder.

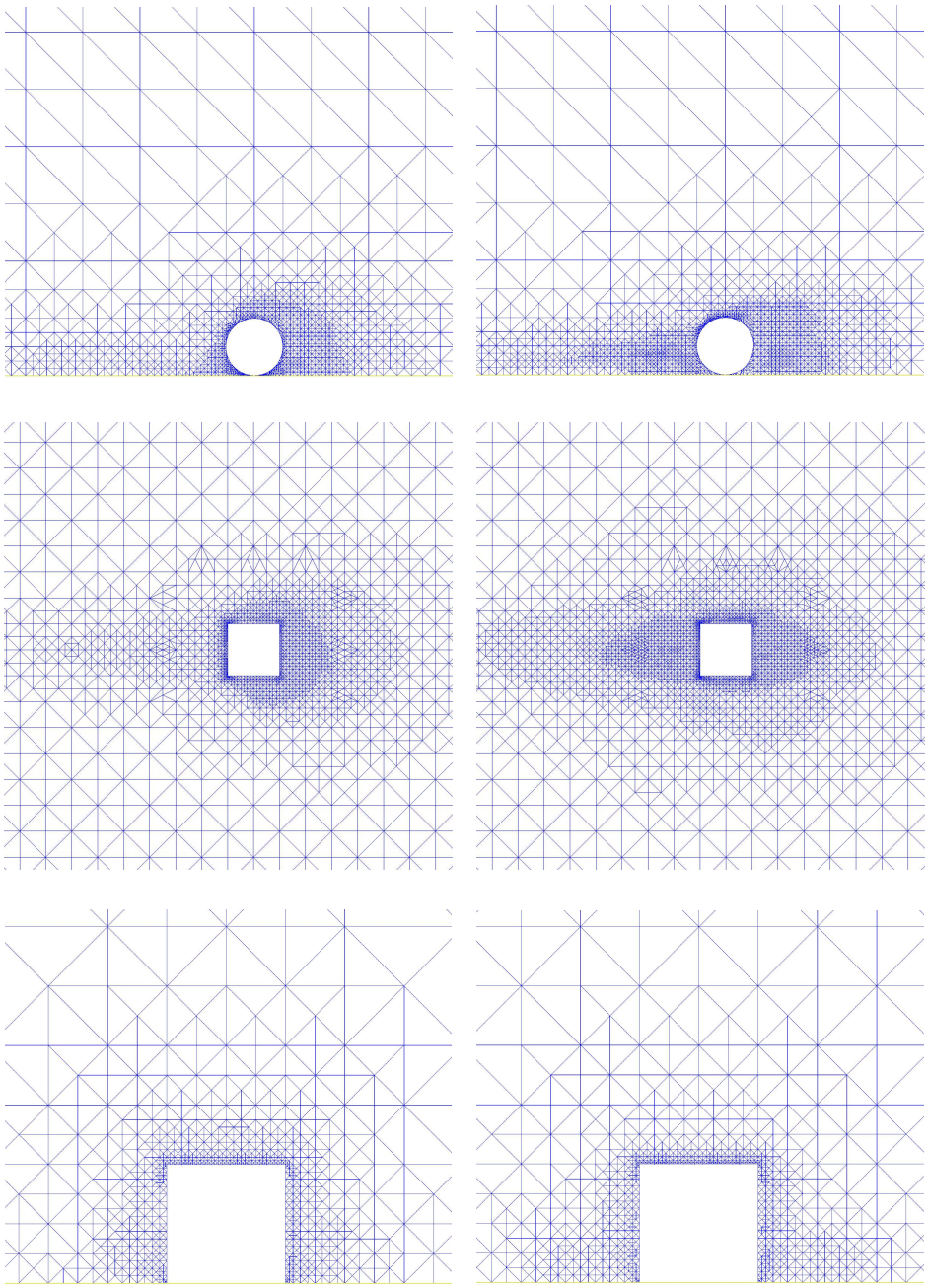

FIGURE 32.9. Refined mesh for the rotating (left) and the stationary (right) cylinder, in the x_1x_2-, x_1x_3-, and x_2x_3-planes.

33
EG2 and Turbulent Euler Solutions

In a reasonable theory there are no dimensionless numbers whose values are only empirically determinable. (Einstein)

I am convinced that human flight is both possible and practical. (Wilbur Wright 1899)

33.1 Turbulent Euler solutions

In Chapter 32 we introduced a skin friction model with friction parameter β, to model the effect of an unresolved turbulent boundary layer.

We now turn to the question of what happens as $\beta \to 0$, corresponding to the Reynolds number $Re \to \infty$.

Our computational model then reduces to G2 for the Euler equations with slip boundary conditions, which we here refer to as an *Euler/G2 model*, or an *EG2 model*. We note that in this model the only parameter is the discretization parameter h, and we show that some mean value output (such as drag) may be independent of h, making EG2 a completely parameter-free model of turbulent flow with respect to that output.

We study the flow past a circular cylinder where we find that as $\beta \to 0$ the separation points (lines) move downstream until they collapse into only one separation point (line), resembling the potential solution with zero drag. The potential solution is not stable and the single separation point (line) starts to oscillate, leading to vortex shedding and turbulence downstream, and for this solution the drag is high, sometimes even higher than for the laminar separation at lower Reynolds numbers.

That is, we have the following scenario as the friction parameter $\beta \to 0$ (corresponding to $Re \to \infty$) for the cylinder: (i) the laminar separation is stable for a range of Reynolds numbers ($Re \approx 10^3 - 10^5$) with drag $c_D \approx 1.0$, (ii) we then for a range of Reynolds numbers have drag crisis with a reduced wake and $c_D \approx 0.4$, when the separation points have moved downstream, and then (iii) the separation points collapse into one separation point which starts to oscillate resulting in vortex shedding and turbulence downstream, corresponding to high drag, with $c_D \approx 1$.

The EG2 solution corresponds to a physical flow with a very high Reynolds number, and we find solutions with similar characteristics of separation in one point and turbulent vortex shedding e.g. in studying geophysical bluff body problems, such as the flow of air past the Guadalupe Island or the Canary Islands.

We note that the need of a reliable computational model for the case $Re \to \infty$ will increase, due to the large dimensions of civil-, offshore and wind engineering structures of today.

33.2 The dual problem for EG2

We recall that in computing the drag for a body, the mesh is refined using the a posteriori error estimate (30.10) based on a discrete approximation of the continuous dual problem (13.4), with unit boundary data for the dual velocity in the streamwise direction on the surface of the body.

The underlying error representation is based on the continuous dual problem, and thus we have to be careful so that the discrete (G2) approximation of the dual problem is a good enough approximation of the continuous dual problem. For the problems in Chapter 30,32 we used no slip boundary conditions for the primal problem, and we found that after some mesh refinement the approximate dual weight in (30.10) is (approximately) independent of the mesh refinement, which is taken as an indication of the validity of (30.10).

Since the normal component of the convection velocity field (the primal velocity) in the dual problem is zero, the boundary data in the dual problem is only transported into the interior of the domain by diffusion. Although, with EG2 we have that $\nu = 0$ and thus it is not obvious how the boundary data is to be transported into the interior of the domain. In irregular parts of the flow, the stabilization will act as a numerical diffusion that will spread the data, but with the slip boundary condition in the primal problem the flow near the boundary will be smooth since there is no boundary layer, and thus the diffusion at the boundary will be very small.

With $\nu = 0$, the skin friction is zero and the mean drag F_D of a body with surface Γ_0 is solely due to the pressure:

$$F_D = \frac{1}{|I|} \int_I \int_{\Gamma_0} p n_1 \, ds \, dt, \tag{33.1}$$

with n_1 the streamwise x_1-component of the normal.

For EG2, we propose in [43] to study instead the following quantity:

$$\tilde{F}_D = \frac{1}{|I|} \frac{|\Gamma_0|}{|\tilde{\Gamma}_0|} \int_I \int_{\tilde{\Gamma}_0} p \tilde{n}_1 \, dx \, dt, \tag{33.2}$$

with $\tilde{n}_1$ a piecewise linear finite element function which is equal to n_1 at all nodes on Γ_0 and zero at all other nodes. We define $\tilde{\Gamma}_0 \subset \Omega$ as the union of all cells in the mesh with at least one vertex on the surface Γ_0. The quantity $\tilde{F}_D$ is then defined in (33.2) as a weighted average of the pressure p, which is of the same order of magnitude as F_D. For example, for Γ_0 a straight line segment in 2d which is normal to the x_1-axis, piecewise linear approximation on uniform triangles, or bilinear approximation on uniform quadrilaterals, gives that $\tilde{F}_D = 1/2 \; F_D$.

Formulating an adaptive method for the computation of $\tilde{F}_D$ instead of F_D leads to the same a posteriori error estimate (30.10), but now with a different set of data for the dual problem. Instead of the boundary data for the dual velocity leading to an error representation for F_D, we are now lead to choose the data in the dual problem as a force in the dual continuity equation; that is we use homogeneous velocity boundary data, and the source term $\hat{\psi} = (\psi_1, \psi_2)$ in (13.4) we choose to be

$$\psi_1 = 0, \quad \psi_2 = \frac{|\Gamma_0|}{|\tilde{\Gamma}_0|} \, \tilde{n}_1. \tag{33.3}$$

With this data the issue of the missing boundary layer for $\nu = 0$ is avoided. Instead the data (33.3) establishes a pressure difference over the body in the dual problem, resulting (as expected) in a similar dual flow field as for the dual problems at lower Reynolds number with a boundary layer, see Fig. 33.1. Here we find that the dual solution with pressure data (33.3) to a large extent resembles the dual solutions for $\beta = 0.1, 0.01$ (modulo the different sizes of the turbulent wake), whereas the dual solution with velocity boundary data is not able to transport the boundary data into the interior of the domain, but only transports the data at the downstream separation point upstream. Similarly we find that the corresponding adaptive mesh refinement algorithms result in different meshes.

We believe that the data (33.3) for the dual problem is more appropriate also at lower Reynolds numbers, when a turbulent boundary layer is not fully resolved.

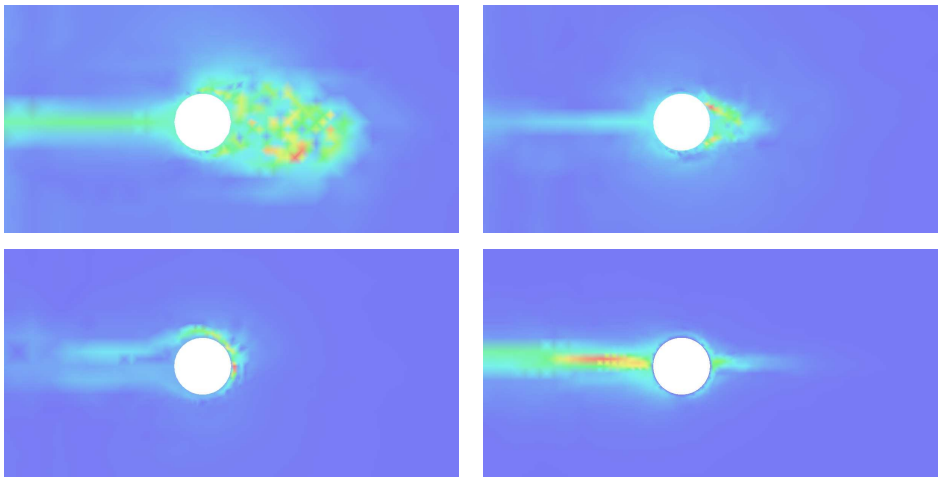

FIGURE 33.1. Magnitude of the dual velocity for $\beta = 0.1$ (upper left), 0.01 (upper right), 0 (lower left), using velocity boundary data, and for $\beta = 0$ using pressure data (loer right), in the x_1x_2-plane for $x_3 = 0.2$.

33.3 EG2 for a circular cylinder

The case of $Re \to \infty$ for a circular cylinder is in [87] referred to as the *ultimate regime* or the *T2 regime*. Experimental results for the circular cylinder is avaliable up to $Re \approx 10^7$ [81, 87], for which drag is low, corresponding to drag crisis.

In the recent book [87] this regime is descibed as the least known and understood state of flow, and the main reason is the lack of data. In wind tunnels there is an upper limit on the size of the cylinder, and increasing the velocity eventually will make the incompressible flow model invalid, due to effects of compressibility and cavitation. To find much higher Reynolds numbers we have to consider flow problems with very large dimensions, such as geophysical flows.

We now consider the case of $\beta = 0$ for the cylinder. As we refine the mesh with respect to the error in drag, we find that the Euler/G2 solution (or EG2 solution) approaches the potential solution, with separation in one point (line) only, and with zero drag. But as the mesh is further refined we find that the potential solution is unstable, and the separation point starts to oscillate, see Chapter 11. The oscillations are not simultaneous along the cylinder, instead there is a significant variation in the spanwise direction. The oscillating separation line generates streaks of vorticity in the streamwise direction, that undergo transition to turbulence causing alternating vortex shedding downstream, see Fig. 33.3.

We note that as soon as the potential solution looses stability, the drag increases due to the assymetry of the flow, and as the vorticity generation intensifies the drag increases further, see Fig. 33.2.

Indeed, studying geophysical bluff body problems, such as the flow of air past the Guadalupe Island or the Canary Islands in Fig. 33.4, it is clear that the flow separates in one point, which is consistent with the EG2 solution, rather than in two points with a wake in between, which is the case for a standard von Karman vortex street at low Reynolds numbers [74].

This indicates that the EG2 model may be very useful for geophysical applications. We note that this model is cheap since we do not have to resolve any boundary layers. The only parameter in the EG2 model is the discretization parameter h, and after some mesh refinement the EG2 solution is independent of h with respect to certain mean value output, such as drag for example. In particular, this means that we are able to determine the dimensionless number c_D (up to a tolerance) using a computational model without any empirical constants.

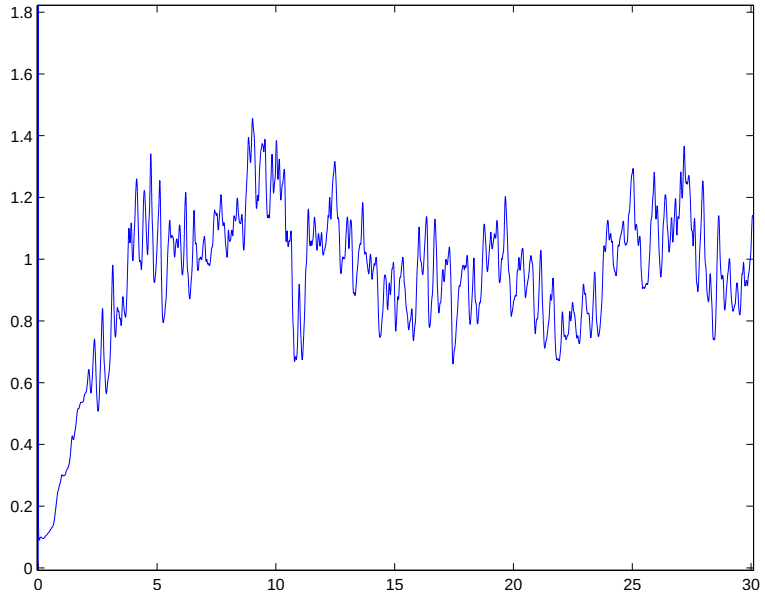

FIGURE 33.2. Time series of c_D for an EG2 solution.

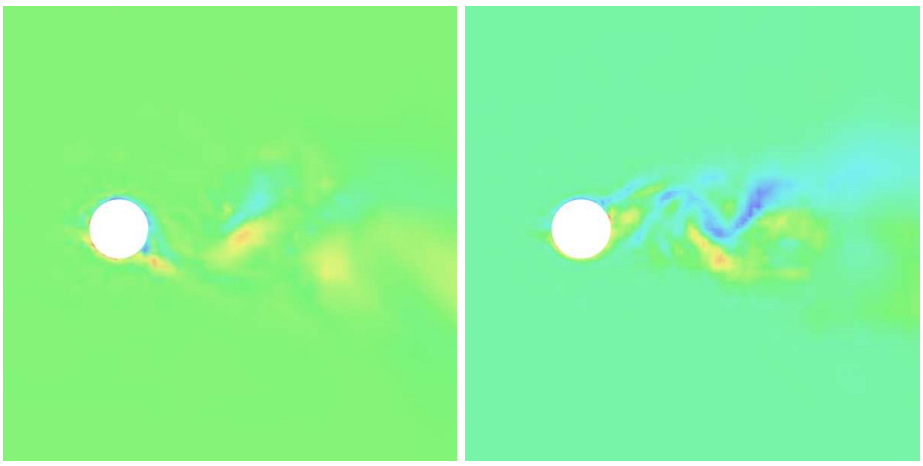

FIGURE 33.3. EG2: x_3-vorticity at two different times, in two different sections parallel to the x_1x_2-plane.

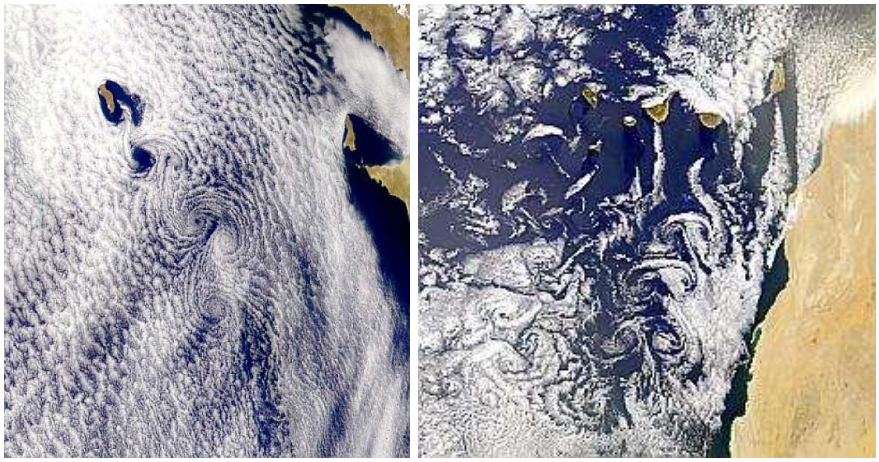

FIGURE 33.4. Clouds over the Guadalupe Islands (left) and the Canary Islands (right).

34
Transition to Turbulence

For a circular Poiseuille flow (pipe flow), as well as Couette flow, the classical linear-instability analysis leads to stability, whatever the Reynolds number and the wavenumber of the perturbation. Experimentally, one observes also turbulent spots in these flows (Marcel Lesieur).

For a time after this negative result (stability of Couette flow for all Reynold's numbers), it was thought that the method of small oscillations (classical theory) was unsuitable for the theoretical solution of the problem of transition. It transpired later that this was not justified, because Couette flow is a very restricted and special example (Hermann Schlichting).

In this book I have tried to bring together into a coherent account what I have learnt of hydrodynamic stability. Perhaps the most serious omission is the absence of any reference to viscous shear flow....in the last an author chooses to write only about those matters in which he has some confidence of his understanding (Subrahmanyan Chandrasekhar 1910-1995).

The sudden transition from smooth, laminar flow to turbulence as the fluid velocity is gradually increased remains one of the least adequately explained phenomena in all of classical physics (James Case, SIAM News, 2002).

34.1 Introduction

We now turn to the phenomenon of *transition* studied so intensively by Reynolds, without conclusive answers. In fact, transition has remained as one of the great mysteries of mechanics and physics. Reynolds unsuccessful experiments clearly exhibits the main difficulty in approaching the question of why and how transition takes place: Placing ourselves in the role of Reynolds, we stand there in front of the transparent pipe waiting to see the flow change from laminar to turbulent in front of our eyes. We stand there many days without transition to occur, and then suddenly it occurs one day, but then again not the next day. How are we to explain this scientifically? The trouble is of course that we seek to observe a phenomen of instability develop in front of our eyes. Now, if the flow we are watching indeed is unstable as laminar flow, then most likely it will be turbulent already from the beginning of the observation, since we would not be able to initialize the flow as an unstable laminar flow. On the other hand, if the flow is stable laminar, then it will continue to be so. In both cases the desired event of transition will not occur in front of eyes and another unsuccessful day of experiments will pass. Clearly, this would be frustrating to any scientist and certainly was for Reynolds.

In relatively recent years starting in the 1970s a picture of the transition process has been emerging which resolves the paradox, but which is still disputed by many fluid dynamicists and is not preseneted in standard fluid dynamics courses. This picture sheds new light on the mechanisms of *perturbation growth*, which is the central theme in any transition scenario, because perturbation growth is necessary for the global change from laminar to turbulent flow to occur. However, we seem to meet the same difficulty as that indicated above, namely: If the perturbation growth is large, then the flow can not be initialized as laminar, because large perturbation growth means the laminar flow is unstable. On the other hand, if the perturbation growth is small, then the flow will stay laminar. In both cases transition will not take place in front of our eyes.

The reason the scientific analysis of transition has been delayed, and still is, seems to be an unfortunate erronous interpretation of the standard mathematical explanation of perturbation growth, namely exponential growth connected to eigenvalues with positive real part of an associated Jacobian in the linearized NS equations. This type of eigenvalue analysis is also referred to as *normal mode analysis* focussed on finding exponentially growing eigenmodes or eigenfunctions. The error comes from forgetting that in order to give correct predictions, this perturbation analysis requires the Jacobian to be *normal* (which means that it has a full set of orthogonal eigenvalues as is the case if the Jacobian is symmetric). However, the Jacobian of the linearized NS equations for laminar flow is *non-normal* with degenerate eigenspaces or almost parallel eigenvectors, and in this case a normal mode eigenvalue analysis is misleading. Because of the degenerate

eigenspaces/vectors. In order for the laminar flow to be initialized there can be no positive eigenvales, and thus all eigenvalues would have to have non-positive real parts. A non-normal Jacobian may allow for *algebraic* perturbation growth over limited time until eigenvalues with (small) negative real part eventually take over. We shall see that this phenomenon may account for a perturbation growth in laminar shear flow which is proportional to the Reynolds number, thus with strong perturbation growth for large Reynolds number. We shall below see that indeed this type of perturbation growth is functional in the critical initial stage of the transition.

The other important aspect of transition is the perturbation level. We already remarked that if the product of perturbation level and perturbation growth is above a certain threshold, then transition will occur, and only then. This explains Reynolds frustrating experience: every day the perturbation growth was the same because the Reynolds number was the same, but the perturbation level varied from one day to next, being large enough for transition one day but not the next. In recent reproductions of Reynolds' experiments in his original basement laboratory at the University of Manchester, a general tendency was noticed of transition occuring at lower Reynolds' numbers today than hundred years ago. Most likely this is due to the increased traffic outside the laboratory, since the experiments were in both cases carefully performed with as small perturbations as possible from the laboratory set-up itself.

The problem of transition to turbulence in shear flow has mathematical features which seem to be present in a range of phenomena outside fluid dynamics, sharing the aspects of transition from order to chaos, occuring in e.g. crashes of stock markets, long-lasting marriages, superpowers, or sudden deaths of living organisms et cet. All these cases share the features of large algebraic perturbation growth arising from non-normality and have perturbation threshold levels for transition.

34.2 The Challenge

We seek to explain transition in stationary *Poiseuille flow* in a pipe studied by Reynolds or the related *Couette flow* between two parallell plates, both representing parallell shear flow also occuring in a laminar boundary layer. We thus consider flows which remains stationary laminar if the perturbation level (in initial/boundary conditions or forcing) is below a certain (small) threshold level, and which undergoe transition to turbulent flow for perturbations above the threshold level. We refer to this type of flow as *conditionally stable*. Depending on the perturbation level, pipe flow may undergo transition for a wide range of Reynolds' numbers from 1000 to 20 000. For sufficiently small Reynolds' numbers, the flow stays stationary laminar even under large perturbations.

We present a new picture of transition which essentially can be found in recent fluid dynamics literature, and which fundamentally differs from the old picture based on normal mode analysis presented by e.g. Orr-Sommerfeld. It is remarkable to note that the conflict between the two pictures/theories has not been settled in the fluid dynamics community: Both theories are usually presented as being valid, while in fact they are so fundamentally different that they can not both be true. We will return below to this intriguing aspect of the development of science.

We thus focus on stationary conditionally stable flow, such as Poiseuille or Couette flow representing *parallel stationary shear flow*, the most basic of all flows. In Poiseuille pipe flow the velocity distribution is parabolic, while in Couette flow the velocity profile is linear, the simplest of all shear flow distributions.

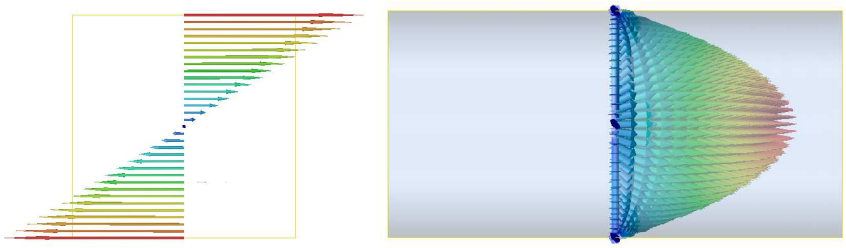

FIGURE 34.1. Couette flow (left) with a linear velocity profile, and Poiseuille flow (right) with a parabolic velocity profile.

We formulate the following *challenge of transition*: Explain physically and mathematically transition in conditionally stable stationary Poiseuille and Couette flow. Note that we require the perturbation threshold to be *small*. With large perturbations we may change the base flow to another completely different flow, and then the original base flow will have no significance. Thus, the introduced perturbations will be small, but if transition occurs then the result of these small perturbations will be a large perturbation of the flow. Accordingly, transition is intimately connected to *large perturbation growth*.

Further, large perturbation growth in Navier-Stokes equations directly couples to large perturbation growth in the linearized Navier-Stokes equations linearized at the stationary base flow. If there is little perturbation growth in the linearized equations, then there is little growth in the full Navier-Stokes equations. We may express the perturbation growth in the linearized equations as the problem of *stability* of this problem. Since the base flow is conditionally stable the linearized equations cannot have any exponentially unstable eigenmodes, that is all eigenvalues of the linearized stationary equations have positive (stable) real part: *there is no exponential modal growth*. The only possibility of perturbation growth in the linearized

equations is then *algebraic growth* connecting to the non-normal structure of the linearized equations. Typically, such algebraic growth is of the form $t\exp(-\nu t)$ which takes on a maximum of size $1/\nu$ for $t \approx 1/\nu$, thus representing large perturbation growth proportional to the Reynolds number. Typically, ν represents the real part of the eigenvalue with smallest real part with the corresponding eigenmode having slowest exponential decay.

34.3 The Failure of Classical Stability Theory

The classical theory of hydrodynamic stability has been unable to explain transition in shear flow, because it is focussed on modal exponential growth, which cannot be present in a conditionally stable flow. In particular, the classical stability analysis predicts Couette flow to be stable for all Reynolds' numbers at severe variance with experiments with transition occuring for Reynolds numbers starting at around 300 depending on the experiment. During the last decades the insight of the possibility of algebraic growth has been developing, which today offers a both mathematical and physical explanation and understanding of the critical first stage in the transition process. Pioneering work in this development was made by Mårten Landahl in the early 1980's, who pointed to the physical mechanism behind of non-modal growth, followed up by many researchers.

If the new picture of non-modal growth is the correct one, then the education of today in fluid mechanics could be rationalized a lot: almost all fluid mechanics text books today present the classical theory including more or less inventive "explanations" of its severe shortcomings concerning transition in e.g. Couette flow, and all this material could be replaced by something meaningful. This very process could itself be viewed as a form of transition to a new education, following the same principles as we are seeking to describe. At any rate, the notion of a critical Reynolds number for transition, which is part of the classical theory, cannot have any meaning. We motivate our standpoint in more detail below, based on a computational study of perturbation growth, and we give more substance to the critics of the old picture.

34.4 Non-modal Algebraic Perturbation Growth

We will below present the new picture of algebraic growth using a quantitative mathematical/computational analysis of *hydrodynamic stability* which concerns stability aspects of the NS equations. In particular, the analysis/computations show that even if the dye injected by Reynolds into the pipe indicates that fluid particles follow (almost) straight lines prior to the transition, the flow actually gets considerably reorganized as a neces-

sary *preparation* before the transition. We will refer to the reorganization as resulting from the *Taylor-Görtler mechanism* (or *lift-up* in Landahl's terminology) through which small transversal velocity perturbations after some time, result in large perturbations in the streamwise velocity, which is the initial and crucial phase of the transition process, and which expresses the large algebraic perturbation growth coupled to the non-normality of the linearized Navier-Stokes equations when linearized at shear flow.

34.5 Different perturbations

The basic problem of transition is thus perturbation growth: if a small perturbation may have a big effect on the flow, it may change the base flow to a new base flow with potentially exponentially unstable modes which in a secondary step may develop into a turbulent flow. The study of transition of stationary shear flow thus must be the study of *threshold levels for different types of perturbations*, with the threshold level being defined as the smallest level of a particular type of perturbation that leads to transition. We may call this a *special threshold level* characteristic of a specific type of perturbation. Correspondingly, we may define a *general threshold level* as the smallest level above which there is *some* perturbation leading to transition, so that perturbations below the general threshold level do not lead to transition.

Different perturbations may have very different perturbation growth, and the perturbations with largest perturbation growth, referred to as *optimal perturbations*, with correspondingly smallest threshold, of course must be the study to find the general threshold level.

The mathematical analysis of initial transition concerns perturbation growth in the linearized Navier-Stokes equations, with focus on identifying optimal type perturbations. In particular one may expect to search for optimal perturbations among eigen-modes which decay slowly.

The detailed analysis of threshold levels for transition can only be made computationally by testing the effect of different perturbations, for example with a focal objective to find optimal type perturbations.

We present below a computational study of transition with different types of perturbations and techniques to identify perturbations with strong growth and the corresponding general threshold levels.

34.6 Hydrodynamic stability

Hydrodynamic stability concerns the quantitative stability properties of the incompressible Navier-Stokes equations, which are of basic importance

for the understanding of phenomena of fluid flow such as bifurcation or transition to turbulence.

The basic study of hydrodynamic stability concerns the linearized Navier-Stokes equations for perturbations $\hat{\varphi} = (\varphi, q)$ of a given solution $\hat{u} = (u, p)$ of (25.1) corresponding to the initial data u_0 and right hand side f, obtained by subtracting $\hat{u} = (u, p)$ from the solution $\hat{u} + \hat{\varphi} = (u + \varphi, p + q)$ corresponding to the perturbed initial data $u^0 + \varphi^0$ and right hand side $f + g$, and omitting the quadratic perturbation term $(\varphi \cdot \nabla)\varphi$:

$$\begin{aligned} \dot{\varphi} + u \cdot \nabla\varphi + (\varphi \cdot \nabla)u - \nu\Delta\varphi + \nabla q &= g && \text{in } \Omega \times I, \\ \nabla \cdot \varphi &= 0 && \text{in } \Omega \times I, \\ \varphi &= 0 && \text{on } \partial\Omega \times I, \\ \varphi(\cdot, 0) &= \varphi^0 && \text{in } \Omega, \end{aligned} \tag{34.1}$$

where $(\varphi \cdot \nabla)u = (\sum_{j=1}^{3} \varphi_j u_{i,j})_{i=1}^{3}$ with $v_{,j} = \partial v/\partial x_j$.

The basic question in hydrodynamic stability is to estimate the solution (φ, q) of (34.1) in various norms in terms of appropriate corresponding norms of the data (g, φ_0), for example in terms of certain *stability factors*. A basic example is given by the *weak stability factor* $S_0(u, T, \varphi^0)$ depending on the base flow $\hat{u}$, final time T and the perturbation φ^0, defined by

$$S_0(u, T, \varphi^0) = \frac{\|\varphi\|_I}{\|\varphi^0\|}, \tag{34.2}$$

or the factor $S_0(u, T)$ depending on the base flow u and the final time T with a maximization over all perturbations, defined by

$$S_0(u, T) = \sup_{\varphi^0 \in L_2} \frac{\|\varphi\|_I}{\|\varphi^0\|}, \tag{34.3}$$

where φ is the solution of (34.1) with $g = 0$ and initial data $\varphi^0 \neq 0$, and $\|v\| = \|v\|_{L_2(\Omega)}$, $\|v\|_I = \sup_{0<t<T} \|v(\cdot, t)\|$. The factor $S_0(u, T, \varphi^0)$ measures the growth over the time interval $(0, T)$ of the perturbation φ^0 of initial data, related to a special perturbation threshold, and the factor $S_0(u, T)$ measures the maximal growth over the time interval $(0, T)$ of a perturbation of initial data, related to a general perturbation threshold. We refer to these stability factors as *weak* because we measure the solution itself and not derivatives thereof.

We now give estimates of the stability factor $S_0(u, T)$ in two extreme cases: a *worst case* with exponential dependence in KT, where K is a measure of the gradient, related to an unstable flow with exponentially growing eigenmodes, and a *best case* with linear dependence in KT related to a conditionally stable flow with no exponentially growing eigenmodes. Assuming that $K = 1$ and $T = \nu^{-1} = Re$, the dependence can be expressed as an exponential or linear dependence in the Reynolds' number Re, with the exponential dependence indicating instability even for moderately large Reynolds' numbers, while the linear dependence corresponds to a smooth laminar flow.

34.7 Worst case exponential perturbation growth

Multiplying the first equation of (34.1) by φ and integrating over $\Omega \times (0,t)$, using the incompressibility of both u and φ, one gets for $t > 0$:

$$\|\varphi(\cdot,t)\|^2 \leq -2\int_0^t \int_\Omega (\varphi\cdot\nabla)u\cdot\varphi\, dxds + \|\varphi^0\|^2,$$

from which follows by the Grönwall inequality that $S_0(u,T) \leq \exp(CKT)$, with $C \approx 1$, which is a worst case exponential estimate. We note that the exponential growth is generated by the presence of the zero order term $(\varphi\cdot\nabla)u$, as in the simple scalar ode $\dot\psi = K\psi$ with solution $\psi(t) = \psi(0)\exp(Kt)$. A flow with this very strong perturbation growth cannot exist as a stable flow. Since there are some more or less stable flows observable in nature, it must be possible in special cases to obtain reduced growth rates by using particular features of the zero order coupling term $(\varphi\cdot\nabla)u$. A basic such case arises in shear flow, with a particular coupling of the perturbations of the velocities in streamwise and transversal directions, which we now turn to.

34.8 Linear perturbation growth in shear flow

Shear flow is a basic type of flow, occuring in pipe flow and boundary layer flow, where the streamlines are almost parallel straight lines and the transversal variation of the streamwise flow velocity is balanced by a shear force. We now show that for such flows the weak stability factor $S_0(u,T)$ defined by (34.3) satisfies $S_0(u,T) \approx CKT$, with $C \approx 1$. This estimate underlies the first crucial step in the scenario of transition to turbulence in shear flow to be presented, showing that a perturbation growth $\approx \nu^{-1}$ over time intervals of length $T = \nu^{-1}$ is possible even for smooth flows with $K = 1$, indicating that a small initial perturbation (of size ν say) in fact may cause the base flow to change significantly if we only wait long enough (over a time interval $\approx \nu^{-1}$).

We consider a smooth parallel stationary base flow (u,p) in an infinitely long straight pipe $\Omega = \mathbb{R}\times\omega$, where ω in the (x_2,x_3)-plane is the cross-section (with smooth boundary) of the pipe of diameter of size 1. The axis of the pipe is oriented along the x_1-axis, and u vanishes on the boundary of the pipe. We assume that the base flow (u,p) is independent of x_1 and satisfies the following assumptions

$$\|u_1\| \approx 1, \qquad \|\bar\nabla u_1\|_\infty = C, \qquad \|\bar u\|_\infty + \|\bar\nabla \bar u\|_\infty \leq c\nu, \tag{34.4}$$

where $\|\cdot\|_\infty$ denotes the maximum norm, $\bar u = (u_2,u_3)$, and $\bar\nabla = (\partial/\partial x_2, \partial/\partial x_3)$ is the gradient with respect to (x_2,x_3). Here and below, c and C denote

positive constants of moderate size, which are independent of ν. The assumption (34.4) including a smooth streamwise velocity $u_1 \approx 1$ in the x_1 direction being independent of x_1, and smooth small transversal velocities $\bar{u}$ of size $\approx \nu$, may be viewed as a basic characteristic of shear flow. A further characteristic may be that the derivatives in the streamwise direction x_1 are one order smaller in ν, so that $u_{1,1} \sim \nu$ and $u_{2,1}, u_{3,1} \sim \nu^2$. We will return to this feature below in the presentation of the scenario of transition to turbulence. We further assume as already indicated that $T \sim 1/\nu = Re$.

Assuming that also the perturbations (φ, q) are independent of x_1, the linearized equations (34.1) take the following form:

$$\begin{aligned} \dot{\varphi}_1 + u \cdot \nabla\varphi_1 + (\bar{\varphi} \cdot \bar{\nabla})u_1 - \nu\Delta\varphi_1 &= 0 \quad \text{in } \omega \times I, \\ \dot{\bar{\varphi}} + u \cdot \nabla\bar{\varphi} + (\bar{\varphi} \cdot \bar{\nabla})\bar{u} + \bar{\nabla}q - \nu\Delta\bar{\varphi} &= 0 \quad \text{in } \omega \times I, \\ \bar{\nabla} \cdot \bar{\varphi} \equiv \varphi_{2,2} + \varphi_{3,3} &= 0 \quad \text{in } \omega \times I, \\ \varphi &= 0 \quad \text{on } \partial\omega \times I, \\ \varphi(\cdot, 0) &= \varphi_0 \quad \text{on } \omega. \end{aligned} \tag{34.5}$$

These equations have a very particular structure. First, the equations for the transversal velocity $\bar{\varphi}$ are fully decoupled from the equation for the streamwise velocity φ_1, and have zero order terms with small coefficients because $|\bar{\nabla}\bar{u}| \leq c\nu$. Secondly, the zero order term $(\bar{\varphi} \cdot \bar{\nabla})u_1$ in the equation for φ_1 does not contain φ_1, because $u_{1,1} = 0$. This means that the zero order terms in (34.5) have a special form, which makes it possible to reduce the general worst case exponential growth of $S_0(T)$, to a linear growth. The basic structure of the equations (34.5) is present in the system of ordinary differential equations $\dot{\varphi}_1 - \varphi_2 = 0$, $\dot{\varphi}_2 = 0$, for $t > 0$, $\varphi^0 = (0, \varphi_2^0)$ with solution $\varphi_1(t) = t\varphi_2^0$, $\varphi_2(t) = \varphi_2^0$, showing a linear growth of φ_1. The growth in this system is very different from the exponential growth obtained by changing the first equation to $\dot{\varphi}_1 - \varphi_1 = 0$, with the exponentially growing solution $\varphi_1(t) = \exp(t)\varphi_1^0$, assuming now $\varphi_1^0 \neq 0$. Clearly, the change from linear to exponential growth is related to the nature of the coupling, with the direct coupling $\dot{\varphi}_1 = \varphi_1$ being much stronger than the indirect coupling $\dot{\varphi}_1 = \varphi_2$, where $\dot{\varphi}_2 = 0$.

We now prove a basic estimate giving a linear growth bound in time of the streamwise velocity perturbation φ_1 generated by a small transversal perturbation $\bar{\varphi}^0$. We refer to the physical phenomena causing this perturbation growth as the *Taylor-Görtler mechanism*, which has a crucial role in transition to turbulence. The bound is based on an energy estimate using the decoupling of φ_1 and $\bar{\varphi}$, resulting from the fact that $q_{,1} = 0$ and $\varphi_{1,1} = 0$. Below we present computations showing that the bound is sharp and that linear perturbation growth actually occurs.

Theorem 34.1 *The stability constant $S_0(u, T)$, defined by (34.3) in the context of x_1-independent pipe flow (u, p) satisfying (34.4), satisfies the*

following bound for $T = \nu^{-1}$:

$$S_0(u,T) \le C\nu^{-1}, \tag{34.6}$$

where C depends on the constant c in (34.4). If the constant c is small enough, then the estimate (34.6) holds for $T \ge \nu^{-1}$ with ν^{-1} replaced by T.

Proof: First, multiplying the equation for $\bar\varphi$ by $\bar\varphi$, and integrating over ω using the fact that $\bar\nabla \cdot \bar u = \bar\nabla \cdot \bar\varphi = 0$, shows that

$$\frac{1}{2}\frac{d}{dt}\|\bar\varphi\|^2 + \nu\|\bar\nabla\bar\varphi\|^2 \le c\nu\|\bar\varphi\|^2.$$

Using Grönwall's inequality, we then find that

$$\|\bar\varphi(\cdot,t)\|^2 \le \exp(C\nu t)\|\bar\varphi^0\|^2, \qquad 0 < t \le T.$$

Next, multiplying the equation for φ_1 by φ_1 and using again the fact that $\bar\nabla \cdot \bar u = \bar\nabla \cdot \bar\varphi = 0$, we get

$$\frac{1}{2}\frac{d}{dt}\|\varphi_1\|^2 + \nu\|\bar\nabla\varphi_1\|^2 \le C(\frac{1}{2}\nu\|\varphi_1\|^2 + \frac{1}{2}\nu^{-1}\|\bar\varphi\|^2),$$

from which the desired estimate follows by integration. The modification with c sufficiently small is straight forward. □

A challenge is to extend the above result to different base flows $\hat u = (u,p)$ with slight x_1-dependence. As a small contribution to this problem we present the following example: we assume in addition to (34.4) that

$$\|u_{1,1}\|_\infty \le c\nu, \qquad \|\bar u_{,1}\|_\infty \le c\nu^2, \tag{34.7}$$

where c is a positive constant, and we allow the perturbation velocity φ to depend on x_1, but we assume for the pressure part q that $q_{,1} = 0$ and that correspondingly the incompressibility condition reduces to $\varphi_{2,2} + \varphi_{3,3} = 0$, which corresponds to a slight compressibility of the original fluid with a pressure perturbation q, which is constant in the x_1-direction. In this case the linearized perturbation equations take the form:

$$\begin{aligned}
\dot\varphi_1 + u\cdot\nabla\varphi_1 + (\varphi\cdot\nabla)u_1 - \nu\Delta\varphi_1 &= 0 && \text{in } \Omega\times I,\\
\dot{\bar\varphi} + u\cdot\nabla\bar\varphi + (\varphi\cdot\nabla)\bar u + \bar\nabla q - \nu\Delta\bar\varphi &= 0 && \text{in } \Omega\times I,\\
\varphi_{2,2} + \varphi_{3,3} &= 0 && \text{in } \Omega\times I,\\
\varphi &= 0 && \text{on } \partial\Omega\times I,\\
\varphi(\cdot,0) &= \varphi_0 && \text{on } \Omega,
\end{aligned}$$

which again decouples and thus is amenable to analysis as above.

The *Orr-Sommerfeld equations* are the linearized Navier-Stokes equations linearized at x_1-directed parallel flow $u = (u_1(x_2),0,0)$ between

two parallel plates with normal in the x_2 direction, assuming the perturbations are independent of the transversal direction x_3 parallel to the plates and also that $\varphi_3 = 0$: find $(\varphi(x_1, x_2, t), p(x_1, x_2, t))$ such that for $|x_2| < d$, $x_1 \in \mathbb{R}$, $t > 0$,

$$\begin{aligned} \dot{\varphi}_1 + u \cdot \nabla \varphi_1 + u_{1,2}\varphi_2 - \nu \Delta \varphi_1 + p_{,1} &= 0, \\ \dot{\varphi}_2 + u \cdot \nabla \varphi_2 - \nu \Delta \varphi_2 + p_{,2} &= 0, \\ \varphi_{1,1} + \varphi_{2,2} &= 0, \end{aligned} \tag{34.8}$$

with $\varphi(x_1, \pm d) = 0$, and the initial condition $\varphi(x_1, x_2, 0) = \varphi^0(x_1, x_2)$, and where $2d$ is the distance between the plates. In the case of Couette flow $u_1(x_2) \propto x_2$ and for Pouiseuille flow $u_1(x_2) \propto (1 - (x_2/d)^2)$, the stability factor $S_0(u, T)$ turns out to be much smaller than the corresponding factor for the linearized problem (34.5) with x_1 independent perturbations. We conclude that x_3-independent perturbations seem to be less significant than x_1-independent perturbations, and thus conclude that the Orr-Sommerfeld equations do not seem to be that relevant in initial transition to turbulence in shear flow.

34.9 Computational transition in shear flows

In Section 34.6 we showed that linear perturbation growth proportional to the Reynolds' number is possible in parallel shear flow. We will now investigate this linear perturbation growth computationally, for conditionally stable Couette and Poiseuille flows.

We now present computational results for Couette flow and Poiseuille flow in a pipe along the x_1-axis with square cross section 1×1, assuming periodicity in the streamwise direction. We use cG(1)cG(1) on the unit cube with a regular tetrahedral mesh with $65 \times 65 \times 65$ nodes, and we set the viscosity to $\nu = 1/10\,000$.

We further consider jet flow with periodic boundary conditions in all directions, with initial streamwise velocity one in the jet and zero streamwise velocity outside the jet, on a computational domain $2 \times 1 \times 1$ using cG(1)cG(1) on a tetrahedral mesh with $65 \times 33 \times 33$ nodes, again with the viscosity set to $\nu = 1/10\,000$.

34.10 Couette flow

The Couette base flow $u = (u_1, 0, 0)$ has a linear streamwise velocity profile $u_1 = 2x_2 - 1$, with streamwise velocity ± 1 on the top and bottom. In the streamwise and spanwise directions we use periodic boundary conditions. We are interested in conditionally stable flows, and we thus first show that Couette flow is conditionally stable.

We present computational results for Couette flow with a random initial perturbation of maximal size 1, centered in $(0.5, 0.5, 0.5)$. That is, for each velocity component we add a random perturbation, uniformly distributed in $(-1, 1)$, times a weight function $64 \times x_1(1-x_1)x_2(1-x_2)x_3(1-x_3)$. The random perturbation may be considered to include contributions from all modes, and in Fig.34.2-34.5 we find that most of these modes are quickly damped out and leaves only a combination of a few modes with a slow decay.

A small streamwise perturbation increases very slowly, but only as long as the decreasing transversal perturbations are above a certain threshold. This streamwise perturbation growth, caused by the Taylor-Görtler mechanism, is here too weak to cause transition to turbulence.

Evidently this computational model of Couette flow is conditionally stable, since there exist perturbations for which the flow is stable.

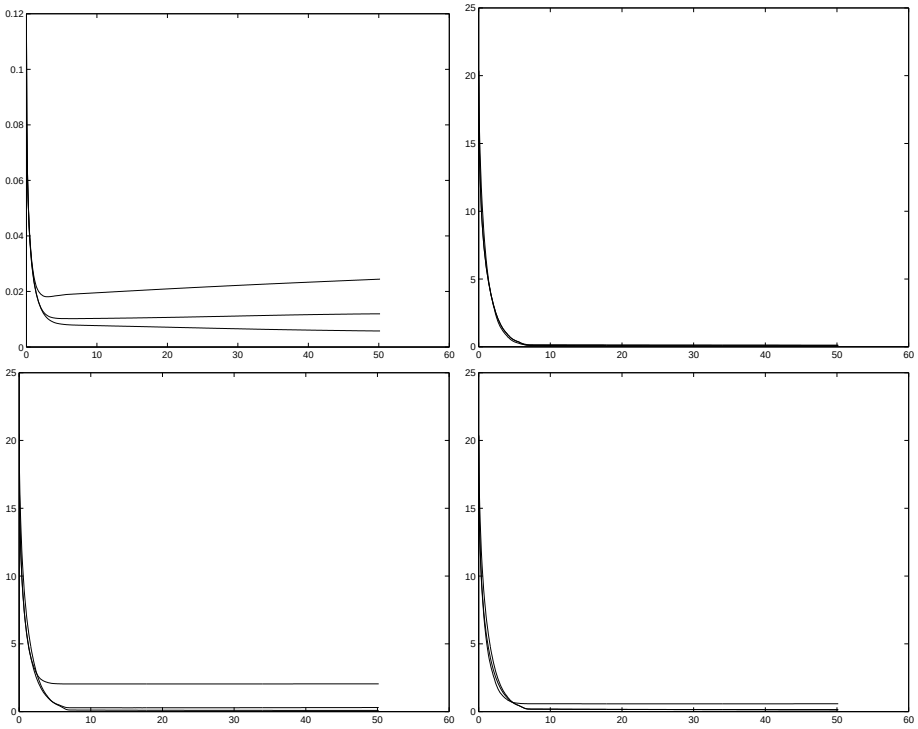

FIGURE 34.2. Couette flow (random initial perturbation): Perturbations $\|\varphi_i\|$ as functions of time (upper left), derivatives $\|\partial u_i/\partial x_1\|$ (upper right), $\|\partial u_i/\partial x_2\|$ (lower left), and $\|\partial u_i/\partial x_3\|$ (lower right) as functions of time.

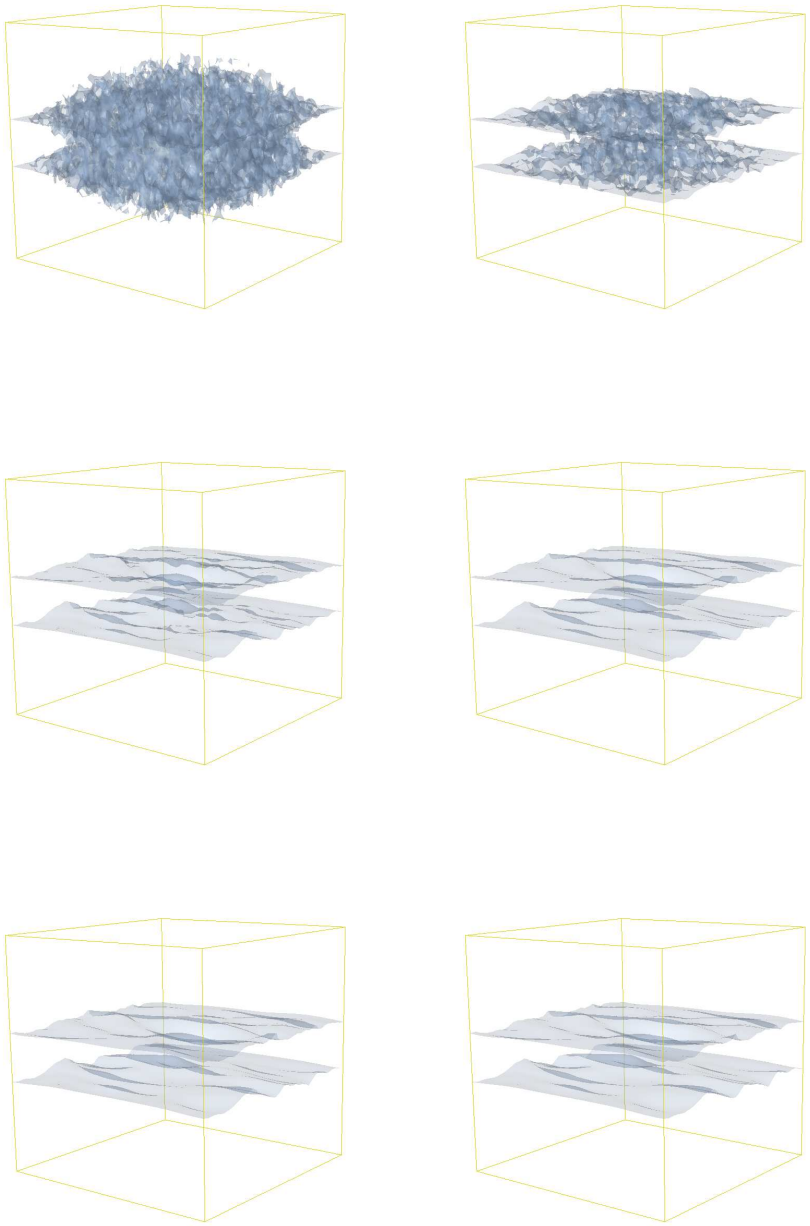

FIGURE 34.3. Streamwise velocity isosurfaces for $|u_1| = 0.2$ in Couette flow (random initial perturbation) for $t = 0, 1, 4, 5, 7, 10$

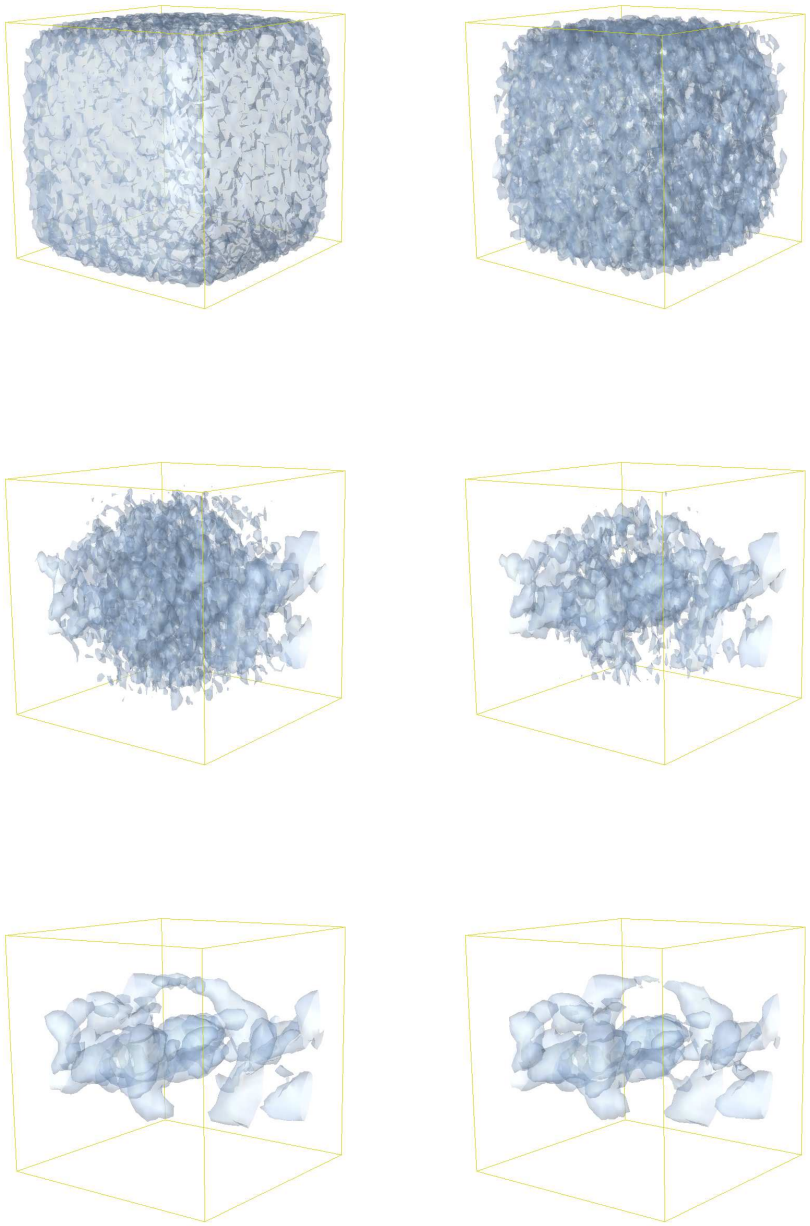

FIGURE 34.4. Streamwise velocity isosurfaces for $|u_2| = 0.015$ in Couette flow (random initial perturbation) for $t = 0, 1, 4, 5, 7, 10$

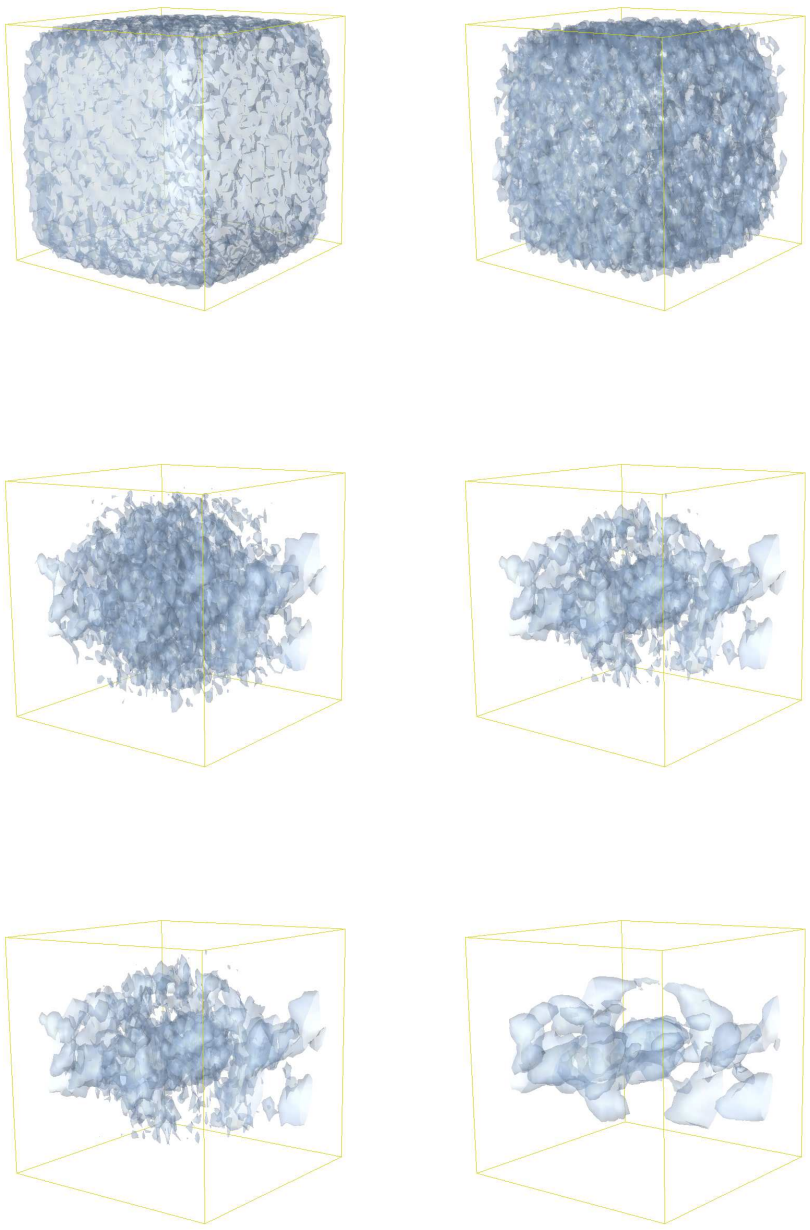

FIGURE 34.5. Streamwise velocity isosurfaces for $|u_3| = 0.015$ in Couette flow (random initial perturbation) for $t = 0, 1, 4, 5, 7, 10$

34.10.1 Algebraic perturbation growth

Since Couette flow is conditionally stable there exist no exponentially growing eigenmodes, but in Section 34.6 we showed that in parallel shear flow, perturbation growth proportional to the Reynolds' number is possible. We will now show that this algebraic perturbation growth may be strong enough to cause the flow to undergo transition to turbulence, by taking the original stable base flow, without any exponentially growing eigenmodes, to a new unstable flow with exponentially growing eigenmodes.

Not only the size of perturbations matter, but also the nature of the perturbations. In the case of a random perturbation we did not get transition even for large perturbations, but since transition is observed in experiments (starting at Reynolds' numbers at around 300) there must be other types of perturbations that leads to transition. It is intuitively clear that a large scale rotational perturbation results in large perturbation growth through the Taylor-Görtler mechanism, slowly shifting particles with different streamwise velocity transversally.

We now present computational results using an initial transversal, x_1-independent, rotational perturbation $\varphi^0 = (0, \varphi_2^0(x_2, x_3), \varphi_3^0(x_2, x_3))$, of the type

$$\begin{aligned} \varphi_2^0(x_2, x_3) &= \kappa\nu \sin(2\pi x_2)\cos(\pi x_3), \\ \varphi_3^0(x_2, x_3) &= -\kappa\nu \cos(2\pi x_2)\sin(\pi x_3), \end{aligned}$$

where $\kappa\nu = 0.5$. We also apply a very small x_1-dependent driving force $f = (0, f_2(x_1), f_3(x_1))$, with $f_2(x_1) = f_3(x_1) = 10^{-3}\sin(10\pi x_1)$, creating and sustaining a very small streamwise variation. We use slip boundary conditions in the spanwise direction, and periodic boundary conditions in the streamwise direction.

Initially, the streamwise perturbation φ_1 grows linearly through the action of the Taylor-Görtler mechanism, causing the formation of high and low velocity streaks, see Fig 34.6-34.9, and the perturbations φ_2 and φ_3 decrease initially. In the same way, transversal derivatives with respect to x_2 and x_3 grow linearly for u_1, and decrease for u_2 and u_3. This linear growth is easy to observe in Fig.34.7, where the isosurfaces for the absolute value of the streamwise velocity is shown for $|u_1| = 0.2$. In Fig.34.6 we see that near $t = 10$ we get a sudden burst, where all x_1-derivatives increase by a factor 100 over a short time interval, corresponding to initial transition when the base flow loses stability. A key observation is that this initial transition is not possible until the perturbation φ_1, and the transversal derivatives $\partial u_1/\partial x_2$ and $\partial u_1/\partial x_3$, has reached a certain threshold. Another important observation, which is not obvious from studying the global norms in Fig 34.6, is that the perturbations of course vary in space, and that the threshold is a local condition that has to be satisfied.

To test the dependence of the size of the perturbation, we present computational results for a smaller initial perturbation $\kappa\nu = 0.1$, instead of

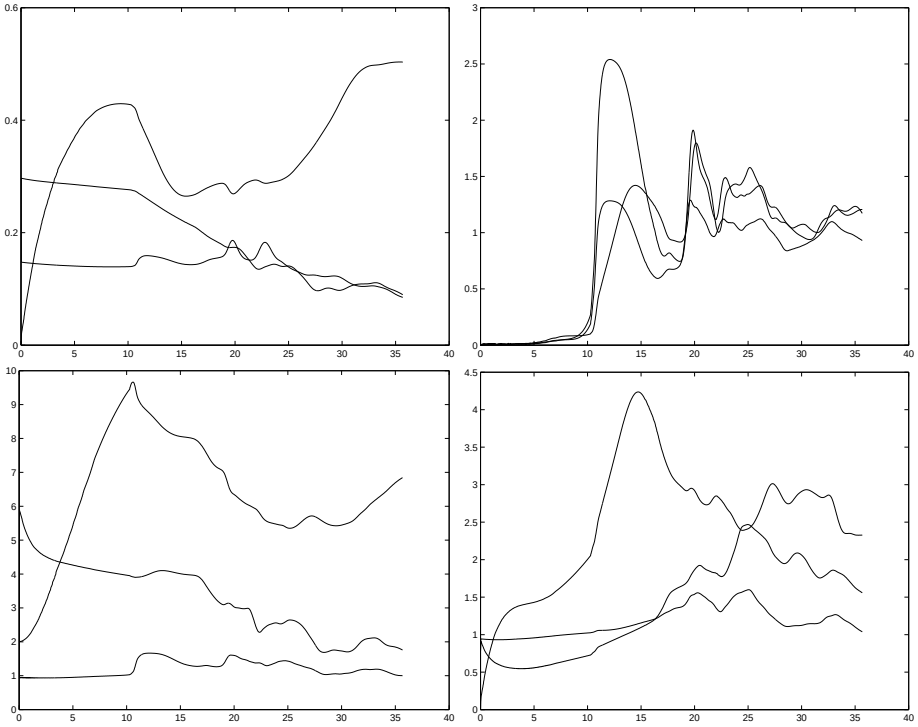

FIGURE 34.6. Couette flow ($\kappa\nu = 0.5$): Perturbations $\|\varphi_i\|$ as functions of time (upper left), derivatives $\|\partial u_i/\partial x_1\|$ (upper right), $\|\partial u_i/\partial x_2\|$ (lower left), and $\|\partial u_i/\partial x_3\|$ (lower right) as functions of time.

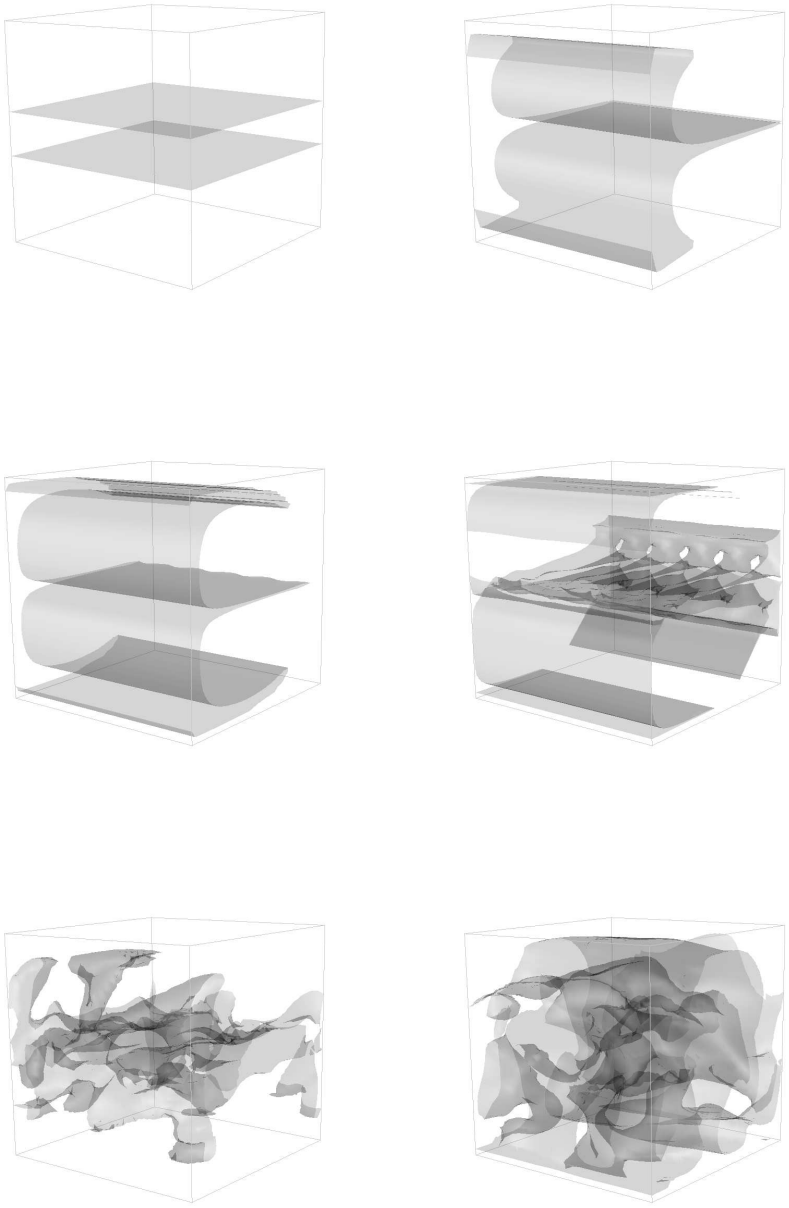

FIGURE 34.7. Streamwise velocity isosurfaces for $|u_1| = 0.2$ in Couette flow ($\kappa\nu = 0.5$) for $t = 0, 5, 10, 15, 20, 30$

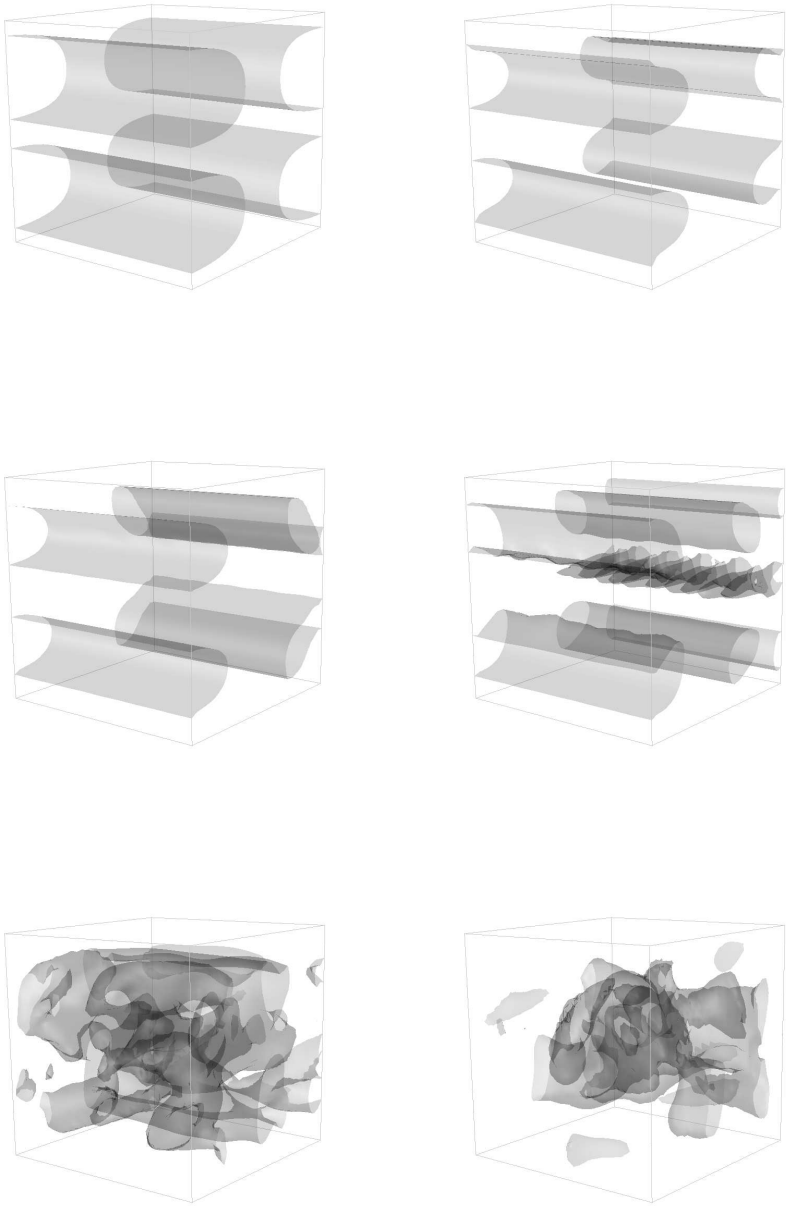

FIGURE 34.8. Transversal velocity isosurfaces for $|u_2| = 0.2$ in Couette flow ($\kappa\nu = 0.5$) for $t = 0, 5, 10, 15, 20, 30$

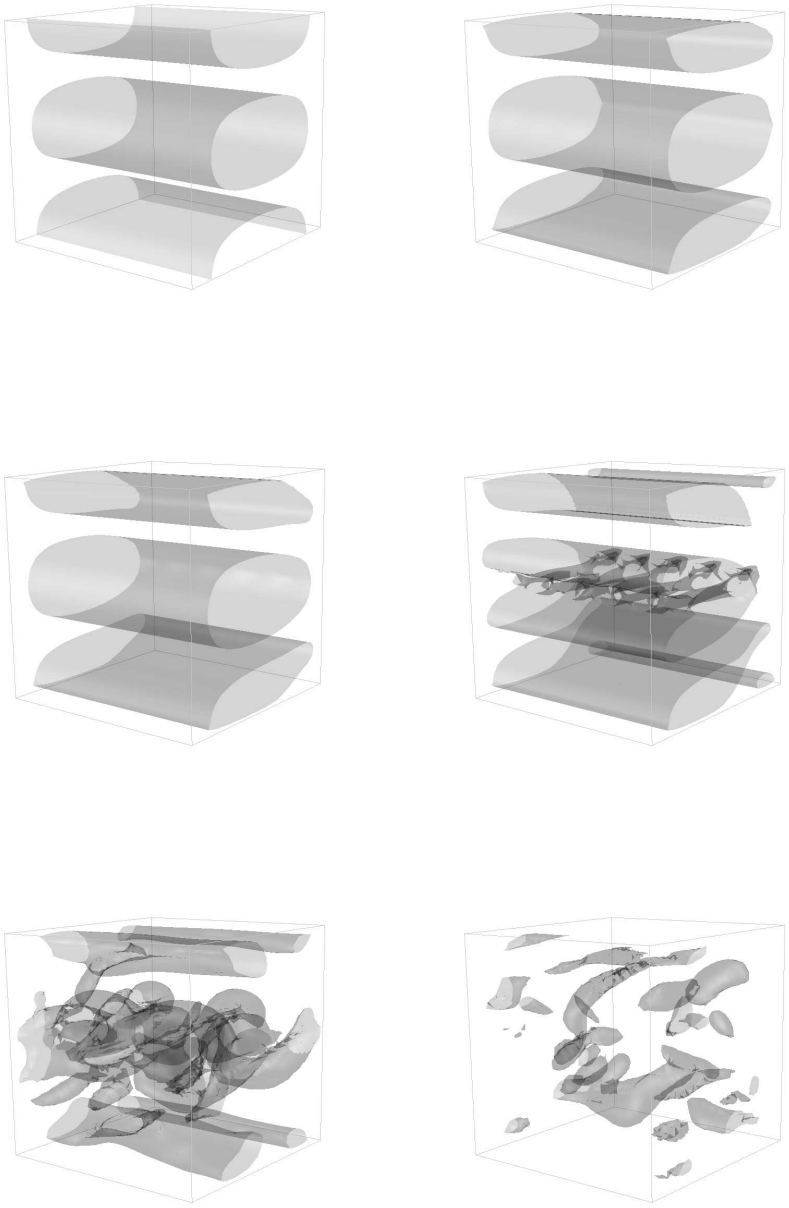

FIGURE 34.9. Transversal velocity isosurfaces for $|u_3| = 0.2$ in Couette flow ($\kappa\nu = 0.5$) for $t = 0, 5, 10, 15, 20, 30$

$\kappa\nu = 0.5$, in Fig 34.10. We get a similar scenario also in this case, although the time scale is longer. We can see that the burst in the x_1-derivatives now takes place at $t \approx 25$, instead of $t \approx 10$ as in the case a with larger initial perturbation. We can see the linear growth of $\partial u_1/\partial x_2$, $\partial u_1/\partial x_3$, and φ_1, until a threshold is reached and the base flow loses stability.

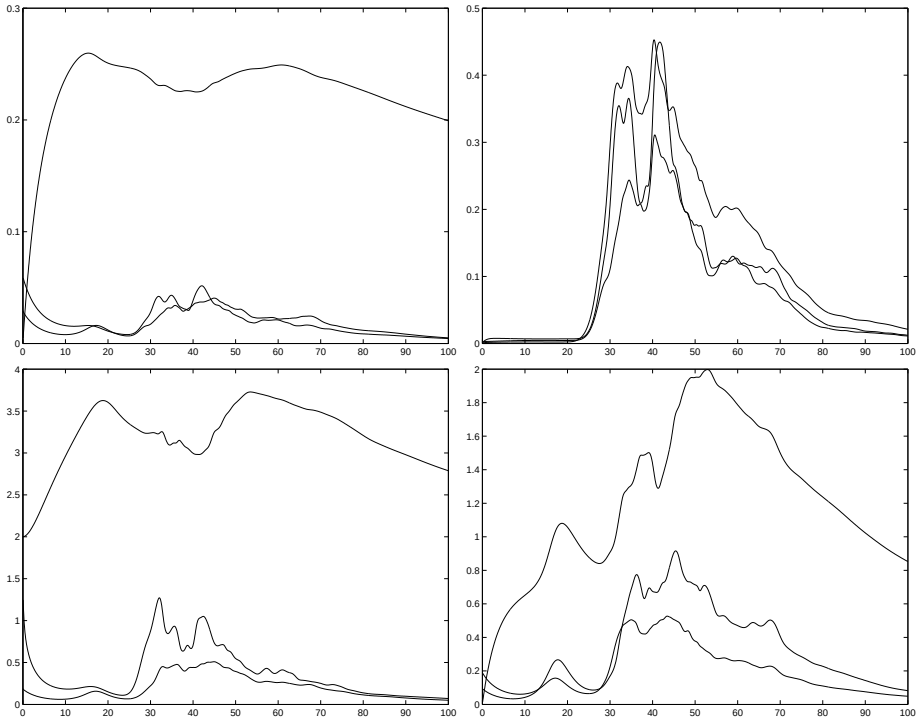

FIGURE 34.10. Couette flow ($\kappa\nu = 0.1$): Perturbations $\|\varphi_i\|$ as functions of time (upper left), derivatives $\|\partial u_i/\partial x_1\|$ (upper right), $\|\partial u_i/\partial x_2\|$ (lower left), and $\|\partial u_i/\partial x_3\|$ (lower right) as functions of time.

There exist a threshold value for the size of this type of perturbation for the (conditionally stable) Couette flow. For $\kappa\nu = 0.01$ we do not get transition since the linear growth is then to weak, and thus the special threshold value for this type of perturbation is somewhere in the interval $(0.01, 0.1)$.

34.10.2 Periodic spanwise boundary conditions

In Section 34.10.1 we used slip boundary conditions in the spanwise x_3-direction. Alternatively, we may use periodic boundary in the spanwise direction. The results for the initial perturbation $\kappa\nu = 0.5$ and periodic boundary conditions in the spanwise direction are presented in Fig.34.11.

We have basically the same scenario also in this case, although there are slight differences in the times scales. In the x_3-periodic case the linear growth of φ_1 is somewhat steeper, and the initial burst takes place earlier.

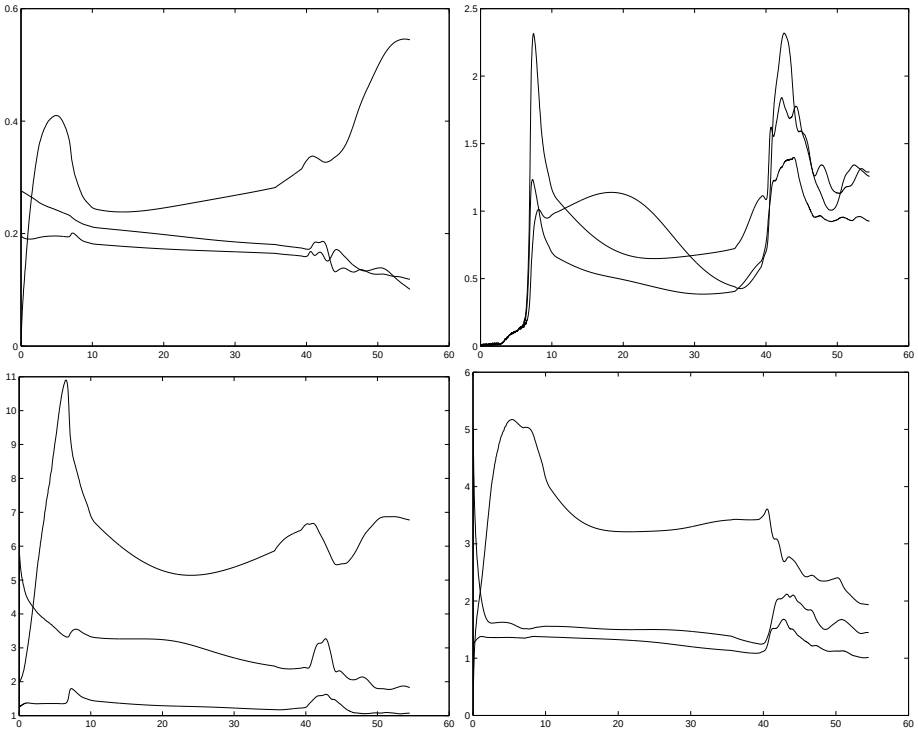

FIGURE 34.11. x_3-periodic Couette flow ($\kappa\nu = 0.5$): Perturbations $\|\varphi_i\|$ as functions of time (upper left), derivatives $\|\partial u_i/\partial x_1\|$ (upper right), $\|\partial u_i/\partial x_2\|$ (lower left), and $\|\partial u_i/\partial x_3\|$ (lower right) as functions of time.

34.10.3 Random force perturbation

In Fig.34.7-Fig.34.9 we make the observation that when the initial base flow loses stability, the flow does not go immediatly into an irregular turbulent flow. Instead we have an intermediate state, a new base flow, that later loses stability and goes turbulent, also referred to as a *secondary instability*. The x_1-period for the intermediate base flow is 0.2, that is 5 periods over the computational domain, and this periodic flow is likely to be triggered by the small force perturbation $f_2(x_1) = f_3(x_1) = 10^{-3}\sin(10\pi x_1)$ with the same period.

We now present results from computations using a small random perturbation of size 10^{-3} instead. That is, at each time step we add a per-

turbation $10^{-3} \times w(x)$ to each velocity component, where $w(x)$ is equally distributed in $(-1, 1)$. The results of the computations are presented in Fig.34.12-Fig.34.15, where we cannot observe any periodic mode after the initial transition, instead we have a lower mode that quickly loses stability before the flow goes into an increasingly unstable turbulent flow.

We conclude that in the case of the secondary stability, many different transition scenarios are possible and the actual scenario may depend on the nature of the perturbations.

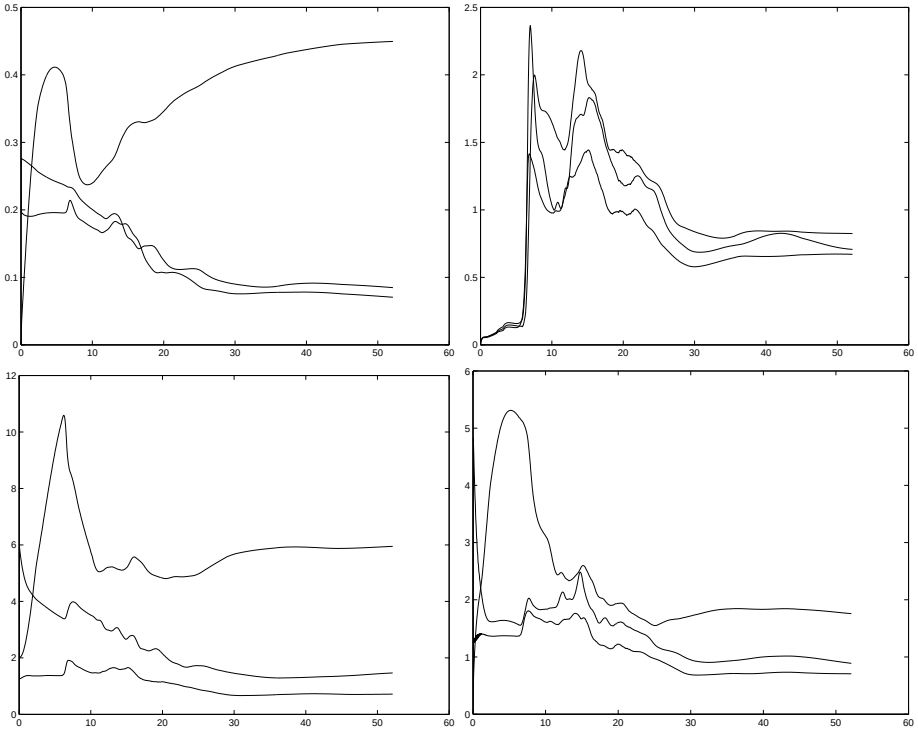

FIGURE 34.12. x_3-periodic Couette flow ($\kappa\nu = 0.5$, random force perturbation): Perturbations $\|\varphi_i\|$ as functions of time (upper left), derivatives $\|\partial u_i/\partial x_1\|$ (upper right), $\|\partial u_i/\partial x_2\|$ (lower left), and $\|\partial u_i/\partial x_3\|$ (lower right) as functions of time.

34.11 Poiseuille flow - Reynolds experiment

We now present results for the conditionally stable Poiseuille flow in a pipe, which is a model of Reynolds original experiments. The Poiseuille base flow has a streamwise velocity profile $u_1(x_2, x_3) = 16x_2(1 - x_2)x_3(1 - x_3)$ in a square channel with no slip walls and a force term $f = (32(x_2(1 -$

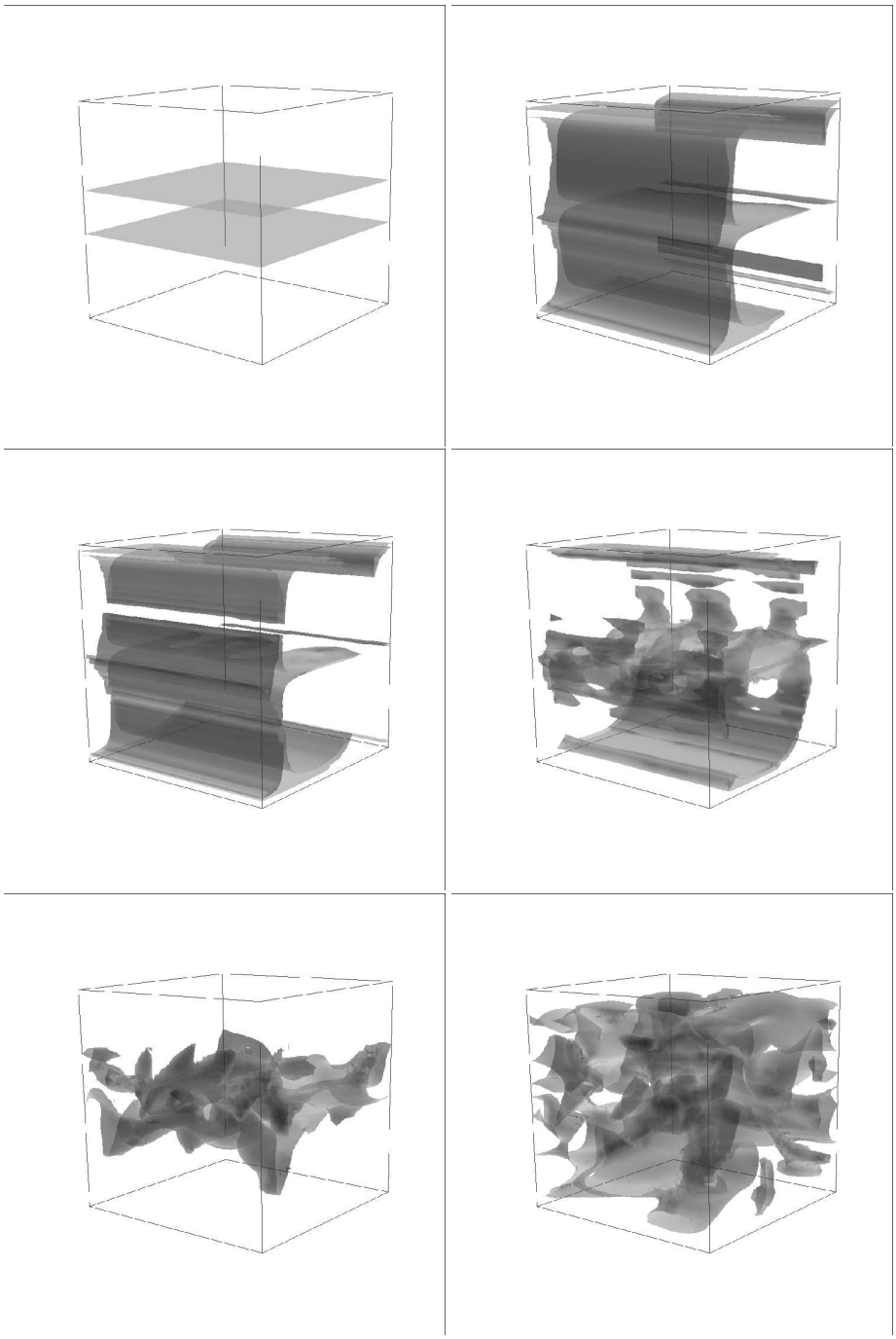

FIGURE 34.13. Streamwise velocity isosurfaces for $|u_1| = 0.2$ in x_3-periodic Couette flow ($\kappa\nu = 0.5$, random force perturbation) for $t = 0, 5, 6, 7, 10, 20$

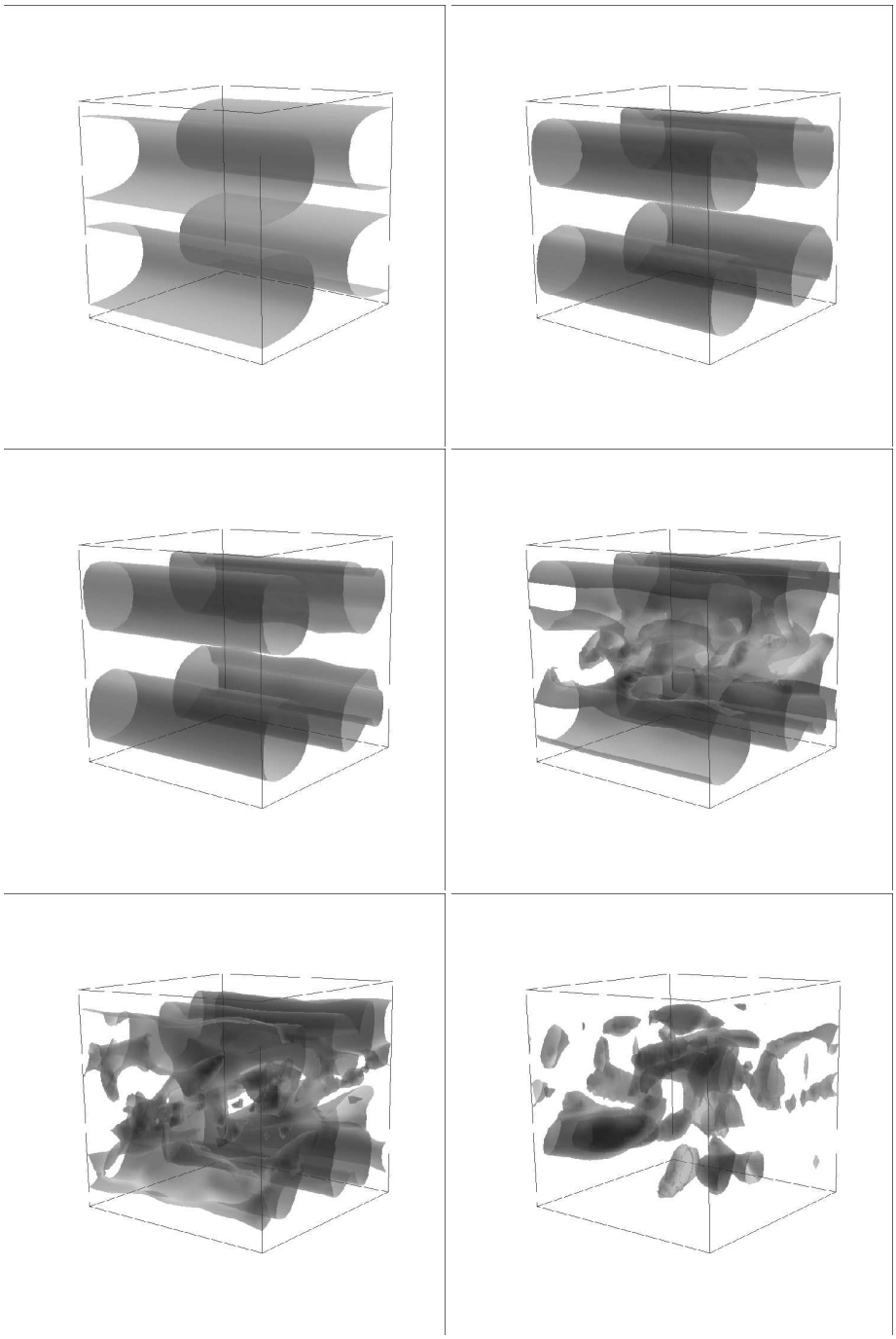

FIGURE 34.14. Transversal velocity isosurfaces for $|u_2| = 0.2$ in x_3-periodic Couette flow ($\kappa\nu = 0.5$, random force perturbation) for $t = 0, 5, 6, 7, 10, 20$

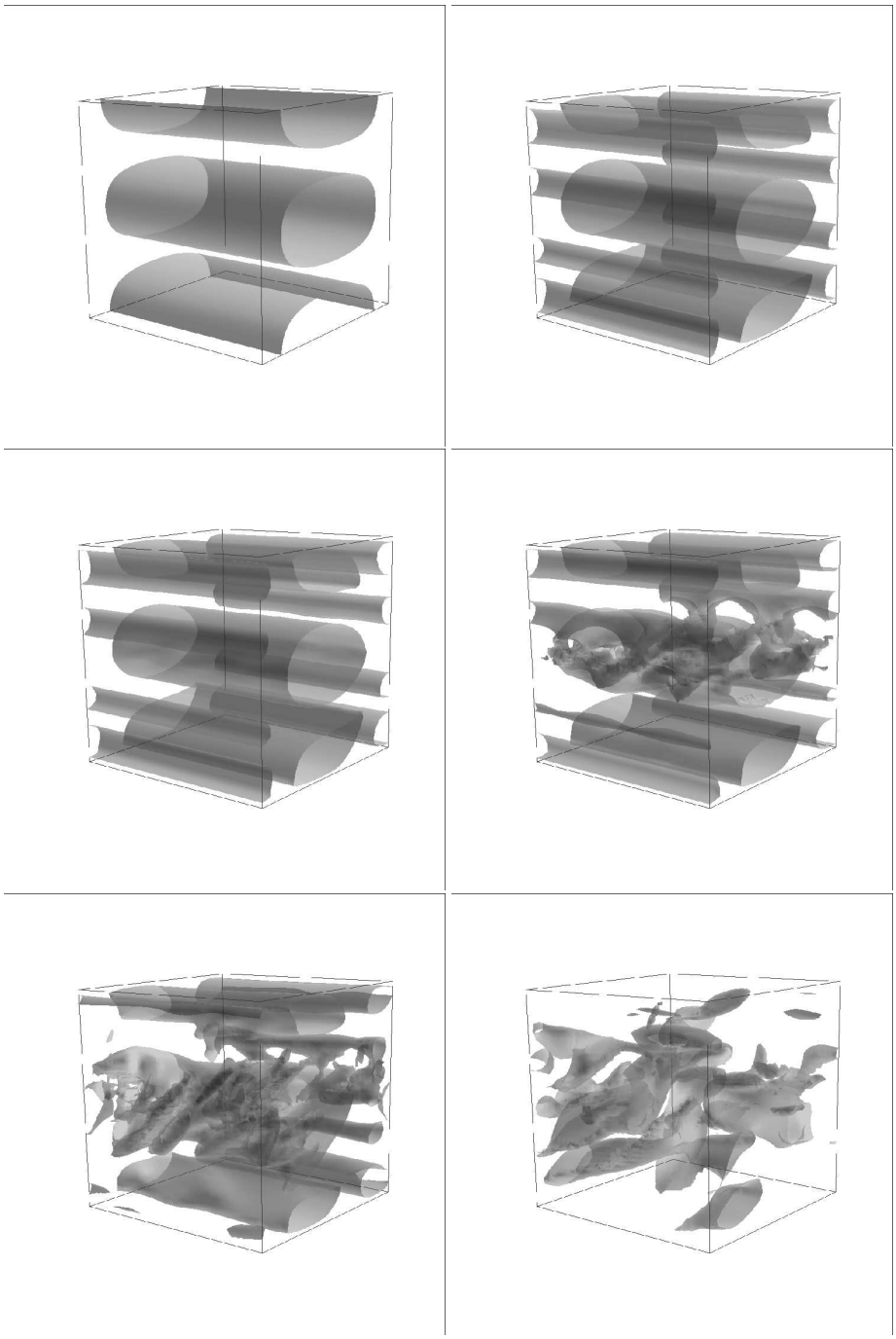

FIGURE 34.15. Transversal velocity isosurfaces for $|u_3| = 0.2$ in x_3-periodic Couette flow ($\kappa\nu = 0.5$, random force perturbation) for $t = 0, 5, 6, 7, 10, 20$

$x_2) + x_3(1 - x_3)), 0, 0)$, where we use periodic boundary conditions in the streamwise direction. In Fig.34.16 we note a linear growth in the streamwise perturbation corresponding to the Taylor-Görtler mechanism, whose action is shown in Fig.34.17, slowly shifting particles with different streamwise velocity transversally resulting in a considerable reorganization of the streamwise velocity. Fig.34.16 also shows the x_1-derivatives as a function of time, with a sudden increase near $t = 6$, similar to the case of Couette flow. Again we note that this increase is not possible until the x_1-perturbation φ_1 (and the transversal derivatives of the streamwise velocity, $\partial u_1/\partial x_2$ and $\partial u_1/\partial x_3$) are large enough.

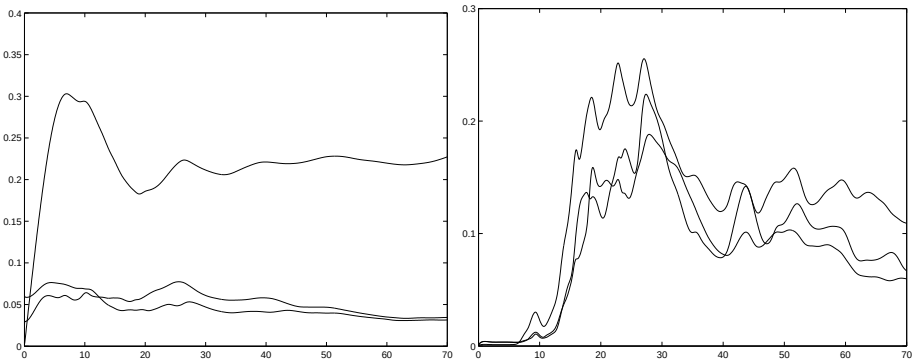

FIGURE 34.16. Poiseuille flow ($\kappa\nu = 0.1$): Perturbations $\|\varphi_i\|$ (left) and x_1-derivatives $\|\partial u_i/\partial x_1\|$ (right).

34.12 Taylor-Görtler perturbations

Rotational perturbations of Taylor-Görtler type used in the previous sections occur naturally. For example, a small object (say a stone) on the bottom of the channel could trigger such a perturbation. To illustrate this, in Fig.34.18 we plot the velocity field downstream the surface mounted cube i Chapter 30, where we see the formation of cigar-shaped structures of high transversal (rotational) velocity after the obstacle, that is perturbations of Taylor-Görtler type.

34.13 Unstable Jet Flow

As an example of an unstable flow, with exponentially growing eigenmodes, we consider a periodic jet flow, with initial streamwise velocity one in the jet and zero streamwise velocity outside the jet on a computational domain

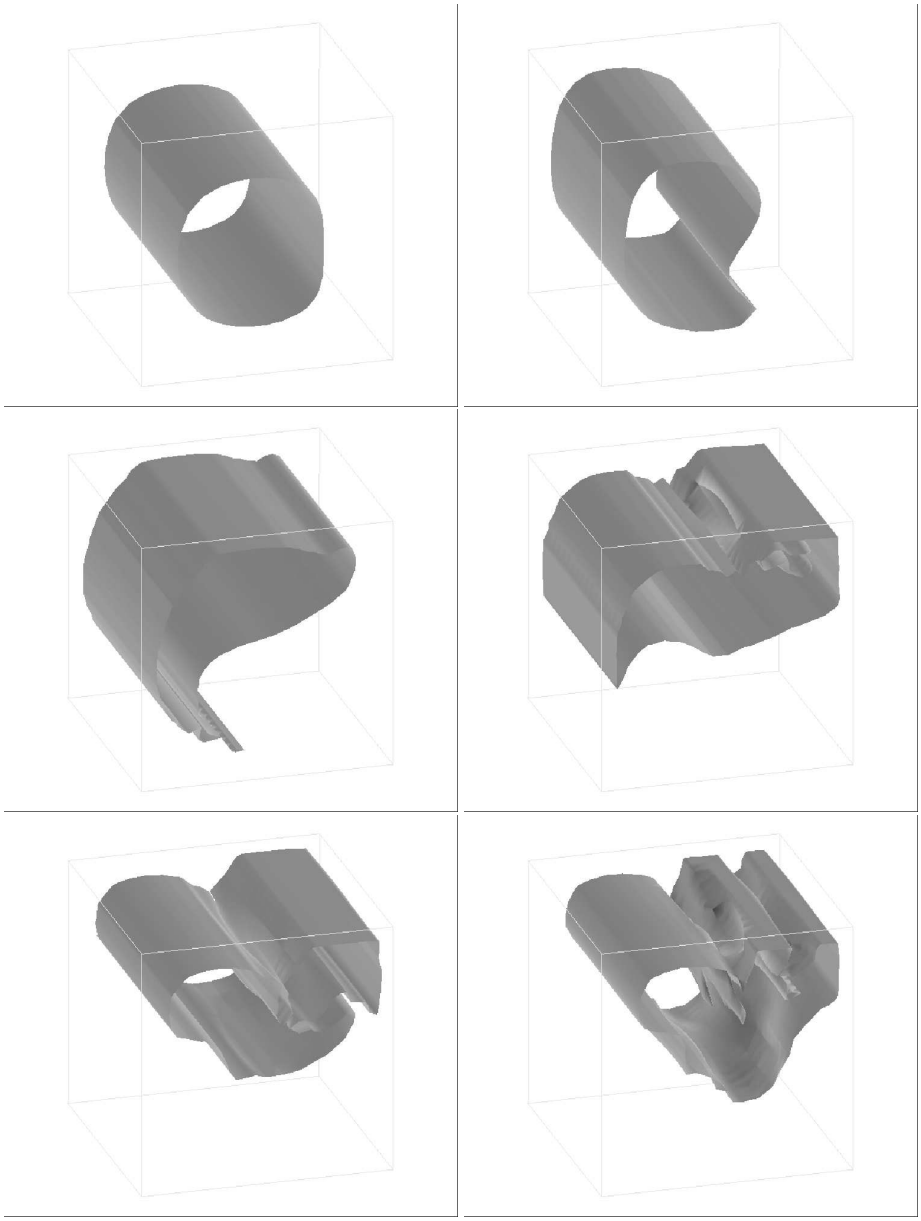

FIGURE 34.17. Velocity isosurfaces in Poiseuille flow ($\kappa\nu = 0.1$) at $t = 1, 3, ..., 15$, illustrating the Taylor-Görtler mechanism

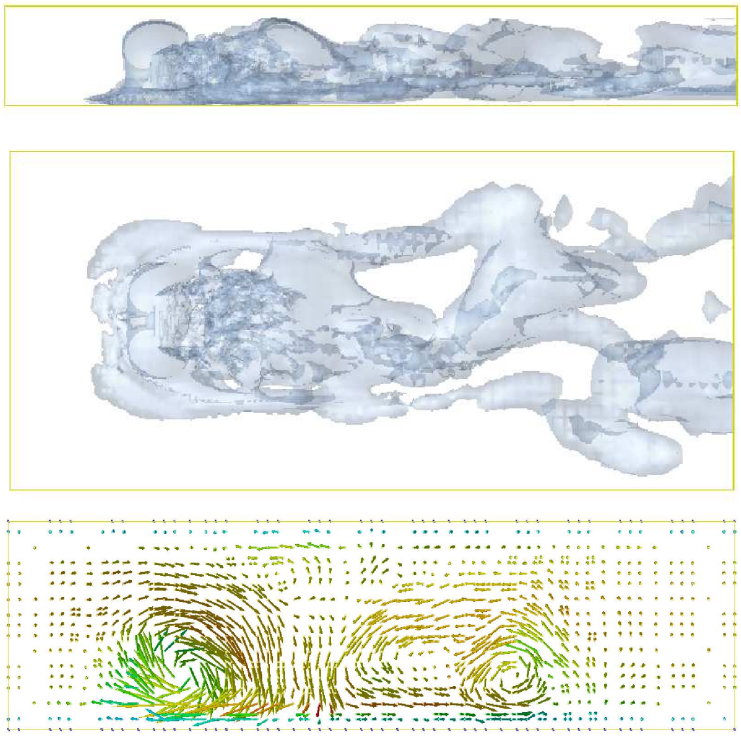

FIGURE 34.18. Surface mounted cube: isosurfaces for $|(u_2, u_3)|$ in the x_1x_2-plane (upper), in the x_1x_3-plane (middle), and the velocity field in the x_2x_3-plane downstream the cube (lower).

$2 \times 1 \times 1$. We set $\nu = 1/10\,000$, and we apply a small random perturbation of maximal size 0.1. That is, for each velocity component we add a random perturbation uniformly distributed in $(-0.1, 0.1)$, times a weight function $16 \times x_1(2-x_1)x_2(1-x_2)x_3(1-x_3)$. In Fig.34.19-Fig.34.22 we see that most modes in the random initial perturbation are quickly damped out, but a low unstable mode is exerted and grows exponentially causing the flow to go unstable. We note that in this case there is no growth in the transversal derivatives of the streamwise velocity before transition.

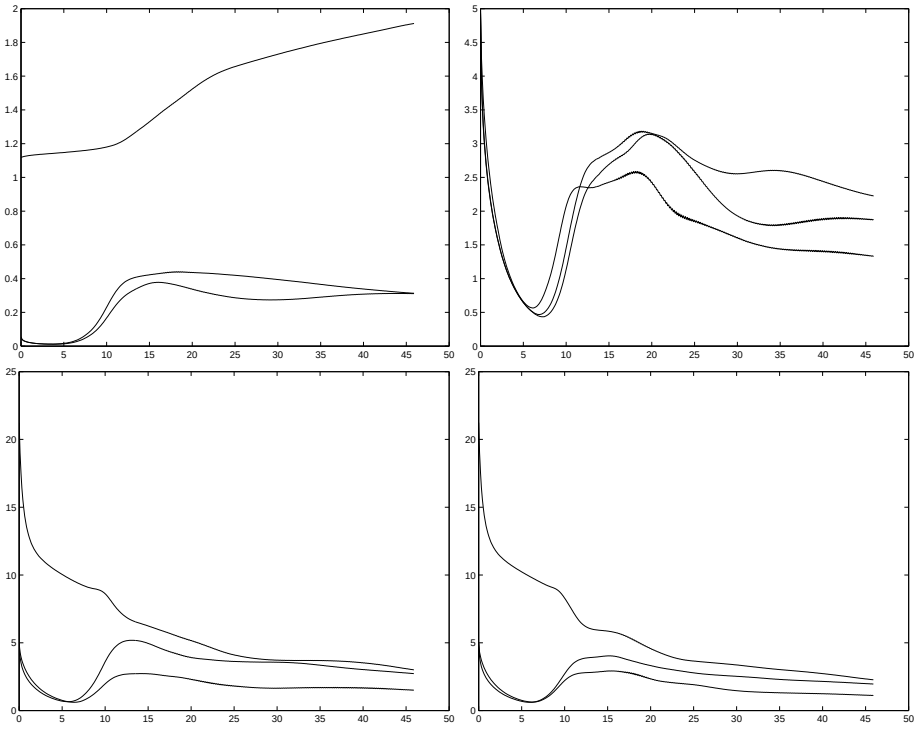

FIGURE 34.19. Jet flow (random initial perturbation): perturbations $\|\varphi_i\|/\|u\|$ (upper left) as functions of time, derivatives $\|\partial u_i/\partial x_1\|/\|u\|$ (upper right), $\|\partial u_i/\partial x_2\|/\|u\|$ (lower left), and $\|\partial u_i/\partial x_3\|/\|u\|$ (lower right).

34.14 Test for Optimal Perturbations

In Section 34.10 we found, by applying a random perturbation, that our computational model of Couette flow is conditionally stable: there exist no exponentially unstable modes. The only way this flow may go unstable from a small perturbation is through algebraic perturbation growth. We

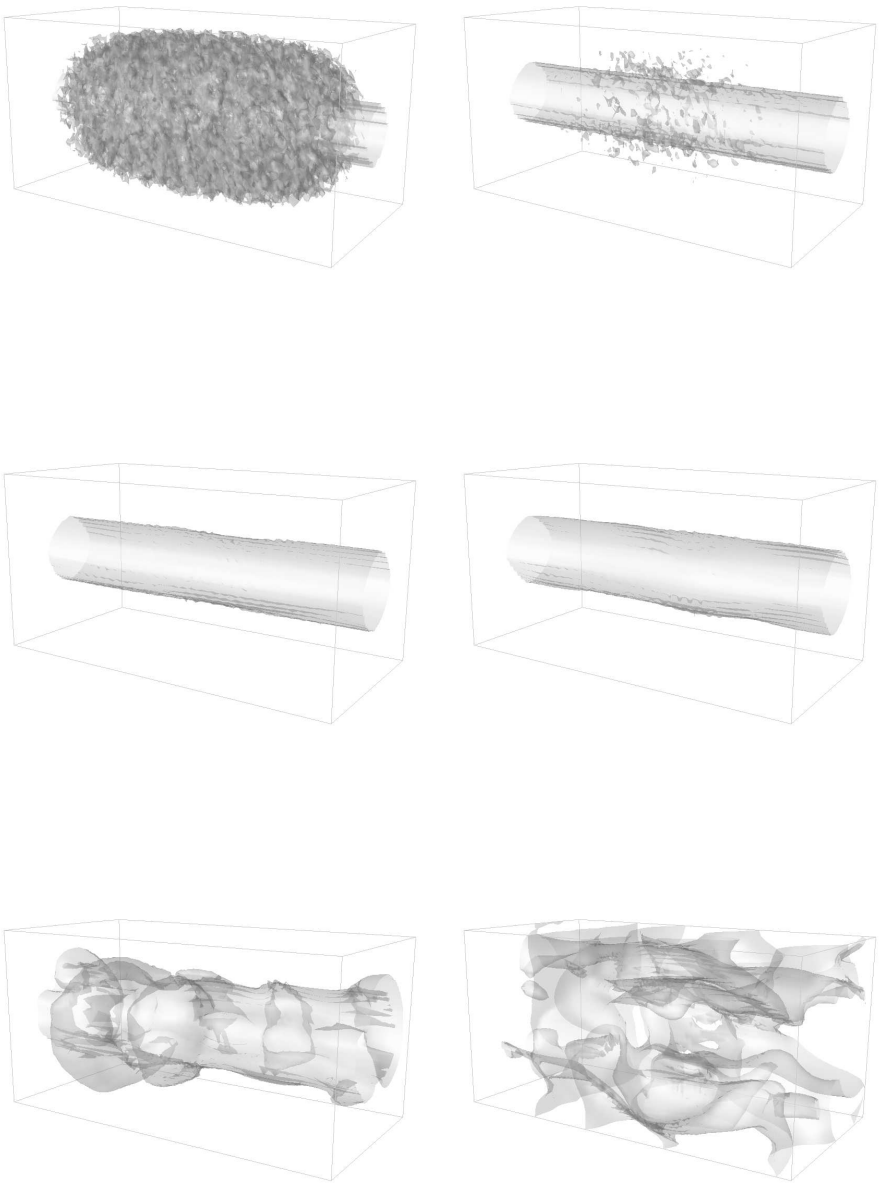

FIGURE 34.20. Streamwise velocity isosurfaces for $|u_1| = 0.02$ in jet flow (random initial perturbation) for $t = 0, 2, 5, 7, 10, 15$

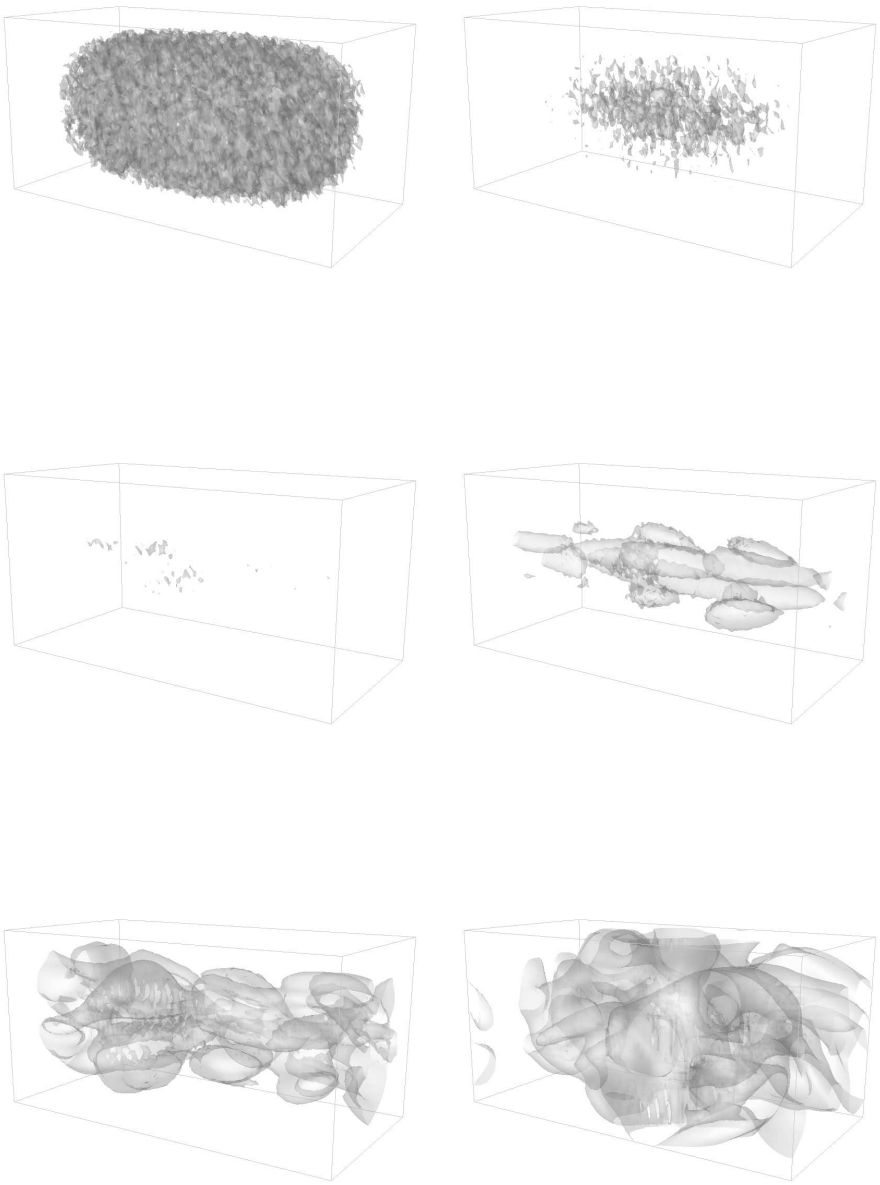

FIGURE 34.21. Transversal velocity isosurfaces for $|u_2| = 0.02$ in jet flow (random initial perturbation) for $t = 0, 2, 5, 7, 10, 15$

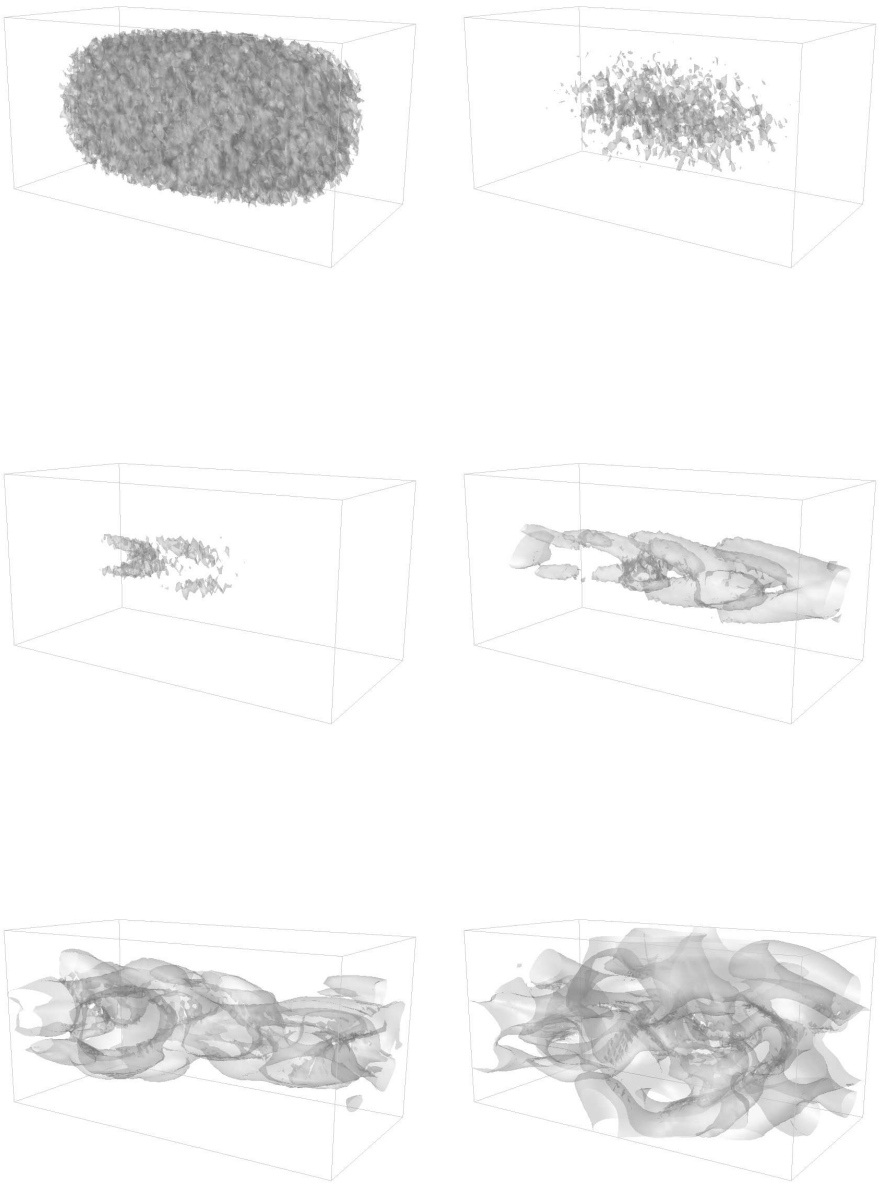

FIGURE 34.22. Transversal velocity isosurfaces for $|u_3| = 0.02$ in jet flow (random initial perturbation) for $t = 0, 2, 5, 7, 10, 15$

now propose a test for finding optimal perturbations, that is perturbations that may lead to large algebraic perturbation growth.

For a perturbation to be able to lead to any significant perturbation growth it must not be damped out too quickly, since the algebraic perturbation growth typically is rather slow. We thus seek the optimal perturbations among the modes that have the slowest decay. A way to do this is to apply a random perturbation as in In Section 34.10. In Fig.34.3-Fig.34.5 the response of a random initial perturbation is shown, and whereas most modes are quickly damped out a few modes decay very slowly. These modes, shown in Fig.34.23, are rotational perturbations of Taylor-Görtler type, shaped as cigars oriented in the streamwise x_1-direction.

Since the amount of these modes in the white noise random perturbation is too small they are unable to take the flow into transition. On the other hand, if we take a cross section at say $x_1 = 0.5$ and apply the transversal components of the modes multiplied by a factor 10 to a Couette flow, we get transition at $t \approx 100$.

34.15 A critical review of classical theory for transition

The classical research on transition to turbulence in fluid flow has been focussed on finding a relation between Reynolds number and transition, with ideally a so called critical Reynolds number for each type of flow, identified by the fact that transition to turbulence takes place if and only if the actual Reynolds number is larger than the critical Reynolds number. As noted above, Reynolds himself had little reason to belive in the existence of such critical Reynolds numbers judging from his own experiments.

Nevertheless, most text books in fluid mechanics still today present "critical Reynolds numbers" for various flows, such as 5772 for Pouiseuille flow between two parallel fixed plates (with parabolic velocity profile), and ∞ for Couette flow between two moving parallel plates (with linear velocity profile), both however at severe variance with experiments. The stated critical Reynolds numbers come out of a normal mode stability analysis of 2d linearized equations, referred to as the Orr-Sommerfeld equations, based on identifying exponentially growing eigenmodes, so-called Tollmien-Schlichting waves. The striking difference in the theoretical predictions and the practical experiments for transition in parallel flow, has driven the classical study of hydrodynamic stability into a severe crisis, with scientifically impossible concepts like "subcritical Reynolds number" and "bypass transition" to handle the disagreement of theoretical predictions and actual observations. We give a couple of citations describing the crisis:

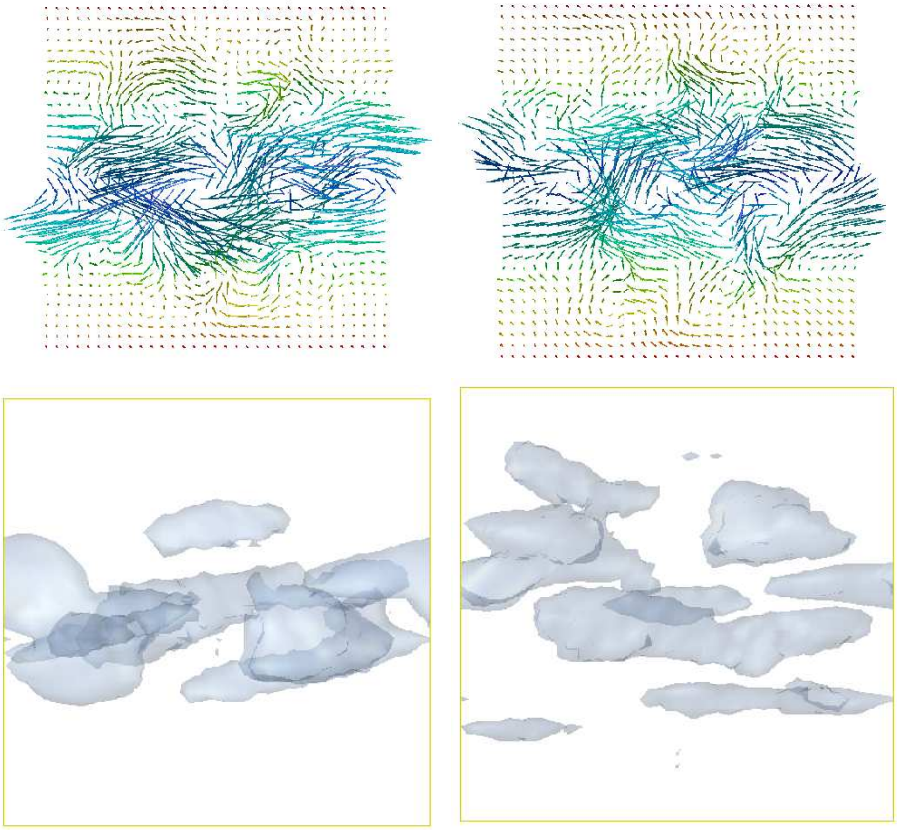

FIGURE 34.23. Slowest decaying modes from a uniformly distributed random perturbation, in the x_2x_3-plane at $x_1 = 0.25$ (upper left) and $x_1 = 0.75$ (upper right), isosurfaces for $|u| = 0.015$ in the x_1x_2-plane (lower left) and in the x_1x_3-plane (lower right).

The sudden transition from smooth, laminar flow to turbulence as the fluid velocity is gradually increased remains one of the least adequately explained phenomena in all of classical physics, (James Case, SIAM News, 2002 [**?**]).

For a circular Poiseuille flow (pipe flow), as well as Couette flow, the classical linear-instability analysis leads to stability, whatever the Reynolds number and the wavenumber of the perturbation. Experimentally, one observes also turbulent spots in these flows, (Lesieur [**?**]).

Apparently, the asymptotic stability of a shear flow to infinitesimal disturbances cannot fully characterize its stability, (Blossey [13]).

Further, transition scenarios based on Tollmien-Schlichting waves are irrelevant because of the large perturbation levels needed to exert these modes, (Henningson-Schmid [82]).

For a time after this negative result (stability of Couette flow for all Reynold's numbers), *it was thought that the method of small oscillations* (classical theory) *was unsuitable for the theoretical solution of the problem of transition. It transpired later that this was not justified, because Couette flow is a very restricted and special example,* (Schlichting [81]).

In this book I have tried to bring together into a coherent account what I have learnt of hydrodynamic stability. Perhaps the most serious omission is the absence of any reference to viscous shear flow....in the last an author chooses to write only about those matters in which he has some confidence of his understanding, (Chandrasekhar, [18]).

The remark by Schlichting is from scientific point of view completely stunning: if the proposed theory does not pass a most simple and basic test, the conclusion is not that there must be something seriously wrong with the theory, but instead that the test should be discarded because of its simplicity! The remark by Chandrasekhar (Nobel Prize in Physics 1983) shows another attitude towards science.

We now give a couple of citations indicating the new view and the role of 3d algebraic growth for transition:

Shortly before his death 1999 Mårten Landahl completed research on the basic theoretical problem of how a 3-D initial disturbance within a shear flow evolves over time. He felt certain his work would form a new fundamental approach to the transition problem (tackled by many in the past 100 years) as opposed to the classical Orr-Sommerfield equation, and he had planned further research on completing the asymtotic long-time evolution of a 3-D disturbance in a parallel shear flow. He then planned to use this

work as the basis for a new transition theory as well as a new turbulence model. (M.I.T. News, 1999 [**?**]).

It should be finally mentioned that the growth of the quasi-linear non-normal longitudinal mode considered in section 2.3 (algebraic perturbation growth) *might be important for the transition in these inconditionally stable shear flows, as well in subcritical situations,* (Lesieur [**?**]).

Thus in a flow that is asymptotically stable to infinitesimal disturbances, transient growth (non modal algebraic perturbation growth) is necessary if finite amplitude disturbances are to lead to transition to turbulence, (Blossey [13]).

Summing up, we get the following picture: Everybody seems to agree that the classical stability theory is inadequate for explaining transition in shear flow, and there is a new view emerging pointing to the crucial role of algebraic growth of 3d perturbations. In the citation above from the review [13] of the recent book [82], we read that classical theory "cannot fully" characterize stability, apparently indicating that that classical theory is partly correct. Our main point is that, in fact, the classical theory based on identifying exponentially growing eigenmodes, is *completely inadequate* for describing the initial and most crucial phase of transition in parallel shear flow. Consequently the concept of "critical Reynolds numbers for transition" cannot have any meaning, and in particular should not be presented in text books and courses in fluid mechanics as is now customary. Neither should there be any place for terms like "bypass transition" and "subcritical Reynolds number".

A possible reason for the survival of the classical misleading normal mode stability analysis for parallel shear flow, despite its lack of experimental support, is probably the fact that there are some other cases where the same type of analysis in fact is correct and conforms with experiments, namely the *bifurcating* Bernard and Taylor-Couette flows, changing from one configuration to another at a certain well defined Reynolds number. The bifurcation of Bernard flow involves the development of organized patterns of convective rolls of fluid in motion. A bifurcation involves a change from one configuration losing stability, to a new stable configuration, which is different from the process of transition to turbulence, with the new configuration being increasingly unstable. Now, a bifurcation in general may be detected through a normal mode analysis based on finding for the linearized equations an eigenvalue with zero real part. In particular, the critical Reynolds number for the first bifurcations in Taylor-Couette and Bernard flow, may be found analytically this way. As indicated this approach does however not work for parallel Couette or Poiseuille flow, which do not bifurcate to find new stable configurations, but instead go into turbulent unstable motion.

This is because in linearizations of Taylor-Couette or Bernard flow, weak algebraic perturbation growth is dominated by slow exponential decay, whereas in parallel Couette or Poiseuille flow, strong algebraic perturbation growth dominates. It appears that the success of the mathematical theory in the bifurcating cases, has overshadowed the failure in the non-bifurcating cases. We discuss these ideas below in the setting of simple ode-models.

34.16 An ode-model for transition

We consider the following initial value problem for a system of two ordinary differential equations: find $w(t) = (w_1(t), w_2(t))$ such that

$$\begin{aligned} \dot{w}_1 + \nu w_1 - \lambda w_1 w_2 &= \nu \qquad t > 0, \\ \dot{w}_2 + 2\nu w_2 - \nu w_2 w_1 &= 0 \qquad t > 0, \\ w_1(0) = 1, \quad w_2(0) &= \kappa\nu, \end{aligned} \tag{34.9}$$

where ν is a small positive parameter, and λ and κ are positive parameters of moderate size. The system (34.9) models almost parallel shear flow with w_1 representing the flow velocity in the main direction of the flow, and w_2 the small velocities transversal to the main flow, and the stationary solution $w = (1, 0)$ corresponds to Couette flow between two plates or Poiseuille flow in a pipe. We shall use the model to describe how the small perturbation $\kappa\nu$ of w_2 may cause the base solution $(1, 0)$ to become unstable if $\lambda\kappa$ is larger than some critical value of moderate size.

We shall see that the model (34.9) contains an essential part of the secret of transition to turbulence in shear flow. The equations for w_1 and w_2 in (34.9) are coupled through the quadratic terms $\lambda w_1 w_2$ and $\nu w_1 w_2$, and model the following selection of terms from the Navier-Stokes equations

$$\begin{aligned} \dot{u}_1 - \nu\Delta u_1 + \bar{u}\cdot\bar{\nabla}u_1 &= \nu \qquad t > 0, \\ \dot{\bar{u}} - \nu\Delta\bar{u} + u_1\partial\bar{u}/\partial x_1 &= 0 \qquad t > 0, \end{aligned} \tag{34.10}$$

from the momentum equations for the main flow velocity u_1 and the transversal velocity $\bar{u}$. The nonlinear coupling terms $\bar{u}\cdot\bar{\nabla}u_1$ and $u_1\partial\bar{u}/\partial x_1$ are modeled in the form $\lambda w_1 w_2$ and $\nu w_2 w_1$, corresponding to assuming that $u_{1,i} = -\lambda u_1$, for $i = 2, 3$, and $\partial\bar{u}/\partial x_1 = -\nu\bar{u}$, connecting transversal derivatives of u_1 with u_1 through the parameter λ, and the streamwise derivative of the transversal velocity $\bar{u}$ with $\bar{u}$ through the small parameter ν. The relation $\partial\bar{u}/\partial x_1 = -\nu\bar{u}$ models a basic feature of parallel flow with the streamwise variations being small. Since we assume initially that $\bar{u} \approx w_2 \approx \nu$, it corresponds to assuming $\partial\bar{u}/\partial x_1 \sim \nu^2$, which is indeed very small. On the other hand, the assumption that $u_{1,i} = -\lambda u_1$, for $i = 2, 3$, with λ of moderate size corresponds to a natural transversal variation of moderate size of the streamwise velocity in a shear flow.

Note that the coupling term $u_{1,1}u_1$ in the equation for u_1 is not modeled in the form of some multiple of w_1^2. This is because (a) assuming $u_{1,1} \approx \nu^2$, with a corresponding very small term $-\nu^2 w_1^2$ in the model, has no destabilizing effect, and (b) assuming $u_{1,1} = -C\nu$ with a corresponding larger term $-C\nu w_1^2$, which may cause exponential growth through self-resonance in w_1, is not realistic. In fact, (b) is more or less the classical scenario based on the 2d Orr-Sommerfeld equations, which require artificially generated perturbation levels in experiments, for example through heavily vibrating ribbons.

In the transition model, we thus seek to build in realistic features of shear flow including realistic perturbation levels. If we assume zero perturbations, then the model reduces to $\dot{w}_1 + \nu w_1 = 0$, $\dot{w}_2 + 2\nu w_1 = 0$, which has no chance of going unstable. If we assume large perturbation levels, then instability may result immediately. However, none of these scenarios occur in reality, and the role of the model is to explain how small but realistic size perturbations, indeed may cause the initially stable base flow to go unstable after some time. Our model builds on the presence of a very small perturbation of order ν^2 of the transversal velocity in the streamwise direction, which naturally may be introduced through the roughness of the pipe. The model does not build on a larger variation of order ν of the streamwise velocity in the streamwise direction, which only seems to be possible with artificially generated perturbations.

The model (34.9) contains the two basic parameters λ and κ, both of moderate size, λ being related to the transversal geometry of the flow such as pipe cross section, $\kappa\nu$ representing a perturbation level in transversal velocities, and $\kappa\nu^2$ a perturbation level in streamwise derivatives of transversal velocities, including both transversal and streamwise perturbations levels. We will see that if $\lambda\kappa$ is larger than some critical value of moderate size, then transition to instability will take place in the model. This indicates that transition in shear flow builds on a combination of features related the transversal geometry and levels of perturbations in both transversal and streamwise direction. The presented computational results for transition to turbulence in Couette and Poiseuille flow presented supports this picture.

The system (34.9) has two stationary solutions $w = (1, 0)$ and $w = (2, \nu/(2\lambda))$, with $(1, 0)$ representing the basic Couette or Poiseuille flow. A classical stability analysis based on the eigenvalues of the corresponding linearized system, indicates that $(1, 0)$ is stable and $(2, \nu/(2\lambda))$ is unstable. For example, the linear system obtained linearizing at $(1, 0)$, takes the form

$$\begin{aligned} \dot{\varphi}_1 + \nu\varphi_1 - \lambda\varphi_2 &= \nu \qquad t > 0, \\ \dot{\varphi}_2 + \nu\varphi_2 &= 0 \qquad t > 0, \\ \varphi_1(0) = \varphi_{10}, \quad \varphi_2(0) &= \varphi_{20}, \end{aligned} \tag{34.11}$$

where the coefficient matrix $A = [\nu \ -\lambda, 0 \ \nu]$ has a double positive eigenvalue ν. The corresponding coefficient matrix linearizing at $(2, \nu/(2\lambda))$,

has one positive (stable) and one negative (unstable) eigenvalue. A classical stability analysis shows that $(1,0)$ is stable under sufficiently small perturbations, and that $(2,\nu/(2\lambda))$ is unstable even under small perturbations. As a result $(1,0)$ is unstable under large perturbations bringing the initial value sufficiently close to the unstable solution $(2,\nu/(2\lambda))$. However, the classical eigenvalue stability analysis is unable to explain the intriguing fact that $(1,0)$ may become unstable even under a small perturbation of the initial data $(1,0)$, if we just have patience to wait! We will now present such a scenario of transition, where the stationary solution $(1,0)$ of (34.9) goes unstable under a small perturbation of initial data of the form $(0,\kappa\nu)$, where κ is a parameter of moderate size, and the scaling with ν makes the perturbation small (since we assume ν to be small). We shall see that if the product $\lambda\kappa$ is above a certain threshold of moderate size, then transition to instability will take place, if we wait over a period of time of length ν^{-1}.

We thus consider the problem (34.9) with the initial data $(1,\kappa\nu)$ close to $(1,0)$, and we ask if the corresponding solution $\bar{w}(t)$ may become unstable after some time. We see that $\dot{\bar{w}}_1(0)/\bar{w}_1(0) = \lambda\kappa\nu$, while $\dot{\bar{w}}_2(0)/\bar{w}_2(0) = -\nu$, which shows that initially $\bar{w}_1$ grows and $\bar{w}_2$ decays at rates $\propto \nu$. Now, $\bar{w}_1$ will continue to grow at that rate as long as $\lambda\bar{w}_2 > \nu$, and further $\bar{w}_2$ will start to grow as soon as $\bar{w}_1 > 2$. Thus, if $\bar{w}_1$ manages to become larger than 2, before $\bar{w}_2$ has decayed below ν/λ, then both components will propel each other to infinity, corresponding to instability. We shall see that this will occur if $\lambda\kappa$ is above a certain threshold. We notice that the time scale for significant changes in both $\bar{w}_1$ and $\bar{w}_2$ is $\sim \nu^{-1}$, which is a long time since ν is small. The scenario is thus that $\bar{w}_1$ grows slowly at the rate ν over a long time, and if $\lambda\kappa$ is above the threshold, then $\bar{w}_1$ may reach the value 2, where also $\bar{w}_2$ starts to grow after which a blow up follows on a usually somewhat shorter time scale (though still $\propto \nu^{-1}$). This scenario is easy to grasp intuitively, and conforms with the every-day experience of a sudden blow-up, as a result of an accumulation of small events over a long period.

Solving the linearized equation (34.11) approximately describing the evolution of $\bar{w} - (1,0)$, we find that

$$\bar{w}_1(t) \approx 1 + \varphi_1 = 1 + \lambda\kappa t\nu \exp(-t\nu), \quad \bar{w}_2(t) \approx \varphi_2 = \kappa\nu \exp(-t\nu), \tag{34.12}$$

which shows the slow growth of $\bar{w}_1$ and slow decay of $\bar{w}_2$ over the long time scale prior to the blow up, occuring if $\lambda\kappa$ is above the threshold. The linear growth in time of φ_1 may be viewed as a consequence of the non-normality of the coefficient matrix A. A classical stability analysis focussing on the double positive eigenvalue ν of $A = [\nu \ -\lambda, 0 \ \nu]$, states that the factor $t\exp(-\nu t)$ eventually will decay to zero as $t \to \infty$, but misses the substantial transient growth to the level $\propto \nu^{-1}$ after time $\propto \nu^{-1}$ prior to decay. This perturbation growth of size $\propto \nu^{-1}$ is capable of bringing a solution from the point $(1,\kappa\nu)$ very close to $(1,0)$, into a neigborhood of the unstable point $(2,\nu(2\lambda))$ with ensuing blow up.

34.17 A bifurcating ode-model

We now consider the following ode-model modeling aspects of Taylor-Couette flow between two rotating cylinders:

$$\begin{aligned} u_{1,t} + u_1 u_2 + \nu u_1 - \gamma u_1 &= 0, \quad t > 0, \\ u_{2,t} - \nu u_1^2 + \nu u_2 &= 0, \quad t > 0, \\ u(0) &= u^0, \end{aligned} \tag{34.13}$$

where γ is a parameter, and u_1 represents a streamwise velocity (modulo a base flow) and u_2 a transversal velocity. This problem admits the *stationary trivial base solution* $(u_1, u_2) = (0, 0)$ for all γ. If $\gamma > \nu$, then also $(\pm\sqrt{\gamma - \nu}, \gamma - \nu)$ is a stationary solution and thus $(u_1, u_2, \gamma) = (0, 0, \nu)$ is a *bifurcation point* with $(\pm\sqrt{\gamma - \nu}, \gamma - \nu)$ the two *bifurcated branches* for $\gamma > \nu$. This is the standard scenario in a *pitchfork bifurcation*. The eigenvalues of the (symmetric) Jacobian $J_0(\gamma)$ at the trivial solution $(0, 0)$ are $\nu - \gamma$ and ν, and thus the trivial branch is stable for $\gamma < \nu$ and unstable for $\gamma > \nu$. The eigenvalues of the Jacobian $J_\pm(\gamma)$ at a bifurcated branch $(\pm\sqrt{\gamma - \nu}, \gamma - \nu)$ for $\gamma > \nu$ are $\frac{1}{2}\nu \pm \sqrt{\frac{1}{4}\nu^2 - 2\nu(\gamma - \nu)}$ and have positive real part, and thus perturbations of the bifurcated branches exhibit exponential decay.

If we follow a transient behavior of solutions of (34.13) with γ slowly increasing with time starting from zero and initial data u^0 small, we will stay close to the trivial branch as long as $\gamma < \nu$, while we will shift to follow close to one of the non-trivial branches when $\gamma > \nu$ depending on the sign of the initial data u_1^0. We will thus always stay close to an exponentially stable branch, and the corresponding Jacobian will always have real parts with positive (stable) real part. The bifurcation point is detected by finding a value of γ_c of γ such that the Jacobian $J_0(\gamma_c)$ has an eigenvalue which is zero (or has zero real part), which in our case is the value $\gamma_c = \nu$. We may call this value a *critical value* of γ. If $\gamma < \gamma_c$, then solutions of (34.13) with u^0 small are stable. However, it is not correct to say that for $\gamma > \gamma_c$, solutions will become unstable, because as we said the solution will then stay close to one of the exponentially stable bifurcated branches. We conclude that detection of a bifurcation point is not a sign of emerging instability, but rather an indication that the flow will seek a new stable configuration with the old (trivial) configuration becoming unstable.

Taylor-Couette flow between two rotationg cylinders may bifurcate at a well determined Reynolds' number identified by an eigenvalue with zero real part of the corresponding Jacobian. However this Reynolds' number, which we may refer to as a critical Reynolds number, has nothing to do with transition to turbulence. Above this critical Reynolds number the flow will find a new stable bifurcated configuration represented by the easily observable rolls in the Taylor-Couette experiments.

We conclude that much of the trouble in classical hydrodynamic stability theory comes from a severe confusion concerning the use of the term *critical Reynolds' number* referring to both (i) bifurcation with a Jacobian having an eigenvalue with zero real part, and to (ii) transition to turbulence with transition occuring above the critical Reynolds number. We have just indicated that (i) and (ii) have very little connection and we have shown above that in fact (ii) cannot have any meaning. So, eliminating (ii) gives a clear definition of a critical Reynolds' number which is then not connected to transition.

We finally remark that the Reynolds experiment is a "hands off" experiment: we just sit and watch the flow suddenly undergo transition to turbulence without any intervention. In the bifurcating Taylor-Couette case on the other hand, we change the speed of at least one of the cylinders slowly through the bifurcation.

34.18 Summary

We sum up our experience from analysis and computation as follows: We consider a given initial laminar highly organized shear flow such as Couette flow between two parallel plates, Poiseuille flow in a pipe or a single jet, at a certain Reynolds number Re of the order of 10000 for Couette and Poiseuille flow, and jet flow. We ask the question if the given flow may undergo transition into a highly fluctuating disorganized turbulent flow under perturbations of initial data and/or driving forces of a certain small magnitude δ with a suitable measure. We may view this as a question of perturbation growth, with a perturbation growth of order $1/\delta$ being necessary for the transition from laminar to turbulent flow, assuming the flow velocity is normalized to be of unit size. Now, perturbation growth in general may couple to exponentially growing eigenmodes in a normal mode analysis, or to algebraic growth because the linearized system is non-normal. To test exponential growth we may use white noise perturbations containing all modes, while the non modal algebraic growth typically is related to the special perturbations of the Taylor-Görtler mechanism.

We find computationally that the jet undergoes transition under small white noise perturbations of initial data. The jet is thus exponentially unstable. We find computationally that Couette flow does not undergo transition under even large white noise perturbations, but does so under small Taylor-Görtler perturbations. We analyze Couette flow analytically and find that linear perturbation growth proportional to the Reynolds number is possible. This resolves the dilemma of traditional hydrodynamic stability analysis claiming that Couette flow is stable based on a modal eigenvalue analysis, and shows that Couette flow may undergo transition under perturbations proportional to the inverse of the Reynolds number. More precisely,

we find transition if the product of a small transversal, streamwise constant, perturbation (of size $\nu \sim 1/Re$) and a very small streamwise perturbation (of size ν^2), is large enough. In particular it follows that the concept of a critical Reynolds number for Couette flow cannot have any meaning: transition or not depends of the size and the type of the perturbations. The experience with Poiseuille flow is similar to that of Couette flow just reported. Concerning the unstable jet flow, we remark that computationally we may set up this problem and study transition, while experimentally it may be very difficult to form the unstable initial jet to be studied.

Of course we may expect to see exponentially growing modes once the transition has been initiated, but we cannot hope to explain the initial phase of transition by the presence of exponentially growing modes. For the (obviously critical) initial phase, we need algebraic growth which is offered by the Taylor-Görtler mechanism in shear flow.

Once again: we focus on the initial most critical phase of transition with large perturbation growth offered by the Taylor-Görtler mechanism, which may change an initially exponentially stable base flow into a new possibly exponentially unstable base flow which may develop into a turbulent flow in a secondary phase. Of course, it is also of interest to study this secondary phase with again computational methods as the only feasible technique because the new base flow may be quite complex, although the original base flow was very simple.

In the computational experiments for Couette and Poiseuille flow we use a 64^3 uniform mesh on the unit cube assuming periodicity in the streamwise direction, with slip or periodic boundary conditions in the horisontal transversal direction. The periodicity in the streamwise direction corresponds physically to recirculation, like in the Taylor-Couette flow between two cylinders.

The periodic boundary conditions may be convenient when studying slow perturbation growth, since a simulation of a channel of say a length 100 is very expensive. A computation of transition to turbulence in a boundary layer, see Fig. 34.24, serves as an example of algbraic perturbation growth in a non-periodic case. When we introduce Taylor-Görtler perturbations of different amplitude at the inflow, where we find that transition is delayed for the perturbation of lower amplitude, again confirming the idea that transition is not a phenomenon determined solely by the Reynolds number, but is a question of perturbation growth, determined by the size and type of perturbations.

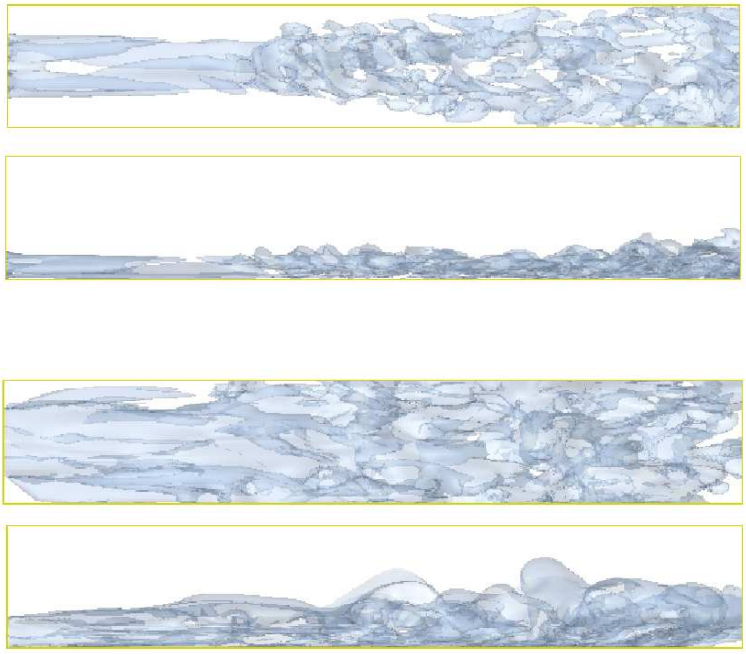

FIGURE 34.24. Isosurfaces for $|(u_2, u_3)| = 0.06$ for transition to turbulence in a boundary layer computation from Chapter 31, for $\nu = 10^6$, $l = 6$, and $b = 1$, introducing Taylor-Görtler type perturbations at the inflow of amplitude 0.1 (upper) and 0.5 (lower), resulting in transition further downstream for the lower perturbation.

References

[1] *Body and soul project*, `http://www.phi.chalmers.se/bodysoul/`.

[2] *Dolfin*, `http://www.fenics.org/dolfin`.

[3] *PETSc*, `http://www-unix.mcs.anl.gov/petsc`.

[4] M. Ainsworth and J. T. Oden, *A posteriori error estimation in finite element analysis*, Computat. Meth. Appl. Mech. Eng., 142 (1997), pp. 1–88.

[5] L. W. Alaways, *Aerodynamics of the curve-ball: and investigation of the effects of angular velocity on baseball trajectories*, PhD thesis, University of California Davis, 1998.

[6] I. Babuška and A. D. Miller, *The post-processing approach in the finite element method, i: Calculation of displacements, stresses and other higher derivatives of the dispacements.*, Int. J. Numer. Meth. Eng., 20 (1984), pp. 1085–1109.

[7] ——, *The post-processing approach in the finite element method, ii: The calculation stress intensity factors.*, Int. J. Numer. Meth. Eng., 20 (1984), pp. 1111–1129.

[8] ——, *The post-processing approach in the finite element method, iii: A posteriori error estimation and adaptive mesh selection*, Int. J. Numer. Meth. Eng., 20 (1984), pp. 2311–2324.

[9] B. Bagheri and L. R. Scott, *Analysa*, http://people.cs.uchicago.edu/ ridg/al/aa.html.

[10] A. T. Bahill, D. G. Baldwin, and J. Venkateswaran, *Predicting a baseball's path*, American Scientist, 93 (1980), pp. 218–225.

[11] R. Becker and R. Rannacher, *A feed-back approach to error control in adaptive finite element methods: Basic analysis and examples*, East-West J. Numer. Math., 4 (1996), pp. 237–264.

[12] ———, *A posteriori error estimation in finite element methods*, Acta Numer., 10 (2001), pp. 1–103.

[13] P. Blossey, *Book review of stability and transition in shear flows*, SIAM Review, 44(1) (2002).

[14] M. Braack and T. Richter, *Solutions of 3d navier-stokes benchmark problems with adaptive finite elements*, Computers and Fluids, 35(4) (2006), pp. 372–392.

[15] A. Brooks and T. Hughes, *Streamline upwinf/petroc-galerkin formulations for convection dominated flows with particular emphasis on the incompressible navier-stokes equations*, Computer methods in applied mechanics and engineering, 32 (1982), pp. 199–259.

[16] S. Buijssen and S. Turek, University of Dortmund, private communication, (2004).

[17] M. J. Carré, T. Asai, T. Akatsuka, and S. J. Haake, *The curve kick of a football ii: flight through the air*, Sports Engineering, 5 (2002), pp. 193–200.

[18] S. Chandrasekhar, *Hydrodynamic and Hydromagnetic Stability*, Dover, 1981.

[19] G. Constantinescu, M. Chapelet, and K. Squires, *Turbulence modeling applied to flow over a sphere*, AIAA Journal, 41(9) (2003), pp. 1733–1742.

[20] G. Constantinescu, R. Pacheco, and K. Squires, *Detached-eddy simulation of flow over a sphere*, AIAA, 2002-0425 (2002).

[21] G. Constantinescu and K. Squires, *Numerical investigations of flow over a sphere in the subcritical and supercritical regimes*, Physics of Fluids, 16(5) (2004), pp. 1449–1466.

[22] J. d'Alembert, *Essai d'une nouvelle théorie de la résistance des fluides*, Paris, http://gallica.bnf.fr/anthologie/notices/00927.htm, 1752.

[23] J. Deng, T. Hou, and X. Yu, *Geometric properties and nonblowup of 3d incompressible euler flow*, Comm. in Partial Differential Equations, 30 (2005), pp. 225–243.

[24] P. Diaconis, `http://news-service.stanford.edu/news/2004/june9/diaconis-69.html`, (2004).

[25] J. Duchon and R. Robert, *Inertial energy dissipation for weak solutions of incompressible euler and navier-stokes solutions*, Nonlinearity, (2000), pp. 249–255.

[26] H. Elman, D. Silvester, and A. Wathen, *Finite Elements and Fast Iterative Solvers: with applications in incompressible fluid dynamics*, Oxford University Press, Oxford, 2005.

[27] K. Eriksson, D. Estep, P. Hansbo, and C. Johnson, *Introduction to adaptive methods for differential equations*, Acta Numer., 4 (1995), pp. 105–158.

[28] K. Eriksson, D. Estep, and C. Johnson, *Applied Mathematics Body and Soul: Vol I-III*, Springer-Verlag Publishing, 2003.

[29] K. Eriksson and C. Johnson, *An adaptive finite element method for linear elliptic problems*, Math. Comp., 50 (1988), pp. 361–383.

[30] L. Euler, *Principes generaux du mouvements des fluides*, l'Academie de Berlin, 1755.

[31] U. Frisch, *Turbulence - The Legacy of A. N. Kolmogorov*, Cambridge University Press, 1995.

[32] M. Germano, U. Poimelli, P. Moin, and W. Cabot, *A dynamic subgrid scale eddy-viscosity model*, Phys. Fluids A, 3 (1991), p. 1760.

[33] M. Giles, M. Larson, M. Levenstam, and E. Süli, *Adaptive error control for finite element approximations of the lift and drag coefficients in viscous flow*, Technical Report NA-76/06, Oxford University Computing Laboratory, (1997).

[34] M. Giles and E. Süli, *Adjoint methods for pdes: a posteriori error analysis and postprocessing by duality*, Acta Numer., 11 (2002), pp. 145–236.

[35] P. Hansbo, *A crank-nicolson type space-time finite element method for computing on moving meshes*, Journal of Computational Physics, 159 (2000), pp. 274–289.

[36] P. Hansbo and A. Szepessy, *A velocity-pressure streamline diffusion finite element method for the incompressible navier-stokes equations*, Computer methods in applied mechanics and engineering, 84 (1990), pp. 175–192.

[37] R. Hartmann and P. Houston, *Goal-oriented a posteriori error estimation for multiple target functionals*, in Hyperbolic problems: theory, numerics, applications, (T.Y. Hou and E. Tadmor, editors), pp. 579-588, Springer, 2003.

[38] V. Heuveline and R. Rannacher, *Duality-based adaptivity in the hp-finite element method*, J. Numer. Math., 11(2) (2003), pp. 95–113.

[39] J. Heywood, *Remarks on the possible global regularity of solutions of the three-dimensional navier-stokes equations.*

[40] J. Hoffman, *On duality based a posteriori error estimation in various norms and linear functionals for les*, SIAM J. Sci. Comput., 26(1) (2004), pp. 178–195.

[41] ——, *Computation of mean drag for bluff body problems using adaptive dns/les*, SIAM J. Sci. Comput., 27(1) (2005), pp. 184–207.

[42] ——, *Adaptive simulation of the turbulent flow past a sphere*, J. Fluid Mech., (accepted).

[43] ——, *Computation of turbulent flow past bluff bodies using adaptive general galerkin methods: drag crisis and turbulent euler solutions*, Computational Mechanics, (accepted).

[44] ——, *Efficient computation of mean drag for the subcritical flow past a circular cylinder using general galerkin g2*, Int. J. Numer. Meth. Fluids, (accepted).

[45] ——, *Adaptive simulation of the turbulent flow due to a cylinder rolling along ground*, (in review).

[46] J. Hoffman and C. Johnson, *Adaptive finite element methods for incompressible fluid flow*, Error Estimation and Solution Adaptive Discretization in Computational Fluid Dynamics (Ed. T. J. Barth and H. Deconinck), Lecture Notes in Computational Science and Engineering, Springer-Verlag Publishing, Heidelberg, 2002, pp. 97–158.

[47] ——, *Irreversibility in reversible systems i: The compressible euler equations in 1d*, Chalmers Finite Element Center Preprint 2005-03, Chalmers University of Technology, (2005).

[48] ——, *Irreversibility in reversible systems ii: The incompressible euler equations*, Chalmers Finite Element Center Preprint 2005-04, Chalmers University of Technology, (2005).

[49] ——, *Irreversibility in reversible systems iii: Compressible euler in 3d*, (in preparation).

[50] ——, *Irreversibility in reversible systems iv: Kinetic gas theory*, (in preparation).

[51] ——, *A new approach to computational turbulence modeling*, Comput. Methods Appl. Mech. Engrg., (in press).

[52] ——, *Stability of the dual navier-stokes equations and efficient computation of mean output in turbulent flow using adaptive dns/les*, Comput. Methods Appl. Mech. Engrg., (in press).

[53] ——, *Is the world a clock with finite precision?*, SIAM J. Sci. Comput., (in review).

[54] J. Hoffman, C. Johnson, and A. Logg, *Dreams of Calculus: Perspectives on Mathematics Education*, Springer-Verlag Publishing, 2004.

[55] J. Hoffman and A. Logg, *Dolfin - dynamic object oriented library for finite element computation*, Chalmers Finite Element Center Preprint 2002-06, Chalmers University of Technology, (2002).

[56] T. Hughes and T. Tezduyar, *Finite element methods for first-order hyperbolic systems with particular emphasis on the compressible euler equations*, Computer methods in applied mechanics and engineering, 45 (1984), pp. 217–284.

[57] T. J. R. Hughes, L. Mazzei, and K. E. Jansen, *Large eddy simulation and the variational multiscale method*, Computer methods in applied mechanics and engineering, 3 (2000), pp. 47–59.

[58] V. John, *Slip with friction and penetration with resistance boundary conditions for the navier–stokes equations - numerical tests and aspects of the implementation*, J. Comp. Appl. Math., 147 (2002), pp. 287–300.

[59] V. John and A. Liakos, *Time dependent flow across a step: the slip with friction boundary condition*, accepted for publication in Int. J. Numer. Meth. Fluids, (2005).

[60] C. Johnson, U. Nävert, and J. Pitkäranta, *Finite element methods for linear hyperbolic equations*, Comput. Methods Appl. Mech. Eng., 45 (1984), pp. 285–312.

[61] C. Johnson and R. Rannacher, *On error control in CFD*, Int. Workshop Numerical Methods for the Navier-Stokes Equations (F.K. Hebeker et.al. eds.), Vol. 47 of *Notes Numer. Fluid Mech.*, Vierweg, Braunschweig, 1994, pp. 133–144.

[62] C. Johnson, R. Rannacher, and M. Boman, *Numerics and hydrodynamic stability: Toward error control in cfd*, SIAM J. Numer. Anal., 32 (1995), pp. 1058–1079.

[63] G.-S. Karamanos and G. E. Karniadakis, *A spectral vanishing viscosity method for large-eddy simulations*, Journal of Computational Physics, 163 (2000), pp. 22–50.

[64] A. N. Kolmogorov, *Dissipation of energy in locally isotropic turbulence*, Dokl. Akad. Nauk SSSR, 32 (1941), pp. 16–18.

[65] ——, *The local structure of turbulence in incompressible viscous fluid for very large reynolds number*, Dokl. Akad. Nauk SSSR, 30 (1941), pp. 299–303.

[66] ——, *On degeneration (decay) of isotropic turbulence in an incompressible viscous liquid*, Dokl. Akad. Nauk SSSR, 31 (1941), pp. 538–540.

[67] S. Krajnović and L. Davidson, *Large-eddy simulation of the flow around a bluff body*, AIAA Journal, 40 (2002), pp. 927–936.

[68] J. Leray, *Sur le mouvement d'un liquide visqueux emplissant l'espace.*, Acta Mathematica, 63 (1934), pp. 193–248.

[69] J. Lions, *Quelques méthodes de résolution des problémes.*

[70] A. Logg, *Automation of Computational Mathematical Modeling*, PhD thesis, Chalmers, 2004.

[71] E. Lorenz, *Deterministic nonperiodic flow*, J. Atmospheric Sciences, 20 (1963).

[72] J. Loschmidt, *Sitzungsber. kais. akad. wiss. wien, math.*, Naturwiss. Classe 73, (1876), pp. 128–142.

[73] J. C. Maxwell, Phil. Trans. Royal Society, (1879).

[74] NASA, *Various views of von karman vortices*, http://disc.gsfc.nasa.gov/oceancolor/scifocus/oceanColor/vonKarman_vortices.shtml, (2005).

[75] C. L. M. H. Navier, *Mémoire sur les lois du mouvement des fluiales*, Mém. Acad. Royal Society, 6 (1823), pp. 389–440.

[76] H. Poincaré, *Science and Method, 1903, Dover 1982.aux limites non linéaires*, Dunod, Paris, 1969.

[77] Prandtl, *Prandtl standard view*, www.fluidmech.net/msc/prandtl.htm, (2006).

[78] R. Rannacher, *Finite element methods for the incompressible navier stokes equations*, Preprint Intsitute of Applied Mathematics, Univ. of Heidelberg, (1999).

[79] W. Rodi, J. H. Ferziger, M. Breuer, and M. Pourquié, *Status of large eddy simulation: Results of a workshop*, ASME Journal of Fluids Engineering, 119 (1997), pp. 248–262.

[80] P. Sagaut, *Large Eddy Simulation for Incompressible Flows*, Springer-Verlag, Berlin, Heidelberg, New York, 2001.

[81] H. Schlichting, *Boundary Layer Theory*, McGraw-Hill, 1955.

[82] P. Schmid and D. Henningson, *Stability and Transition in Shear Flows: Applied Mathematical Sciences 142*, Springer, 2001.

[83] J. Smagorinsky, *General circulation experiments with the primitive equations, part i: The basic experiment*, Mon. Wea. Rev., 91 (1963), p. 99.

[84] A. Sommerfeld, *Ein beitrag zur hydrodynamischen erklärung der turbulenten flüssigkeitsbewegungen*, Atti del 4. Congr. Internat.dei Mat. III, Roma, (1908), pp. 116–124.

[85] S. Turek, *Efficient Solvers for Incompressible Flow Problems: An Algorithmic and Computational Approach*, Springer, Berlin, 1999.

[86] R. Verfürth, *A Review of A Posteriori Error Estimation and Adaptive Mesh Refinement Teqniques*, Wiley/Teubner, New York/Stuttgart, 1996.

[87] M. M. Zdravkovich, *Flow around circular cylinders: a comprehensive guide through flow phenomena, experiments, applications, mathematical models, and simulations. Vol.1 [Fundamentals]*, Oxford Univ. Press, Oxford, 1997.